INDEPENDENT AND COMPETING ROLES OF FLUID EXUDATION AND

REHYDRATION IN CARTILAGE MECHANICS AND TRIBOLOGY

by

Axel C. Moore

A dissertation submitted to the Faculty of the University of Delaware in partial fulfillment of the requirements for the degree of Doctor of Philosophy in Biomedical Engineering

Fall 2017

INDEPENDENT AND COMPETING ROLES OF FLUID EXUDATION AND

REHYDRATION IN CARTILAGE MECHANICS AND TRIBOLOGY

by

Axel C. Moore

Approved: _____
Dawn M. Elliott, Ph.D.
Chair of the Department of Biomedical Engineering

Approved: _____
Babatunde A. Ogunnaike, Ph.D.
Dean of the College of Engineering

Approved: _____
Ann L. Ardis, Ph.D.
Senior Vice Provost for Graduate and Professional Education

I certify that I have read this dissertation and that in my opinion it meets the academic and professional standard required by the University as a dissertation for the degree of Doctor of Philosophy.

Signed: _____

David L. Burris, Ph.D.
Professor in charge of dissertation

I certify that I have read this dissertation and that in my opinion it meets the academic and professional standard required by the University as a dissertation for the degree of Doctor of Philosophy.

Signed: _____

Jason P. Gleghorn, Ph.D.
Member of dissertation committee

I certify that I have read this dissertation and that in my opinion it meets the academic and professional standard required by the University as a dissertation for the degree of Doctor of Philosophy.

Signed: _____

Dawn M. Elliott, Ph.D.
Member of dissertation committee

I certify that I have read this dissertation and that in my opinion it meets the academic and professional standard required by the University as a dissertation for the degree of Doctor of Philosophy.

Signed: _____

Christopher Price, Ph.D.
Member of dissertation committee

I certify that I have read this dissertation and that in my opinion it meets the academic and professional standard required by the University as a dissertation for the degree of Doctor of Philosophy.

Signed: _____

Jennifer Buckley, Ph.D.
Member of dissertation committee

This dissertation is dedicated to my parents (Layton and Margaret Moore), my sister (Sophia Moore), and my wife (Esther Moore) and Her fur babies (Sir Isaac Newton, Purrfessor Johannes Kepler, and Madame Marie Skłodowska Curie).

ACKNOWLEDGMENTS

I thank my dissertation committee (Drs. Dawn Elliott, Jason Gleghorn, Christopher Price, and Jennifer Buckley) for their support, mentoring, and willingness to read this dissertation. Furthermore, I am grateful for the wonderful staff at the Delaware Biotechnology Institute, namely Michael Moore, and the Keck Electron Microscopy facility, namely Drs. Chow Ni, Jennifer Sloppy, and Fe Deng.

Throughout my time here I have worked on numerous collaborative projects that have helped to challenge and further my scientific interest. I gratefully appreciate the collaborations formed with Drs. Christopher Price, Dawn Elliott, Lucas Lu, Xinqiao Jia, and Jason Gleghorn and their students Brian Graham, John DeLucca, Chen Xingyu, Kevin Dicker, Wade Stewart, and Dr. Shuang Liu.

For the generally fun and enjoyable graduate school experience I thank my wonderful lab mates (Drs. Harman Khare, Jiaxin Ye and Diana Haidar, and Nikolay Garabedian, Benjamin Gould, Arnab Bhattacharjee, Istiaque Alam, and Viraj Sachpara). To my wonderful undergraduate researchers, who are too numerous to list, I thank you for teaching me how to teach and for running experiments in my absence.

For teaching me mental and physical endurance and reminding me to enjoy the small things in life I thank my wonderful parents (Margaret and Layton Moore) and

sister (Sophia Moore). For giving me both the small and big things in life I thank my wife (Esther Moore) for whom my love is and will always be endless.

Finally, to my adviser, mentor, collaborator, and friend, Dr. David Burris, you have guided me these last five years and given me an unwavering interest, energy, excitement and dedication to science.

TABLE OF CONTENTS

LIST OF FIGURES

LIST OF ABBREVIATIONS AND IMPORTANT TERMS

Analysis of Variance (ANOVA) – a statistical method to test the hypothesis that the observed differences happened by random chance and thus the 'treatment' had no effect

Anterior Cruciate Ligament (ACL) – a stabilizing structure found in many mammalian (human, bovine) knee joints

Articular Cartilage (AC) – a 1 to 5 mm thick tissue that covers the ends of long bones in articulating joints

Computer Numeric Control (CNC) – a digitized method for controlling the motion of motorized equipment

Convergent Stationary Contact Area (cSCA) – when the stress field on the sample doesn't move despite relative motion at the interface; furthermore, convergence zones are present at the leading and trailing edge of the contact; the most common configuration is placing a curved sample of interest in contact with a sliding rigid flat

Hyaluronic Acid (HA) – an unbranched biopolymer found in the joint space. HA is known for its hydrophilicity and shear thinning effects

Hydrodynamic – the mechanics of fluids as they move relative to themselves and other bodies

Interstitial Fluid – the fluid contained within a matrix

Interstitial Fluid Pressure (IFP) – the liquid stress generated when forced to permeate a semi-permeable membrane or matrix

Joint Space Narrowing – the distance between the terminal ends of bones in articulating joints; the distance is assumed to be representative of the cartilage thickness for 2 surfaces

Linear Biphasic Theory (LBT) – a continuum mechanics model based on the interaction between a fluid and solid phase. The solid phase is linear elastic.

Tension-Compression Nonlinear Theory (TCN) – a continuum mechanics model based on the interaction between a fluid and solid phase. The solid phase possesses a unique modulus in tension and compression.

Migrating Contact Area (MCA) – when the stress field on the sample moves with the relative motion of the interface; the most common configuration is to place a sliding curved body in contact with a sample of interest

Osmotic Swelling – the electro-chemical gradient established by enmeshed proteoglycans and dissolved ionic salts

Osteoarthritis (OA) – a generic term to describe articular cartilage degradation and removal

Stationary Contact Area (SCA) – when the stress field on the sample doesn't move despite relative motion at the interface; the most common configuration is placing a sample of interest in contact with a sliding rigid flat

Tribological Rehydration – sliding induced fluid recovery

Tribology – the science and study of surfaces undergoing contact and relative motion

Wet Lubrication (WL) – a generic term used to describe the role of hydration on reducing friction in cartilage contacts

LIST OF SYMBOLS

A – sample or contact area

a – contact radius

D – sample or contact diameter

E – Young's modulus of elasticity

E_c – effective contact modulus (substrate corrected)

E_{c0} – equilibrium contact modulus

E_c', E' – effective contact modulus (non-substrate corrected)

E_t, E_{y+} – tensile modulus

E_{y-} – compressive modulus

E^* – tensile to compressive modulus ratio

F, F_n – normal force

F_e – elastic load support

F_f – friction force

F_{inf} – reaction force on an infinite layer

F_{layer} – reaction force on an elastic layer

F_p – fluid load support

f_p – reaction force reduction fraction

F_t – total applied load

F' – fluid load fraction

F'_{max} – maximum fluid load fraction

H_a – aggregate modulus

h_{min} – central film thickness

k – effective permeability

k_0 – reference permeability

M – solution molarity

M – flow limiting constant

P – fluid pressure

p value – probability that the null hypothesis is correct and the observed difference/s happened by random chance

Pe – Péclet's number

q – fluid velocity

R – radius of curvature

r – radial position

R_a – average roughness

R' – effective radius of curvature

$R*$ – dimensionless contact radius

R^2 – coefficient of determination

t – tissue thickness

t^* – dimensionless thickness (t/a)

U – dimensionless sliding speed

V, u – sliding velocity

W – Dimensionless load

x – compression

x_{max} – maximum compression

x_{min} – minimum compression

x^* – compression fraction

ξ – fiber modulus

ε – strain

δ – compression

δ_{eq} – equilibrium compression

δ_{off} – surface offset

η – effective viscosity

σ, σ_- – mean normal stress, contact stress, compressive stress

σ_e – elastic stress

σ_+ – tensile stress

τ – mean shear stress

θ - angular position

μ – friction coefficient

μ_{eff} – effective friction coefficient

μ_{eq} – equilibrium friction coefficient

v – Poisson's ratio

ABSTRACT

Articular cartilage is the load bearing and lubricating material of articulating joints. While the exact mechanism/s of joint lubrication still remain a topic of scientific debate it is well accepted that tissue hydration plays a pivotal role in this process. The first part of this dissertation focuses on the development, extension, validation, and application of a tribo-mechanics model to describe the role of interstitial fluid (hydration) in cartilage mechanics and lubrication. The second part of this dissertation details the discovery of a phenomenon termed tribological rehydration (sliding-induced fluid recovery) and attempts to provide mechanistic insights into the governing features.

An analytical tribo-mechanics model was developed to study articular cartilage contacts. The model was developed for rate based sliding and indentation as well as creep loading with a spherical indenter. Each iteration of the original model included additional parameters that were relevant to the physiological condition (substrate effects, strain dependent permeability). Furthermore, each iteration applied different techniques for model validation (comparisons to literature, other testing methods, and other accepted models). The final step in the development of these tribo-mechanics models was to demonstrate their utility by studying the regional variations in cartilage material and tribological properties.

While the analytical models were developed to study the mechanical and tribological effect of fluid exudation, it was discovered that interfacial sliding was capable of driving fluid back into articular cartilage. This novel sliding-induced fluid

recovery phenomenon was termed tribological rehydration. Following a series of investigations, it was demonstrated that sliding develops significant hydrodynamic pressures and that the role of the permeable interface is to provide a preferred path for fluid flow into the tissue. This alternate path of fluid flow is capable of restoring cartilage lubricity, load bearing, and its hydrated nature. It was also found that the hydrodynamic parameters: sliding speed; load; contact geometry; and fluid viscosity greatly influence the efficacy of tribological rehydration, suggesting that hydrodynamic forces drive this phenomenon. Finally, by replicating in-vivo experiments ex-vivo it appears that tribological rehydration may play a major role in maintaining normal joint function and health.

Chapter 1

INTRODUCTION

1.1 Articular Cartilage and Osteoarthritis

Articular cartilage (AC) is the load bearing and lubricious material of mammalian joints [1]. In healthy joints, the AC effectively shields the ends of long bones from making bone-on-bone contact and enables pain-free use of joints. Unfortunately, for more than 40 million people the cartilage lining (1 to 5 mm thick) of one or more joints is compromised and results in intimate contact between bony surfaces [2,3]; this results in substantial joint pain and loss of joint function. The disease attributed to the loss of the AC lining is commonly referred to as osteoarthritis (OA) [4,5]. Mechanisms that initiate and drive OA are thought to be an interplay of biological (enzymatic and cellular) and mechanical (stress, strain, rate and frequency) factors [6–10].

1.2 Cartilage Shouldn't Last, but it Does

The overarching goal of the cartilage research field is to provide therapeutic approaches to OA. Researchers, engineers, scientists, and clinicians are trying to develop ways to prevent or delay tissue degradation [3,5,9,11–13], repair damaged tissue [14–17], and in the end, replace it [18–20]. However, predicting and assessing the efficacy of each therapeutic approach requires prior knowledge of how healthy cartilage functions and why it is an effective bearing material.

Articular cartilage is a unique bearing material because it violates some of the most fundamental principles on how bearings should be made. In general, man-made bearings are smooth, conformal, and impermeable. Furthermore, they tend to operate in a single axis of motion with a fluid that has a sufficient viscosity to match the typical operation conditions (e.g. load and speed). Cartilage on the other hand is a rough (0.5 to 5 µm) [21,22], non-conformal [23–25], and permeable (0.01 to 0.0001 mm^4/Ns) [1,6,26–31] material bathed in a fluid that is only ~2X the viscosity of water at physiological speeds [24,32–34]. The mechanical environment of human joints is also highly undesirable from a general engineered bearing point of view. Engineered bearings are designed to work in specific load regimes, at specific operating speeds, and preferably in a single axis and direction of motion (e.g. hydrodynamic journal bearings) [35]. Human joints undergo wide fluctuations in contact stress (~0 to 5+ MPa in the human knee joint) and surface speeds ranging from 0 to 100 mm/s (mean walking speed in the human knee joint) [4,36–38]; in addition, every cycle includes a reversal where the speed by definition must go to 0 mm/s and reverse direction [23]. Clearly the tissue properties, fluid, and mechanical environment of mammalian joints do not adhere to the basic design of man-made bearings.

How does cartilage, this seemingly unfit bearing material, last for 50+ years for much of the population? One thought is that the cartilage cells, chondrocytes, have a synthesis rate comparable to the wear rate of the tissue. However, nearly everything known about cartilage suggests that it has one of the slowest turnover and synthesis rates of any tissue in the body [39]. Cartilage has a limited ability to grow and repair because once the tidemark (a semi-impermeable boundary of calcified cartilage)

forms, the articular cartilage loses its vascular network and thus a major source of nutrient supply and waste removal [40]. This means that the only source of nutrient and waste transport for the chondrocytes must come from the surrounding synovial fluid bath via free diffusion [41,42] or mechanical pumping [41–44].

Clinicians have tried to circumvent the nutrient supply problem by punching or drilling holes into the tidemark (micro-fracture surgery) to allow blood and mesenchymal stem cells to populate areas of damaged tissue in the hopes of creating new AC [14]. Unfortunately, the resulting tissue possesses inferior mechanical and tribological properties and resembles fibro cartilage rather than AC [14]. While other repair and treatment strategies exist, there has been limited ability to recapitulate the unique structure and function of AC [20].

Thus far there is little evidence to support Nature's decision to use cartilage as the bearing material of natural joints. Cartilage has seemingly poor bearing properties, it has a slow synthesis rate, and even when it is supplied with plenty of nutrients and a cell source it tends to make a mechanically inferior repair tissue. It is for these reasons and others that conventional wisdom would suggest that activity (e.g. running, walking) will cause joints to wear out quicker [45]. However, there is little evidence to support that claim. In fact, recent work has demonstrated that those who regularly exercise without the use of high impact (e.g. football) or cutting type movements (e.g. basketball) are at a substantially lower risk for developing OA [45–49]. And so this begs the questions: why is joint activity chondro-protective and is cartilage actually a poor bearing material.

Chapter 2

BRIEF HISTORY OF CARTILAGE MECHANICS AND LUBRICATION

2.1   Where it All Began

While the mechanical role of AC has been known for many centuries, the first real investigation into the mechanics and function of the tissue wasn't carried out until the 1930's. That is when Jones measured the friction of whole intact ox joints and found friction coefficients on the order of 0.02 [50]. This ultra-low friction coefficient, coupled with the observation that cartilage surfaces created convergent zones along their axis of articulation, led MacConaill to proposed the theory of hydrodynamic lubrication for human joints [51]. This well-known lubrication theory was quickly adopted by others and is the standard textbook description of cartilage lubrication [21,50,52–54]. However, Charnley later demonstrated that even at nearly zero sliding speed the friction coefficient was virtually unaffected and thus proposed boundary lubrication as the mechanism of animal joints [23].

The final major rift in cartilage lubrication theory came from the work of McCutchen who proposed the theory of weeping lubrication [1,55]. The theory of weeping lubrication, which will be explained in more detail later, models cartilage as a deformable hydrostatic bearing where deformation of the solid matrix causes fluid to flow through the permeable tissue inducing internal fluid pressurization. To understand the justifications behind each cartilage lubrication theory requires a general understanding of lubrication fundamentals.

2.2   Fundamentals of Lubrication

The role of a lubricant is to form a low shear strength interface between two surfaces that would otherwise make direct contact [56]. If direct contact occurs conditions of high friction and more importantly wear or damage may result [22]. There are two primary regimes of lubrication: (1) fluid film and (2) boundary or dry (Figure 2.1).
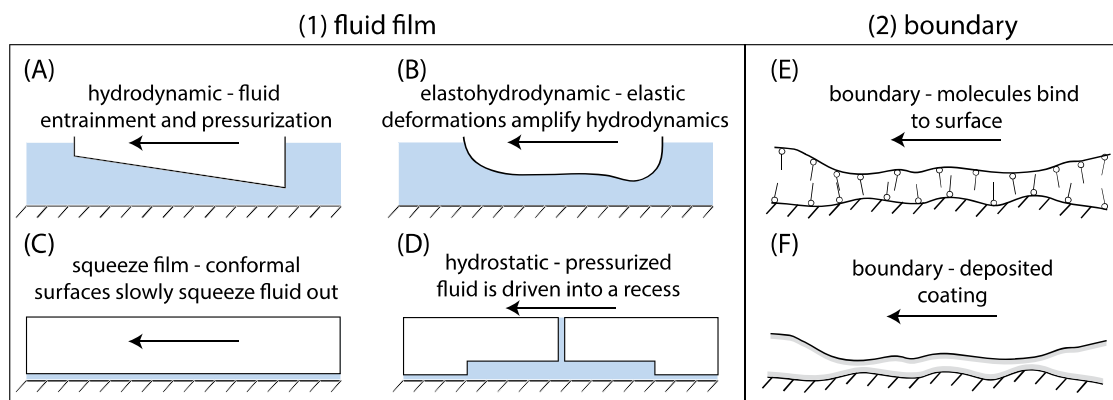
Figure 2.1   Classical theories of lubrication. (1) Fluid film theories include (A) hydrodynamic, (B) elasto-hydrodynamic, (C) squeeze film, and (D) hydrostatic lubrication. (2) Boundary lubrication theories include (E) the attachment of surface active molecules and (F) deposited films. Note that this list does not encompass all lubrication theories.

2.2.1   Fluid Film Lubrication

Fluid film lubrication protects surfaces by physically separating them via a layer of fluid; there are three principle ways to separate surfaces. The first mechanism, hydrodynamic lubrication (Figure 2.1A and 2.1B), uses relative motion of the surfaces to draw fluid into a convergent wedge. As the wedge narrows the fluid becomes further confined and pressurized, and under sufficient conditions of speed, load, viscosity, modulus, and curvature a fluid film will form [21,50,51,56,57]. The second

mechanism, squeeze film lubrication (Figure 2.1C), describes the approach of two surfaces that were previously separated. The two surfaces will approach one another based on the separation distance, fluid viscosity, load, and geometry [52,53,58–60]. The last major mechanism for developing fluid films is hydrostatic lubrication (Figure 2.1D). In this system, an external pump drives pressurized into a recessed pocket acting to support a fraction of the applied load. Hydrostatic lubrication is dependent upon geometry, supply pressure, load, and fluid viscosity [61]. It should be noted that in every form of fluid film lubrication there is a strong dependence on the applied load, geometry, and fluid viscosity. Additionally, roughness, a parameter that can be difficult to model, also plays a significant role in these forms of lubrication [21,62,63].

2.2.2 Boundary and Dry Lubrication

Boundary lubrication can occur under two major conditions: (1) boundary films adsorbed on to surfaces (Figure 2.1E) and (2) solid/dry lubricant coatings or materials (Figure 2.1F) [64–66]. Boundary films are created when surface active molecules (typically polar) are exposed to the bearing surface and get adsorbed [1,65,67]. While the boundary molecules can attach tenaciously or weakly, their role is to create a molecular layer of protection that can be replenished after each cycle. Unlike boundary films, dry lubricants do not get recycled on each pass and thus must be tenaciously bound or sufficiently thick to prevent the failure of the film [65,68,69].

2.3 Applying Classical Lubrication Theories to Articular Cartilage

While the classical lubrication theories create a convenient framework for studying AC lubrication, nearly every one of them has been refuted to some degree experimentally and/or theoretically.

Hydrodynamic lubrication is arguably the most well-known form of lubrication (not the most common) and was also the first mechanism suggested for joints [32,50–52,70]. The observed convergent nature of human joints, presence of deformable fibrous structures (e.g. menisci), and remarkably low friction coefficients (~0.01) are highly suggestive of hydrodynamics. However, it was discovered that even at nearly zero speed the friction coefficient was unchanged; this lack of speed dependence experimentally refutes hydrodynamic fluid film theory in joint lubrication [23].

Squeeze film lubrication requires the separation of joint surfaces either through pulling them apart or by the development of a fluid film. While neither a fluid film or joint separation is likely, it has been demonstrated that squeeze films will last no more than a fraction of a second should they form [71–73]. This result is supported by McCutchen who demonstrated that briefly separating cartilage from a glass counterface doesn't restore its original lubricity [1].

Traditional hydrostatic lubrication requires the use of an external pump to drive pressurized fluid into the contact interface. While the idea of an external fluid pump for joints violates basic anatomy, a hybrid form of this theory will be introduced in section *2.4 Hydration and its Role in Cartilage Lubrication*.

Boundary lubrication has been possibly the most intensely debated topic of joint lubrication. The debate has little to do with whether or not boundary lubricants exist in synovial fluid and if they play a role, but rather how much they contribute to friction reduction versus wear reduction [22]. Synovial fluid is a distillate of blood plasma with the addition of hyaluronic acid (large non-sulfated glycosaminoglycans) and lubricin [24,74–79]. Prior research suggests that boundary lubrication does occur, that lubricin [24,76,77] is the primary boundary lubricant, and that it is capable of

reducing the friction coefficient by a factor of ~2X when compared to saline or deionized water [1,22,80].

2.4   Hydration and its Role in Cartilage Lubrication

While cartilage has been shown to be speed independent [23] and only weakly dependent on the lubricating fluid [1,22,24,67,80–82], McCutchen demonstrated that the friction coefficient was strongly dependent on tissue deformation. He reasoned that articular cartilage, a fluid soaked tissue, would deform under load and thus drive/weep fluid from its matrix (Figure 2.2C). This fluid flux, as described by Darcy's Law, generates a fluid pressure gradient with maximum pressure at the contact interface and minimum pressure at the free surface [1,22,28,31,83,84]. From a mechanics point of view, interstitial fluid pressurization (IFP) plays 2 critical roles: (1) effectively stiffens the tissue [22,28,85–87] and (2) shields the matrix from damaging shear stresses [1,22,24,28,29]. McCutchen's theory on AC lubrication simultaneously explained why friction was independent of speed, virtually independent of the 'lubricating' fluid, and increased with loading duration, tissue deformation, and loss of hydration.

Contemporary Lubrication Theories for Hydrated Materials
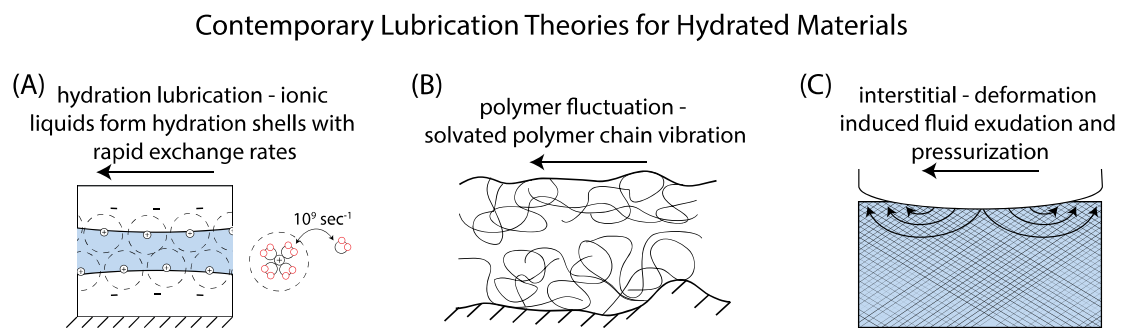
Figure 2.2   Contemporary forms of cartilage lubrication: (A) hydration, (B) polymer or thermal fluctuation, and (C) interstitial. Note that this list does not encompass all of the lubrication theories; however, it represents the theories most commonly applied to cartilage lubrication.

In the years following McCutchen's weeping lubrication theory, many other lubrication theories were established based on a similar framework, e.g. boosted [58,59,88], biphasic [4,29,89], hydration (Figure 2.2A) [90], polymer or thermal fluctuation (Figure 2.2B) [91,92], consolidation [93,94], and interstitial (Figure 2.2C) [22,28,86]. While minor differences can be pointed out between these theories they are for the purposes of this work the same. From here on the lubricating phenomenon related to cartilage hydration will be referred to as 'wet lubrication' (WL).

2.4.1   Time Dependence of Interstitial Fluid Pressure and Wet Lubrication

While the concept of IFP was generally acknowledged, there was no direct measure of the phenomenon until 2004, when Ateshian and co-workers simultaneously measured fluid pressure, friction and strain [95]. Here, the authors demonstrated that IFP was capable of supporting nearly 100% of the applied load (i.e. fluid pressure = contact stress), and that tissue strain, friction, and IFP were all directly related and interchangeable (i.e. high IFP = low strain = low friction), see Figure 2.2. As previously discussed, WL depends on tissue hydration which is directly related to tissue strain. This relation assumes that the individual constituents of cartilage are incompressible at physiological loadings [96], Poisson's ratio is ~0 [86,97], and flow-independent viscoelastic effects are minimal and short lived (compared to the flow-dependent effects) [98]. The results of Ateshian and co-workers demonstrated that IFP was directly related to WL, and that its role in cartilage lubrication was much more powerful and dominant than previously acknowledged. While boundary lubricants in synovial fluid may reduce friction by a factor of ~2X (relative to saline or deionized water) [1,22,24,80,81], the loss of IFP and thus WL, can increase friction by more than a factor of 50X (relative to the fully hydrated condition) [1,6,24,28,37,80,83,84].
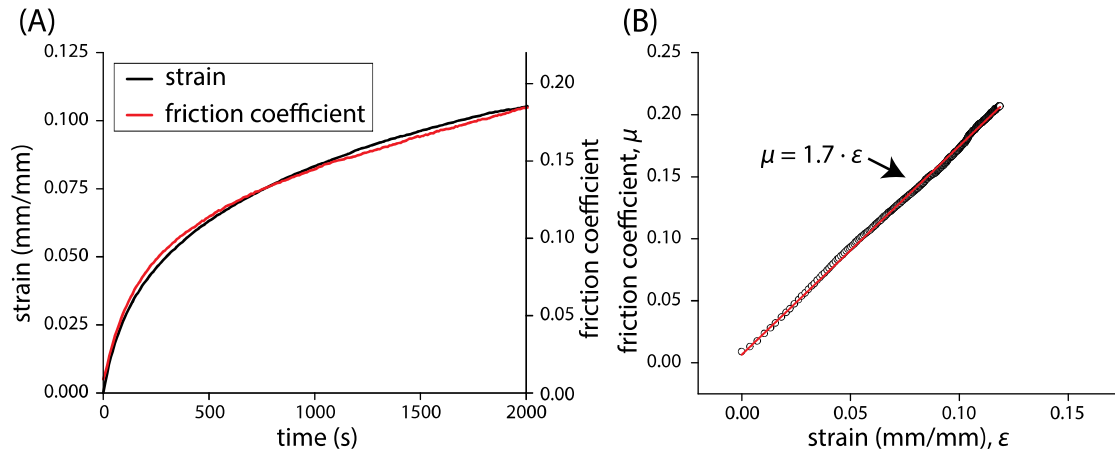
Figure 2.3   (A) A representative data set illustrating the relationship between tissue strain (compression, deformation, loss of fluid) and friction versus time. (B) As previously demonstrated friction coefficient and tissue strain are linearly proportional [95], suggesting an intimate relationship. Data were collected on the in-situ materials tester, section *8.2.4 In-Situ Materials Tester.*

2.4.2   Maintaining Wet Lubrication

However, there was one major fault to IFP theory — it wasn't sustainable; thus, neither was WL (Figure 2.3A). This finding would suggest that joint use (walking, running, etc.) is bad and may predispose a person for developing OA. Thankfully, interstitial theory predicted a mechanism to prevent the eventual loss of fluid and function [28,84,99].

The ability to maintain hydration and IFP was framed around the concept that fluid cannot flow instantaneously, meaning that when IFP is first developed no flow has occurred. Therefore, if the load can be removed fast enough then fluid content (hydration) and function can be retained. In other words, making contact with cartilage results in IFP; this pressure gradient will drive fluid out of the tissue unless it goes back to ambient or sub-ambient pressure. Depressurizing the contact can be done by

10

pulling the surfaces apart or by moving/sliding the contact area to a new region on the cartilage surface [84].

This concept led to the development of what is now known as a migrating contact area in which the contact area on the cartilage surface slides back and forth across the tissue, see Figure 2.4B. The experiment is typically performed using a rigid sphere sliding on cartilage, but a cylinder or opposing cartilage surface works equally well [84,99]. The key aspect to the phenomenon is that the contact migrates faster than the pressurized fluid can flow and that it completely uncovers the area of contact (i.e. long enough track lengths) [22,37,84,99]. A secondary mechanism thought to benefit a migrating contact area is osmotic swelling in which the electro-chemical gradient between the cartilage and bath solution will pull fluid back into the cartilage when the contact is exposed. While osmotic swelling does participate in tissue recovery its driving force should be no greater than the absolute environmental pressure; for cartilage, this is approximately the osmotic pressure (0.2 MPa) + atmospheric pressure (0.1 MPa). The exudation force (pushing fluid out) can easily exceed 5 MPa [4,38] and thus free swelling is generally assumed to only participate in cartilage recovery during long periods of joint unloading (rest) [1,24,100].

The take home message thus far is that tissue hydration and IFP is only sustainable if fluid exudation is prevented through the use of a migrating contact or long periods of joint unloading [22,84,99]. However, extrapolating this to the physiological case this would require mammalian joints to be active or unloaded a majority of the time. This is certainly not the case as daily life styles involve a significant portion (~90% [101]) of near motionless joint loading (e.g. sitting and standing); thus significant fluid exudation is expected to occur on a daily basis.
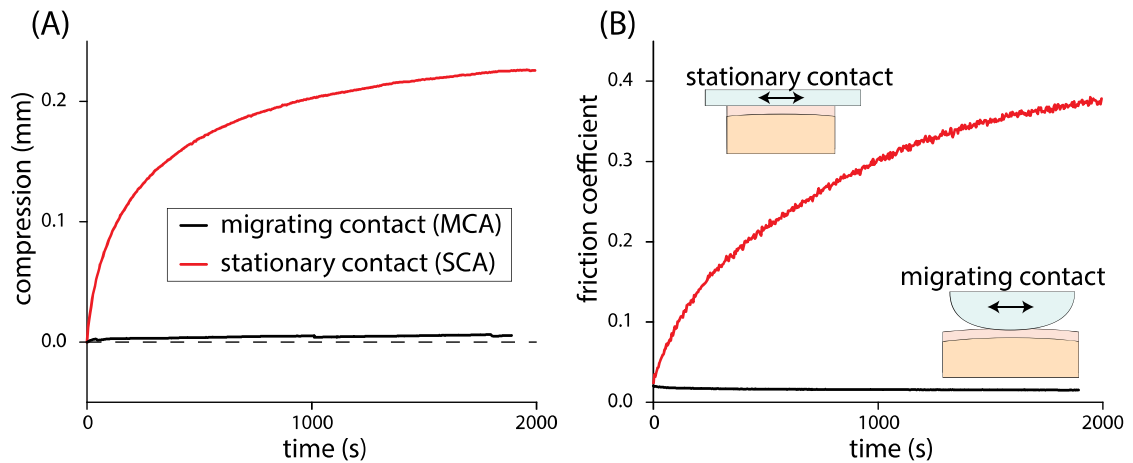
Figure 2.4   Representative data set demonstrating the effect of sliding duration on (A) compression (strain, deformation, hydration, fluid pressure) and (B) friction. The data demonstrate that migrating contacts are able to arrest tissue compression and can thus maintain IFP. Data were collected on the spherical micro-indenter and in-situ materials tester sections *7.2.4 Tribological Characterization* and *8.24 In-Situ Materials Tester*, respectively.

2.4.3   Without Contact Migration and Contact Exposure Interstitial Fluid Pressure and Wet Lubrication Cannot be Maintained

Based on IFP theory, without contact migration or contact exposure IFP cannot be maintained; therefore, nor can WL. The ability to extinguish and decouple WL has motivated a host of studies that have investigated other forms of cartilage lubrication. By first fully equilibrating (zero IFP) tissue specimens, Bonassar and co-workers have investigated the speed, strain, load, and viscosity effect on articular cartilage [77,102]. Their results demonstrate a friction response reminiscent of hydrodynamic lubrication. Specifically, it was shown that as the sliding speed or viscosity was increased the friction coefficient decreased, and as the strain or load was increased the friction coefficient increased. While the authors were aiming to develop hydrodynamic fluid films they proposed that the permeable nature of the cartilage may have provided a

12

preferred path for fluid flow and thus prevented the development of a full fluid film. They proposed that the flux of fluid into the cartilage prevented the development of a full fluid film and thus only a mixed lubrication regime could be established under the conditions studied. Dowson and co-workers also demonstrated a speed dependent effect, but noted that it was only evident when the sample maintained a natural convergent wedge [58]. Bonassar and co-workers found a similar result when using a fixed versus pivoted rod system for holding their tissue specimens [102]. While these results suggest hydrodynamics play a role in cartilage lubrication it is unclear if fluid films are capable of developing [60,71,72,103–105].
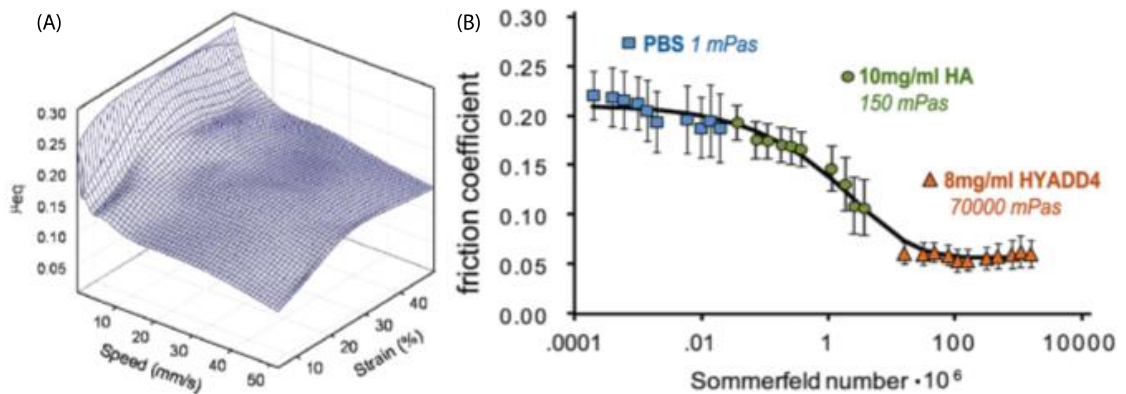
Figure 2.5   Prior work suggesting a hydrodynamic origin to the friction coefficient. (A) The effect of speed and strain on the coefficient of friction between pre-equilibrated cartilage and glass. (B) The effect of viscosity on the coefficient of friction between pre-equilibrated cartilage and glass. Note that experiments were performed in a stationary contact area configuration under a fixed strain and linear reciprocation. Images adapted with permission [77,102].

Chapter 3

OBJECTIVES

To date it is well accepted that hydration drives the dominant load bearing and lubrication mechanisms of articular cartilage. The pioneering works of McCutchen [1,55], Mow and co-workers [4,31,106–108], and Ateshian and co-workers [109–113] have demonstrated that load-driven fluid exudation leads to the pressurization of interstitial fluid, which stiffens the tissue and effectively supports a fraction (~90%) of the applied load. It has also been shown that as IFP, or tissue hydration, decreases so does the lubricity of articular cartilage [22,24,81,84,111,114–117]. While a host of highly sophisticated numerical and finite element solutions exist for modeling the mechanics of interstitial fluid pressurization, the solutions are quite complex and involve a deep understanding of continuum mechanics and numerical methods [86,106,113,118–122]. Furthermore, the contact configurations (plane-ended indentation, confined compression, unconfined compression) these model are based on make large population based studies difficult (spatial resolution and testing duration).

The objectives of this work were to take an analytical approach to modeling the tribo-mechanics of articular cartilage for sliding and indentation with a rigid impermeable sphere. An analytical approach was chosen as it gives a closed-form solution making relationships between model inputs and outputs very apparent. A rigid sphere was chosen as it facilitates localized contacts, rapid equilibration, no stress concentrator, and is directly applicable to sliding. The specific objectives of this work were to: (1) develop a migrating contact area (sphere sliding on cartilage) tribo-

mechanics model of articular cartilage [28], (2) used that model to develop and validate a rate based indentation method to quantify material properties and account for substrate effects [26] and (3) extend the model to handle spherical creep based indentation and account for substrate effects and non-linear permeability [123]. The final objective was to implement these methods and models to quantify the regional variations in tribological and material properties of the bovine stifle joint [6].

As mentioned previously, hydration appears to drive cartilage lubrication; thus load-induced fluid exudation (loss of hydration) leads to a loss of lubrication. To date the only demonstrated mechanisms of fluid recovery are free-swelling and mechanical pumping. Free-swelling is driven by the electro-chemical gradient between charged proteoglycans and the surrounding ionic fluid [4,124]. Mechanical pumping is believed to be driven by sub-ambient pressures during loading and unloading [43,125]. Based on the work of Gleghorn and Bonassar, it seems likely that the permeable articular cartilage prevents the development of hydrodynamic fluid films by instead driving fluid into the articular cartilage, and potentially restoring hydration.

The final objectives of this work are to: (1) determine if significant hydrodynamic forces exist in cartilage contacts, (2) determine if the permeable cartilage interface provides a preferred path of fluid flow into the tissue, and (3) demonstrate the role of the mechanical environment in governing the tribological response of articular cartilage.

Chapter 4

AN ANALYTICAL TRIBO-MECHANICS MODEL FOR ARTICULAR CARTILAGE

4.1   Introduction

McCutchen slid cartilage against a large glass flat and was the first to propose interstitial (weeping) lubrication to explain the unusual response [55]. He noted that fluid pressure, which develops under loading, reduced friction by ~10-100X while boundary lubrication with synovial fluid reduced friction by ~2X. In the joint, interstitial pressurization increases load capacity [119], shields the matrix from stresses [4], signals the biochemical response [7,126], and reduces friction and wear [1,22,127].

Generally speaking, IFP subsides over time. Direct measurements of the fluid load fraction have shown that the effective friction coefficient, μ_{eff}, obeys the following relationship with the equilibrium friction coefficient, μ_{eq}, and the time-dependent fluid load fraction, F' [128]:

$$\mu_{eff} = \mu_{eq} \cdot (1 - F')$$
Eq. 4.1

McCutchen recognized that interstitial lubrication must be restored in-vivo and proposed that dynamic loading and unloading was responsible [1]. However, this hypothesis was rejected by direct observations of time-dependent friction during dynamic loading [129].   In 2008, it was discovered that interstitial lubrication is maintained during sliding when cartilage is self-mated [84]. In a follow-up test, the authors demonstrated that a rigid impermeable sphere, when slid against cartilage, also

maintained low friction. They proposed that fluid pressure is maintained when hydrated tissue is continually introduced into the contact; they call this the migrating contact area (MCA). This discovery explained how fluid pressure is maintained in-vivo. Based on prior modeling of biphasic cylindrical layers in rolling contact [110], Ateshian proposed that fluid load support is sustainable in MCA when the Péclet number (Pe) >>1 and negligible when $Pe \leq 1$; $Pe = V \cdot a / (H_a \cdot k)$, where V is sliding velocity, a is the contact radius, H_a is aggregate modulus, and k is permeability [22].

Despite the rapid recent advancements in the field of cartilage lubrication, there remain major gaps that inhibit our ability to predict how tribological conditions and material properties impact tissue function. The state of the art provides a relationship between friction and fluid load fraction [22,128], but there remains no analytical expression to quantitatively relate the Péclet number to the fluid load fraction for MCA sliding conditions. This paper describes and experimentally supports an analytical model that relates measurable material properties and controllable mechanical conditions to the fluid load fraction and dependent functional parameters, including contact radius, effective contact modulus, contact stress, fluid pressure, friction coefficient, and shear stress.

4.2   Model

4.2.1   Contact of a Biphasic Semi-Infinite Half-Space

The force response of cartilage to deformation consists of components due to elastic stresses and those due to fluid pressure [1,130]. The coupling of elastic deformation and fluid flow creates a challenging non-linear contact mechanics problem. To improve the tractability of the Hertzian contact problem, we initially treat

the solid and fluid mechanics independently. Although cartilage violates nearly each of Hertz's assumptions, we find that Hertz's theory provides a reasonable contact model when the contact diameter is less than the cartilage thickness. The elastic foundation model is more appropriate in physiological conditions and the analysis follows an identical strategy.

We develop the Hertz solution over the elastic foundation solution here because we can test the Hertz solution under controllable experimental conditions. Consider the indentation of a rigid impermeable sphere into cartilage as illustrated in Figure 4.1. According to Hertz's theory, the elastic force component, F_e, is the following function of sphere radius, R, contact modulus (a material property), $E_{c0} = E/(1-\nu^2)$, and penetration depth, $\delta = a^2/R$:

$$F_e = \frac{4}{3} \cdot \frac{E}{1-\upsilon^2} \cdot R^{0.5} \cdot \delta^{1.5} = \frac{4}{3} \cdot E_{c0} \cdot R^{0.5} \cdot \delta^{1.5} = \frac{4}{3} \cdot \frac{E_{c0} \cdot a^3}{R} \qquad \text{Eq. 4.2}$$

where E is Young's modulus of elasticity and ν is Poisson's ratio.
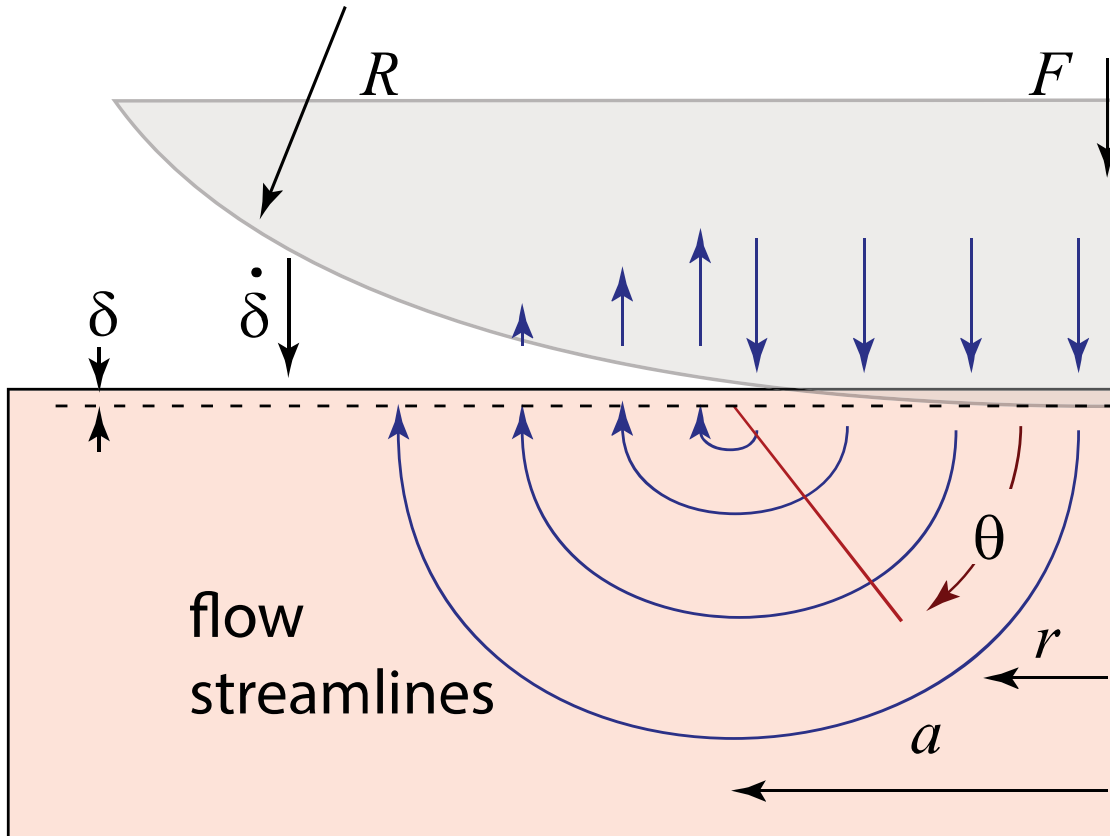
Figure 4.1   Axisymmetric contact model of a rigid sphere indenting cartilage. Streamlines show likely paths of fluid flow. Figure is adapted with permission [28].

Volume-changing deformations like indentation cause interstitial fluid flow. According to Darcy's law, fluid flow through a permeable medium induces a pressure gradient:

$$\frac{dP}{dx} = \frac{q}{k}$$

<div align="right">Eq. 4.3</div>

where q is the flow speed along a streamline, k is the permeability of the solid to the fluid of interest, and dP/dx is the pressure gradient along the streamline. Finite

element models [83,131] have demonstrated that the streamlines during indentation and sliding approximate semi-circular arcs as shown in Figure 4.1. Each streamline starts at the sphere surface at a distance r from the axis of symmetry with a speed of $\dot{\delta}$ in the compression direction. Conserving volume along each streamline gives the velocity as a function of starting point, r, and angle, θ:

$$q(r,\theta) = \frac{\dot{\delta} \cdot r}{a - (a-r) \cdot \cos(\theta)} \qquad \text{Eq. 4.4}$$

Assuming that the pressure outside the tissue is zero, Darcy's law can be integrated along each streamline to obtain the pressure acting on the sphere as a function r. The matrix compacts downward at a rate $\dot{\delta}$ under the contact so there is no relative flow at $\theta = 0$. We estimate the relative flow rate by considering only the transverse component of q within the contact (i.e. when $0 < \theta < \pi/2$). In this case, pressure on the counterbody takes the form:

$$P(r) = \int_0^{\pi/2} \frac{\dot{\delta} \cdot r \cdot (a-r) \cdot \sin(\theta)}{k \cdot (a - (a-r) \cdot \cos(\theta))} d\theta + \int_{\pi/2}^{\pi} \frac{\dot{\delta} \cdot r \cdot (a-r)}{k \cdot (a - (a-r) \cdot \cos(\theta))} d\theta \quad \text{Eq. 4.5}$$

Integrating the pressure distribution yields an estimate of the fluid pressure force contribution:

$$F_p = 1.37 \cdot \frac{\dot{\delta} \cdot a^3}{k} \cong \frac{4}{3} \cdot \frac{\dot{\delta} \cdot a^3}{k} \qquad \text{Eq. 4.6}$$

The fluid load fraction, F', has been shown to be highly correlated with the lubrication of cartilage. By definition, F' is the ratio of the fluid pressure force, F_p, and

the total applied normal force, $F = F_p + F_e$. Inserting Eqs. 4.2 and 4.6 into this definition yields:

$$F' = \frac{F_p}{F_p + F_e} = \frac{\dfrac{4}{3} \cdot \dfrac{\dot{\delta} \cdot a^3}{k}}{\dfrac{4}{3} \cdot \dfrac{\dot{\delta} \cdot a^3}{k} + \dfrac{4}{3} \cdot \dfrac{E_{c0} \cdot a^3}{R}} = \frac{Pe}{Pe + 1} \qquad \text{Eq. 4.7}$$

where $Pe \equiv \dfrac{\dot{\delta} \cdot R}{E_{c0} \cdot k}$ for indentation.

The mechanics of a migrating contact are analogous to those of indentation. When the sphere in Figure 4.1 travels a distance, a, the tissue is consolidated by δ. Thus, the average deformation rate is: $\dot{\delta} = \dfrac{V \cdot \delta}{a}$, where V is sliding velocity. By definition from Hertzian theory, $\delta = a^2 / R$, so the Péclet number for sliding becomes: $Pe \equiv \dfrac{V \cdot a}{E_{c0} \cdot k}$, which is identical to that reported previously [22].

Eq. 7 suggests that $F' \rightarrow 1$ as $\dot{\delta} \rightarrow \infty$ and only holds for an infinite tensile modulus. For real materials, Eq. 4.7 is limited to an asymptotic limit that depends on the elastic properties and contact geometry. Soltz and Ateshian demonstrated that this asymptotic limit for F' in unconfined compression is essentially governed by the ratio of tensile modulus to compressive modulus, E^* [86]. The same mechanism applies here and is important to understand. Consider Figure 4.2, which illustrates the unconfined compression of a biphasic material. Assuming that Poisson's ratio is 0 (Soltz and Ateshian show that this is true to an excellent approximation [86]) and that the deformation shown occurs instantaneously (flow cannot occur), the deformed shape conserves volume and the transverse strains are half the normal strain. Soltz and Ateshian use E_{-y} and E_{+y} to represent the compressive and tensile moduli, respectively. The transverse tensile stress, σ_+, on the matrix is: $\sigma_+ = \dfrac{\sigma_-}{2} \cdot \dfrac{E_{+y}}{E_{-y}} = \dfrac{\sigma_-}{2} \cdot E^*$. If the

21

interface is frictionless, fluid pressure (P) must balance the tensile stress (globally speaking) and $\sigma_- = 2P/E^*$. Therefore, the fluid load fraction is $F' = P/(P+\sigma_-) = P/(P+2P/E^*)$. Rearranging yields:

$$F'_{max} = \frac{E^*}{E^*+2} \text{ or } F'_{max} = \frac{E^* \cdot (0.5 - v)}{E^* \cdot (0.5 - v) + 1} \qquad \text{Eq. 4.8}$$

This is identical to the expression from Soltz and Ateshian [86]. For a linear material, $F'_{max} = 33\%$ which is identical to the biphasic solution [31]. For $E^* = 10$, $F'_{max} = 83\%$. This analytical model of the asymptotic limit ($Pe = \infty$) is equivalent to the numerical solutions for unconfined compression [86,108].
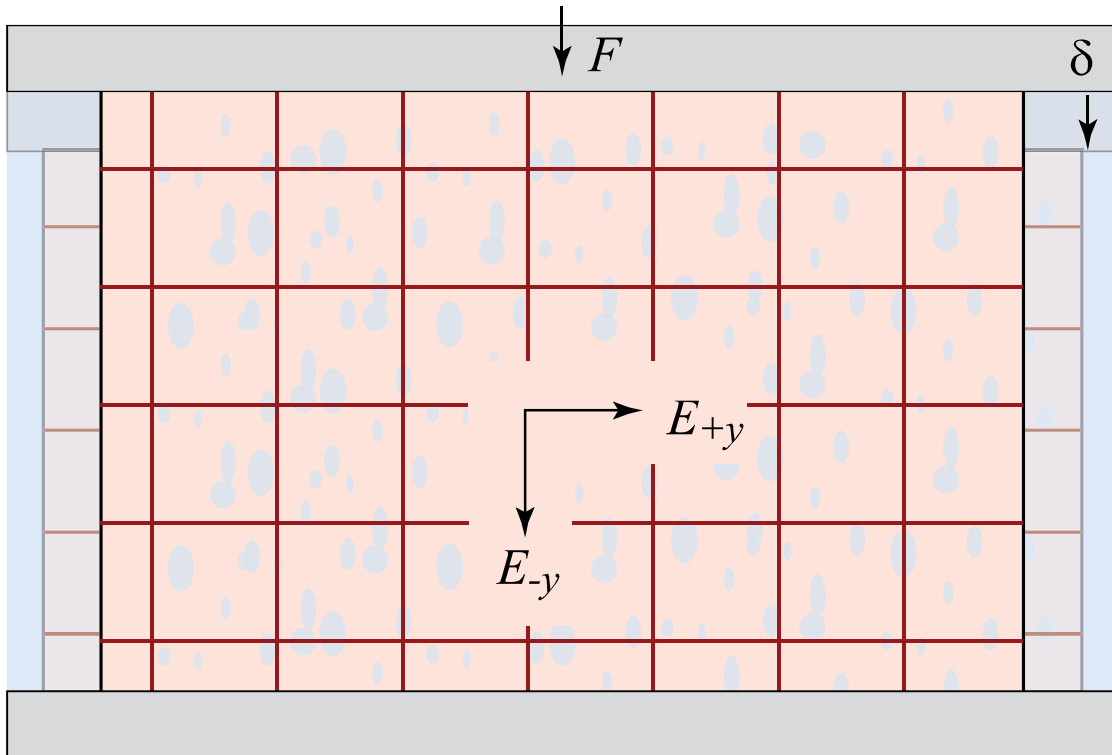
Figure 4.2   Unconfined compression experiment exemplifying the tissue's initial conservation of volume. Figure is adapted with permission [28].

Although Eq. 4.8 is inapplicable for Hertzian contacts, the idea that volume conserving deformations require infinite pressure gradients as E_{+y} approaches infinity holds equally well: $F' \rightarrow 1$ as $E^* \rightarrow \infty$. Since the general form and limit are known, a single additional reference point is needed. Numerical solutions indicate that the asymptotic limit of fluid load support is 50% when $E^* = 1$ [132,133]. The general asymptotic limit for fluid load support in a Hertzian contact is:

$$F'_{max} = \frac{E^*}{E^*+1}$$

Eq. 4.9

The general expression for fluid load support in a Hertzian contact becomes:

$$F' = \frac{E^*}{E^*+1} \cdot \frac{Pe}{Pe+1}$$

Eq. 4.10

Eq. 10 is a direct quantitative link between interstitial function, measurable material properties, and controllable mechanical conditions.

4.3 Model Demonstration and Testing

4.3.1 Materials

Adult bovine (12-20 month) cartilage, obtained from Herman's Quality Meats, Newark, DE, was chosen to demonstrate and test the model. A single full-thickness osteochondral plug (12.7 mm diameter by 10 mm) was harvested from the central aspect of the medial femoral condyle. The sample was rinsed in phosphate buffered saline (PBS) (21-040-CM, Mediatech). A rigid impermeable 440C stainless steel

23

sphere with a nominal radius of 3.175 mm and an average roughness of 80 nm (measured with a Veeco NT9100) was used as the indenting body. All measurements were performed within 4 hours of extraction to maintain nominally constant material properties.

4.3.2   Sliding Measurements

In the interest of space, we refer the reader to Bonnevie et al. [78], where we described the apparatus and experimental methodologies in detail. Briefly, the paper describes a method for measuring the fluid load fraction and contact radius in-situ during migrating contact area tribology experiments with cartilage or other biphasic materials. The tribometer makes direct measurements of sliding velocity (V), normal force (F_n), friction force (F_f), and penetration depth (δ). Sliding velocities were randomized and run in the following order: 200, 800, 300, 5000, 100, 1000, 50, 3000, 80, 500, and 2000 µm/s. In each measurement, the Z-stage was commanded to move 175 µm into the cartilage. The penetration depth is the difference between the stage motion and load cell compression, both of which are measured directly. Data were collected for the larger of 30 seconds and 5 cycles following steady state.

The performance metrics in regular font on the right of Table 4.1 are calculated from direct measurements. The effective contact modulus is given by Hertz as:

$E_{c'} = \dfrac{3}{4} \cdot \dfrac{F_n}{R^{0.5} \cdot \delta^{1.5}}$, the fluid load fraction is calculated with:

$F' = \dfrac{F_n - F_e}{F_n} = \dfrac{E_{c'} - E_{c0}}{E_{c'}}$, and contact radius is given by Hertz as: $a = \sqrt{R \cdot \delta}$. The

mean contact stress is the total force divided by the contact area. The elastic force contribution, by definition, is: $F_e = F_n \cdot (1 - F')$ and the mean elastic contact stress is

the elastic force divided by area. The mean shear stress is the friction force divided by area.

4.3.3 Results

Experimental results are shown in Table 4.1; only V, μ, δ, and F_n were directly measured. It is interesting to note the general trends of the direct measurements. With a 100X reduction in speed from 5000 µm/s to 50 µm/s, the penetration depth increased by 30%, the normal force decreased by 13%, and the friction coefficient increased by nearly 600%.

Table 4.1 Direct measurements (bold) and calculated performance metrics (regular) from migrating contact area sliding measurements of an osteochondral plug from a bovine stifle joint. The probe radius, R, is 3.175 mm. Table is adapted with permission [28].

V (µm/s)	μ	δ (µm)	F_n (mN)	$E_{c'}$ (MPa)	F' (%)	a (mm)	σ (MPa)	σ_e (MPa)	μ_{eq}	τ (MPa)
4510	0.0118	54.4	182.8	8.57	85.8	0.294	0.673	0.0957	0.0831	0.00795
2869	0.0128	56.1	180.3	8.09	84.9	0.298	0.645	0.0971	0.0847	0.00822
1908	0.0133	55.7	180.9	8.19	85.1	0.297	0.651	0.0968	0.0898	0.00869
980	0.0149	58.4	176.8	7.46	83.7	0.304	0.607	0.0991	0.0910	0.00902
788	0.0176	57.4	178.4	7.73	84.3	0.302	0.624	0.0982	0.1120	0.01100
449	0.0213	58.0	177.4	7.57	83.9	0.303	0.614	0.0987	0.1326	0.01309
281	0.0278	58.8	176.2	7.37	83.5	0.305	0.601	0.0994	0.1684	0.01674
192	0.0361	62.0	171.3	6.61	81.6	0.314	0.554	0.1021	0.1958	0.01999
98	0.0510	64.9	167.0	6.02	79.8	0.321	0.516	0.1044	0.2518	0.02630
79	0.0576	66.7	164.1	5.67	78.5	0.325	0.493	0.1059	0.2681	0.02840
50	0.0702	70.4	158.5	5.05	75.9	0.334	0.451	0.1088	0.2911	0.03167
0	N/A	119.7	84.7	1.22	0.0	0.436	0.142	0.1419	N/A	N/A

Figure 4.3 demonstrates the strong dependence of friction on the fluid load fraction as predicted by Eq. 4.1. As suggested in the preceding section, the fluid load

fraction approaches an asymptote as the speed approaches infinity. In this case, the fluid load fraction approaches $F'_{max} = 0.86$. Eq. 4.9 can be used to estimate $E*$ directly; rearrangement yields: $E* = \dfrac{F'_{max}}{1 - F'_{max}} = 6.14$; therefore $E_{y+} = 6.14 \cdot 0.87$ MPa

$= 5.34$ MPa. Permeability is only important at speeds that are sufficiently slow to cause significant reductions in fluid load support. Using the fluid load fraction measurement from the slowest case leaves Pe as the only unknown in Eq. 4.10:

$0.756 = 0.86 \cdot \dfrac{Pe}{Pe + 1} \Rightarrow Pe = 7.27$. The Péclet number can now be used to make a

single point estimation of permeability: $k = \dfrac{0.05 mm/s \cdot 0.473 mm}{7.27 \cdot 0.87 N / mm^2} = 0.0037$ mm^4/Ns.
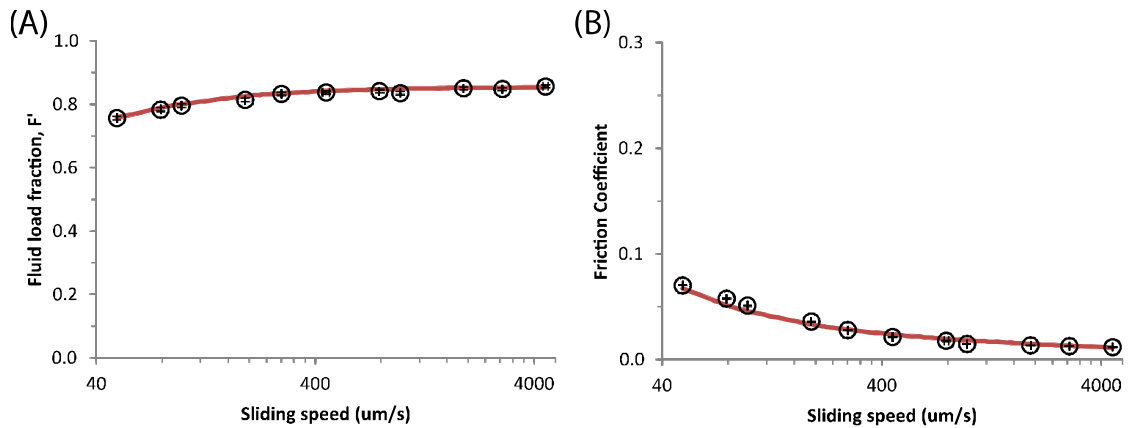
Figure 4.3   (A) Fluid load fraction plotted versus sliding speed. The fit to the model (Eq. 10) are shown in red and reflect $k = 0.0036$ mm^4/Ns and $E* = 5.9$. (B) Friction coefficient plotted versus sliding speed. Error bars represent experimental uncertainty [134] and are smaller than data labels. Figure is adapted with permission [28].

The same equations were used to create a model curve and the fitting parameters, k and $E*$, were adjusted to obtain the least squared error. The best fit for

F' yields $k = 0.0036$ mm^4/Ns and $E* = 5.9$ with $R^2 = 0.95$ (Eq. 10). In addition to the high quality of fit, the material properties obtained are quite reasonable for cartilage. For example, Mow et al. [130] report a mean permeability of $k = 0.0076 \pm 0.003$ mm^4/Ns for bovine cartilage and Ebara et al. [135] report a tensile modulus of 5.7 ± 2.4 MPa for the superficial layer of the bovine glenoid. The results suggest that the model, despite its many simplifying assumptions, captures the important physics of interstitial lubrication during contact migration.

We used Eq. 4.10 as the basis for developing similar expressions for other functional metrics. By definition, $F' = \dfrac{F_n - F_e}{F_n} = \dfrac{E_{c'} - E_{c0}}{E_{c'}}$ and rearrangement gives:

$$E_{c'} = \frac{E_{c0}}{1 - F'} \qquad \text{Eq. 4.11}$$

The mean contact stress, fluid pressure, elastic contact stress, and shear stress, respectively, are:

$$\sigma = \frac{1}{\pi} \cdot \left(\frac{16}{9} \cdot \frac{F_n \cdot E_{c'}^2}{R^2} \right)^{\frac{1}{3}} \qquad \text{Eq. 4.12}$$

$$P = \sigma \cdot F' \qquad \text{Eq. 4.13}$$

$$\sigma_e = \sigma \cdot (1 - F') \qquad \text{Eq. 4.14}$$

$$\tau = \mu_{eq} \cdot \sigma_e = \mu_{eq} \cdot \sigma \cdot (1 - F') \qquad \text{Eq. 4.15}$$

The effects of sliding speed on effective modulus, total contact stress, fluid pressure, elastic contact stress, and shear stress are illustrated in Figure 4.4 along with the model predictions (Eqs. 4.11-4.15) based on material properties from the fit to F'; $R^2 > 0.95$ in each case.
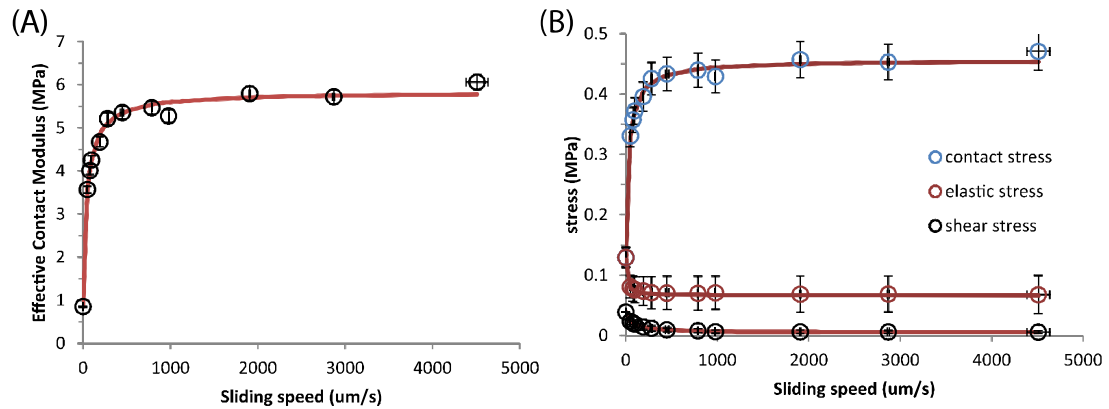
Figure 4.4   (A) Effective contact modulus versus sliding speed. (B) Total contact stress, fluid pressure, elastic contact stress, and shear stress plotted versus sliding speed. Experimental data are plotted as points, fits to the model (Eqs. 4.11-4.14) are shown in red and reflect $k = 0.0036$ mm^4/Ns and E^* = 5.9. In each case, $R^2 > 0.95$ and error bars represent experimental uncertainty. Figure is adapted with permission [28].

4.4   Discussion

Analytical contact models from Hertz, Winkler, and JKR are used to predict contact stresses, characterize material properties, and select appropriate experimental conditions (e.g. geometries and loads) for scaled studies of engineering problems [136]. This paper presents and experimentally supports an analogous model for biphasic materials.

This model, like all mathematical models, is limited because it represents a simplified variant of the physical system of interest. We have neglected numerous complexities including heterogeneity, anisotropy, viscoelasticity, and substrate effects among others. However, the mechanical response of cartilage agrees quite well with Hertz's theory just as the elastic response of cartilage agrees with Hooke's law within certain limits. The use of a representative contact modulus, $E_{c'}$, is as limited as the use of a representative Young's modulus, E, or a representative aggregate modulus, H_a. While there is no direct evidence yet that heterogeneity, anisotropy, viscoelasticity, and substrate effects have important influences on interstitial lubrication, the literature provides strong evidence that biphasic structure [137] and tension-compression nonlinearity [86] are critical elements of the interstitial phenomenon. This model has been restricted to the simplest form that is still able to quantitatively reproduce experimentally observed features. Future studies will focus on model validation and refinement.

The model is limited to small contacts ($a \ll$ thickness); this promotes experimental testing but prevents extension to physiologically relevant problems. Because cartilage is thin, most contact problems require an elastic foundation (Winkler) approach. Applying the modeling philosophy presented earlier to the elastic foundation problem gives: $F_e = \dfrac{\pi}{4} \dfrac{H_a \cdot a^4}{R \cdot t}$ and $F_p = \dfrac{4\pi}{9} \dfrac{\dot{\delta} \cdot a^4}{k \cdot t}$. Retaining the assumption that the tensile modulus provides the primary confinement effect, the total fluid load fraction becomes: $F' = \dfrac{E*}{E*+2} \cdot \dfrac{Pe}{Pe + 9/16}$, which only differs from Eq. 4.10 by the constants. Consider a joint with the properties from the results section, a composite radius of 20 mm, a speed of 50 mm/s and a force of 500 N. In both models, Pe ~ 10^5 and the second term approaches 1. The Hertz model gives $F' = 86\%$ and $\sigma =$

1.4 MPa. The Winkler model (thickness = 1 mm) gives $F' = 74\%$ and $\sigma = 2.6$ MPa. The Winkler model is inherently stiffer and provides larger contact stresses that are more consistent with physiological values, which range from 1-5 MPa [138]. Unlike the Hertz model, the Winkler model is sensitive to the additional confining effect of the bone, which has been neglected in the analysis above. As Ateshian and Wang showed, even linear ($E^* = 1$) biphasic materials can provide realistic fluid pressure (F' >> 33%) when the layer is thin relative to the contact radius [110]. Differences in the two confinement mechanisms may be important; while tension-compression nonlinearity generates large tensile stress along the collagen axis, the substrate supported model generates high shear stress at the bone-cartilage interface.

One application of the model is prediction of mechanical effects. Park et al. found no evidence of interstitial lubrication with microscale contacts on cartilage and proposed the use of small contacts for controlled studies of boundary lubrication [139]. Ateshian analyzed these results in the more recent context and indicated that interstitial lubrication was negligible because $Pe < 1$ [22]. In that case, Pe ~ 0.1 ($V =$ 0.1 mm/s and $a = 1$ µm) and, assuming $E^* = 5$ for healthy cartilage, the model suggests 7.5% fluid load support, which is indeed small. It is actually remarkable how tolerant the interstitial lubrication mechanism is to extreme reductions in size scale and sliding speed. We routinely measure substantial interstitial load support at speeds and contact radii below 0.1 mm/s and 200 µm, respectively (Pe ~ 20).

The fluid load support model can also be used to study potential effects of mechanical factors, like obesity and inactivity, which increase risk of osteoarthritis (OA). Reconsider the joint from before. If the load increases to 2,000 N or speed reduces to 1 mm/s, the model predicts no change in F' or µ because $Pe >> 1$

(~100,000). However, the increased force does increase the tensile stress from 1.9 to 3.9 MPa. The collagen network ruptures when tensile stresses exceed its strength [140], which ranges from 10-30 MPa [141]. Local collagen rupture would reduce E^*, which would reduce interstitial lubrication under all conditions. Long periods of complete inactivity ($V = 0$) would lessen fluid pressure over time and damage could result if joint articulation resumed in the absence of significant fluid pressure. This might explain the risk of temporomandibular disorders from third molar (wisdom tooth) extraction, a procedure that requires the jaw to be propped open for an extended period of time [142].

Ateshian and Wang first proposed that increased permeability from degradation could impede the stress-shielding effect of interstitial lubrication and might therefore catalyze future degradation [110]. Ateshian later noted several studies in the literature citing no change in friction with various forms of degradation [115,143–145] and concluded that degradation must not necessarily lead to an increase in friction. Since degradation generally increases k and decreases Ha, he notes that the changes may offset one another, leaving Pe and interstitial lubrication unaffected [22]. Our model supports this notion; in the physiological case, $Pe \sim 100,000$ and although a 10X increase in k alone would reduce Pe by an order of magnitude, the change has no effect on F'. The model suggests that interstitial lubrication is far more sensitive to changes in E^* than to changes in V, F, H_a, and k because E^* is much closer to 1 than Pe. In an OA joint, collagen disorganization is reported to occur before any compositional changes, resulting in reduced tensile modulus [146–148] and a 'softening' condition known as chondromalacia [149]. Our recent experiments showed that a very mild papain digestion had no effect on composition but caused a two-fold

increase in friction ($Pe \gg 1$) that was consistent with a reduction in F' from 92% to 84% and a reduction in E^* from 11 to 5 [150].

Although there is no definitive evidence in the literature that degradation impedes interstitial lubrication, we consistently find reduced interstitial lubrication with mechanical or chemical degradation using Hertzian contacts. We believe that discrepancies may be the result of one of several possibilities. Firstly, most studies use the effective friction coefficient as the only indicator of interstitial lubrication, even though it depends on μ_{eq} and F'. Krishnan et al., for example, found that removal of the superficial zone removal had no effect on μ_{eff} but significantly decreased μ_{eq} [151]. Thus, F' (interstitial lubrication) must have decreased (Eq. 1). The decrease in μ_{eq} likely reflects compromised surface integrity, reduced shear strength, and degradation of interstitial lubrication; it should not be considered a lubrication attribute. The decrease in F' causes a reduction in stress shielding, load support, and stiffness, and manifests as arthroscopic 'softening'. Direct fluid load support measurements are needed for comprehensive assessment of the functional consequences of degradation as suggested previously [22]. Secondly, reduced E^* would not significantly impede joint lubrication if the confinement burden simply transitioned from tensile stresses in the collagen network to shear stresses at the bone-cartilage interface. This transition, while impossible in our localized contacts, will occur if E^* drops in a macroscale contact. Although this transition might have no immediate effect on interstitial lubrication, it could have significant downstream mechanical or biological effects.

A related question is whether such functional changes have biochemical consequences. Based on the hypothesis that fluid pressure and shear stress favor

matrix synthesis and degradation, respectively [7,126], we consider the ratio $\tau^* = \tau/P$ as a metric of biochemical degradation. Based on this model, a reduction in E^* from 11 to 5 causes τ^* to increase from 0.021 to 0.050. Although the relationship between the stress state and biochemical response remains uncertain, the model suggests that OA causes a significant increase in tribological shear stress relative to fluid pressure.

In summary, we have developed an analytical model for interstitial lubrication of migrating contacts involving biphasic materials. The model has been quantitatively supported by controlled experimental measurements and suggests that the interstitial lubrication response in-vivo is sensitive to changes in E^* and relatively insensitive to changes in V, F, H_a, and k. It enables the design of scaled-down experiments and prediction of the functional response to changes in mechanical conditions and materials properties. It suggests mean contact stresses above 2.6 MPa in a typical joint which is consistent with measured values. Additionally, it suggests that degenerative changes associated with OA will inhibit interstitial lubrication and significantly alter the stress state, either of which may signal negative cellular responses. Finally, the model provides basic insights into the design of materials that mimic cartilage function. Fibril reinforced hydrogels, for example, may provide significant interstitial lubrication and could prove invaluable for cartilage repair and replacement.

Chapter 5

HERTZIAN BIPHASIC CONTACT MECHANICS MODEL OF CARTILAGE: RATE-CONTROLLED SPHERICAL INDENTATION

5.1 Introduction

McCutchen first modeled the mechanical response of cartilage to estimate its permeability [1]. His analytical solution to unconfined compression, $F_p = \dfrac{\pi \cdot \dot{h} \cdot R^4}{8 \cdot k \cdot h}$, gives considerable insight into the tissue's flow dependent mechanical response and is easy to apply to engineering problems. The solution predicts, for example, that the deformation rate is proportional to the force carried by fluid pressure, which can be no larger than the total applied force. For articular cartilage at physiological conditions, relaxation times on the order of a day are required before strains reach a magnitude for which elastic contact stresses become significant [89]. Because deformation cannot occur instantaneously without an infinite deformation rate and force, the model predicts zero elastic load support and zero friction at the instant contact occurs. By measuring deformation rates of cartilage during unconfined compression, McCutchen was able to estimate a radial permeability of 0.0005 mm^4/Ns.

Agbezuge and Deresiewicz solved the Hertzian contact problem of a hard probe contacting a linear poroelastic half-space under a step load [132]. Unlike McCutchen's work, this solution predicted an instantaneous deformation due to a redistribution of volume that allows deformation without requiring instantaneous fluid flow. At the instant load is applied, it was predicted that the mean fluid pressure is equal to half the mean applied stress and decreases over time at a rate that depends on

the permeability, modulus, and contact radius. Initially, the friction force is expected to be half the equilibrium value (since only half the load is supported by frictional contact). Oyen empirically curve-fit this numerical solution and adapted it for characterization of Poisson's ratio, permeability, and aggregate modulus in Hertzian creep testing [152].

Armstrong et al. [31] used linear biphasic theory (LBT) to solve the unconfined compression problem previously considered by McCutchen [1]. As the authors note, the nonlinear coupling of fluid flow and elastic deformation creates a very difficult problem that requires numerical solution, even in the simplest loading conditions. This solution also differed fundamentally from McCutchen's solution in its response to an instantaneously applied load due to the coupling of fluid and solid mechanics. In McCutchen's solution, which is mechanically analogous to a spring in parallel with a damper, fluid pressure supports the entire load at the instant load is applied, just as the damper would in the analogous mechanical system. According to Armstrong et al., who used truly unconfined boundary conditions, fluid pressure causes cartilage to expand laterally, enabling a volume conserving deformation without the need for instantaneous flow [31]. Tensile stresses balance the increase in internal pressure, and since the tensile strain is half the compressive strain on average, the fluid pressure is also half the compressive stress. This solution theoretically limits fluid load support and the corresponding friction reduction to 33% [31,111].

Experimental measurements with cartilage show far greater stresses, fluid load fractions, and frictional reductions. In fact, while attempting to validate the theoretical predictions, Armstrong et al. [31] discovered far higher contact stresses than the model allowed. They proposed that adhesion to the loading platen restricted lateral

35

expansion and made the tissue behave more like the confined tissue in McCutchen's model. However, a much more likely explanation, given its low adhesive friction coefficient, is that the stiff internal collagen matrix resists lateral expansion under load as suggested by Soltz and Ateshian [86]. In other words, the high tensile modulus of internal matrix, the rigid (bone) substrate and any other physical impediments to volume-conserving expansion during contact directly increase the tissue's ability to build high fluid pressure; these confining properties are chiefly responsible for the very low friction coefficients observed in practice with this material.

The unconfined compression test presents several experimental challenges for the purposes of materials characterization. First, cartilage has varying thickness across the surface making the boundary conditions difficult to satisfy. Second, it is not possible to make measurements in-situ on a surface within a joint. Third, the bulk nature of the test prevents the spatial resolution necessary to probe heterogeneity with location and depth. Mak et al. solved LBT for indentation with a plane-ended porous indenter to address some of these limitations [153]. Later, Mow et al. developed the experimental protocol necessary to apply the solution to the characterization of aggregate modulus, Poisson's ratio and permeability [120] using a single indentation creep test. This method has since become one of the gold standards for the characterization of biphasic materials.

The linear plane-ended indentation method has limitations of its own. Firstly, the solution was derived numerically and its use requires access to the custom curve-fitting program developed by the authors. Secondly, the plane-ended contact produces a stress concentrator along the periphery that can damage the surface [122]. Thirdly, the influence of the stress concentrator on the results increases with decreased contact

radius, thus limiting spatial resolution. Fourthly, results from the linear biphasic

model cannot reproduce the magnitudes of stress observed in-vivo (1-5MPa [138]).

This is especially important given the fact that permeability is strain-dependent [154]

and thus pressure-dependent.

Moore and Burris recently developed an analytical solution to the Hertzian

contact problem for biphasic materials to address the limitations of linear theory [28];

here on we call the solution HBT. The solution introduces no stress concentrator and

reproduces physiologically consistent pressures. In this paper, we describe how

standard indentation measurements can be used to characterize the material properties

of articular cartilage and other biphasic materials. The reader is referred to Moore and

Burris for a description of the derivation of the model equations [28].

5.2   Methods

5.2.1   Theoretical Background

Eq. 1 gives the fluid load fraction, F', as a function of mechanical conditions (

$\dot{\delta}$: indentation rate, R: probe radius) and material properties (E_t: tensile modulus, E_{c0}:

equilibrium contact modulus, k: permeability) [28]:

$$F' = \frac{E_t}{E_t + E_{c0}} \cdot \frac{\dot{\delta} \cdot R}{\dot{\delta} \cdot R + E_{c0} \cdot k} \qquad \text{Eq. 5.1}$$

The first term, $\dfrac{E_t}{E_t + E_{c0}}$, is an asymptotic limit governed by the resistance to

lateral expansion. In the limit of perfect confinement, the asymptote goes to 1. For an

unconstrained Hertzian contact, it is governed by tension-compression nonlinearity of

the solid matrix [86,111]. By inspection, linear biphasic materials ($E_t = E_{c0}$) are

limited to 50% fluid load support as first shown by Agbezuge and Deresiewicz [132].

Experimentally, it is known that cartilage is capable of much higher levels of fluid load support and friction reduction; this is due to the confining effects of high lateral stiffness of the collagen matrix and the underlying bone.

Eq. 1 assumes a semi-infinite half-space. Although it is common to neglect substrate effects when the indentation depth is less than 10% the layer thickness, the difference in stiffness, as it turns out, is not negligible. The method for eliminating the substrate effect is addressed in section *5.2.3 Characterization by spherical indentation*.

The second term of Eq. 5.1 describes the rate-driven approach toward the asymptote and is governed by the Péclet number, $Pe = \dot{\delta} \cdot R/(E_{c0} \cdot k)$. Fluid load support is negligible when $Pe << 1$, 50% the asymptote when $Pe = 1$ and at the asymptote when $Pe >> 1$ [22]. It is important to recognize here that other forms of Pe apply to other contact configurations; for example, $Pe = V \cdot a/(E_{c0} \cdot k)$ during Hertzian sliding, where V is sliding velocity and a is contact radius.

By definition, the fluid load fraction is the ratio of the force carried by fluid pressure, F_p, to the total applied force, F_t. The force carried by fluid pressure is the difference between F_t and the force carried by the solid, F_s: $F' = \dfrac{F_p}{F_t} = \dfrac{F_t - F_s}{F_t}$. Using Hertzian theory, we can redefine the fluid load fraction in terms of the moduli, which eliminates the need to maintain constant indentation depth during measurements:

$$F' = \frac{\frac{4}{3} \cdot E_c \cdot R^{0.5} \cdot \delta^{1.5} - \frac{4}{3} \cdot E_{c0} \cdot R^{0.5} \cdot \delta^{1.5}}{\frac{4}{3} \cdot E_c \cdot R^{0.5} \cdot \delta^{1.5}} = \frac{E_c - E_{c0}}{E_c} \qquad \text{Eq. 5.2}$$

The effective contact modulus, E_c, includes contributions from fluid and solid stresses, while E_{c0}, a material property, is the equilibrium contact modulus of the

tissue [78]. Inserting Eq. 5.1 into 5.2 and rearranging gives the following equation for the effective contact modulus of a biphasic half-space entirely in terms of controllable mechanical conditions and measurable material properties:

$$E_c = \frac{E_{c0}}{1 - \left(\dfrac{E_t}{E_t + E_{c0}} \cdot \dfrac{\dot{\delta} \cdot R}{\dot{\delta} \cdot R + E_{c0} \cdot k} \right)}$$

Eq. 5.3

5.2.2   Materials and Equipment

A single 12 mm diameter osteochondral plug was used to demonstrate and validate the method. The sample was removed from the center of the medial femoral condyle of a mature bovine stifle joint. The custom spherical indenter shown in Figure 5.1 was used to indent the cartilage sample. Smooth ($R_a < 80$ nm) and impermeable stainless steel spherical ball bearings were used as the indenter; the diameter was either 6.35 mm or 3.175 mm as noted. The sample was submerged in phosphate buffered saline (PBS) (21-040-CM, Mediatech) during indentation tests. The load cell consisted of a calibrated cantilevered beam (0.95 ± 0.0005 mN/μm) and a 150 ± 0.007 μm capacitive displacement sensor (C11-E, Lion Precision) to measure beam deflection. A 250 μm piezoelectric stage (P-622, Physik Instrumente) with capacitive displacement feedback (± 25 nm) was used to control each indentation. The sample was positioned with an X-Y translation stage and aligned relative to the Z-axis with a 2-axis tilt-stage prior to measurement.
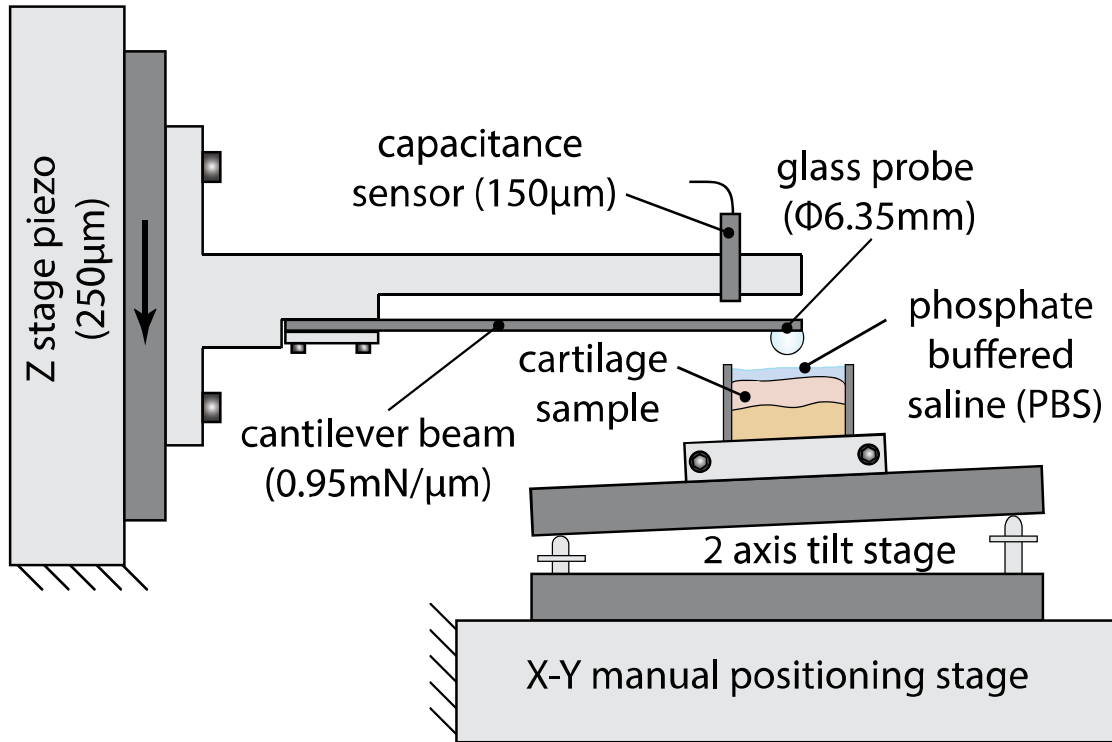
Figure 5.1   The spherical indentation rig used in this study. Figure is adapted with permission [26].

5.2.3   Characterization by Spherical Indentation

The sample was indented at 100, 50, 10, 5, 1, 0.5, and 0.1 µm/s, either in that descending order or in a randomized order, as noted. The stage was commanded to travel either 150 µm or 50 µm into the sample as noted. The actual indentation depth and indentation rate are measured using the difference between measurements of the stage and the load cell displacements. Following the last indent in each variable-rate series, the Z-stage was held at 150 µm until equilibrium was reached to determine E_{c0}.

One practical challenge with characterizing cartilage properties, in general, is the identification of 'full' equilibrium. There are no universally observed standards for determining the amount of time required to observe full equilibrium, however,

many investigators use a criterion involving a critical rate of change of indentation depth. In this study, equilibrium was declared when the indentation depth changed by less than 1 µm over a five-minute window.

The surface is located using the position for which the first statistically significant non-zero force is detected. The probe is then pulled 3 µm above the surface to prepare for indentation. The Z-stage is then driven to the desired depth at the prescribed rate and immediately retracted at 10 µm/s (except for the final equilibration measurement). This retraction rate helps pull expelled fluid back into the sample and almost entirely restores the pre-test condition. The sample is then given one minute to fully normalize between indents.

The amount by which a substrate effectively stiffens any elastic layer during contact depends on the dimensionless layer thickness, $t^* = t/a$ (t is the layer thickness), as first described by Hayes et al. [118]. Unfortunately, applying this model requires expertise in numerical computation, which makes it inconvenient for general use. Stevanovic et al. [155] provide an approximate analytic solution to the problem based on the formulation from Chen and Engel [156]. According to the solution, the force exerted by a fictitious semi-infinite solid (F_{inf}) is a factor of f_p smaller than the force measured for a bonded layer (F_{layer}) of the same material when indented to the same depth (the substrate must be $> 40X$ stiffer than the layer in this case):

$$F_{\text{inf}} = F_{layer} \cdot f_p = F_{layer} \cdot \left(1 - 1.04 \cdot \exp\left(-1.73 \cdot t*^{0.734}\right)\right)^3 \qquad \text{Eq. 5.4}$$

Each force measurement is corrected based on Eq. 5.4 to give the force of an equivalent semi-infinite solid when indented to the corresponding depth.

Because cartilage and other biphasic materials can have fibrillated, bumpy or otherwise poorly defined surfaces, the surface is not defined by the location at which

force is first detected. Instead, each force-displacement curve is fit to Hertz solution:

$F_t = \frac{4}{3} \cdot E_c \cdot R^{0.5} \cdot (\delta - \delta_{off})^{1.5}$, where δ_{off} represents the offset above the 'true' surface

of the half-space. This method forces the mechanics to define the surface and

eliminates surface location uncertainty. Figure 5.2 demonstrates how the corrected

force-displacement data (unfilled) is fit to Hertz equation (red line). Generally, the

effective surface starts a few microns below the location at which forces are first

detected, which is consistent with the measured magnitude of the surface roughness.

The equilibrium measurement used the offset from its parent indent (the last indent in

the series).

Once the contact moduli data are obtained for each indentation rate, the

unknown tensile modulus, E_t, and permeability, k are obtained by fitting the data to

Eq. 5.3. To assist other researchers in implementing this method, we have developed

a template and user guide, which can be downloaded at:

http://www.axelcmoore.com/software/ .
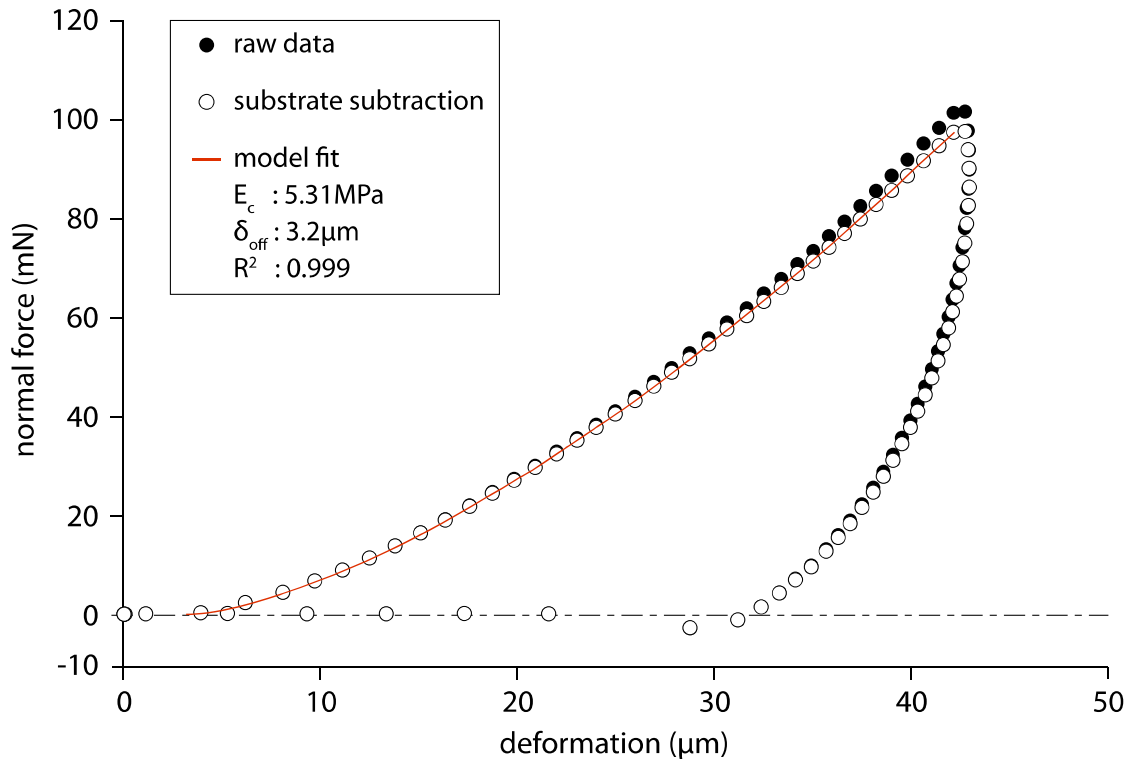
Figure 5.2   A representative force-displacement curve for the cartilage sample used in this study. The spherical indenter had a radius of 3.175 mm and a nominal indentation rate of 10 μm/s. The raw data (solid) is corrected for substrate effects using the analytical solution of Stevanovic et al. [155]. Using Hertzian mechanics the zero-surface offset is determined and Hertz solution is best fit (red line) to the substrate corrected force-displacement data (unfilled) to determine the effective modulus. Figure is adapted with permission [26].

5.2.4   Characterization by Plane-Ended Indenter

Creep indentation with a porous-permeable plane-ended indenter tip is considered the gold standard for indentation testing to characterize biphasic properties. We use it here as a measure of validation for the present method. A 1.6 mm diameter porous punch was used to indent the same 1.3 mm thick cartilage sample in the same location as the Hertzian measurement. The osteochondral core was glued to the bottom of a bathing chamber which was filled with PBS, and the cartilage surface was leveled

perpendicular to the indenter tip with a 2-axis tilt stage. A 50 mN preload was applied to ensure complete contact at the interface and establish the zero-time reference surface. Following 5 minutes of preload the indenter was commanded to maintain a constant 200 mN load [120]; the test was stopped when the rate of deformation change fell below 1 µm in five minutes. The contact stress was ~0.1 MPa and the maximum deformation was 120 µm. For comparison, the pressures and depths during spherical indentation ranged from 0.02-0.46 MPa and 41-121 µm, respectively. The creep deformation under constant loading was analyzed by a custom LBT curve-fitting program [157] which simultaneously determined Poisson's ratio, aggregate modulus, and permeability.

To consider the prominent tension-compression nonlinearity of the solid phase and address the large IFP found in practice [86], we developed an analogous tension-compression nonlinear elastic (TCN) finite element model in FEBio [158]. The solid matrix of cartilage was defined as an isotropic homogeneous Neo-Hookean material reinforced by fibers in three orthogonal directions. The energy function of the fibers followed an exponential-power law, where E_t is the tensile modulus defined at zero tensile strain. The three mechanical properties, aggregate modulus, tensile modulus and permeability, were determined by curve-fitting the experimental creep response.

5.3   Results

The processed contact modulus results for spherical indentation at monotonically decreasing rates are provided in Table 5.1. The high quality of each fit to the Hertzian contact model is reflected by the proximity of the coefficient of determination (R^2) to 1.

Table 5.1   Hertzian model fits to the substrate corrected indentation curves from Figure 5.2. Note that the probe had a radius of 3.175mm.

vertical stage speed (μm/s)	indentation rate (μm/s)	effective contact modulus (MPa)	coefficient of determination (R^2)	fluid load fraction
100.0	60.0	7.89	0.9999	0.93
50.0	35.9	7.57	0.9998	0.93
10.0	9.5	5.31	0.9999	0.90
5.0	5.6	4.38	0.9999	0.87
1.0	1.6	2.40	0.9994	0.77
0.5	0.8	1.82	0.9998	0.69
0.1	0.2	1.02	0.9998	0.45
0.0	0	0.56	N/A	0.00

The effective contact modulus is plotted as a function of indentation rate in Figure 5.3. The effective contact modulus is a sigmoidal function of indentation rate. Below 0.1 µm/s, the effective contact modulus approaches the equilibrium contact modulus as shown by the logarithmic axis-scaling in Figure 5.3B. The effective contact modulus approaches an asymptotic limit at high speeds; according to the HBT model, that limit is equal to the sum of the equilibrium contact modulus and the tensile modulus. Between these speeds, the tissue effectively stiffens with speed as it becomes more and more difficult to force fluid through the cartilage at the rate of indentation. Fitting the dataset to Eq. 5.3 gives $E_t = 8.0$ MPa, $k = 0.00217$ mm^4/Ns, and $R^2 = 0.996$. The solution to the fit is unique in the HBT model because the tensile modulus and permeability have independent effects on the tissue response [120]. To demonstrate this fact, the fitted properties have been adjusted and the resulting solutions plotted in Figure 5.4. Changes in permeability shift the inflection speed without affecting the asymptote (Figure 5.4A). Changes in tensile modulus increase the asymptote without affecting the inflection speed (Figure 5.4B). Likewise, changes in the equilibrium contact modulus shift both asymptotes by equal amounts.
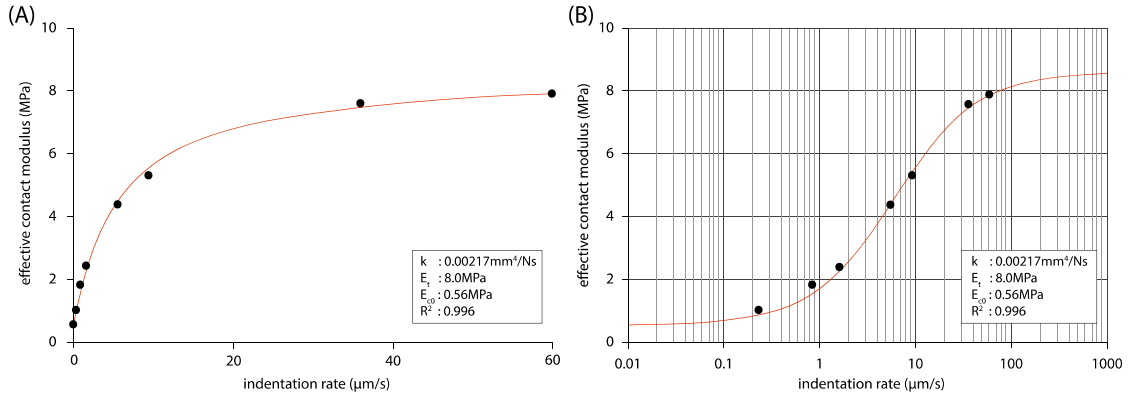
Figure 5.3   (A) The solid line is the biphasic model fit to the experimental data. Note that the probe had a radius of 3.175 mm. (B) The same data and model fit are plotted on a logarithmically scaled X-axis. Figure is adapted with permission [26].
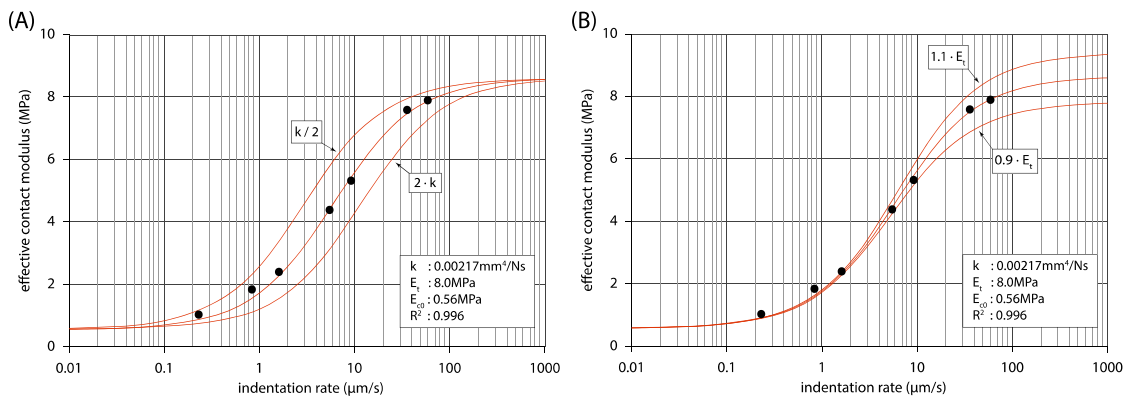
Figure 5.4   (A) The effects of permeability on the model shape. (B) The effects of tensile modulus on model shape. Note that the probe had a radius of 3.175 mm. Figure is adapted with permission [26].

Several follow-up experiments were conducted to illustrate sensitivity of the method to variations in the experimental protocol. In the first variation, the indentation rates were randomized to determine if hysteresis has significant effects; the testing conditions were otherwise constant. The order of indentation was set at:

46

0.5, 50, 0.1, 10, 100, 5 and 1 µm/s followed by equilibration. The effects of randomization are shown in Figure 5.5. Monotonically descending and randomized speed conditions did not significantly affect the results of characterization: the equilibrium modulus decreased by 7%, the tensile modulus increased by 5%, while the permeability remained unchanged.
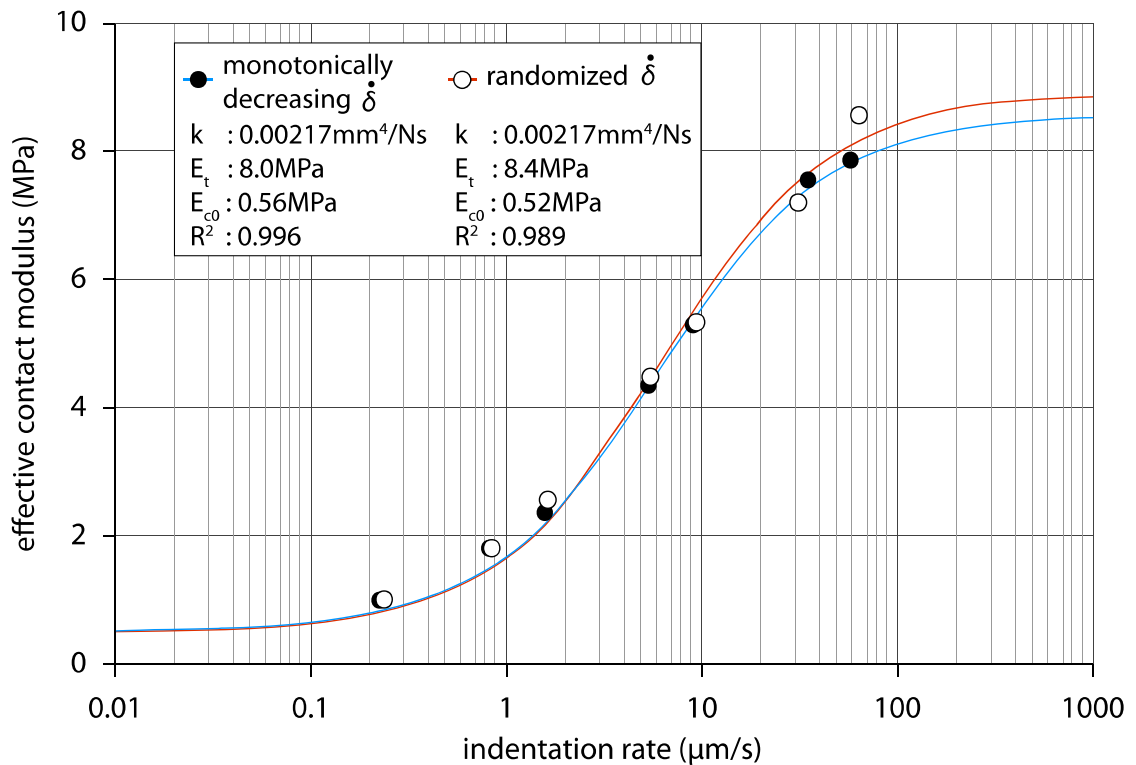
Figure 5.5   Randomized order of indentation rates are compared to the monotonically decreasing indentation rates. The solid lines are the biphasic model fit to the experimental data. Note that the probe had a radius of 3.175 mm. Figure is adapted with permission [26].

In a second variation, probe diameter was cut in half (to 3.175 mm). Figure 5.6A demonstrates that a reduction in probe size resulted in decreased equilibrium

contact and tensile moduli along with increased permeability. In addition to decreasing the sampling area, the smaller probe decreased the effective sampling depth thereby making the measurement more surface-sensitive (the depth under stress is proportional to contact radius not actual penetration depth). A third variation tested the depth effect directly by limiting the indentation depth to 50 µm (conditions were otherwise constant). Figure 5.6B demonstrates the depth dependent properties of articular cartilage. Decreasing indentation depth by 3X caused a 57% increase in permeability, a 20% decrease in tensile modulus and a 27% decrease in the equilibrium contact modulus compared to the results from 150 µm deep indentation measurements under the same conditions.
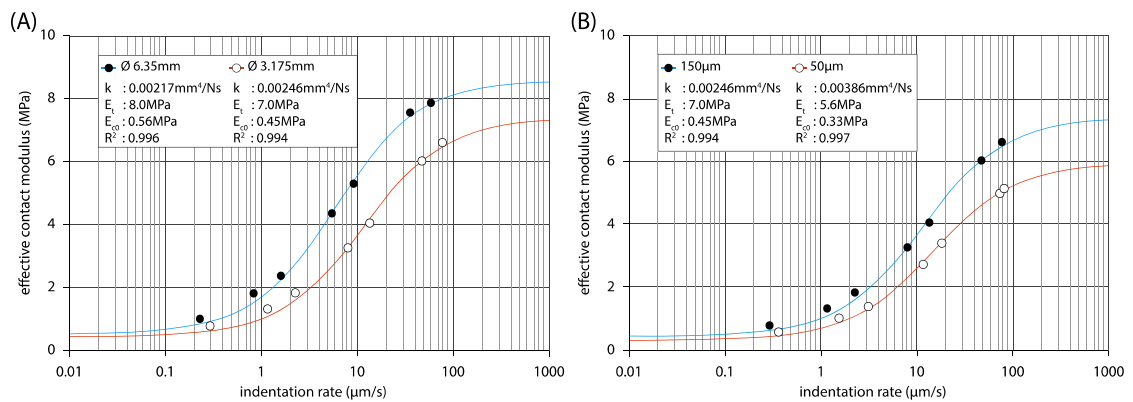
Figure 5.6   (A) The effects of probe radius on the effective contact modulus are plotted as a function of the indentation rate (in descending order with a commanded depth of 150 µm). (B) The depth dependent properties of articular cartilage can be determined using the biphasic model. The Z-stage was commanded to translate 150 and 50 µm into the cartilage sample with a probe of radius = 1.5875 mm. The solid lines are the biphasic model fit to the experimental data. Figure is adapted with permission [26].

We used this method to quantitatively test McCutchen's observation that cartilage, a notoriously difficult tissue to preserve, can be preserved by drying out the tissue and rehydrating it prior to testing [1]. The sample was dried and stored in ambient lab conditions for 4 days; the sample would be extremely degraded after 4 days at ambient temperatures if not dehydrated first. It was rehydrated by submersion in PBS for several hours. The baseline experiments in Figure 5.3 were repeated and the results are compared in Figure 5.7. The permeability and tensile modulus of the preserved cartilage had increased by 18% and 9% respectively, while the equilibrium contact modulus decreased by 16%. The result support McCutchen's observations as these are relatively minor changes given the extreme nature of the storage conditions.
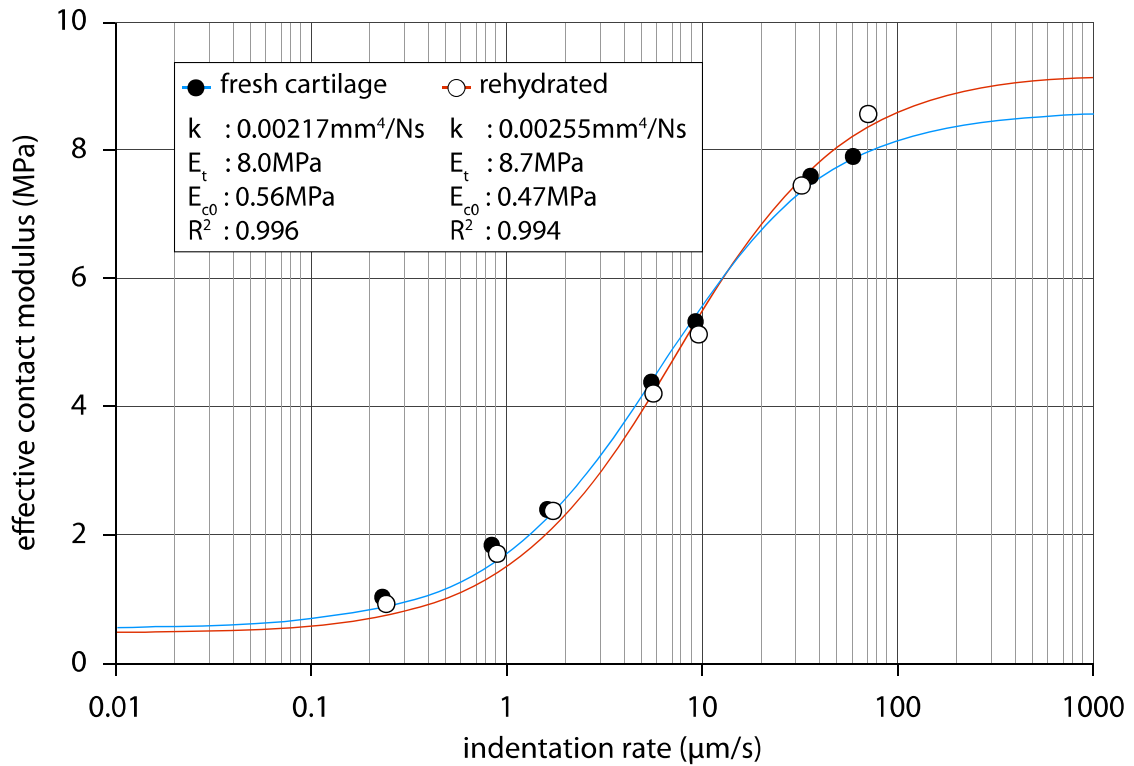
Figure 5.7   The effects of dehydrating (4 days) and rehydrating (several hours in PBS) a single sample of bovine articular cartilage. The solid lines are the biphasic model fit to the experimental data. Note that the probe had a radius of 3.175 mm. Figure is adapted with permission [26].

Following Hertzian indentation testing, the same sample was creep-tested with a porous plane-ended indenter at the same location to determine the properties of the sample with the two gold-standard methods. The experimental results of the creep experiment, which were used by both methods, are shown in Figure 5.8. The fit to the LBT for plane ended indentation gives a Poisson's ratio $\nu = 0.1$, aggregate modulus H_a = 0.47 MPa and permeability $k = 0.0014$ mm^4/Ns ($E = E_t = E_{c0} = 0.46$ and $H_a = 0.47$ MPa for a linearly elastic material with $\nu = 0.1$). The fit illuminates obvious disagreement between the dataset and the model at small deformations; this is a known

limitation of linear biphasic theory and occurs because linear materials are unable to support fluid pressures comparable to the elastic stress unless the layer becomes very thin relative to the contact radius; since pressure drives lubrication, this implies that linear biphasic materials cannot lubricate well. It is for this reason that LBT best-practice is to fit only the data in the upper 30% of strain measurements, which we have done here.
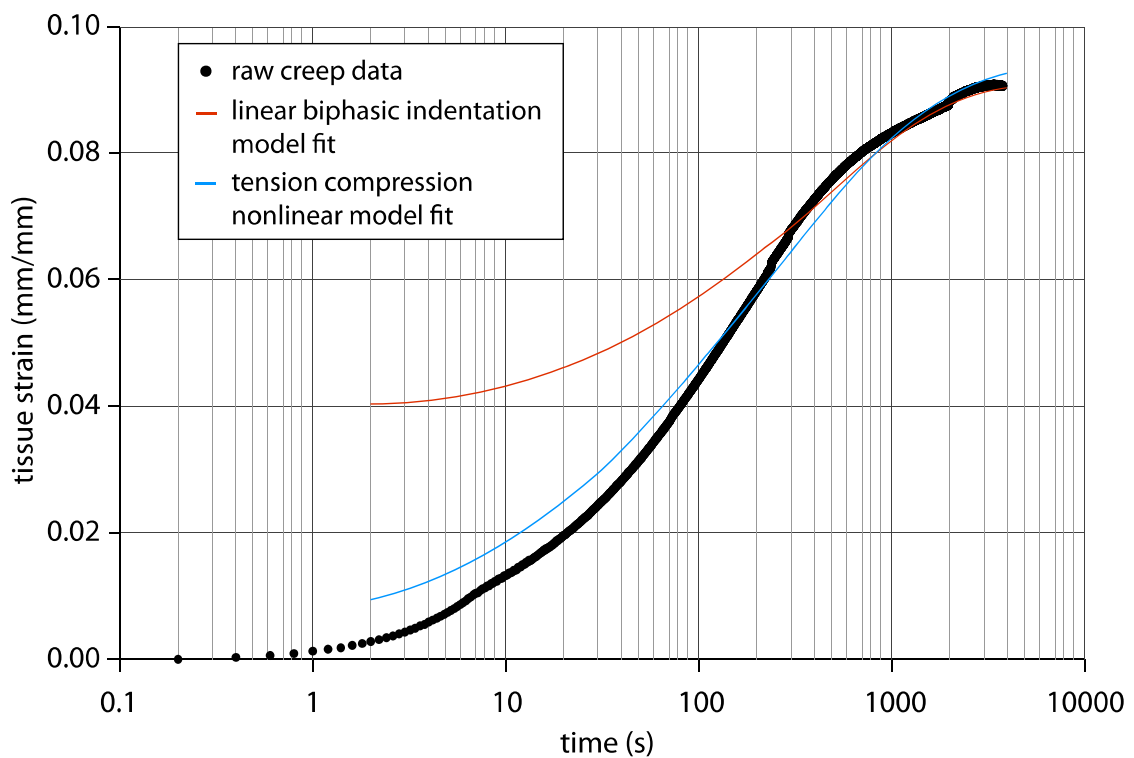
Figure 5.8   The porous plane ended indentation creep response of the rehydrated cartilage sample. The sample was loaded to 200 mN. The linear biphasic indentation model (LBT) was fit using published analysis methods: $k =$ 0.00135 mm^4/Ns, $H_a = 0.47$ MPa, $\nu = 0.11$ and R$^2 = 0.979$ (upper 30% of strain only). Fitting the tension compression nonlinear model (TCN) to the data gives: $k = 0.00158$ mm^4/Ns, $H_a = 0.40$ MPa, $E_t = 10.3$ MPa and R$^2 = 0.984$ (entire fit from 2 seconds). The TCN model is far better able to represent the early response where fluid pressures are large. Figure is adapted with permission [26].

51

The TCN model better reflects the actual mechanical response of cartilage under indentation loading with $R^2 > 0.98$ for a fit to the whole dataset. The properties were $H_a = 0.40 \pm 0.02$ MPa, $k = 0.0016 \pm 0.0001$ mm^4/Ns, and $E_t = 10.3 \pm 2.2$ MPa; confidence intervals reflect the standard error in the estimate of the mean. The mean results from each of the three models are given in Table 5.2 for direct comparison.

Table 5.2   Material properties obtained for a single location of the cartilage sample from HBT, LBT, and TCN characterization methods during tests with maximum penetration depths of ~100 µm. The aggregate and equilibrium contact moduli are equal to within 0.006 MPa when $v < 0.1$. The asterisk denotes the fact that the fit was limited to the data in the upper 30% of strain.

Property	v	H_a / E_{c0} (MPa)	k (mm^4/Ns)	E_t (MPa)	R^2
HBT	N/A	0.47	0.0026	8.7	0.994
LBT	0.1	0.47	0.0014	0.46	*0.979
TCN	N/A	0.40	0.0016	10.3	0.984

5.4   Discussion

Although LBT is the most common method for characterizing biphasic materials, it is only able to represent the response of the tissue accurately when interstitial pressures are below the elastic compressive stress. The tensile modulus dominates the maximum achievable pressures and is therefore more closely related to tissue function (lubrication and load capacity) than Poisson's ratio, aggregate modulus, or even permeability [86]. The TCN model can reproduce physiological magnitudes of fluid pressure by allowing the tensile modulus to be much larger than the aggregate modulus. However, this solution requires specialized computational

tools and is therefore uncommon as a characterization method in the literature. The HBT model has a similar capacity to predict physiological magnitudes of fluid pressure without requiring specialized computational tools, with shorter experiments and with better quantitative agreement with experimental curves (at least in this case).

The most important goal of this paper is to establish confidence in the HBT method by direct comparison to the gold standards using comparable measurements at the same location on the same sample. First, consider the tensile modulus. In this case, the result from HBT differs from TCN by less than 16%, which we consider strong agreement. Additionally, both measures agree quantitatively with published values for healthy cartilage, which range from 3.5-14 MPa [86,146,148,159]. It should be noted, however, that the tensile modulus isn't as clearly defined for cartilage as it is for most engineering materials. Because the tensile stiffness comes from a collagen fiber network that aligns in the direction of loading, it tends to increase with strain. Nonetheless, the models are self-supporting, which provides confidence in their respective uses for in-situ tensile modulus characterization, which has no established standard to date.

Next, consider permeability. LBT gives the smallest permeability ($k = 0.0014$ mm^4/Ns), TCN gives a slightly larger permeability ($k = 0.0016$ mm^4/Ns), and HBT gives the largest permeability ($k = 0.0026$ mm^4/Ns). Each of these falls in a relatively narrow band within the wide range of values found in the literature (0.0004-0.008 mm^4/Ns) [1,86,120,130,159–161].

Permeability is not a constant even from measurements made at the same location. It depends strongly on the proteoglycan content and the predominant collagen alignment, both of which vary with depth. Consequently, the permeability

varies with the predominant flow direction and depth. As a result, the variations in observations from these experiments are reasonable given the differing effective depths of the measurements and the differing flow profiles.

Because LBT and TCN results were based on the same experimental dataset, their differences cannot be due to the possible sources cited above. In this case, differences are likely affected by differing effective dilatations. Compressive strains consolidate internal pathways to reduce permeability while IFP expand internal pathways to increase permeability [154]. The LBT model only fits the data for which fluid load support is less than ~30%; lateral tensile strains are minimized and normal compressive strains are maximized in this method. The TCN model included data for which fluid load support reached 80%; using the same dataset, TCN predicted a 17% larger permeability than LBT simply by involving data from the high-pressure part of the curve in the fit. In contrast, the permeability from HBT was more than 60% larger than either plane-ended method. In plane-ended (LBT and TCN) indentation only ~2% of the data involved more than 50% fluid load support, while 75% of the spherical (HBT) test involved more than 50% fluid load support. We can validate this mental model by fitting only the low-speed (low pressure) range of the HBT dataset from 0.1-1 µm/s; in this case, the permeability decreases to $k = 0.0014$ mm^4/Ns, which is in-line with that from LBT.

This analysis suggests that these differences are due primarily to significant differences in the mean effective pressure of fit datasets. Manipulation of the HBT fit to better control the pressure range illustrates that each method supports the others. Therefore, it is not a question of which is correct or incorrect, but a question of which conditions are most relevant to the application of interest. The HBT results may be the

most relevant for cartilage under physiological conditions since fluid load support is typically on the order of 90% in-vivo [138]. However, it is important to recognize that the reported values from HBT will always be biased above those from LBT for otherwise identical conditions.

Finally, consider comparisons of the aggregate modulus. The LBT model gives an aggregate modulus of 0.47 MPa compared to 0.40 MPa from TCN. The HBT model gives the equilibrium contact modulus, not the aggregate modulus, but at $\nu <$ 0.1, the difference is < 0.01 MPa. At 0.47 MPa, the HBT modulus is equal to LBT, both of which are 18% greater than that from TCN. The aggregate modulus of the TCN model is reduced to compensate for the stiffening effect of embedded fibers in tension. Fibers in the TCN model develop significant tension during plane-ended indentation, particularly near the edge contact.

Repeat testing revealed that the curves and fitting results were repeatable and not particularly sensitive to the order of the indents. This is perhaps surprising considering that fluid is squeezed from the tissue during indentation, especially when rates are slow. Interestingly, we have noticed that the act of pull-off actually pulls fluid back into the tissue. The apparent adhesive force in Figure 5.2 is attributable to suction, not adhesion. Even more interestingly, this suction affect almost entirely restores the sample to its pre-indented level of hydration, which is why there is no noticeable hysteresis effect. This suction effect in combination with the 1-minute rest is apparently enough to virtually eliminate cartilage consolidation throughout a typical series of indentation measurements.

When probe radius decreased, the modulus decreased and the permeability increased. We believe this is attributable to actual depth-dependences. The

interaction depth in a Hertzian contact increases with probe radius and penetration depth; decreasing either makes the measurement more sensitive to surface properties. The results of this study consistently suggest that the near surface has decreased aggregate modulus and increased permeability. This is consistent with results from Chen et al. [162] who demonstrated that human cartilage had reduced modulus and fixed charge density toward the surface. It is also consistent with known trends of increased water content and decreased glycosaminoglycans in the superficial region [124].

The model underlying the procedure has numerous limitations related to the over-simplified material model (a porous permeable solid with different linearly elastic compressive and tensile moduli). In reality, cartilage is heterogeneous, anisotropic, nonlinear, viscoelastic, and variably permeable. In developing this model, we incorporated only the complexities that were absolutely necessary to reproduce the essential features of the measured mechanical response. A high tensile modulus is unquestionably responsible for elevating fluid pressure in the tissue and it is important that this detail be carried over into models of its mechanical response. Variable permeability does affect the results as discussed previously, but the HBT model minimizes the effects of variable permeability on aggregate and tensile modulus; the permeability from the fit can be thought of as an effective permeability in the range of conditions of the experiments. Heterogeneity also has a significant impact on results. The superficial layer is clearly softer than the rest of the tissue and our variable depth measurements reflect that. The measurements made here are localized toward the surface and the properties likely reflect a composite of the entire near-surface region, the depth of which depends on the contact radius.

The HBT offers unique flexibility in the spatial and depth sensitivity of the method. Under normal conditions, like those described here, the smaller contact areas result in 80-95% reduced time constants relative to the gold standard for increased throughput; time is a significant challenge for these measurements since hydrated samples degrade over time. The method can be used with high confidence based on the comparisons against the gold standards and its use requires no specialized computational tools. A fitting template written by the authors is available at: http://www.axelcmoore.com/software/ .

Chapter 6

HERTZIAN BIPHASIC CONTACT MECHANICS MODEL OF CARTILAGE: SPHERICAL CREEP AND CREEP-RELAXATION

6.1 Introduction

Quantifying the material properties of cartilage, which is nonlinear, anisotropic, heterogeneous, and viscoelastic, has been historically challenging. Early studies used indentation measurements to study the elastic properties of cartilage [163–169], but two problems with this approach emerged. First, because cartilage is a thin layer attached to a stiff substrate, it is difficult to know the extent to which the underlying bone contributes to the deformation response. Second, the tissue creeps over time. Kempson et al. addressed the substrate problem by experimentally determining a layer correction factor [163,164], which Hayes et al., later solved for theoretically [170]. The time-dependence problem was initially addressed by defining different moduli at different times after loading (e.g. instantaneous modulus [169] and 2-second creep modulus [164]).

McCutchen demonstrated that the time-dependence of the mechanical response was due to the exudation of interstitial fluid, which constitutes ~80% of cartilage. His weeping lubrication theory explained creep and low friction of cartilage simultaneously [55,116]. Armstrong et al. and Mow et al. used linear mixture theory, a continuum mechanics-based approach, to solve for the biphasic (solid and fluid phase) response to unconfined and confined compression [154,171]. However, the simplifying assumptions that make these configurations theoretically attractive are

impossible to achieve experimentally: 1) samples are not flat or parallel, 2) flow occurs between the cartilage and the impermeable boundary, and 3) removal of the cartilage from the bone fundamentally changes the collagen structure and therefore tissue properties. In an effort to overcome some of these experimental challenges, Mak et al. developed a linear mixture theory solution to creep indentation of a porous plane-ended cylinder into a cartilage layer to enable in-situ characterization of the compression modulus and permeability [153]. A follow-up paper describing the experimental procedure required to use the solution has since become the gold standard for quantifying the biphasic compressive properties of cartilage [120].

The use of a plane-ended indenter was motivated by the theoretical benefits of a constant contact area. However, the edge of the plane-ended indenter is a stress concentrator. Spherical indenters, which eliminate the stress concentration and better represent physiological contacts, are experimentally favorable for quantifying material and tribological properties [78,133,172,173]. Spherical indentation of a linearly elastic half-space was first solved by Hertz [174] and later by Agbezuge and Deresiewicz for a linearly elastic biphasic half-space [132]. Oyen digitized their master curve, fit the points to an analytical function, and used that function to develop a method of quantifying Poisson's ratio, permeability, and shear modulus from Hertzian creep measurements [152].

Ling recognized the importance of mechanical nonlinearity (cartilage is much stiffer in tension than in compression) and, to the best of our knowledge, was the first to develop a non-linear mixture model of cartilage mechanics and tribology [175]. Whereas linear mixture theories are known to under-predict interstitial pressure and the resulting stress-shielding and lubrication effects [171], Soltz and Ateshian [176]

59

showed that a non-linear mixture model accurately predicts the experimentally measured response. Explicitly, it was demonstrated that the stiff tension modulus effectively confines the tissue, thus providing the resistance against which interstitial pressure builds. The tension modulus is as important as the compression modulus and permeability to cartilage mechanics and tribology.

There are relatively few studies in which the compression modulus, tension modulus, and permeability have been determined for a single sample. Soltz and Ateshian [176] used a combination of unconfined compression, confined compression, and shear testing. Huang et al. [177] used a combination of tension testing and unconfined compression while Setton et al. [178] used a combination of tension testing and porous plane ended indentation. In each of these studies, cartilage samples were removed from the bone and properties quantified with multiple testing modalities, each requiring significant test time. We recently described a method with which contact modulus, tension modulus, and permeability can be quantified using Hertzian indentation measurements on any osteochondral surface [26]; however, the fact that each indent represents a single data point limits the number of flow conditions that can be probed. This paper develops a creep-based method to quantify the best-fit contact modulus, tension modulus, and permeability properties for all possible flow rate conditions. The goal of this paper is to describe the method, apply it to a representative collection of cartilage samples, probe its limitations and compare its output against the solutions from Oyen [152], a common biphasic characterization method, and FEBio, an open source finite element package that is considered the current gold standard for soft tissue mechanics modeling [158].

6.2 Methods

6.2.1 Materials and Equipment

Thirteen osteochondral cores were removed from three mature bovine stifles;
ten samples came from the femoral condyle and three came from the tibial plateau.
Unless noted otherwise, each sample had a diameter of 12.7 mm. Samples were stored
at 2°C in 0.15M phosphate buffered saline (PBS) (21-040-CM, Mediatech) and tested
within two days of removal. The thickness of each cartilage sample was measured
before the test with a calibrated optical microscope (MM-400/S, Nikon). The thickness
was defined as the mean of four equally spaced measurements, which typically varied
by less than 0.1 mm. The thickness values ranged from 0.89 to 2.34 mm. The custom
indentation rig shown in Figure 6.1 was used to perform creep indentation
experiments. A single smooth and impermeable borosilicate glass sphere was used to
indent each sample; the radius $R = 3.175$ mm. After mounting the sample in the
indenter, a 2-axis tilt stage was used to orient the sample normally with respect to the
loading Z-axis; an X-Y translation stage was then used to locate the sample under the
indenter. The sample was then submerged in PBS for the duration of the test. For
repeat testing, the sample was left submerged for 20 min to equilibrate before
subsequent testing.

A displacement controlled 800 ± 0.0018 µm piezoelectric stage (P-628, Physik
Instrumente) was used to control each indentation. A custom load cell consisted of a
calibrated cantilevered beam (0.926 ± 0.0012 mN/µm) and a 150 ± 0.014 µm
capacitance sensor (C11-E, Lion Precision), used to measure beam deflection. The
contact force was calculated by multiplying the beam deflection by the spring

constant. The indentation depth of the sphere into cartilage was calculated as the difference between the stage displacement and the beam deflection.

Two tests were used: 1) creep and 2) creep relaxation. The creep test, which is used as the standard given its prevalence in the literature, applies a constant force. A custom Labview program was written to achieve load-control by updating the Z-stage position based on the difference between the target load and the measured load. Creep relaxation was used to 1) demonstrate generality of the results for different testing modalities and 2) to provide an experimentally simpler alternative to constant load testing. For creep relaxation, an open-loop voltage was applied to the stage. In this case, load decreases as the sample deforms with a ratio equal to the spring constant of the loading beam.

Prior to each indentation test the vertical stage approached the surface until the measured force exceeded zero by three times the standard error. The probe was then retracted 3 µm above the surface before driving the probe into the sample to achieve the target load; the target load was reached within 0.7 s for each measurement. Equilibration was defined when the indentation rate fell below 0.3 µm/min, which corresponds to less than 5 Pa/min for the samples in this study [161,173].
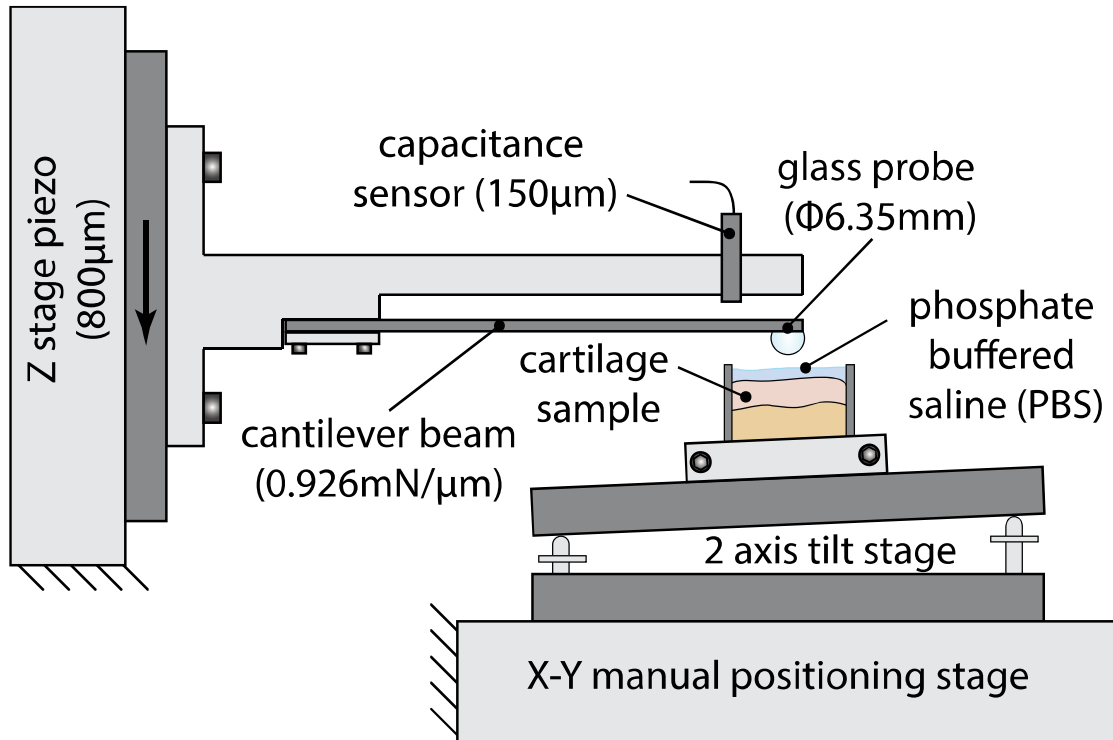
Figure 6.1 Spherical micro-indenter. A capacitance sensor measures beam deflection, which is proportional to force through the spring constant. As the cartilage exudes fluid and deforms the Z-stage piezo actuates to maintain a constant load. Figure is modified with permission [26].

6.2.2 Hertzian Biphasic Theory (HBT) Method

The method implemented here was based on the analytical model from Moore and Burris [28], which we refer to as Hertzian biphasic theory (HBT). The model assumes: no adhesion, isotropic, homogeneous, linearly elasticity in compression, linearly elasticity in tension (different compression and tension moduli), a Poisson's ratio of zero, and biphasic with strain-dependent permeability. The first advantage to this method is that it provides an analytical framework for estimating properties.

At equilibrium, IFP falls to zero and the indentation depth is only a function of the effective contact modulus ($E_{c'}$). The effective contact modulus can be determined directly from Hertz's theory using the equilibrium indentation depth:

$$E_{c'} = \frac{3}{4} F \cdot R^{-0.5} \cdot \delta_{eq}^{-1.5}$$
Eq. 6.1

where δ_{eq} is the indentation depth at equilibrium, R is the radius of the indenter, and F is the applied force. Because Eq. 6.1 assumes a semi-infinite half-space, the "effective" contact modulus includes contributions from the substrate. The corrected contact modulus (E_c) of the cartilage is a function of $E_{c'}$, R, δ_{eq} and cartilage thickness, t [155]:

$$E_c = E_{c'} \cdot \left(1 - 1.04 \cdot e^{\left(-1.73 \left(\frac{t}{\sqrt{R \cdot \delta_{eq}}} \right)^{0.734} \right)} \right)^3$$
Eq. 6.2

The initial indentation depth only depends on the contact and tension moduli; therefore, the tension modulus (E_{y+}) can be determined directly from the initial indentation depth:

$$E_{y+} = \frac{3}{4} F \cdot R^{-0.5} \cdot \delta_{init}^{-1.5} - E_c$$
Eq. 6.3

The subscript *init* denotes the initial response to an instantaneously applied load.

Lai et al. showed that the intrinsic permeability (k) is not a material property; it is a function of tissue dilatation according to the function: $k = k_0 \cdot e^{-M \cdot \varepsilon}$ [179,180], where ε is the trace of the strain tensor, k_0 is the un-strained permeability constant, and M is the non-linear flow-limiting constant. Because fluid cannot flow instantaneously,

the volume change is zero initially and k_0 can be determined using the initial deformation rate $\dot{\delta}$ and indentation depth:

$$k_0 = \frac{4}{3} \frac{\left(R \cdot \delta_{init}\right)^{1.5}}{F - 4/3 \cdot E_c \cdot R^{0.5} \cdot \delta_{init}^{1.5}} \cdot \dot{\delta}_{init} \qquad \text{Eq. 6.4}$$

The intrinsic permeability can be determined analytically by replacing initial conditions in Eq. 6.4 with those at any other point; thus M can also be determined analytically. However, a least squares regression is performed to determine the best fit to the entire dataset. A downloadable template and user guide for the HBT method are available at: http://www.axelcmoore.com/software/ to help other researchers obtain material properties after inserting experimental creep data.

Uncertainty analyses were performed to quantify the propagation of individual measurement uncertainties into each measured property [181]. The input measurement uncertainties were: u(time) = 0.3 s, u(F) = 0.5 mN, u(δ) = 1 µm, u(R) = 3 µm, u(t) = 100 µm. Because the method involves numerical optimization, Monte Carlo simulations were performed to simulate the propagation of error. The Monte Carlo procedure involved 1) perturbing the measured data by a random amount based on the appropriate uncertainties and 2) using 20 random simulated data sets with the HBT method to determine 20 unique combinations of material properties. The uncertainty in our reported measurements represents the standard deviation from those simulations.

Finally, it is important to point out some inherent limitations of the model. The anisotropic and heterogeneous nature of cartilage means that properties depend on the material volume probed in the measurement. The Hertzian contact confines the stress field (primarily) to a hemispherical volume of the same radius as the contact; this fact

provides a degree of control over the zones of the cartilage probed (e.g. the superficial zone extends from the surface to approximately 100 µm below the surface and is structurally distinct from the middle and deep zones). In addition, the flow model assumes semi-circular flow streamlines, which theoretically holds as long as the contact radius is less than the cartilage thickness and half the radius of the cylindrical sample.

6.2.3 Comparison Studies

A subset of the measurements was fit with two accepted biphasic creep models to determine if they extract different properties from the same datasets. The first, FEBio, is an open source finite element software package for computational tissue mechanics studies [158]. FEBio has been validated against several closed-form solutions and is considered the gold standard for the purposes of this study. FEBio was used to solve for the contact between a rigid sphere and a tension-compression nonlinear biphasic layer of cartilage bonded to a rigid substrate. The constitutive relationship assumed for articular cartilage consists of a neo-Hookean ground matrix reinforced with a spherical fiber distribution [182,183]. The FEBio algorithm adjusted compressive modulus ($E_{y-} = E_c$), fiber modulus (ξ), and permeability (k) to minimize the sum-squared error between the FE-calculated force and the experimental force at each time step.

The second is Oyen's method, another established method of characterizing biphasic properties from Hertzian creep measurements; the method is described in detail elsewhere [152]. The method assumes linear elasticity, constant permeability, and a semi-infinite layer; we correct for the substrate effect here using Eq. 6.2. The

Oyen method outputs contact modulus, permeability, and Poisson's ratio. A template for this procedure can be found on a separate tab of the HBT template.

The three methods (HBT, FEBio, Oyen) provide different outputs; only the contact modulus is common among them. To compare methods, outputs were transformed into comparable parameters. The FEBio and Oyen methods provide a single effective permeability based on the best curve fit. To provide a consistent measure of permeability from HBT, a second fit is performed in which permeability is assumed constant ($M = 0$); this has no effect on the elastic constants E_c and E_{y+}. The Oyen method assumes linear elasticity; as a result, the tensile modulus is set equal to the contact modulus. Since the FEBio method solves for the fiber modulus ξ, the tension modulus is taken as the slope of the stress-strain curve at 0% strain in a simulated tensile test using the optimized material properties from indentation.

Solutions were obtained for all three methods using each of four independent creep tests. Paired t-tests were conducted to determine whether E_c, E_{y+}, and k from HBT and Oyen methods were statistically different from those of FEBio with $p < 0.05$.

6.3 Results

6.3.1 HBT Method and Limitations

Three repeat creep curves are shown in Figure 6.2A to illustrate a representative creep response and the extent to which that creep response is reproducible. The line represents the best-fit from HBT for curve #1a (the worst fit of the three) and clearly represents the dataset well with $R^2 = 0.9995$. The means and standard deviations from these repeat measurements, which are shown in Figure 6.2B, were: $E_c = 0.59 \pm 0.01$ MPa, $E_{y+} = 7.8 \pm 0.2$ MPa, $M = 7.4 \pm 1.1$, $k_0 = 2.20 \pm 0.24$ x 10^-

[3] mm^4/Ns. The experimental uncertainties were: u(E_c) = 0.02 MPa, u(E_{y+}) = 0.3 MPa, u(M) = 0.3, u(k_0) = 0.06 x 10^{-3} mm^4/Ns; the fact that the standard deviations were consistent with the accompanying experimental uncertainties suggests that the scatter in repeat measurements was driven at least as much by measurement uncertainty as they are by changes in the response of the cartilage itself. This demonstrates that the response is a consistent function of material constants regardless of the extent to which interstitial fluid is lost during each creep test.
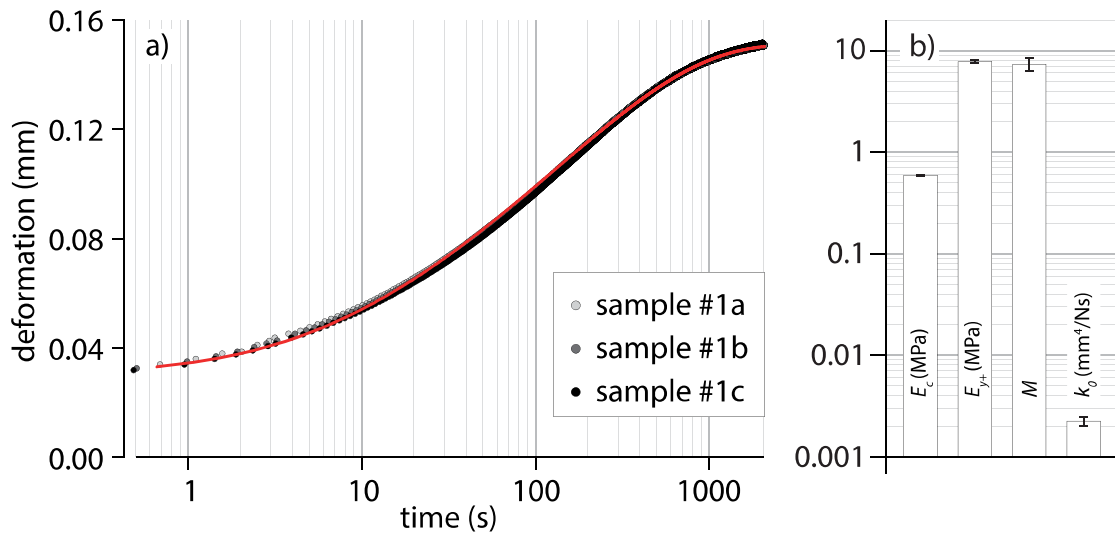
Figure 6.2   (A) Creep deformation versus time for sample 1 at a constant load of 120 mN. Sample #1a was the first test and #1c was the last repeat; each repeat was conducted after 20 minutes of free swelling. (B) Comparisons of E_c, E_{y+}, M and k_0 for sample 1. Error bars represent the standard deviation of repeat measurements and fits. Figure is adapted with permission [123].

In theory, the flow model is valid until the contact radius exceeds the thickness or half the sample radius. Additional indents were performed to test for these effects. Figure 6.3A illustrates the effect of creep load (35, 50, and 120 mN) on material

68

properties. Increased loads sampled increased depths, which tended to increase E_c and E_{y+}, and decrease k_0; these changes are consistent with known depth dependences of cartilage [124,184]. The increase in E_c reflects increased solid content in the deeper zones [124,184], while the increase in E_{y+} reflects the fact that tensile modulus increases with increased tensile strain due to fiber uncrimping [124]. The contact radius never exceeded 55% of the thickness so apparent changes in permeability with load most likely reflect actual differences between the effective depths sampled [124,184].

To evaluate the potential effects of sample size on the infinite biphasic layer assumption a third sample was tested after trimming from 19 ➔ 12.7 ➔ 6.35 ➔ 4.8 mm diameter; the results are shown in Figure 6.3B. Unlike the variable load test, this test effectively eliminates the confounding effect of variable sampling depth. As Figure 6.3B demonstrates, the method was insensitive to variations in sample size down to 3.5X the contact diameter.
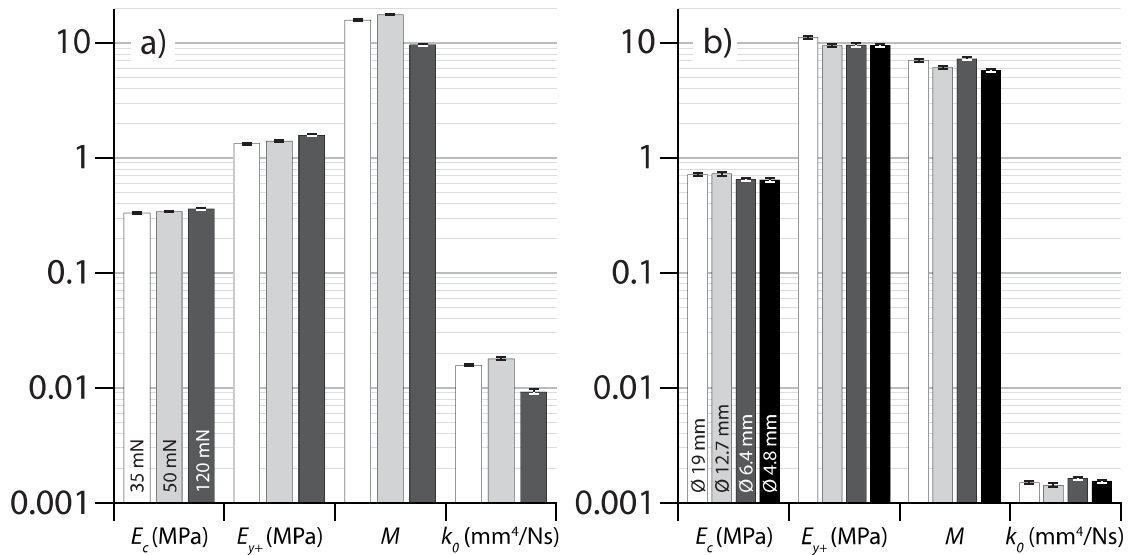
Figure 6.3   Additional tests were conducted to evaluate the HBT method. (A) Three different creep loads (35, 50, and 120 mN) were applied to the same location on sample 2 to determine the effect of creep load on tissue properties. (B) Sample 3 was used to test the assumption of an infinite biphasic layer. The sample was evaluated after sequentially reducing its diameter from 19 to 4.8 mm. Figure is adapted with permission [123].

A third test of method generality was conducted by comparing results from two different loading cases: creep and creep relaxation. As Figure 6.4 illustrates, creep relaxation simultaneously involves creep and stress relaxation. There are several noteworthy features. Firstly, the predictability (R^2) of the HBT method is equally good for both tests. Secondly, the material constants are insensitive to the experimental method. The permeability decreased by nearly 50% in creep relaxation, which is consistent with the fact that a higher initial load probes a deeper zone with lower permeability (consistent with Figure 6.3). Whereas the properties clearly depend on the volume being sampled, these results suggest that the HBT method is insensitive to the nature of the test itself.

		E_c (MPa)	E_{y+} (MPa)	M	k_0 (mm^4/Ns)	R^2
creep	● deformation ○ normal force	0.34	1.37	16.6	0.016	0.9997
creep relaxation	● deformation ○ normal force	0.35	1.40	16.3	0.009	0.9994
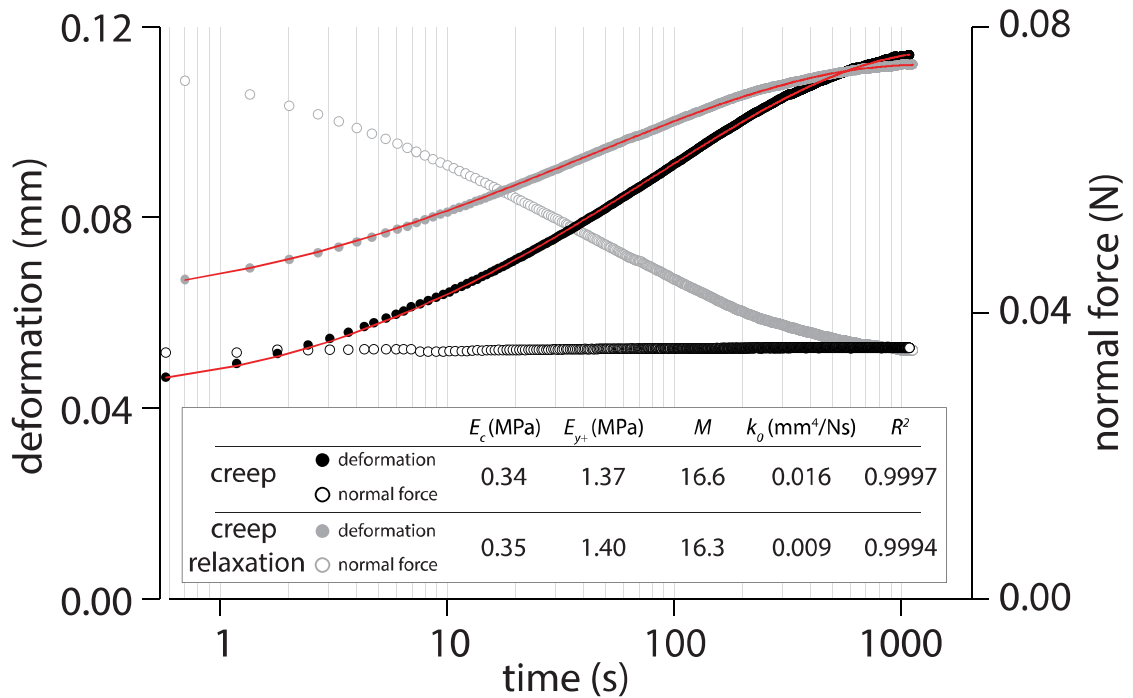
Figure 6.4   Comparison of results from HBT fits to creep and creep relaxation. Creep relaxation is a hybrid of creep and stress relaxation. Figure is adapted with permission [123].

Lastly, measurements were performed on two different populations of cartilage; one from the tibial plateau and the other from the femoral condyle to test for sensitivity to differences between populations. The results of these measurements are shown in Figure 6.5. The mean and standard deviation in the coefficient of determination for all 13 fits was $R^2 = 0.999 \pm 0.001$, which demonstrates that all samples were well-fit by the method, despite obvious differences between sample populations [6]. On visual inspection, the tibial plateau appears to have smaller moduli and greater permeability, which is the expected result [6]; interestingly, there is no obvious effect of joint surface on M, which varies by less than a factor of four for all samples tested. Student t-tests detected statistically significant differences in moduli

only, which is reasonable considering the relatively small sample size from the tibial

plateau (N=3).
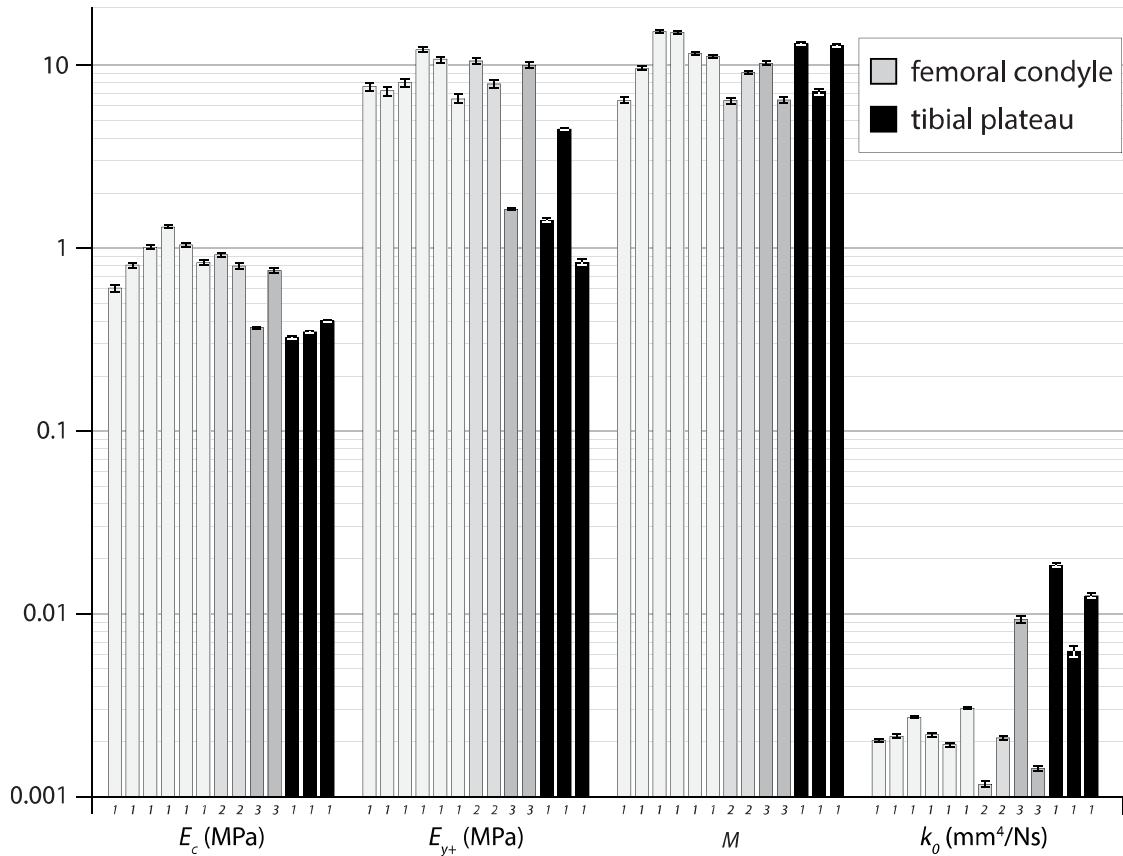
Figure 6.5   Material properties for 13 samples from 3 bovine stifles as determined by
HBT. Samples are grouped by their respective cartilage surface, femoral
surface (light grey) or tibial surface (dark grey). Tibial samples were only
obtained from joint 1. Femoral surfaces from different joints (1, 2 and 3)
are shaded differently to highlight their differences. Error bars represent
experimental uncertainty. Figure is adapted with permission [123].

6.3.2 Methods Comparisons

The converted values from each method are given in Table 6.1 for N=4 samples. It is worth noting that the effective permeability from HBT is typically less than half k_0 due to the decrease in permeability with strain. Figure 6.6 compares the percent differences from the FEBio standard. The HBT method differed from FEBio by +3, +7, and -33% for E_c, E_{y+}, and k, respectively. The Oyen method differed from FEBio by -11, -88, and -37% for E_c, E_{y+}, and k, respectively. Differences in both moduli from the Oyen method were statistically significant; no differences were detected between HBT and FEBio.

Table 6.1   Converted values of E_c, E_{y+}, and k from the FEBio, HBT and Oyen methods. Values are given as the mean $\pm$ standard deviation for N=4 samples. Table is adapted with permission [123].

method	E_c (MPa)	E_{y+} (MPa)	k x 10^{-3} (mm^4/Ns)
FEBio	0.73 ± 0.39	6.5 ± 3.6	2.2 ± 2.3
HBT	0.76 ± 0.41	7.1 ± 4.4	1.0 ± 0.8
Oyen	0.66 ± 0.36	0.7 ± 0.4	1.4 ± 1.8
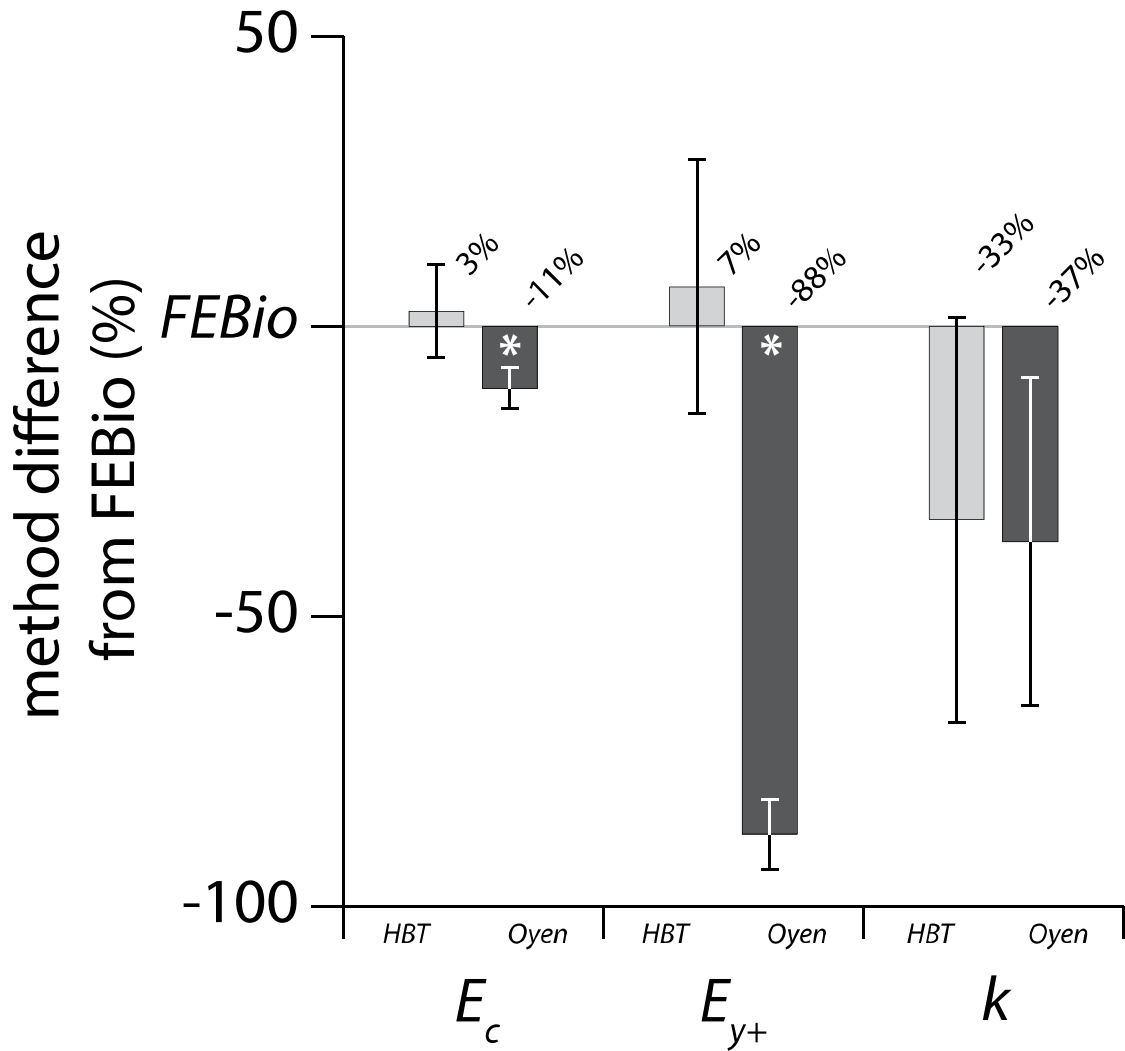
Figure 6.6   The % difference between FEBio and the HBT (light grey) and Oyen (dark grey) methods. Error bars represent the standard deviation for N=4. Asterisks (*) represent significant differences from FEBio. Figure is adapted with permission [123].

6.4   Discussion

This study developed and illustrated a simple method of determining the contact modulus, tension modulus, and permeability properties of cartilage using a single Hertzian creep test. The key questions are whether or not the creep response is

actually a function of material constants, and whether or not the material constants from the model reflect actual constants of the tissue. The results of this study help build the case that the creep response does reflect material constants and that the values output by HBT reflect actual values based on direct comparisons against the finite element method and indirect comparisons against values reported in the literature.

Firstly, the creep response was repeatable in three subsequent measurements, which suggest that it is a function of material constants independent of the fact that previous experiments cause significant exudation of the interstitial fluid. Thus, the method can be used to determine material constants directly prior to tribological testing, for example.

Secondly, the properties output by the method were independent of variations in applied load, sample size, and test configuration (creep versus creep relaxation) when the contact radius was less than 55% the cartilage thickness and less than 28% the radius of the cylindrical plug. In cases for which the interaction depth did change (variable load and creep relaxation), stiffness increased and permeability decreased as expected based on known changes in structure and properties with depth [124,184].

Thirdly, the HBT method fit to each dataset well regardless of the test configuration (creep versus creep relaxation) and sample population tested (femoral versus tibial); the coefficient of determination for the 13-sample dataset was $R^2 = 0.9990 \pm 0.001$. The fact that the tibial plateau tended to be softer and more permeable than the femoral condyle is also consistent with the published literature [6].

Fourthly, direct comparison against FEBio revealed no statistically significant differences. On average, the HBT method differed from FEBio by +3, +7, and -33%

for E_c, E_{y+}, and k, respectively. Although none of the differences were statistically significant, the variations in effective permeability do stand out. However, these differences appear less significant when considered in the context of strain dependent permeability. For example, the intrinsic permeability of the sample from Figure 6.2 decreased from 2.0 x 10^{-3} mm^4/Ns during initial contact to 0.5 x 10^{-3} mm^4/Ns at the end of the test. The 33% mean difference in effective permeability between FEBio and HBT is actually relatively small compared to the 300% variation in intrinsic permeability that was typical of these experiments.

Fifthly, these large variations in intrinsic permeability are supported by the literature. The best resource for this analysis comes from Mow et al. [154], who directly measured intrinsic permeability under controlled external pressures and pre-strains. For sample 1 (Figure 6.2), the peak interstitial pressure decreased from ~0.35 MPa to ~0 MPa and the effective strain increased from ~0.05 to ~0.2 during the creep test. Based on their results [154], this change in pressure corresponds to a ~65% reduction in permeability from 2.0 to 0.7 x10^{-3} mm^4/Ns, while the change in strain corresponds to an additional ~35% reduction, bringing the intrinsic permeability to 0.5 x 10^{-3} mm^4/Ns. It is purely coincidental that our intrinsic permeability values perfectly match those of the sample in their study; nonetheless, their results provide direct experimental evidence that typical cartilage is expected to exhibit ~4-fold reductions in intrinsic permeability under the conditions of these measurements. In this light, a single 'effective' permeability analysis of creep and stress relaxation curves can be misleading, especially given that they largely reflect conditions of large strain and small pressure while physiological conditions typically involve small strains (~5% [185]) and large pressures (1-5 MPa [138]); we expect intrinsic permeability values in

the joint to be close to k_0 (or a factor of 2 to 3 larger than the effective permeability from a typical creep or stress relaxation experiment).

Finally, the reported values from HBT and FEBio are consistent with those of direct measurements from the literature (consistency with the Oyen method is limited to contact modulus and permeability). The tension modulus of articular cartilage is reported to range from 3.5 to 14 MPa [146,148,159,176]. The samples in this study had means and standard deviations of: $E_{y+} = 6.5 \pm 3.6$, 7.1 ± 4.4 and 0.7 ± 0.4 MPa, using FEBio, HBT, and Oyen fitting methods, respectively. The results from FEBio and HBT were consistent with those from the literature; the fact that they tended to fall on the lower half of the spectrum likely reflects the fact that tensile strains were small and the measurements effectively sampled closer to the toe-region of the stress-strain curve. The Oyen method is unable to output a meaningful measurement of the tension modulus due to the assumption of linear elasticity. Effective permeability values for cartilage from the literature range from $k = 0.4$ to 3.6×10^{-3} mm^4/Ns [6,26,28,176,186]. The means and standard deviations from FEBio, HBT, and Oyen were: $k = 2.2 \pm 2.3$, 1.0 ± 0.8 and $1.4 \pm 1.8 \times 10^{-3}$ mm^4/Ns, respectively. In each case, the effective permeability was consistent with previously reported results. Finally, aggregate moduli in the literature range from $H_a = 0.47$ to 0.90 MPa for a variety of joints, species, and methods [6,26,28,176,186]. The contact moduli in this study from FEBio, HBT, and Oyen were $E_c = 0.73 \pm 0.39$, 0.76 ± 0.41 and 0.66 ± 0.36 MPa, respectively, and are consistent with compression and aggregate modulus measurements reported in the literature (all three moduli are equal if Poisson's ratio is zero [176,187,188] and if fiber tension has no significant effect on the contact modulus at equilibrium).

This paper develops and validates the HBT method of quantifying contact modulus, tension modulus, and permeability from Hertzian creep indentation. The method was demonstrated using creep measurements from 13 independent mature bovine cartilage samples. The results of repeat testing showed that the measured creep response is a repeatable function of material constants. In addition, any small changes in properties from variable creep loads and loading profiles were consistent with the expected effects of changes in the sampling depth. The HBT method fit experimental data well ($R^2 = 0.9988 \pm 0.0011$), detected expected differences between the tibial plateau and femoral condyle, and agreed quantitatively with FEBio, the gold standard for comparison. Both HBT and FEBio produced properties that were consistent with values in the literature obtained via more direct means. The strain-dependent permeability properties from HBT also agree well with those previously published through direct means. The analysis of the results builds a strong case in favor of the HBT method, which possesses notable advantages of experimental utility, time required, model fit quality, and consistency with prior literature.

Chapter 7

**TRIBOLOGICAL AND MATERIAL PROPERTY DISTRIBUTIONS IN THE
BOVINE STIFLE JOINT**

7.1   Introduction

Anterior cruciate ligament (ACL) ruptures and meniscal tears are among the
known risk factors for OA. The increased risk of OA under these conditions has been
attributed to altered joint kinematics, which includes increased stresses, abnormal
motions, unfavorable muscle adaptations, and new cartilage contact patterns [8,189].
Andriacchi et al. found that ACL deficiency in humans causes a shift in contact
location [8]. They hypothesize that these kinematic shifts can initiate OA when they
initiate contact in areas that are unaccustomed to or otherwise functionally
underprepared for normal tribological contact stresses; we call this the 'altered
loading' hypothesis hereon. Previous animal model studies appear to support this
hypothesis. Bendele, for example, found that medial meniscus transection in a rat
model caused nearly immediate fibrillation on the tibial plateau [190], but had no
damaging effect on the mating condylar cartilage until far later in the progression of
the disease. This observation suggests that the two tissues respond differently to the
same tribological stresses. Furthermore, damage consistently occurred at a specific
location (outer third of the surface). This suggests that the region normally covered by
meniscus may be functionally underprepared compared to areas that contact the
femoral condyle in a healthy joint.

Several studies have demonstrated that properties of cartilage vary systematically. Ebara et al. showed that the tensile stiffness of bovine humeral cartilage was significantly higher than that of bovine glenoid cartilage [135]. Akizuki et al. showed that the tensile modulus of human cartilage was higher for the patellar groove than the femoral condyle [146] while Mow et al. showed that the aggregate modulus of bovine cartilage was higher on the lateral condyle than on the patellar groove [89]. Others have shown that cartilage properties, namely thickness, vary systematically across a single surface in the human knee [191–194]. Generally, the regions of highest contact pressures (locations of heel strike and toe off) [191] and direct cartilage-cartilage contact (as opposed to interposed meniscus) [89,192,193] are thickest. The cartilage shielded by the meniscus is correspondingly thinner and has a higher aggregate modulus than the cartilage not shielded by meniscus [89]. These results indicate that properties reflect the local mechanical spectrum in the healthy joint and support the altered loading hypothesis of OA [8].

Despite strong evidence that material properties of cartilage vary in response to the local mechanical environment of the healthy joint, there is no direct experimental evidence to suggest that tribological properties or preparedness vary concurrently. In fact, most studies of tribological properties do not report the sample extraction location from the surface of interest [78,116,195], which implies a degree of location-independence. It is known, however, that interstitial lubrication depends on biphasic material properties [22]. For example, Ateshian and Wang [110] and Li et al. [196] used biphasic theory to show that thickness and aggregate modulus should theoretically affect tribological function (fluid load support). It is therefore reasonable

to expect that tribological properties also vary according to the local mechanical environment of the healthy joint.

Although location-specific tribological properties have significant implications for our understanding of OA, it remains unclear if and to what extent such variations exist. This paper aims to establish the location-specific functional properties (fluid load support, contact modulus, effective friction coefficient) and material properties (permeability, aggregate modulus, tensile modulus) of bovine stifle cartilage to test the hypotheses that: 1) functional properties vary spatially; 2) material properties vary spatially; 3) location-specific variations in properties are consistent with location-specific differences in the mechanical environment.

7.2   Methods

7.2.1   Specimen Preparation

Each of the N=10 mature (18-24 months) bovine stifle joints used in this study was retrieved on the day of butchering. Half of the freshly butchered joints (N=5) were frozen at -80°C to test for an effect of freezing. Frozen joints were thawed overnight in ambient lab conditions prior to sample extraction. Osteochondral plugs, 12.7 mm in diameter, were removed by a coring saw either on the day of retrieval or after defrosting. Twenty samples were extracted from each joint, with the locations shown in Figure 7.1. The tibial plateau was divided into shielded (by meniscus) and uncovered regions, whereas the femoral condyle was subdivided based on the variations in the contacting surface during articulation. The outer sample primarily makes contact with the meniscus, the inner primarily contacts cartilage, and the central contacts cartilage and meniscus throughout full articulation. Following extraction,

specimens were rinsed in copious tap water to remove debris and submerged in 0.15M

phosphate buffered saline (PBS) (21-040-CM, Mediatech). Samples were stored at

2°C immediately following dissection and extraction. Because each test required

several hours to complete, each sample spent anywhere from 0 to 5 days in

refrigerated storage prior to testing. The testing order of the locations was randomized

to test for storage time effects.
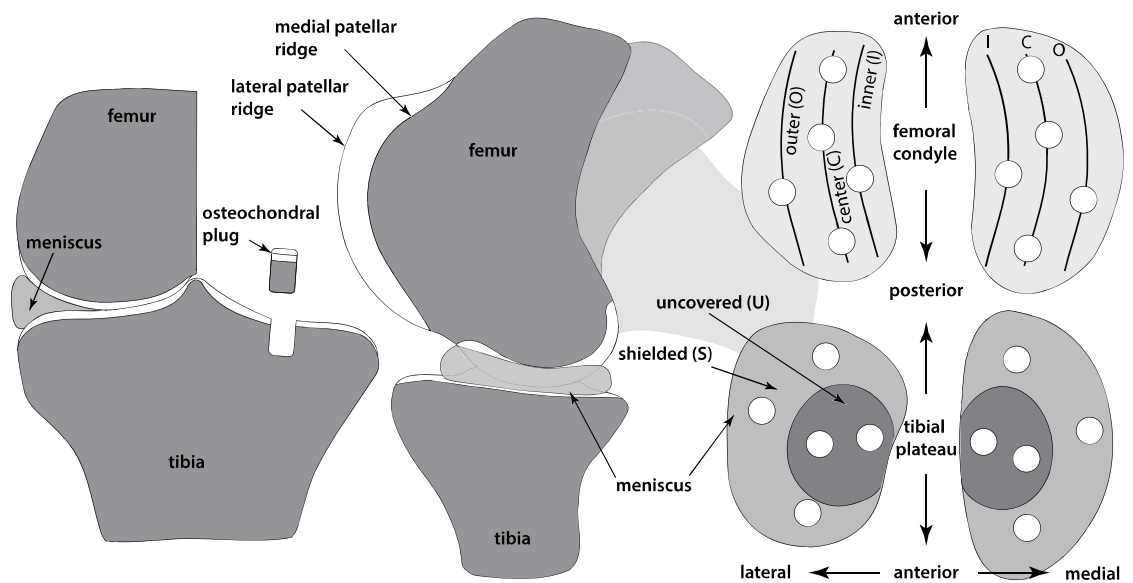
Figure 7.1   Definitions of sample sites within the bovine stifle and the regions
classified for purposes of comparison. (Left) A frontal plane view of a
bovine stifle joint. (Center) A sagittal plane view for three flexion angles
in which different samples experience cartilage-cartilage contact. (Right)
Sampling locations on the femoral condyles and tibial plateau. The
comparisons of interest are the femoral condyles vs tibial plateau, medial
vs lateral, and outer femoral condyles (O) vs central femoral condyles (C)
vs inner femoral condyles (I) vs shielded tibial plateau (S) vs uncovered
tibial plateau (U). Figure is adapted with permission [6].

7.2.2 Testing Apparatus and Functional Characterization

Tribological and material properties were measured using the spherical micro-tribometer described in section *6.2 Methods* and illustrated below in Figure 7.2. The vertical loading assembly consists of a 250 ± 0.025 µm vertical piezoelectric stage (P-622, Physik Instrumente), which is used to indent the cartilage, and a two-directional load cell (C11-E, Lion Precision) for measuring normal and friction forces. A 3.175 mm diameter stainless steel sphere with an average roughness of $Ra < 80$ nm was submerged in a PBS bath during testing. A tilt-stage (not shown) was used to align the surface normal to the z-axis of the instrument prior to indentation. A linear translation stage imposed the prescribed sliding conditions.
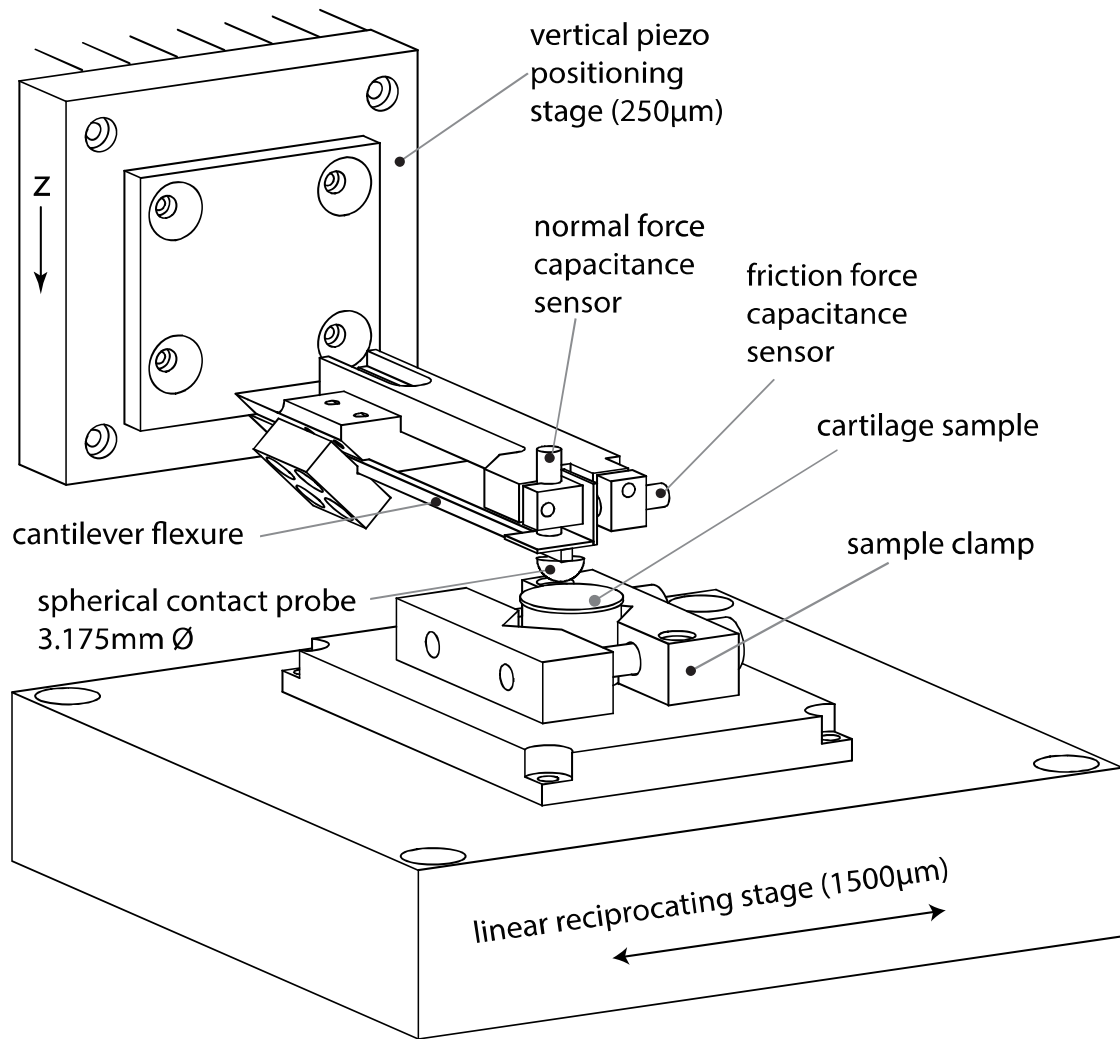
Figure 7.2   Illustration of the spherical micro-tribometer used to measure the
material and functional properties of bovine articular cartilage. Figure is
adapted with permission [6].

7.2.3   Material Properties Characterization

The indentation solution for a sphere on cartilage [28] was chosen for materials

characterization over the traditional plane-ended creep solution [120,153] due to

several important advantages: 1) it is analytical and generally applicable without

requiring master-solution datasets or interpolation from published curves, 2) it

presents no stress concentrators that can damage tissue, thus enabling follow-up

tribological testing at the same location, 3) it probes areas and depths that are

consistent with those probed during sliding, 4) permeability fits involve

physiologically-consistent combinations of fluid pressures and strains (as opposed to

large strains, small fluid pressures), 5) the same setup can be used for tribological

testing. The solution, provided in Eq. 7.1 [28], gives the fluid load fraction (F') as a

continuous function of mechanical conditions: indentation rate $\dot{\delta}$, probe radius R and

material properties: tensile modulus E_t, equilibrium contact modulus E_{c0}, and

permeability k:

$$F' = \frac{E_t}{E_t + E_{c0}} \cdot \frac{\dot{\delta} \cdot R}{\dot{\delta} \cdot R + E_{c0} \cdot k}$$

Eq. 7.1

The physical meaning of this equation is important. The first term is an

asymptotic limit governed by the dimensionless modulus, $E^* = \dfrac{E_t}{E_{c0}}$ [86,197]. The

second term describes the rate-driven approach toward the asymptote and is governed

by the Péclet number, $Pe = \dot{\delta} \cdot R / (E_{c0} \cdot k)$. Fluid load support is negligible when $Pe \ll$

1, 50% of the asymptote when $Pe = 1$, and at the asymptote when $Pe \gg 1$ [22]. It

should be noted that this form of Pe is specific to Hertzian indentation and not

necessarily appropriate for other contact situations [198].

The rate-dependent fluid load fraction was measured for each sample using

indentation at nominal rates of 50, 0.5, 5, 20, and 10 µm/s; this randomized order was

chosen to remove any hysteresis effects. The rate-dependent force-displacement

curves for a representative sample are shown in Figure 7.3. Each curve was best-fit to

Hertz' equation: $E_c = \dfrac{3}{4} \cdot F_n \cdot R^{-0.5} \cdot \delta^{-1.5}$ (normal force F_n and deformation δ) to

determine the effective contact modulus, E_c, as a function of indentation rate.

Following the last indent, the Z-stage was held at 175μm for 3x the observed time

constant (~10 min) to determine E_{c0} directly (based on the equilibrium force and

indentation depth) [78]. The fluid load fraction at each indentation rate was calculated

using the equilibrium contact modulus and effective contact modulus: $F' = \dfrac{E_c - E_{c0}}{E_c}$

[198]. The fluid load fraction is plotted for representative high and low-functioning

samples as a function of indentation rate in Figure 7.3.

These data were fit to Eq. 7.1 to determine k and E_t of the sample. The

asymptotic limits ($Pe = \infty$) for the samples shown Figure 7.3 were 97% and 80%,

giving E^* values of 32 and 4, respectively. These values are used with the measured

equilibrium contact modulus of the sample to determine E_t. Permeability, the only

remaining unknown, is fit independently using the shape of the rate dependence. For

illustration, the filled data in Figure 7.3 represent a tensile modulus of 10.9 MPa and a

permeability of 0.0031 mm^4/Ns. The unfilled data represent a sample with a much

lower tensile modulus (0.9 MPa) but comparable permeability (0.0030 mm^4/Ns).

7.2.4 Tribological Characterization

The cartilage was restored (rehydrated) by sliding the probe under load (~100

mN) against the surface for 2 minutes at 5 mm/s over the ± 0.75 mm test track. By

tracking the cartilage surface following fluid exudation, we have found that this

conditioning step reduces the time to recovery by a factor of 20 or more. The sample

was taken out of contact for 5 additional minutes before initiating reciprocation (5

mm/s over ± 0.75 mm) and displacing the Z-stage 175 μm; the resulting tissue

deformation depended on the effective modulus of the specimen, but was generally ~5% the thickness. This migrating contact configuration (MCA) [84] promoted a physiologically consistent lubrication environment with $Pe \gg 1$, $Pe = V \cdot a / (E_{c0} \cdot k)$ [22,28,84,110,198]. The lowest Péclet number for any sample during functional characterization was 100 and, according to Eq. 7.1, the fluid load fraction was within 1% of the asymptotic value.

The effective friction coefficient, μ_{eff}, was calculated with $\mu_{eff} = \dfrac{F_{Xf} - F_{Xr}}{2 \cdot F_{Zavg}}$,

where F_{Xf} is the tangential force in the forward direction, F_{Xr} is the tangential force in the reverse direction, and F_{Zavg} is the average normal force [199]. Deformation measurements were used with the measured force and probe radius to determine the effective contact modulus based on Hertz's equation: $E_c = \dfrac{3}{4} \cdot F_n \cdot R^{-0.5} \cdot \delta^{-1.5}$. The fluid load fraction was determined for each sample as described in the previous section. Only depth and force data from the central 200 µm portion of the track (at the indentation location) were used to determine statistics on a cycle-by-cycle basis; this strategy eliminates transient effects near reversals, maintains spatial specificity, and eliminates curvature effects. Data were collected for 50 cycles after reaching steady state conditions. It is important to realize that this is a dynamic equilibrium that maximizes IFP and minimizes solid phase stresses. The tribological values for each sample were taken as the averages of two tests; the average deviation between repeat measurements was $< 2\%$.
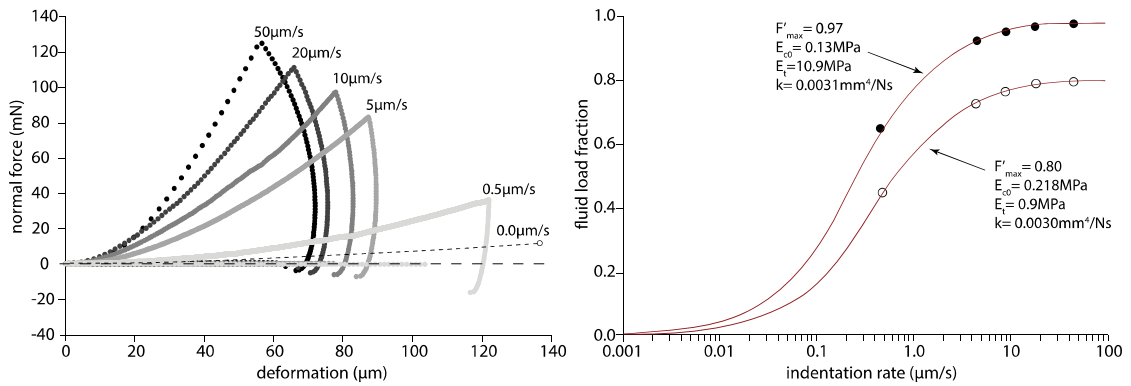
Figure 7.3   Representative data to illustrate the characterization of material properties. (Left) Force versus displacement curves for nominal speeds of 50, 0.5, 5, 20, and 10µm/s, in that randomized order for a representative high functioning sample. Following the last indent the stage is held fixed until equilibrium is reached. The equilibrium contact modulus is obtained directly from that point and the dotted line represents the predicted Hertzian relationship between force and deformation. (Right) The fluid load fraction is calculated for representative high and low functioning samples as a function of the prescribed indentation rate. The dark labels correspond to the force-displacement data on the left. The fits to the biphasic model from Moore and Burris [28] are shown in red and were used to determine tissue permeability and tensile modulus. Figure is adapted with permission [6].

7.2.5   Statistical Analysis

The effective friction coefficient, effective modulus, and fluid load fraction, were correlated to each tested material property (E_{c0}, E_t, and k) and the combinations appearing in Eq. 7.1 (E_t/E_{c0} and $E_{c0} \cdot k$) to explore the relationships between material and functional properties. The model type chosen for the fit reflects obvious visual trends observed after the dependent variable was plotted against the independent variable; a linear fit was used if no trend was obvious.

One-way ANOVAs, significance set at $p < 0.05$, were run to test whether freezing, refrigeration and location significantly affected material and tribological properties. When a significant difference was detected a Tukey-Kramer post-hoc test

was conducted to determine significantly different pairs. Since multiple measures were taken in each region per joint, e.g. 3 measures were made in the tibial region C, the sample population was redefined from N=200 to N=10 to avoid false positives [200].

7.3 Results

The mean tribological and material properties for the effects of storage are presented in Table 7.1. Neither freezing (-80°C, < 2 months) nor refrigerated storage time (2°C, 0 to 5 days) had a statistically significant effect on the tribological or material properties of the cartilage.

The results of 200 samples from N=10 bovine stifle joints are provided in Table 7.2.   Overall, cartilage from the bovine stifle had an equilibrium contact modulus of $E_{c0} = 0.62 \pm 0.10$ MPa, a tensile modulus of $E_t = 4.3 \pm 0.7$ MPa, and a permeability of $k = 2.8 \pm 0.9$ x 10^{-3} mm^4/Ns. Under physiologically consistent tribological conditions ($Pe >> 1$) the effective friction coefficient (PBS lubrication) was $\mu_{\text{eff}} = 0.024 \pm 0.004$, the effective contact modulus was $E_c = 3.9 \pm 0.7$ MPa and the fluid load fraction was $F' = 0.81 \pm 0.03$.

Table 7.1   Sample means ± standard deviations for different storage conditions. p-values for each comparison are listed. Storage conditions did not present any significant differences, p > 0.05. Table is adapted with permission [6].

sample size (N=)	tribological properties			material properties		
	effective friction coefficient	effective contact modulus (MPa)	fluid load fraction	equilibrium contact modulus (MPa)	permeability (10^{-3}·mm^4/Ns)	tensile modulus (MPa)
fresh (100)	0.025±0.014	4.0±2.6	0.81±0.09	0.62±0.37	2.5±1.8	4.1±2.2
frozen (100)	0.022±0.010	3.8±2.4	0.81±0.09	0.63±0.40	3.1±4.0	4.5±2.4
P value	0.7383	0.4481	0.4761	0.9662	0.1415	0.5332
day 0 (25)	0.021±0.009	4.1±2.8	0.84±0.06	0.62±0.40	2.9±3.2	4.4±2.4
day 1 (66)	0.023±0.009	4.1±2.7	0.81±0.10	0.65±0.40	3.1±4.5	4.4±2.6
day 2 (63)	0.026±0.017	3.7±2.2	0.80±0.10	0.63±0.37	2.9±2.0	4.1±2.1
day 3 (26)	0.024±0.012	3.9±2.5	0.81±0.08	0.65±0.37	2.2±1.4	4.4±2.4

day 4 (10)	0.022±0.006	3.5±3.7	0.82±0.11	0.45±0.41	2.4±1.4	4.1±3.1
day 5 (10)	0.020±0.003	3.4±2.2	0.84±0.06	0.51±0.29	2.4±1.8	4.0±1.7
P value	0.0586	0.2810	0.6733	0.1175	0.7940	0.3394

Table 7.2   Regional means ± standard deviations for N=10 joints. p-values for each comparison are listed. Significantly different pairs are indicated by dissimilar letters. A significant difference is defined as $p < 0.05$. Table is adapted with permission [6].

spatial region (N=10)	tribological properties			material properties		
	effective friction coefficient	*effective contact modulus* (MPa)	*fluid load fraction*	*equilibrium contact modulus* (MPa)	*permeability* (10^{-3}·mm^4/Ns)	*tensile modulus* (MPa)
all samples	0.024±0.004	3.9±0.7	0.81±0.03	0.62±0.10	2.8±0.9	4.3±0.7
medial	0.025±0.006	3.6±1.2	0.80±0.04	0.60±0.19	3.4±1.7	3.8±1.3
lateral	0.022±0.004	4.2±0.6	0.82±0.03	0.65±0.11	2.3±0.2	4.7±0.9
P value	0.3581	0.1688	0.1507	0.5145	0.0586	0.1051
femoral	0.021±0.004	4.9±1.0 **A**	0.83±0.03	0.77±0.14 **A**	1.9±0.6 **A**	5.2±0.9 **A**
tibial	0.026±0.005	2.9±0.9 **B**	0.79±0.03	0.48±0.14 **B**	3.8±1.3 **B**	3.4±1.0 **B**
P value	0.1789	0.0142	0.5189	0.0052	0.0064	0.0427
femoral C	0.020±0.005 **A**	5.9±1.1 **A**	0.85±0.03 **A**	0.88±0.21 **A**	1.5±0.4 **A**	6.0±1.0 **A**
femoral O	0.021±0.003 **A**	3.6±0.9 **B**	0.85±0.03 **A**	0.55±0.19 **B**	2.6±1.2 **A**	4.2±1.0 **B**
femoral I	0.022±0.004 **A**	3.1±1.6 **B,C**	0.77±0.05 **B**	0.66±0.26 **A,B**	2.2±1.4 **A**	3.6±1.7 **B**
tibial S	0.024±0.008 **A,B**	3.5±0.9 **B**	0.85±0.02 **A**	0.50±0.10 **B**	2.7±0.6 **A**	4.2±0.8 **B**
tibial U	0.030±0.007 **B**	2.1±0.6 **C**	0.70±0.06 **C**	0.46±0.14 **B**	5.3±2.5 **B**	2.1±0.8 **C**
P value	0.0039	0.0001	0.0001	0.0001	0.0001	0.0001

7.3.1   Correlation Between Functional and Material Properties

The correlations and their associated functions presented in Figure 7.4 provide further insight into how material properties influence the functional response of cartilage. Each functional property correlated best to a tensile property (either tensile modulus or modulus ratio); the correlations are shown in the top row of Figure 7.4. The friction coefficient was the most difficult functional property to predict based on material properties ($R^2 = 0.354$); generally, friction decreased with increased tensile modulus. The effective contact modulus, when fit to a linear function of the tensile modulus, produced $R^2 = 0.810$. The fluid load fraction, when fit to a logistical function

of the modulus ratio (chosen because of its sigmoidal behavior and asymptotic limit $F'_{max} = 1$) produced $R^2 = 0.831$.

The best correlations to a property or combination of properties not including tensile modulus are shown in the bottom row of Figure 7.4. The effective contact modulus was best fit to a non-tensile property with a power law fit to permeability producing $R^2 = 0.54$; otherwise, permeability and aggregate modulus were relatively poor predictors of tribological function. However, the trends suggest that increased tensile modulus and decreased permeability are generally beneficial for promoting tribological function, which is in-line with published literature [159,176].
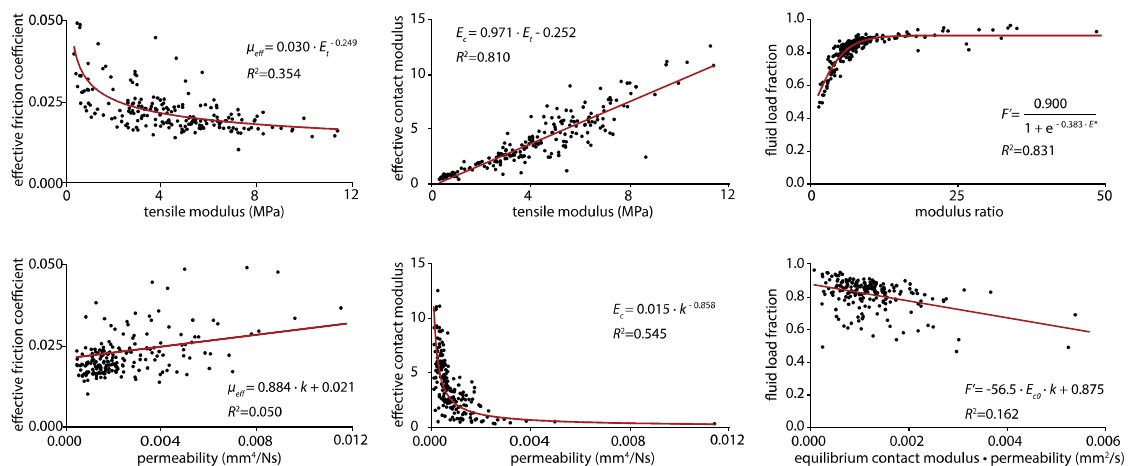
Figure 7.4   Correlations between the functional performance and material properties for bovine articular cartilage. The functional properties of interest are the effective friction coefficient (Left), effective contact modulus (Center) and fluid load fraction (Right). The Top row contains the best overall correlation for each functional metric. The Bottom row contains the best overall correlation for each functional metric against E_{c0}, k, and $E_{c0} \cdot k$. Figure is adapted with permission [6].

7.3.2 Medial vs Lateral

The comparison of tribological and material properties between the medial and lateral regions is shown in Table 7.2. The cartilage in the lateral compartment uniformly produced more favorable average tribological and material properties, although not significantly.

7.3.3 Femoral vs Tibial

The cartilage samples of the femoral condyles consistently and significantly outperformed those of the tibial plateau (Fig. B5). With $\mu_{eff} = 0.021 \pm 0.004$, $E_c = 4.9 \pm 1.0$ MPa, and $F'_{max} = 0.83 \pm 0.03$ the femoral condyles exhibited superior functional properties although only the effective contact modulus was statistically significant. In addition to the tribological differences, the equilibrium modulus and tensile modulus of femoral cartilage were 60% and 50% greater than those of the tibial cartilage (Table 7.2). The permeability of femoral cartilage (1.9 ± 0.6 x 10^{-3} mm^4/Ns) was half that of the tibial cartilage. It is also worth noting that the femoral cartilage exhibit far lower variability in permeability with the standard deviation being roughly half that of tibial cartilage.
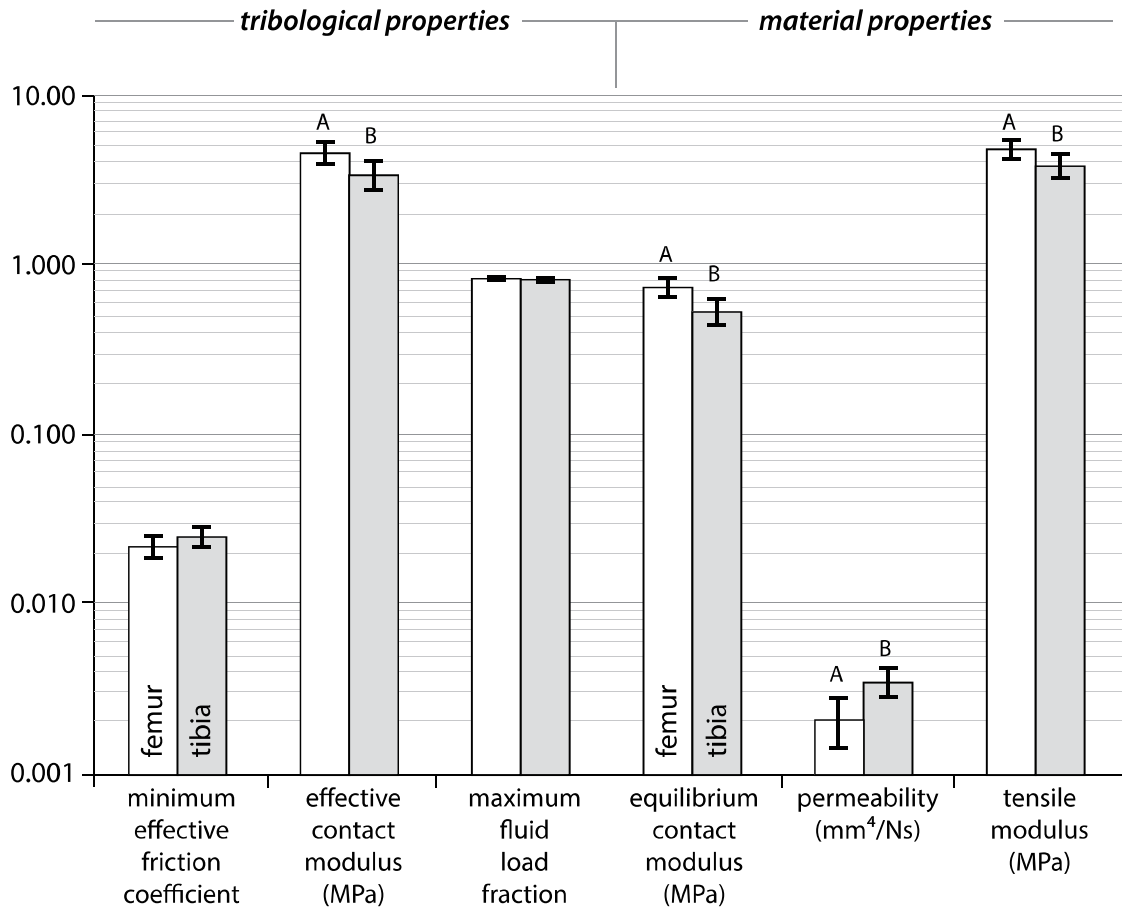
Figure 7.5   Comparisons of the tribological and material properties for the femoral condyles and tibial plateaus of the bovine stifle joint. Error bars represent 95% confidence intervals. Significant differences are indicated by dissimilar letters, $p < 0.05$. Figure is adapted with permission [6].

7.3.4   Variations Due to Differences in Local Contact

Figure 7.6 demonstrates clear evidence that functional metrics are related to material properties. In general, tribological functionality (reduced friction, increased modulus, increased fluid load support) increases with increasing equilibrium contact modulus, decreasing permeability, and increasing tensile modulus.

The differences in mean values between the groups were statistically significant in many cases. The central femoral and uncovered tibial regions were the best and worst performers, respectively, and were statistically different with $p < 0.005$ for each metric. The effective friction coefficient of uncovered tibial cartilage was 50% higher than that of central femoral cartilage (0.030 vs 0.020). In addition, the mean effective contact modulus and fluid load fraction of the central femoral region were 180% and 20% greater than those of the uncovered tibial region, respectively. The difference in material properties between these two regions were of comparable magnitude; the equilibrium and tensile moduli of the central femoral cartilage were 90% and 185% greater, respectively, than those of the uncovered tibial region. The permeability of the uncovered tibial cartilage was 350% larger than that of the central femoral region; the standard deviation in permeability was 600% larger in the uncovered region.

The outer femoral cartilage and the shielded tibial cartilage, the only regions in the study that are continually mated against the meniscus, were statistically indistinguishable in every metric. Interestingly, the product $E_{c0} \cdot k$, which governs time constants and flow rates [201], was statistically insignificant between regions except for the uncovered tibial region, which had a $p < 0.005$.
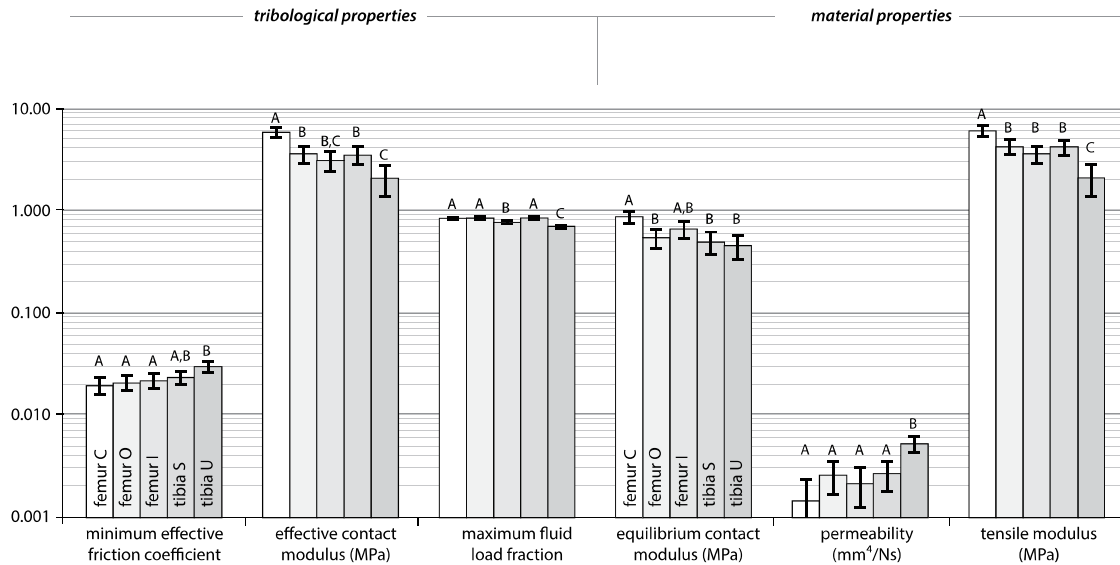
Figure 7.6 Comparisons of the tribological and material properties for the femoral central (C), outer (O), inner (I), and tibial shielded (S) and uncovered (U) regions of the bovine stifle joint. Error bars represent 95% confidence intervals. Significant differences are indicated by dissimilar letters, p < 0.05. Figure is adapted with permission [6].

7.4   Discussion

7.4.1   Mean Properties of the Bovine Stifle Joint

A new high spatial-resolution method was used here to characterize the well-studied material properties and less well-studied tribological properties of bovine articular cartilage to determine whether properties vary spatially. The primary limitation of the study is that it uses an untested Hertzian contact model to characterize biphasic properties. While validation is outside the scope of this paper, comparison against existing results helps establish credibility. A second limitation is the reporting of the equilibrium contact modulus, $E_{c0} = \dfrac{E_{-y}}{1-v^2}$, assuming a Poisson ratio $v = 0$.

Although earlier studies using linear biphasic theory report values upward of $v = 0.3$

[120,153], more recent and direct measurements suggest that $v \sim 0.04$ [176,187,188] in the directions relevant to this loading configuration; this value is close enough to zero $(0.04^2 = 0.0016)$ to neglect differences between E_{c0}, aggregate modulus H_a, and equilibrium Young's modulus E_{-y}.

The values of $E_{c0} = 0.62 \pm 0.10$ MPa reported here are consistent with published results for hyaline cartilage, which typically range from $H_a = 0.55$ to 0.90 MPa from a variety of joints and species [116,120,154,159,184,187,188,202]. The permeability measurements reported here were 2.8 ± 0.9 x 10^{-3} mm^4/Ns for the whole population. These values fall in the middle of the reported values of permeability which range between 0.4 and 7.6 x 10^{-3} mm^4/Ns [116,120,154,159,161,176,184,202]. The permeability can vary by an order magnitude due to variations in effective strain [154] and reported differences are at least partially attributable to experimental differences. The tensile moduli from this study (4.3 ± 0.7 MPa) are similarly aligned with those from the literature, which range from 3.5 to 14 MPa [146,148,159,176]. The mean values reported here are on the low end, which likely reflects the fact that the measurements occur toward the nonlinear 'toe' of the stress-strain curve.

This study also revealed statistics for the tribological response of bovine cartilage. The friction coefficient is not a material property but an interface property that involves the nature of both contacting surfaces and the lubricant [91]. The steel-on cartilage configuration used here was decidedly non-physiological, but necessary to eliminate a second cartilage sample as a variable. As Caligaris and Ateshian showed, the friction coefficient of a rigid sphere on cartilage is quantitatively similar to that of self-mated cartilage [84]. The use of PBS as the lubricant detracted further from physiological relevance but was important to eliminate synovial fluid variability from

the measurements. Our own unpublished measurements and those from Caligaris and Ateshian have failed to detect statistical differences [84] when using PBS in place of synovial fluid, most likely because the bound species responsible for boundary lubrication remain strongly adhered under the mild conditions of relatively brief MCA testing (~250 passes per sample).

Caligaris and Ateshian report similar friction statistics for the tibial plateau using MCA glass on cartilage with PBS lubricant ($\mu_{eff} = 0.024 \pm 0.010$ versus 0.026 ± 0.005); this suggests general agreement between measurement approaches, consistency among different populations of bovine subjects, and a lack of effect from the probe material (glass and stainless are expected to be effectively inert in this environment). The fluid load fraction values reported here are consistent with our prior measurements of fluid load support [28,78] and published ratios of the effective and equilibrium friction coefficients [84,95,115]. The effective contact modulus was $E_c = 3.9 \pm 0.7$ MPa for the whole joint and is a measure of the tissue's capacity for load support (force per area) in Hertzian contact. To our knowledge, we are the first to report the effective contact modulus of cartilage during MCA sliding.

7.4.2   The Distribution of Cartilage Properties

This study revealed significant differences across the bovine stifle. While there were no statistically significant differences between the material and functional properties of medial and lateral compartments it is worth noting that for every property measured the lateral aspect of the joint was superior to the medial compartment, which carries most of the joint load [203]. The more obvious differences were observed between the femoral condyle and the tibial plateau. In a purely tribological sense, the femoral condyles outperformed the tibial plateau in every metric. The favorable

tribological properties are accompanied by increased equilibrium modulus (60%), increased tensile modulus (50%) and decreased permeability (50%).

These differences in tribological and material properties have interesting implications for OA. Firstly, the medial compartment tends to be more prone to OA, which is consistent with the added load and less favorable properties. Secondly, Bendele and coworkers consistently find fibrillation of the tibial cartilage almost immediately following medial meniscus transection surgery with no evidence of damage on the mating femoral cartilage despite the fact that the tissues experience the same interface conditions [190]. This observation and the trends from this study suggest that femoral cartilage is better equipped than tibial cartilage for tribological contact.

Although we have demonstrated differences in the cartilage properties in the joint, it is unclear how significant those differences are in the context of joint disease. Prior studies provide the framework necessary to interpret this significance. Kempson, for example, has shown that the superficial zone of human articular cartilage reaches a peak tensile strength near age 25 and decreases by 75% at age 90 [204]. Such changes in tensile modulus have been mainly associated with changes in the superficial zone, the zone that dominates the tribological response [205]. Akizuki et al. reported that fibrillation decreases the mean tensile modulus of human articular cartilage 5.6 MPa to 4.5 MPa; with osteoarthritic tissue, the tensile modulus decreases to 1.8 MPa [146]. Interestingly, they found that cartilage from low-weight bearing regions had higher tensile moduli than cartilage from high weight bearing regions, which is consistent with differences observed here between the lateral and medial compartments as well as between shielded and uncovered regions of the tibial plateau.

Elliott et al. found that osteoarthritis caused by meniscectomy in a canine model caused a 40% decrease in tensile modulus [148]. Similarly, Setton et al. found that anterior cruciate ligament rupture in a canine model caused a 60% decrease in tensile modulus, a 20% decrease in the equilibrium compression modulus, and a 50% increase in permeability [178]. In this study, we found that the uncovered region of the tibial plateau was 65% less stiff in tension and 250% more permeable than the central femoral condyle. These variations, being consistent with those induced by OA, supports the hypothesis that altered loads can initiate OA by causing contact in underprepared regions.

The results were inconsistent with our expectation that the shielded region would exhibit poorer tribological and material properties due a lack of exposure to sliding in a healthy joint. Instead, the uncovered regions, which appear to be subjected to continuous tribological contact in the healthy joint, exhibited far worse performance by every metric. Perhaps more alarmingly, this region had significantly increased variability and was therefore much more likely to exhibit very poor properties. These results combined with Bendele's observation that OA initiates in the thinner, stiffer, covered region following meniscectomy [190] suggests that damage is favored in the region with more favorable material and tribological properties. In this case, we believe initiation is driven by stresses not properties. The rapid transition to thinner and stiffer cartilage at this location would significantly increase contact stresses at this location relative to the uncovered region.

Bovine results have limited implications for human OA. However, these differences in regional properties are almost certainly driven by the same fundamental biological processes that govern tissue development in other animal joints. This

suggests that the results are generally applicable and can be extended to the human knee. Although the results support the hypothesis that overloading of underprepared regions causes damage, it remains unclear whether differences in strength, tribological response to sliding contact, or cellular sensitivity to tribological stresses dominate a region's tolerance to damage. It is clear, however, that 1) different regions do have different damage tolerance, 2) OA causes significant changes in material properties, 3) regions of the healthy tibial plateau have properties comparable to those of osteoarthritic cartilage, 4) those regions also suffer deficits in tribological performance that cause increased shear stresses, which can initiate OA by mechanical failure, biochemical degradation, or a combination of the two.

Chapter 8

COEXISTENCE OF HYDRODYNAMIC FORCES

8.1 Introduction

The earliest and possibly the most commonly held belief about joint lubrication is that fluid films form during joint articulation [21,58,206]. MacConaill first proposed this mechanism of joint lubrication based on the observation that articulating joints formed convergent wedges consistent with hydrodynamic bearings [51]. This hypothesized mechanism of joint lubrication is further supported by the low friction coefficients of whole joints (0.001-0.02) [23,50,80,207–209]. Extensive modeling by Dowson and co-workers further supports the development of hydrodynamic fluid films [21,210,211]. However, to date the only experimental findings that support the development of hydrodynamic fluid films are the presence of convergence zones and low friction joint articulation.

For reasons discussed previously (interface permeability [60,71,102,212,213], non-conformal geometry [51,72], and high surface roughness [214]), there are reasons to doubt that hydrodynamic fluid films form in cartilage contacts. The main culprit of this disagreement comes from the permeable nature of the tissue [60,71,102,212,213]. In model contacts, bearing surfaces are impermeable; thus, forcing fluid to flow through (fluid film) and/or around the interface. In cartilage, it is unknown whether the interface or tissue is more permeable. Therefore, the first step in understanding the potential for cartilage to develop hydrodynamic fluid films is to eliminate the tissue's permeable interface. By shutting down the permeable interface fluid can no longer (if

ever) flow into the tissue; this forces the fluid to flow through or around the contact interface.

Based on the current literature, there remains no experimental demonstration that cartilage is capable of developing hydrodynamic fluid films. The objective of this study is to demonstrate the formation of hydrodynamic fluid films in impermeable cartilage contacts. The results will help to establish whether external (hydrodynamic) fluid pressures are significant and if they should be considered in the context of joint lubrication.

8.2 Methods

8.2.1 Sample Extraction

A single mature bovine stifle joint (18-24 months) was obtained from a local abattoir (Herman's Quality Meats, Newark, DE) on the day of butchering. Following joint dissection, two osteochondral cores (19 mm diameter with ~1.5 mm of cartilage and ~15 mm of bone) were removed from the femoral condyles using a coring bit [6,26–28,215]. Specimens were immediately rinsed and stored in phosphate buffered saline (PBS) (21-040-CM, Mediatech) for 1+ hours before being clamped via the subchondral bone for tribological testing on the in-situ materials tester.

8.2.2 Creating an Impermeable Interface

The fields of hydrodynamic and elasto-hydrodynamic lubrication are rich with techniques for measuring [216–219] and modeling [21,57,220,221] fluid film development. Unfortunately, no theory to date is capable of describing how hydrodynamically pressurized fluid would respond as it flows over the permeable surface of articular cartilage. Most researchers who have worked on topics related to

this (fluid flow over a permeable boundary) have demonstrated theoretically [74,211,222–224] and experimentally [224] that fluid will flow into the boundary.

Rather than trying to decouple the two possibilities of fluid flow (i.e. through the interface and/or into the cartilage), the permeable interface was eliminated. In other words, fluid was forced fluid to flow through (fluid film) and/or around the interface. To do this a thin (10 µm thick) polymer membrane was stretched over the cartilage surface and anchored to the bone. As demonstrated by Figure 8.1 this did not influence the biphasic mechanics of the tissue and due to the thinness of the layer the effect on modulus and curvature was minimized. Unfortunately, the use of the polymer membrane certainly altered the surface chemistry and likely the interface roughness. While the surface chemistry is thought to have little influence on the development of fluid films, the surface roughness will most certainly play a major role [21,62,225].
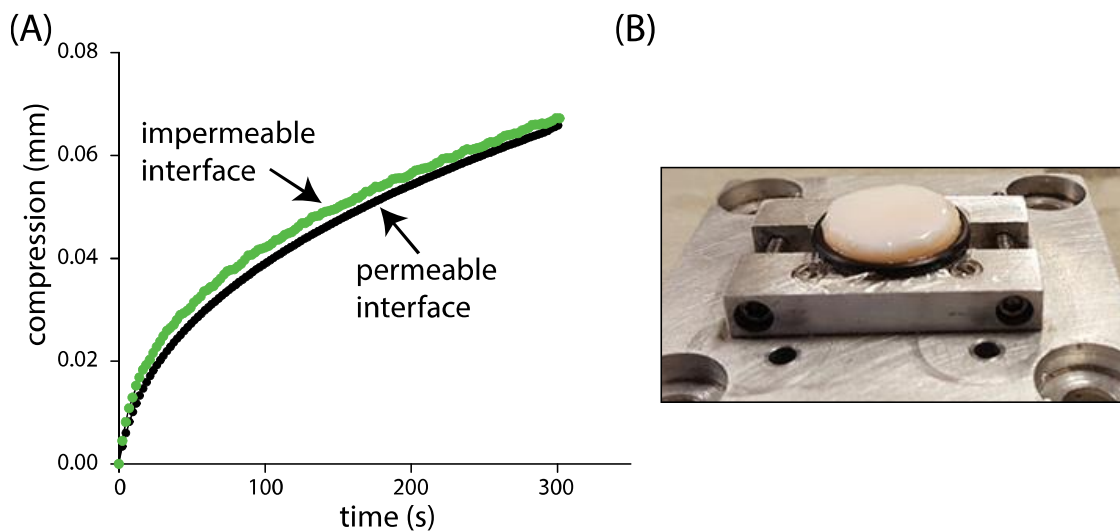
Figure 8.1   (A) The compression response of articular cartilage against glass with a permeable interface (native – black data points) and impermeable interface (polymer film – green data points). Data were collected on the in-situ materials tester section *8.2.4 In-Situ Materials Tester*. (B) Polymer film stretched over a cartilage sample. Figure is modified with permission [215].

8.2.3   Lubricating Fluid

Based on hydrodynamic theory, the pressure developed at the convergent wedge and within the contact is strongly dependent on the fluid viscosity [57,225]. Understanding the role of fluid viscosity in cartilage lubrication will provide insight as to whether or not hydrodynamics plays a role. While natural joints are 'lubricated' by synovial fluid, and the use of synovial fluid would add physiological relevance to this study, its complex composition and mechanics limit fundamental studies of hydrodynamics. For example, hyaluronic acid, a major constituent of synovial fluid, has been shown to undergo more than a 3 order of magnitude change in viscosity with shear rate [226,227]. Glycerol (G9012, Sigma Aldrich), an almost perfectly Newtonian fluid (constant viscosity with shear rate), was chosen to demonstrate the potential for fluid film development and thus the role of hydrodynamics. Pure glycerol has a viscosity ~1000X that of pure water, PBS, and synovial fluid at physiological shear rates [32–34]. Unfortunately, glycerol is highly hydroscopic and effectively dehydrates cartilage; therefore, its use was limited to studies where the interface was made impermeable.

8.2.4   In-Situ Materials Tester

The in-situ materials tester is shown in Figure 8.2 and has been explained in more detail elsewhere [215]. Briefly, the device is composed of two stages (loading

and translation). The loading stage raises and lowers the cartilage sample to make contact with a glass microscope slide (25 X 75 X 1.0 mm, Fisher Scientific). The loading assembly is equipped with a 12 N capacity 6 axis load cell (Nano 17, ATI), which has a resolution of 0.005 N. The displacement of the cartilage with respect to the glass slide (cartilage deformation) is monitored by a vertical linear variable differential transducer (GT2500, RDP electrosense), which has a resolution of 100 nm. The translation stage uses a linear actuator (MDrive 14, Schneider Electric) to reciprocate the glass slide along a set of linear bearings (up to 80 mm/s). Stage position is monitored by a horizontal linear variable differential transducer (2000HK, RDP electrosense).
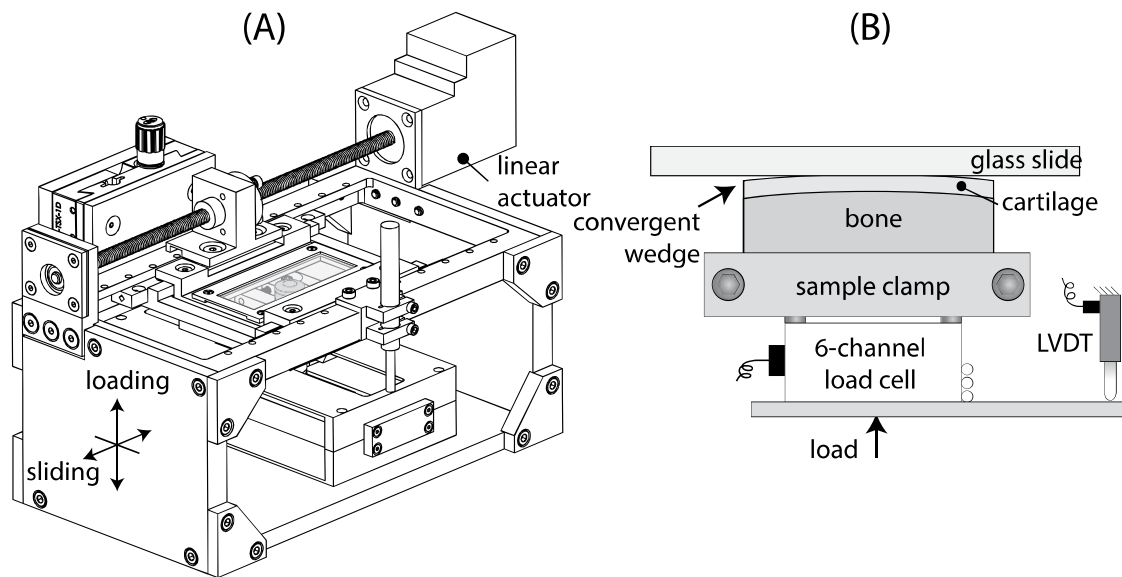
Figure 8.2   The in-situ materials tester. (A) Solid model drawing of the in-situ materials tester. (B) Schematic of the in-situ materials tester. Figure is modified with permission [215].

8.2.5 Experiments

Two different experiments were performed to demonstrate the presence of hydrodynamic forces. In the first experiment, the sample was brought into contact (5N load) under linear reciprocated sliding at 60 mm/s. After 600 s of continuous sliding, reciprocation was halted. This same start-stop procedure was repeated once more at 725 and 900 s respectively, see Figure 8.3. In this first experiment three different conditions were studied: (1) impermeable interface lubricated by PBS, (2) impermeable interface lubricated by glycerol, and (3) native (permeable) interface lubricated by PBS. All three tests were performed on the same sample and the polymer film was replaced during lubricant exchanges.

The second experiment used a stop-start speed sweep to quantify lubricant film thickness as a function of sliding speed. The sample was again loaded to 5N and was made to be either impermeable + lubricated by glycerol or permeable + lubricated by PBS. The speed sweep was conducted in a monotonically increasing order (5 to 80 mm/s) with intermittent stopping. The rationale behind stopping is discussed in section *8.3.2 Method for Quantifying Fluid Film Thickness in Cartilage Contacts*.

8.3   Results

8.3.1   Demonstrating Hydrodynamics in Cartilage Contacts
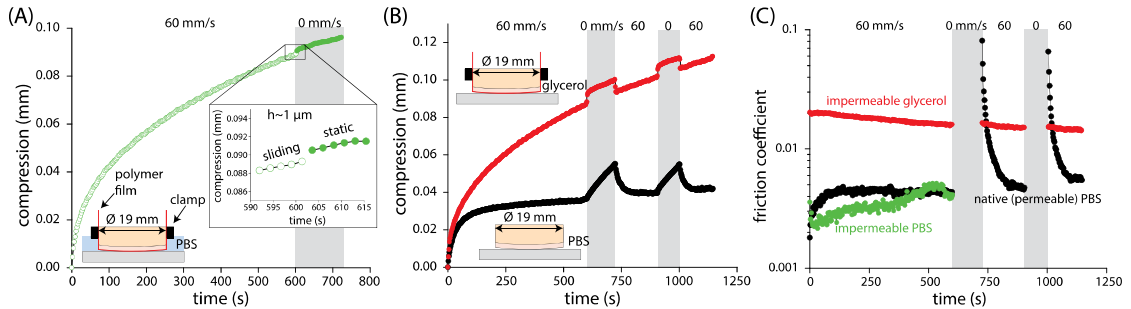
Figure 8.3   (A) A sliding impermeable articular cartilage sample, lubricated by PBS, was abruptly stopped demonstrating the collapse of a ~1 µm thick fluid film. (B) Film collapse and formation dynamics on an impermeable cartilage sample lubricated by glycerol (red). Film thicknesses were on the order of 10 µm. When the polymer film was removed and PBS lubrication was restored (black) the compression dynamics demonstrated a distinctly different phenomenon. (C) Friction coefficients for the fluid film dynamics study described in A and B. Note that all experiments were performed on the same sample of cartilage. Figure is modified with permission [215]. Data were collected on the in-situ materials tester section *8.2.4 In-Situ Materials Tester*.

A start-stop experiment was conducted, Figure 8.3, to demonstrate the formation and collapse dynamics of fluid films on impermeable cartilage surfaces, and to provide insight into the hydrodynamic forces present in cartilage contacts. The collapse of a fluid film presents an apparent increase in compression (cartilage thinning), whereas the formation of a fluid film presents an apparent decrease in compression. Figure 8.3A (impermeable interface lubricated by PBS) demonstrates the collapse of a ~1 µm thick fluid film, while Figure 8.3B shows the collapse of a ~10 µm thick fluid film. The 10 µm thick fluid film was formed under glycerol lubrication,

107

~1000X the viscosity of PBS [228]. Interestingly, when the polymer film was removed and PBS lubrication was restored (Figure 8.3B) the compression dynamics demonstrated a distinctly different phenomenon; the reasons for this will be investigated in more detail in Chapter 9. It is worth noting that due to high shear forces and small film thicknesses produced during startup with an impermeable interface lubricated by PBS the polymer film was unable to withstand multiple start-stop cycles.

To further shed light on the proposed hydrodynamics in cartilage contacts, the friction coefficients for the same sample and conditions mentioned above are shown in Figure 8.3C. As demonstrated by Figure 8.3C, an impermeable interface lubricated by glycerol or PBS produces low and steady friction coefficients, 0.02 and 0.003 respectively. Furthermore, these contacts experience almost no friction transient during start-up. However, when the native cartilage interface (permeable) is restored and lubricated by PBS the frictional response is quite different. The initial steady state friction response (0 to 600 s) is nearly identical to that of the impermeable interface with a friction coefficient of ~0.004. However, resuming motion after a period of static loading (fluid exudation) leads to an unremarkable friction coefficient of ~0.07, and for the next 90 s the friction coefficient monotonically decreases back down to its initial value. The high friction coefficients and long transients demonstrated by the native cartilage interface are uncharacteristic of fluid film lubrication.
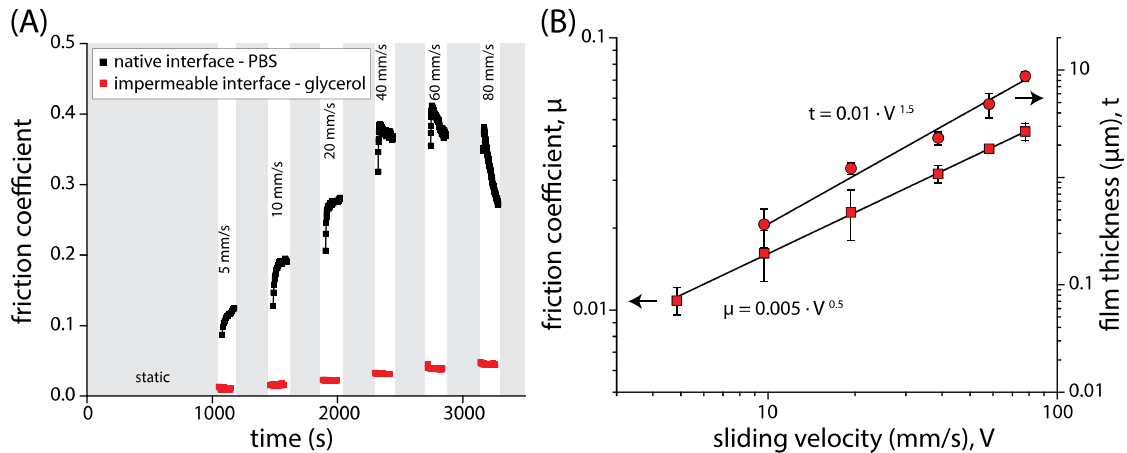
Figure 8.4 (A) Friction coefficients for a permeable PBS lubricated (black) and impermeable glycerol lubricated (red) cartilage interface are plotted for different sliding speeds. (B) The average friction coefficient (square) and film thickness (circle) for the impermeable interface lubricated by glycerol is plotted as a function of sliding velocity. A power law was fit to the friction and film thickness data. Note that the samples used for the permeable and impermeable interface were paired. Data were collected on the in-situ materials tester section *8.2.4 In-Situ Materials Tester.*

A stop-start speed sweep (5 to 80 mm/s) was conducted on a single sample, shown in Figure 8.4, to further support the idea that elasto-hydrodynamic fluid films are generated at the impermeable cartilage interface and that they produce reasonable friction coefficients and film thicknesses. The friction magnitudes and dynamics demonstrated in Figure 8.4A are dramatically different for the permeable and impermeable interface. The permeable interface produces a generally increasing friction coefficient with speed until 80 mm/s. However, it is worth noting that at speeds as low as 40 mm/s there appears to be a reversal in the friction trend (decreased friction with time). There is almost no friction transient with an impermeable interface lubricated by glycerol, and friction steadily increases with speed, albeit not to the levels experienced by the native interface.

The measured film thickness for the same experiment under glycerol lubrication (impermeable interface) is shown in Figure 8.4B. At the slowest speed, the fluid film was below the resolution of the linear variable differential transformer (~100 nm). However, as speed increased the fluid film grew, eventually reaching a maximum value of ~9 μm at 80 mm/s. As demonstrated by the figure, film growth occurred in a highly predictable fashion with speed to the 3/2 power.

To demonstrate that the observed results are consistent with hydrodynamic fluid films on 'model' materials the experiment was reproduced on a spherical silicone sample, 35 mm radius. The experimentally determined contact modulus (Eq 4.2) was 5.2 ± 0.2 MPa. Due to the higher contact modulus of the silicone sample, which leads to lower hydrodynamic lift, the load was reduced to 1 N. The film thickness results are displayed in Figure 8.5 for silicone lubricated by glycerol. The figure demonstrates that film thickness is a strong function of velocity and increases with speed to the 0.65 power. The results are qualitatively similar to Figure 8.4B and further supports the notion that significant hydrodynamic forces were developed in cartilage contacts.
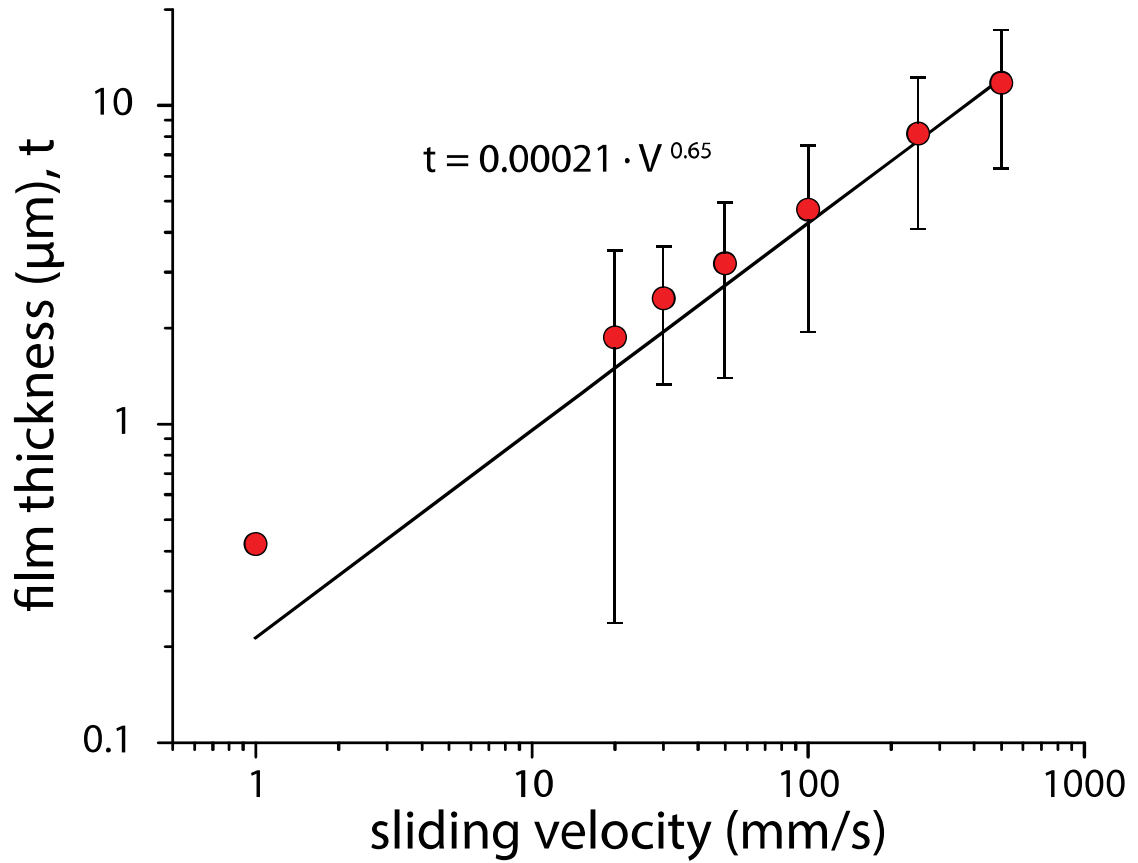
Figure 8.5   Film thickness as a function of sliding velocity for a silicone sample molded to 35 mm radius and 5.2 MPa. The sample was slid at 1 N under glycerol lubrication. The test was repeated on four separate occasions with the same silicone sample. Data were collected on the pin on disc materials tester section *10.2.3 Pin on Disc Materials Tester.*

8.3.2   Method for Quantifying Fluid Film Thickness in Cartilage Contacts
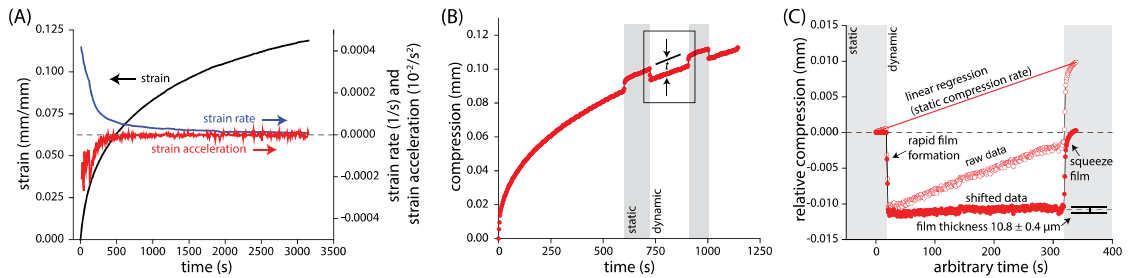
Figure 8.6   Method and rationale for determining the fluid film thickness on a time dependent material. (A) Cartilage strain versus time for a typical cartilage sample loaded to 5 N. Taking the first derivative of strain with respect to time gives strain rate. Taking the second derivative of strain with respect to time gives strain acceleration. (B) Measured tissue compression for a representative glycerol lubricated start-stop experiment. (C) Relative tissue compression is plotted as a function of arbitrary time. The data comes from the boxed region in (B). A linear regression is fit to the static data before and after sliding. The difference between tissue compression and the interpolated compression from the linear regression gives fluid film thickness, ~10.8 μm. Data were collected on the in-situ materials tester section *8.2.4 In-Situ Materials Tester.*

Quantifying the film thickness on a permeable, time-dependent material, such as cartilage, is not straight forward and therefore warrants a brief discussion of the method and rationale. Two problems exist when attempting to study fluid films on cartilage: (1) the permeable interface and (2) the nonlinear time dependent compression response. In the preceding section, it was demonstrated that the application of a thin polymer film can be used to eliminate the permeable interface. Figure 8.6A depicts a typical strain versus time curve for a statically loaded cartilage sample and highlights the nonlinear fluid exudation (compression) response. One option for solving this dilemma is to wait until the sample has fully equilibrated and

then initiate sliding. However, this equilibration creates an experimental complication in which the polymer film loses its pre-stress due to excessive tissue consolidation; this then leads to film wrinkling and eventually tearing, which interfere with fluid film development. The second option, and the one chosen for this study was to define a threshold for which the change in exudation rate is negligible over the time frame of interest. In other words, the goal was to determine when the compression or strain acceleration is ~ 0 s^{-2}. The first and second derivatives of strain with respect to time are shown in Figure 8.6A. The specific strain acceleration threshold, used to identify a region of constant strain rate, will depend on the necessary resolution in film thickness. With a roughly constant strain rate, a linear regression can be used to fit the data just before film development and just after film collapse. This fit allows the user to predict what the static compression response would have been, had the sample never undergone sliding (Figure 8.6C). Taking the difference between the raw compression data and the interpolated static deformation gives the fluid film thickness. Figure 8.6C also highlights some important film dynamics. First, the fluid film is very stable showing a variation of only ~ 0.4 μm in a 10.8 μm film. Second, the fluid film formed within the first few sliding cycles demonstrating the rapid dynamics fluid film bearings are known for. Third, the collapse of the fluid film resulted in the characteristic squeeze film effect [60,63,71,103,105,212,225,229,230].

The magnitude of the second derivative of strain (strain acceleration) provides an estimate for the uncertainty or error associated with using a linear regression on nonlinear data. At 50, 500, and 1000 s, the strain acceleration ($\ddot{\varepsilon}$) was 10^{-6}, 10^{-7}, and 10^{-8} strain/s^2, respectively. To provide a conservative estimate for film thickness uncertainty, a 1.3 mm thick (t) cartilage sample and 300 s analysis window (w) are

modeled below. The uncertainty in film thickness (U_cf) assuming a linear regression is given as:

$$U_cf = 1/2 \cdot \ddot{\varepsilon} \cdot t \cdot w^2$$

Eq. 8.1

Short equilibration times (50 s) resulted in large deformation uncertainties (~60 μm) due to the highly nonlinear deformation response. Moderate equilibration times (500 s) resulted in moderate deformation uncertainties (~6 μm). At 1000 s of pre-equilibration the deformation uncertainty was on the order of 0.6 μm. Long equilibration times (1000 s) were necessary to resolve the sub-micron film thicknesses displayed in Figure 8.4. However, large film thicknesses, Figure 8.6, only required moderate equilibration times.

8.4   Discussion

8.4.1   Film Thickness Measures

The goal of this study was to determine if hydrodynamic forces are present in cartilage contacts and if fluid films are capable of developing. As demonstrated by Figures 8.3, 8.4, and 8.6 fluid films are capable of forming on cartilage if the cartilage interface is impermeable. To provide a theoretical comparison of film thickness, the elasto-hydrodynamic solution (minimum film thickness) of Hamrock and Dowson is [57]:

$$h_{\min} = 2.8 \cdot U^{0.65} \cdot W^{-0.21} \cdot R'$$

Eq. 8.2

Where U, W, and R' are the dimensionless speed, load, and effective radius, respectively. Dimensionless speed is:

$$U = u \cdot \eta \cdot E'^{-1} \, R'^{-1}$$

Eq. 8.3

Dimensionless load is:

$$W = F \cdot E'^{-1} \cdot R'^{-2}$$
<div align="right">Eq. 8.4</div>

Where u is the entrainment speed or sliding velocity, η is the fluid viscosity, E' is the effective contact modulus, R' is the effective radius, and F is the applied load. The effective contact modulus is taken as the modulus of the cartilage assuming a near zero Poisson's ratio [28,86,97,187] and that the counter body (glass) has a near infinite modulus (50,000 MPa) compared to cartilage (0.5 MPa) [6,26,86,89]. The effective radius of curvature is taken as the cartilage's radius of curvature, assuming the counter body (glass) has a near infinite curvature (i.e. flat).

In this study, the sliding velocity (5 to 80 mm/s), fluid viscosity (PBS ~1 mPa s, glycerol ~1000 mPa s [228]), and load (5 N) were controlled. Therefore, the only remaining variables were contact modulus and radius of curvature. The modulus of cartilage was measured using Hertzian creep-relaxation method described in Chapter 6. The curvature was measured along the principle sliding axis using stylus profilometry [215]. An example profilometry scan and material properties can be found in sections *Appendix A.3 Profilometry Scan* and *Appendix B.1 Material Properties and Profilometry*. For demonstration purposes E' = 1.29 MPa and R' = 20.5 mm were assumed. Applying the solution of Hamrock and Dowson [231], the predicted minimum film thicknesses under PBS and glycerol lubrication (80 mm/s) are ~0.45 and ~40 μm, respectively. Using the modified soft-elasto-hydrodynamic solution of Myant et al. [216], film thicknesses are expected to be ~0.24 and ~26 μm under PBS and glycerol lubrication at 80 mm/s, respectively.

Obvious disagreements exist between the theoretical and measured film thicknesses. Experimental measures at slow speeds were about 20-30X smaller than

theory predicted under glycerol lubrication. However, the measures converged to within a factor of 3-5 at higher sliding speeds. One source that may be responsible for this disagreement is the dynamic modulus of cartilage. In making an estimate for the film thickness, a single static value was used (1.29 MPa). However, the speed sweep took several 1000 s to complete, and thus a substantial change in modulus is likely to have occurred. From Table 7.2, it can be expected that on average cartilage will undergo a 6.5X reduction in contact modulus. The implication of this is that as the experiment progresses the conditions become more favorable for hydrodynamics and thus may not follow the 2/3 power relation suggested by theory and experimentally demonstrated by Figure 8.5 for silicone lubricated by glycerol.

Another very likely source for disagreement comes from the modeling assumptions of an elastic-isoviscous contact; meaning that the contacting bodies can be assumed to respond in a linearly elastic manner and that the fluid remains Newtonian. While glycerol has been shown to apply very well to the isoviscous (Newtonian) assumption [216,228], cartilage and the polymer membrane are certainly not linearly elastic materials. In addition, most experimental studies used to validate these theoretical models were performed on materials much harder than cartilage (10's of MPa). Myant et al., de Vicente et al., and Hooke were some of the first to study truly soft contacts with moduli approaching 10 MPa [216,232,233]. Their experimental results demonstrated that soft-elasto-hydrodynamic contacts have a much smaller film thickness than theory predicts [216], and that the relationship between film thickness and speed may follow a different power law relation depending on the location of minimum film thickness [233]. The reduced film thickness in soft-elasto-hydrodynamic contacts (contact modulus of silicone ~5.2

116

MPa) is further supported by the experimental results in Figure 8.5, which are on average 6X smaller than that predicted by elasto-hydrodynamic theory.

Other likely sources of disagreement come from the inelastic response (flow-dependent viscoelasticity) of cartilage, the variable curvature, micro-motion of the polymer, lack of fully flooded contact, and the unknown properties of the polymer. Regardless of the potential confounding factors, the take away message is that cartilage contacts are capable of producing significant hydrodynamic forces during sliding, and that the lift generated in these impermeable contacts increases with sliding velocity.

8.4.2   Friction Measures

From the measured film thickness, the shear stress in the film can be computed. Shear stress, τ, is related to film thickness, h, by:

$$\tau = \eta \cdot u \cdot h^{-1}$$
Eq. 8.5

Where η is the viscosity and u is the sliding velocity. Taking the viscosity of glycerol (1000 mPa·s), a sliding speed of 80 mm/s, and an average film thickness of 9 μm, the predicted fluid shear stress is ~0.01 MPa. With an estimated normal stress, σ, of 0.25 MPa the friction coefficient can be computed by Eq. 8.6.

$$\mu = \tau / \sigma$$
Eq. 8.6

The computed fluid shear (friction) coefficient is ~0.04, which is in excellent agreement with Figure 8.4B, further supporting the fact that a full fluid film was formed at 80 mm/s.

The results of Aim 1 demonstrate 5 things about hydrodynamics in AC contacts. First, by removing the permeable interface via a thin polymer membrane

fluid films were formed under PBS and glycerol lubrication. Second, the fluid shear stress generated at 80 mm/s under glycerol lubrication matches the frictional shear stress, suggesting that friction was solely caused by fluid shear. Third, the friction and film dynamics on impermeable interfaces demonstrate that transient conditions are very rapid and agree with theory. Fourth, the impermeable experiments under PBS lubrication suggest that should a fluid film form at a permeable cartilage interface, it should be no thicker than 1 μm. Finally, when cartilage retains its permeable interface (under the same external conditions) it has almost no resemblance to the impermeable contact. The focus of Chapter 9 is to determine how the tribological response changes when hydrodynamic pressures act at a permeable interface.

Chapter 9

TRIBOLOGICAL REHYDRATION: HYDRODYNAMIC PRESSURES AT THE PERMEABLE CARTILAGE INTERFACE

9.1   Introduction

For more than 75 years, scientists, engineers, and clinicians have sought to better understand the mechanisms responsible for the unusual frictional properties of animal joints [1,4,22–24,28,50,51,58,80,83,102]. MacConaill discovered that joint incongruity is a ubiquitous feature of joint anatomy and concluded that the unusually low friction coefficients must be the result of hydrodynamic fluid films [51]. Charnley made several observations that were inconsistent with this hypothesis, most notably, that low friction coefficients were retained at zero sliding speed and that exact geometric Perspex joint replicas in synovial fluid were unable to achieve low friction under even the most favorable conditions [23]. He concluded that the nature of the cartilage surface and its interaction with synovial fluid must be critical to the lubrication of joints.

Charnley made a second interesting observation; after wiping the surface free of synovial fluid the tissue expressed fluid under load [23]. This finding led McCutchen to propose that cartilage, a soft, porous, and fluid soaked material, might function as a weeping bearing [1]. As he expected, the remarkably low friction coefficients (~0.01) observed at the beginning of sliding experiments with cartilage against glass eventually increased toward more typical values (0.2-0.5). Brief contact separation to replenish any previously formed squeeze film had no effect on friction;

119

however, a 10 min soak of the sample in water fully restored lubrication. These observations indicated to him that his observations of low friction could not be attributed to fluid or boundary films. In-situ compression measurements revealed that the lubrication response was essentially proportional to the water content in the tissue, particularly in the near-surface.

Numerous independent studies have since supported this hydration-based lubrication effect and provide strong experimental evidence of distinct and sometimes conflicting interpretations of lubrication. Some of the most noteworthy examples include weeping [1], interstitial [22,24,28,83], biphasic [4], hydration [90], aqueous [234], and polymer fluctuation lubrication [235]. To avoid the need to pick from a field of qualified candidates, we will simply refer to this general lubrication phenomenon as 'wet lubrication' (WL) from here on. Regardless of the interpretation, WL is governed by the same well-established features of biphasic mechanics, namely: 1) interstitial fluid within the biphasic material is pressurized during contact; 2) interstitial pressure drives fluid from the material; 3) the loss of interstitial fluid causes increased friction, decreased interstitial pressure, and decreased flow rates over time [1,4,22,24,28,83,95].

This inevitable loss of hydration, thickness, and lubrication appears to necessitate other lubrication modes to sustain low friction over the long term [54]. Like MacConaill, Dowson and co-workers noted the incongruent shape of joint surfaces and proposed that hydrodynamic effects must play an important role in joint lubrication [58]. To test this hypothesis, they duplicated McCutchen's cartilage-on-glass flat friction experiments with three important differences: 1) the sample was larger than the contact area to retain the convergent wedge necessary for

hydrodynamic effects during sliding; 2) samples were equilibrated prior to sliding to eliminate effects from WL; 3) sliding speeds were increased over time to increase hydrodynamic fluid pressure. They observed high friction coefficients at slow speeds, which confirmed the absence of fluid film, boundary, and WL. During sliding at elevated speeds, however, they observed a transition to low friction, which they attributed to the formation of a hydrodynamic fluid film between the cartilage and glass. At present, many biomechanics textbooks appear to support the hypothesis that joints are primarily lubricated by fluid films and secondarily by wet and boundary lubrication [54,141,206].

If fluid films do form, theoretical studies indicate that at least a portion of that fluid film will flow into the porous cartilage surface [60,72,175,211,236]. The objective of this study is to determine whether or not interfacial sliding is capable of driving fluid back into articular cartilage restoring hydration, compression, and WL.

9.2 Methods

9.2.1 Sample Extraction

Seven mature bovine stifle joints (18-24 months) were obtained from a local abattoir (Herman's Quality Meats, Newark, DE) on the day of butchering. Following joint dissection, osteochondral cores (19 mm diameter with ~1.5 mm of cartilage and ~15 mm of bone) were removed from the femoral condyles using a coring bit [6,26–28,215]. Specimens were immediately rinsed and stored in phosphate buffered saline (PBS) (21-040-CM, Mediatech). A total of 26 osteochondral cores were used in this study. Due to testing time constraints several whole joints were frozen (-20°C) for future use; however, it has been demonstrated that freezing causes no detectable

changes in material or tribological properties of articular cartilage [6,237–239]. Previously frozen joints were allowed to thaw for two days in a laboratory refrigerator at 4°C before undergoing a similar sample extraction protocol.

Following extraction, specimens were given a 1+ hour soak in PBS before being clamped via the subchondral bone for tribological testing. Samples not tested immediately were submerged in PBS in a laboratory refrigerator at 4°C for no more than 4 days, a duration insufficient to cause detectable changes in material and tribological properties [1,6]. Furthermore, any specimens unable to be tested in this time frame were dehydrated under rough vacuum and stored at 4°C for future use in the study. Dehydration of cartilage has been shown to preserve both the material [26,100] and tribological properties of cartilage [100], further evidence is provided in section *Appendix A.1 Effects of Dehydration*. Rehydration was performed by submerging samples in PBS for 24 hours at 4°C.

9.2.2 Sample Geometry

It has been suggested previously that maintaining a convergence zone between cartilage and the counter body leads to the development of hydrodynamic fluid films [58,102]. A convergence zone or wedge is created when two bodies of different curvature come into contact (ball on plate). Based on hydrodynamic theory, the ability to develop a fluid film is greatly dependent upon the radius of curvature and length of the convergence zone [225]. It is difficult to classify and control the radius of curvature for cartilage as its natural geometry is extremely complex [25,240,241] (Figures 9.1 and 9.2), both macro and microscopically. Therefore, to maintain the natural curvature of cartilage, yet test the effect of path length, a single sample was milled from 19 to 12.7 and 6.35 mm diameter using a computer numerically controlled

(CNC) mill (Figure 9.1B and 9.1C). The CNC mill was programed using G-code programing language; an example script is shown in section *Appendix A.2 G-Code*.
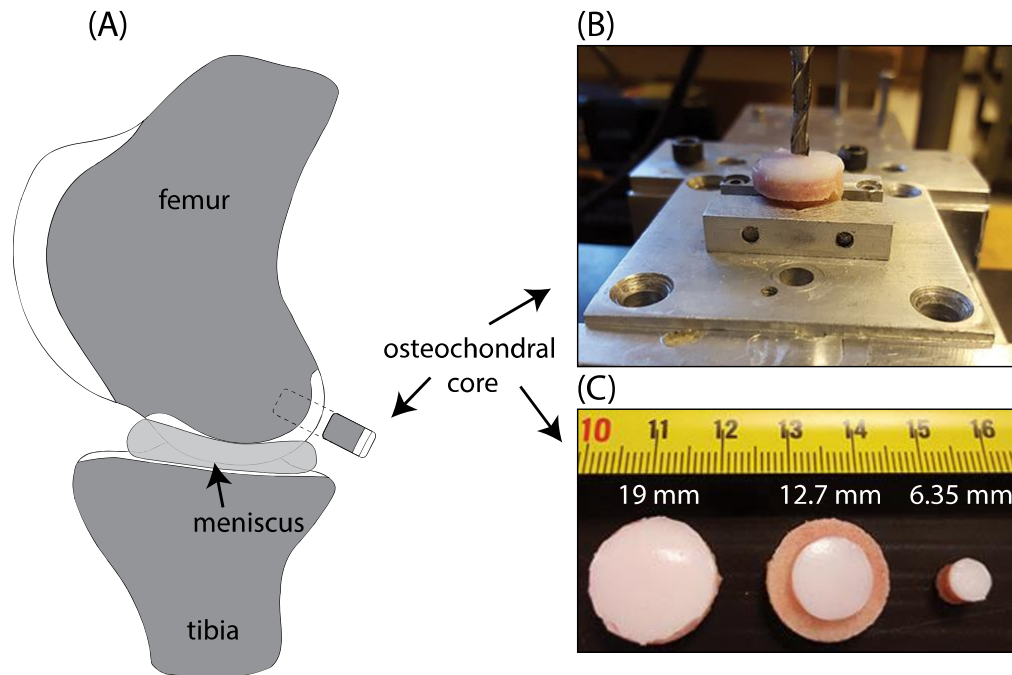
Figure 9.1   (A) Schematic of the bovine stifle joint in a sagittal plane view. Samples are extracted as osteochondral cores (cartilage attached to bone), 19 mm diameter. Image is adapted with permission [6]. (B and C) Specimens are clamped in a CNC mill and reduced to diameters of 12.7 or 6.35 mm. Note that the cartilage is the white-ish top layer and the subchondral bone is the pink-ish material.

To verify the presence of a convergent wedge a particle exclusion assay was conducted [215,242], Figure 9.2. Samples were placed in the in-situ materials tester (section *8.2.4 In-Situ Materials Tester*) and submerged in India ink. India ink is a colloidal suspension of carbon particles (~250 nm diameter [243]) that is commonly used to make fiducial marks in soft tissues [96,115]. Immediately following the

application of India ink the sample was brought into contact with the transparent glass counter body and imaged using a Nikon D3200 camera mounted on a stereomicroscope. Contact between the opaque semi-translucent cartilage and the glass slide displaces the ink, reveling regions of direct contact. A similar technique has been used to identify the contact area between soft hydrated gels and rigid counter bodies [242]. Based on the work of Dunn et al. the suspension of a 250 nm particle (larger than the mesh size of cartilage) will yield an error or measurement uncertainty of < 0.1% [242]. This error is caused by the inability of small particles to fully penetrate the convergent wedge.

The contact area was measured by summing the number of bright pixels and multiplying by their unit area. If the contact area (A) or mean contact diameter (D), $D = \sqrt{4A/\pi}$, was less than the sample's ($A = 284$ mm^2; $D = 19$ mm) then a convergence zone existed. Preliminary experiments demonstrated that a 5 N load produced a contact diameter of ~5 mm and thus all cases (19, 12.7, and 6.35 mm) initially produced a convergence zone. Furthermore, the initial contact stress $\sigma = F/A$, where F is the applied normal force, is approximately equivalent for all three conditions. Figure 9.2B demonstrates contact area as a function of load for two different samples. The power law curve fits were used to model the data after Hertz's theory for contact between curved elastic bodies. Based on Hertz's theory contact area should scale with force to the 2/3 power; however, the best fits suggest a power of ~1/2. This deviation from Hertz's theory is to be expected as cartilage (a nonlinearly elastic, multiphasic, anisotropic, heterogenous, layer bonded to a rigid substrate) violates nearly all of the theory's assumptions. The significance of this reduced power (1/2 vs 2/3) is reflective of the substrate stiffening effect caused by the 'rigid'

subchondral bone [155]. The substrate stiffening effect was specifically addressed in Chapters 5 and 6 for a sphere indenting an elastic layer bonded to a ridged substrate.

For the purposes of this study samples were only taken from the femoral condyles as they have an almost exclusive convex curvature (see section *Appendix A.3 Profilometry Scan*) while the tibial plateau and patellar groove have both convex and concave profiles [25,240,241,244]. The drawback of a concave profile is that it opposes the development of hydrodynamic pressures when interfaced with a rigid flat [57]. It is important to note that the contact area was never perfectly circular and often times resembled an ellipse (Figure 9.2A), a feature that reflects the complex curvature in natural joints. Furthermore, a single area of contact didn't necessarily develop (occasionally 2 non-continuous contact areas were found); this again reflects the complexity of natural joints.
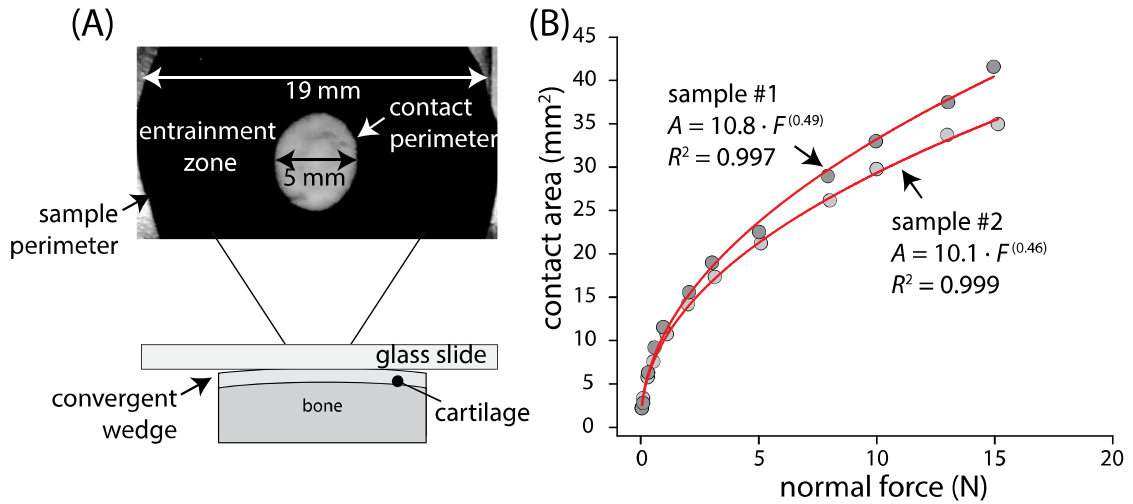
Figure 9.2 (A) A representative image demonstrating that the contact area (white region) can viewed through a glass microscope slide. The convex curvature of the femoral cartilage produces a contact area smaller than the sample area demonstrating the presence of a convergent wedge or entrainment zone. (B) Loads even as high as 15 N do not seal off the contact (~7 mm diameter). Note that India ink was used as a contrast agent and is routinely used in tissue mechanics studies [96,115]. Figure is adapted with permission [215,245]. Data were collected on the in-situ materials tester section *8.2.4 In-Situ Materials Tester.*

9.2.3 Material Properties

Spherical creep-relaxation (see Chapter 6) was performed to quantify the material properties of select samples. Table B.1 in section *Appendix B.1 Material Properties and Profilometry* lists the material properties and curvature of each sample.

9.2.4 Tribological Evaluation

The lubrication of articular cartilage is complex and involves at least two unique mechanisms (WL and boundary lubrication). In an attempt to study the proposed hydrodynamic forces without the confounding effects of WL [58,77,84,102], a non-migrating contact was used (i.e. cartilage sliding on a rigid flat, SCA).

Furthermore, PBS was used as the lubricating solution as it contains no known boundary lubricants. For fear of damaging the superficial layer, no direct attempts were made to remove existing boundary lubricants from the cartilage surface. However, the 1+ hour equilibration in PBS [77], long testing durations, and accumulated sliding distance were thought to remove most boundary molecules.

9.2.5 Experimental Variations

Two different experimental configurations were used to probe the tribological response of a permeable cartilage interface to hydrodynamic forces. First, the sample was cut with a CNC mill from 19 to 6 mm in diameter in an effort to reduce the size of the entrainment zone and therefore, the hydrodynamic effect. Second, sliding speed was reduced to 10 mm/s and 0 mm/s to vary hydrodynamic effects without changing sample geometry.

9.3 Results

9.3.1 Maintaining Hydration and the Role of the Convergence Zone

The SCA contact is typically configured as a small osteochondral core interfaced with a flat glass or metal countersurface. This configuration is popular for three main reasons. First, the small sample size allows for rapid fluid wring out and depressurization, typically on the order of 2 hours [77,102]. Second, the depressurization of the cartilage allows for the decoupling of the hydration based lubrication effect (WL) and other forms of lubrication such as boundary or hydrodynamic. Third, the small sample size is easily flattened (Figure 9.2) which eliminates hydrodynamic effects and promotes isolated studies of boundary lubrication with constant contact area and contact stress [24,77,81,84]. However, as Walker et al.

127

point out, if the convergent wedge is maintained a fluid film will develop at the

cartilage interface. These convergent SCA contacts are sub-classified here as cSCA's.
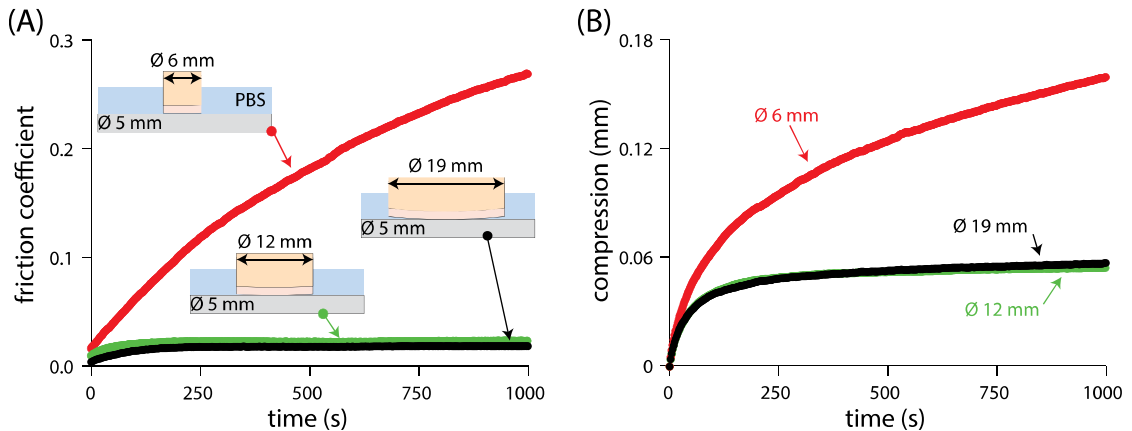
Figure 9.3   (A) Friction coefficient and (B) compression of a single representative
cartilage sample cut to varying size (19, 12.7, 6.35 mm diameter). A
convex shape and larger sample size leaves a convergence zone for fluid
entrainment and hydrodynamic pressurization, cSCA. When the sample
size approached the contact area, friction and compression increased with
time as expected for the SCA [1,24,84,95]. The testing configuration
used here was 60 mm/s sliding speed, 20 mm track length, and 5 N of
normal load on the in-situ materials tester, see section *8.2.4 In-Situ
Materials Tester*. PBS lubrication was maintained throughout the
experiment. Figure is adapted with permission [215].

Experiments conducted to isolate the effect of the convergent wedge are shown

in Figure 9.3. The friction coefficient (μ) and compression are plotted versus time for

a representative sample as a function of explant diameter. In all cases the friction

coefficient starts below 0.02, which is the expected result [22,24,81,84,116,215]. At

6.35 mm diameter, the contact area was approximately equal to the sample area

(Figure 9.2), which effectively eliminated the convergent wedge. Friction increased

over time as predicted by biphasic theory and as demonstrated previously for the SCA

configuration [22,24,81,84,116,215]. At 12.7 and 19 mm diameters, the sample was large enough to provide an entrainment zone (convergent wedge) for hydrodynamic pressurization and, in both cSCA cases, the friction coefficient increased only slightly toward $\mu = 0.02$ at steady state.

Initially the compression rate also appears independent of sample size, which is consistent with biphasic theory (Figure 9.3B). The 6.35 mm size displayed the familiar runaway compression response characteristic of the SCA [1,95]; in this case, the loss of fluid leads to reduced IFP, increased solid load carrying and increased friction over time as previously observed [22,24,81,84,116,215]. At larger sizes, the same sample stabilized at a compression of about 0.06 mm. The results suggest that hydrodynamic effects arrested the anticipated fluid exudation process, which is ultimately responsible for increased compression and friction over time.

9.3.2 Maintaining Hydration and the Role of Interfacial Sliding

To understand when the effects of sliding induced rehydration become competitive with load driven fluid exudation a start-stop test was conducted. A 19 mm diameter osteochondral core was slid at 60 mm/s for 600 s in the cSCA configuration; after which sliding was abruptly halted. The compression response is shown as a function of time in Figure 9.4. In this case, exudation ceased at a compression asymptote of 0.04 mm during sliding, but resumed as expected once sliding stopped. Following a 1 hour period of free swelling in PBS, the sample was compressed statically at the same load to obtain the static equilibration response. Comparison against the original test results produced two noteworthy observations. Firstly, the initial compressive response during sliding was identical to the initial response under static loading, which suggests that the competing effects of hydrodynamic

pressurization were negligible initially. Only after 0.015 mm of compression did the curves begin diverging, which suggests that significant deformations are required to produce competitive hydrodynamic pressurization (the coupling of deformation and hydrodynamic pressurization is the defining feature of elasto-hydrodynamics [57]). Secondly, the static exudation response following sliding overlays nearly perfectly onto the control equilibration response, indicating the exudation response is strain dependent and history independent. Finally, and most importantly, the results demonstrate that the compression attenuation (Figure 9.3) was not a result of sample size. Figure 9.4 demonstrates that the static compression rate is much faster and proceeds to a much greater equilibrium value than when sliding at 60 mm/s. This finding, however, does not establish whether sliding halted fluid exudation or balanced it with fluid imbibition.
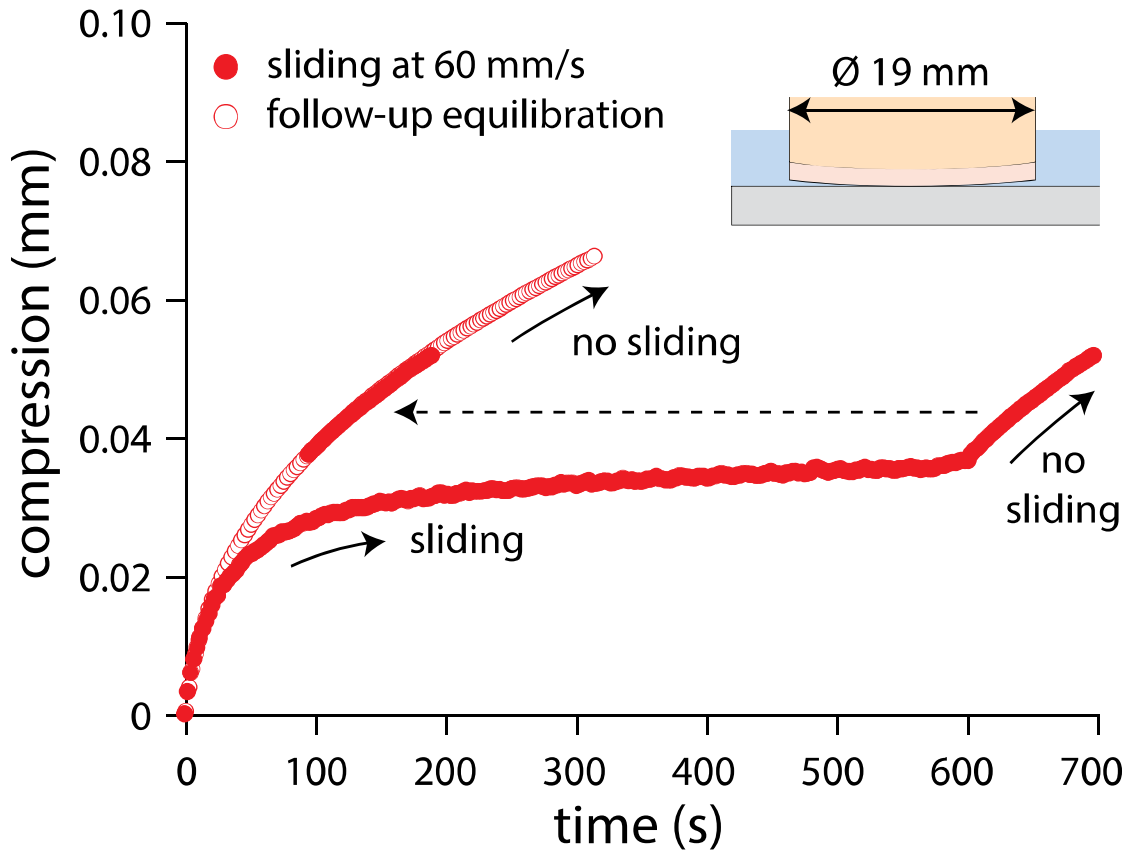
Figure 9.4   Compression of a representative cartilage sample (19 mm diameter) versus time in a start-stop cSCA test configuration. The sample was loaded to 5 N and slid at 60 mm/s. Reciprocation was stopped at 600 s to provide a period of static equilibration. The sample was then unloaded and soaked for 1 hour to restore interstitial fluid and equilibrated again under static loading at 5 N. The experiment was conducted on the in-situ materials tester under PBS lubrication, see section *8.2.4 In-Situ Materials Tester*. Figure is adapted with permission [215].

9.3.3   Recovering Hydration

While the previous sections have established the potential for sliding to arrest or compete with load driven fluid exudation it is unknown as to whether or not sliding can recover tissue hydration and lubricity. Figure 9.5 illustrates the recovery of interstitial fluid following static loading and gross exudation. In this case, a 19 mm

diameter sample was compressed by 0.09 mm over 600 s of static loading. On the first sliding cycle at 60 mm/s the friction coefficient was $\mu = 0.16$, which clearly suggests an absence of a hydrodynamic fluid film. Thereafter the friction coefficient and compression decreased monotonically with continued cycling, reaching asymptotes of ~0.005 and ~0.06 mm (~5% strain), respectively. The correspondence between strain and friction strongly implicates the recovery of interstitial fluid and pressure as the mechanism underlying the friction and strain reductions [1,80,128,215]. Although hydrodynamic pressures are typically associated with fluid film (or mixed) lubrication, it appears that hydrodynamic pressurization acted primarily to restore interstitial hydration by combating the persistent exudation process with competitive inflow.

Reducing the sliding speed from 60 mm/s to 10 mm/s caused increased compression and friction over time. As the overlay in Figure 9.5 illustrates, the compression rate at 10 mm/s was less than that under static conditions. This suggests that the driving force for recovery was substantially reduced but not eliminated at the slow speeds typical of SCA measurements [1,24,77,81,84,102,128]. If we calculate the rehydration rate as the difference between the static compression rate and the sliding compression rate, we find that at 60 mm/s and 10 mm/s the rehydration rates are $4.3 \cdot 10^{-4}$ mm/s and $4.3 \cdot 10^{-6}$ mm/s, respectively. In general, increased speeds caused thickening and decreased friction, while decreased speeds caused compression and increased friction; this observation is consistent with the hypothesis that load-induced exudation was offset by speed-induced inflow from hydrodynamic pressurization, which is strongly speed dependent [231].
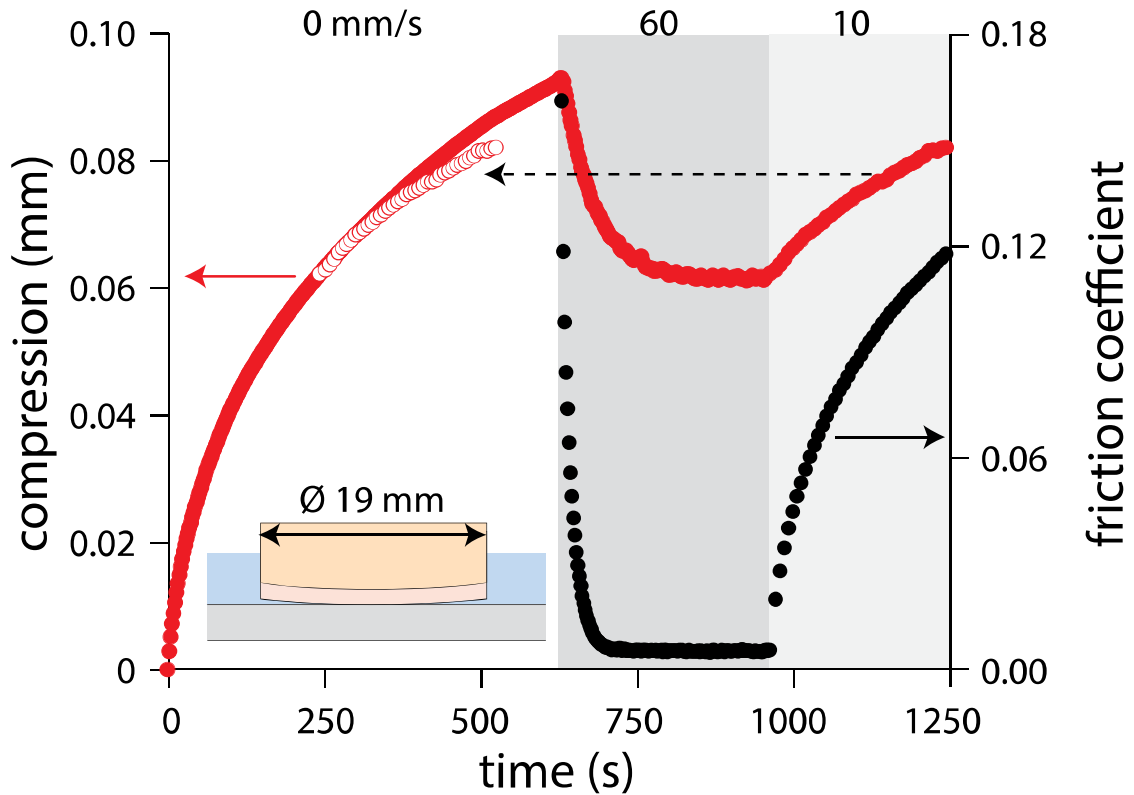
Figure 9.5.   Compression and friction versus time for a representative 19 mm
diameter sample (cSCA) in a stop-start test configuration. Following a
period of static equilibration at 5 N, the sample began sliding at 60 mm/s
until reaching a dynamic equilibrium; at which point the sliding speed
was reduced to 10 mm/s. The experiment was conducted on the in-situ
materials tester under PBS lubrication, see section *8.2.4 In-Situ Materials
Tester*. Figure is adapted with permission [215].

9.4   Discussion

The cSCAs of this study lost, maintained, and recovered compression,
lubrication, and fluid during sliding depending on the sliding conditions, contact
stress, and strain. The deformations observed cannot be explained by wear, shear-
induced compression, or variations in film thickness. Therefore, the deformations
observed in this study for natural cartilage can primarily be attributed to a competition
between the loss and recovery of interstitial fluid by the tissue. As such, this study

133

presents the first direct experimental evidence that interstitial fluid can be retained and recovered in the absence of unloading and contact migration, a result with important scientific and clinical implications to be discussed later. This recovery process has been termed 'tribological rehydration' because it was sliding-induced rather than unloading or migration-induced (MCA).

The cSCAs in this study (Figure 9.6) produced fluid load fractions, friction coefficients and compressive strains at steady state that were consistent with measurements from previous cartilage explant and whole joint studies. The estimated mean fluid load fraction from this study of ~90% is comparable with maximum values from unconfined compression measurements of bovine patellofemoral cartilage [85] (94% ± 4% at the articular surface and 71% ± 8% in the deep zone cartilage) and steady state values from MCA studies of bovine cartilage from the femoral condyle [6] (83% ± 3%). Likewise, the mean friction coefficient from this study (0.011) compares well with those from MCA measurements of Moore and Burris [6] (0.021) and Caligaris and Ateshian [84] (0.022) as well as those from whole joint measurements of Charnley [23] (0.013) and Linn [80] (0.012). The slightly larger values from the MCA measurements are likely the result of an additional plowing component from the smaller probe sizes [78]. Lastly, and perhaps most interestingly in the context of joint space, the observed compressive strains (dynamic equilibrium) of ~5% in this study are comparable to those observed by Eckstein et al. [185,244,246–249] (in-vivo, 5-12% during activity) and Linn [80] (excised joint, ~5% strain). The remarkable consistencies in these numbers across studies and contact configurations suggests that tribological rehydration may play a significant role in physiological joint hydration and lubrication.
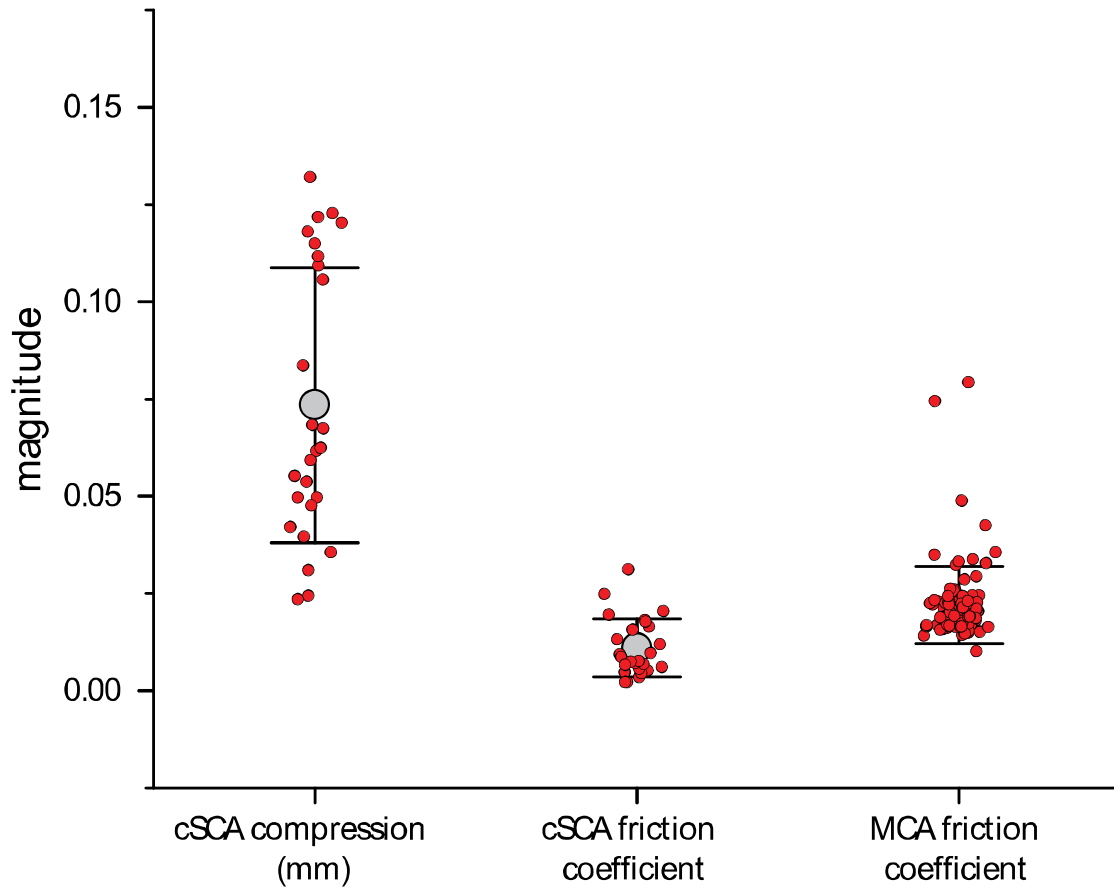
Figure 9.6 The dynamic equilibrium responses for 26 samples tested in the cSCA and MCA configurations. Data is adapted with permission [215]. Data were collected on the in-situ materials tester section *8.2.4 In-Situ Materials Tester.*

From biphasic theory, it is not obvious why interstitial pressure would be maintained or recovered in any stationary contact area including those used here. Biphasic theory predicts that interstitial pressure drives exudation and is therefore self-defeating in the absence of contact migration [99]. However, this study suggests that

the coupling of interstitial and hydrodynamic pressure fields cannot be neglected, as is almost always the case in theoretical analyses of biphasic contacts [37,83,99,158,250]. Theoretical evidence that hydrodynamic pressures develop in the convergence zones of joints suggests to many that low friction coefficients occur because hydrodynamic fluid films separate joint surfaces [21,50,51,58]. However, Gleghorn and Bonassar [251] and Ateshain [22] point out that lubricating fluid films in joints are likely compromised due to flow into the porous surfaces. The previous study, Chapter 8, showed that a thin fluid film did develop when an impermeable membrane prevented flow into the surfaces, which supports the hypothesis that hydrodynamic fluid pressurization is significant as previous literature suggests [21,50,51]. Currently, there have been no theoretical or experimental studies investigating the interaction between hydrodynamic and interstitial pressure fields. However, from biphasic theory it is known that the applied load causes interstitial pressurization within the bulk of the cartilage, which causes bulk exudation [154]; it is also known that relative motion from sliding causes fluid entrainment into a convergent wedge, which leads to rapid pressurization very near the wedge tip [57]. The simplest mental model of the fluid mechanics based on existing theory suggests a competition between hydrodynamic pressure-driven inflow and interstitial pressure-driven outflow, this will be discussed in more detail in Chapter 11.

In summary, it was demonstrated that sliding led to the recovery of hydration and lubricity in articular cartilage. This recovery phenomenon was termed tribological rehydration as it was sliding induced rather than migration or exposure induced. The findings suggest that hydrodynamic forces are the underlying mechanism of tribological rehydration. In addition, the results agree with the suggestions of previous

136

authors, in which the permeable cartilage interface impedes the development fluid films [22,212,251]. While the results don't refute the development of fluid films they do suggest that fluid films are not necessary for tribological rehydration to occur (the greatest rehydration rates occurred when friction was greatest).

Chapter 10

ROLE OF THE MECHANICAL ENVIRONMENT ON THE TRIBOLOGICAL RESPONSE OF ARTICULAR CARTILAGE: SPECIFIC EMPHASIS ON TRIBOLOGICAL REHYDRATION

10.1 Introduction

Chapter 9 demonstrated a unique phenomenon termed tribological rehydration, which is defined as the sliding-induced fluid recovery of articular cartilage. The important result of this finding is that loaded sliding contacts can maintain and recover hydration and thus don't require contact exposure [1,80], unloading [125], or migration [84,110]. While the observation was made that sliding was a necessary condition for tribological rehydration it does not inform the underlying mechanism.

From Chapter 8 it was demonstrated that significant hydrodynamic forces exist in cartilage contacts. In light of this finding and the apparent speed and size effects on tribological rehydration it seems reasonable to expect hydrodynamic forces to play a pivotal role. The objective of this section is to investigate the dynamic equilibrium response of cartilage to various changes in the mechanical environment that are known to alter hydrodynamic forces. Specifically, the roles of sliding speed, load, sample size (inlet zone), and viscosity are investigated.

10.2 Methods

10.2.1 Sample Extraction

Mature bovine stifle joints (18-24 months) were obtained from a local abattoir (Herman's Quality Meats, Newark, DE or Bowman's Butcher, Aberdeen, MD). Following joint dissection, osteochondral cores (19 mm diameter with ~1.5 mm of cartilage and ~15 mm of bone) were removed from the femoral condyles using a coring bit [6,26–28,215]. Specimens were immediately rinsed and stored in phosphate buffered saline (PBS) (21-040-CM, Mediatech). Due to testing time constraints several whole joints were frozen (-20℃) for future use; however, it has been demonstrated that freezing causes no detectable changes in material or tribological properties of cartilage [6,237–239]. Previously frozen joints were allowed to thaw for two days in a laboratory refrigerator at 4℃ before undergoing a similar sample extraction protocol.

Following extraction, specimens were given a 1+ hour soak in PBS before being clamped via the subchondral bone for tribological testing. Samples not tested immediately were submerged in PBS in a laboratory refrigerator at 4°C for no more than 4 days, a duration insufficient to cause detectable changes in material and tribological properties [1,6]. Furthermore, any specimens unable to be tested in this time frame were dehydrated under rough vacuum and stored at 4℃ for future use in the study. Dehydration of cartilage has been shown to preserve both the material [26,100] and tribological properties of cartilage [100], further evidence is provided in section *Appendix A.1 Effects of Dehydration*. Rehydration was performed by submerging samples in PBS for 24 hours at 4℃.

Two different tribological materials testers were used in this study. Both of the materials testers mentioned below (in-situ and pin on disc) offer the same general contact geometry (cartilage loaded against a sliding rigid flat); however, several key differences are noted below.

10.2.2 In-Situ Materials Tester

The in-situ materials tester was shown and described previously, see section *8.2.4 In-Situ Materials Tester*. The biggest advantages of the in-situ materials tester are bi-directional sliding (a motion that replicates many physiological joints), smooth sliding at very slow speeds (< 0.1 mm/s), and constant speed across the entire interface. The reversal nature of the device is also important for proper quantification of friction and compression. As demonstrated by previous authors [80,199,252], transducer misalignments (inherent in every system) can lead to substantial errors when measuring small friction coefficients. Burris and Sawyer demonstrate that for cartilage relevant friction coefficients (0.01) a transducer misalignment of less than 0.5° produces a 50% error in the measured friction coefficient [199]. This error is eliminated with the reversal method and is it accuracy only depends on the precision of the load cell.

The primary disadvantages or limitations of the in-situ materials tester are changes in velocity and direction that occur during reversals, no automated load or deformation control, and an upper speed limit of 80 mm/s. It is also worth noting that while the cartilage is kept hydrated during these experiments it is not a flooded contact. Hydration is maintained through a suspended fluid meniscus between the cartilage sample and the glass slide. Non-flooded contacts can have significant impacts on the formation and stability of hydrodynamic fluid films [225,253];

however, the pin on disc materials tester described in section *10.2.3 pin on disc materials tester* uses a fully flooded contact and the results seem to demonstrate that the effects are not diminished when using the non-flooded contact.

10.2.3 Pin on Disc Materials Tester

The pin on disc materials tester is shown in Figure 10.1. The device is composed of two stages (loading and rotary). The loading stage uses an 800 μm piezoelectric stage (P-628, Physik Instrumente) to raise and lower the cartilage sample toward the glass disc (∅115 mm X 3.175 mm, McMaster-Carr). The load and deformation of the tissue specimen was measured through a 12 N capacity 6 axis load cell (Nano 17, ATI) and the piezoelectric stage's onboard capacitive displacement sensor (±10 nm). Due to the limited travel range of the piezoelectric stage, coarse positioning was provided by a manually driven vertical stage (not shown). The rotary stage is driven by a stepper motor (MDrive 23, Schneider Electric) and timing belt.

The biggest advantages of the pin on disc materials tester is that it maintains a constant angular velocity (no reversals), is capable of automated load or deformation control, and can attain speeds greater than 500 mm/s, which is beyond the physiological speed of human joints. The walls on the side of the rotating disc allow for the containment of a lubricant bath (flooded contact). To help support this flooded contact condition an external head-pressure driven feed-tank was used to deliver a continuous, but slow, supply of deionized water to the bath to balance the empirically determined evaporation rate. While the feed rate was by no means perfect and the only mixing during equilibration was provided by diffusion, the compression curves remained stable and did not indicate substantial cartilage softening (hyperosmotic solution) or stiffening (hypoosmotic solution) [254,255], see section *Appendix A.4*

Long Term Equilibration. Due to the ability to maintain hydration and proper salinity for much longer time periods than the in-situ materials tester many of the experiments with the pin on disc materials tester were able to undergo long testing durations (> 24 hours).

To limit cartilage degradation during these long testing durations a broad-spectrum protease inhibitor cocktail (P2714, Sigma Aldrich) was added to the bath in a concentration recommended by the manufacture (1:100 dilution in PBS). While the efficacy of this treatment has yet to be established, it does not appear to cause any detrimental effects on the tribological performance of the articular cartilage.

The disadvantages of the pin on disc materials tester are that the substantial mass of the rotating disc makes bi-directional sliding studies difficult (slow acceleration); slow speeds (< 1 mm/s) are difficult to achieve even when using substantial gear ratios as the stepping motion of the motor creates transients in the data; and a speed gradient exists since speed varies linearly along a rotating disc (Figure 10.1B). Furthermore, a mean speed uncertainty also exists. The center of each 19 mm diameter sample is placed 21 mm from the center of rotation. At an angular velocity of 24 rad/s the mean speed is 500 mm/s. However, taking into account the complex curvature of cartilage and approximating a 5 mm contact diameter (Figure 9.2) the mean speed may be as low as 340 mm/s or as high as 670 mm/s (unknown center of contact). This means that for any given speed there is a ± 30% uncertainty in the mean speed; this is certainly a worst-case scenario and care was taken to try and position the contact in the center of the sample.

The angular rotation creates an additional complexity in which the friction force vectors are not aligned parallel to the measurement axis, except in the center of

the contact. As Sidebottom and Krick demonstrate, the error associated with this condition increases as the contact diameter (~5 mm in these studies) approaches the wear track diameter (~42 mm in these studies) [256]. Following their analysis, the contact ratio (contact diameter/track diameter) is 0.12, which results in a frictional error of ~0.1%. In other words, the true friction coefficient during pin on disc testing is 0.1% greater than that reported by the device. Since the sample to sample variation in friction coefficient and the uncertainty in contact location are much larger sources of error, the measured friction coefficient is not adjusted.

The final complication of rotating disc instruments that is rarely addressed is a feature known as run-out. Run-out is a misalignment between the disc and the rotational axis of the spindle (the surface normal vector changes). To ensure orthogonality the components are typically machined on a high precision lathe and should not be removed until the completion of manufacturing. The pin on disc materials tester was built by the author in this fashion; however, machining tolerances are rarely better than ~25 μm. In addition, the axial run-out of most lathes is on the same order; this run-out is then propagated into the spindle which reflects this misalignment. An additional source of run-out comes from the addition of a glass disc to the top of the spindle. Should any debris be trapped beneath the glass or should the glass not be perfectly flat the run-out condition will be amplified. Despite the many potential sources of error the measured run-out of the pin on disc tribometer rarely exceeds 10 μm.
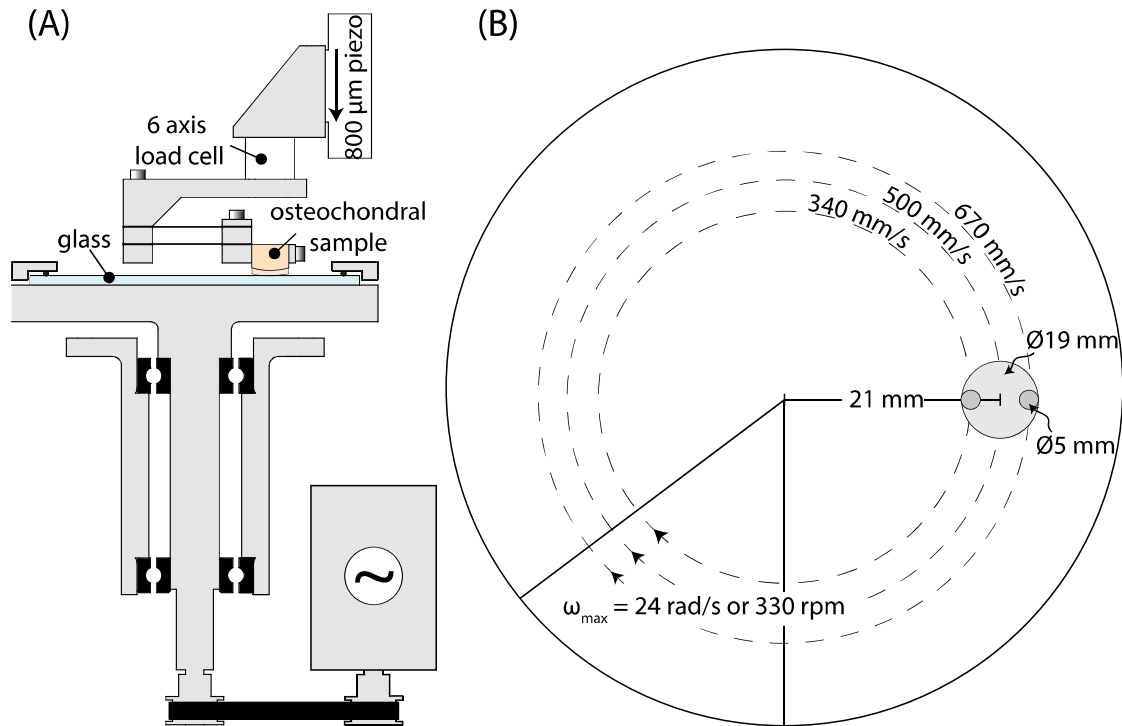
Figure 10.1 (A) The pin on disc materials tester. The primary advantage of the pin on disc is its ability to attain much greater translation speeds — 500 mm/s compared to 80 mm/s on the in-situ materials tester. (B) The primary disadvantage to the pin on disc materials tester is the linear variation in speed across the disc interface and the in ability to precisely identify the center of contact.

10.2.4 Tribological Preconditioning

Each cartilage sample underwent a series of preconditioning steps (Figure 10.2) that were specific to each materials tester. Sample preconditioning is a common step in nearly any tissue mechanics study [257,258], in tribological systems it is typically referred to as run-in [253]. Run-in is defined as an initial period of transient friction and wear. Properly running-in a bearing surface can lead to a longer service life and better performance. While much is unknown about the run-in process, factors that can contribute to it are: the removal of surface oxides [66], alignment of surfaces

144

[66,68], circulation of oil or grease [66], production of degradation products [65,68,259,260], nucleation of tribofilms [261], and grain structure alterations [262,263]. Currently, there is no gold standard method for cartilage preconditioning prior to tribological evaluation. Since the overall theme of this work revolves around fluid exudation and sliding induced recovery, the preconditioning procedures that follow are designed to drive fluid from the tissue during static loading and recover fluid both through sliding and free swelling. Run-in of cartilage samples may help to adapt the existing boundary films to the new tribological environment.

Prior to tribological evaluation on the in-situ materials tester each sample was loaded to 5 N and held static for 2 min followed by 2 min of linear reciprocated sliding at 60 mm/s with a 5 N load. The final step was a 2 min period of static (no sliding) unloading (0 N), termed free swelling. A similar preconditioning exercise was conducted on the pin on disc materials tester. First each sample was loaded to 5 N and held static for 5 min followed by 5 min of uni-directional sliding at 100 mm/s with a 5 N load and finally a 5 min unloading (0 N) period where the rotary stage was held stationary (free swelling). A schematic of the specific precondition exercises can be seen in Figure 10.2.
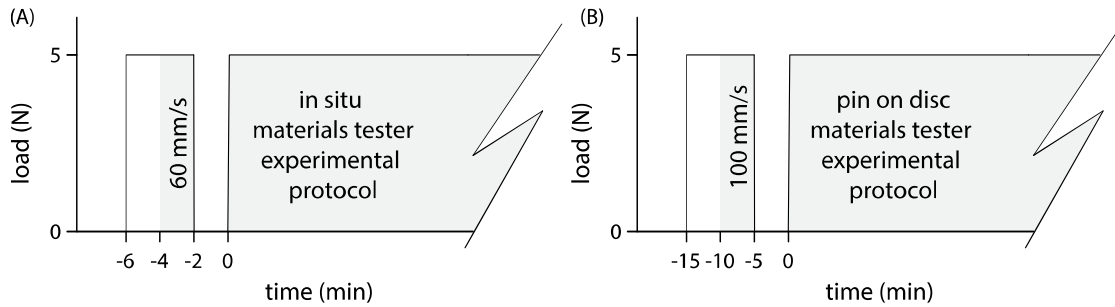
Figure 10.2 (A) Preconditioning protocol used on the in-situ materials tester. (B) Preconditioning protocol used on the pin on disc materials tester. Image is adapted with permission [264].

10.2.5 Experimental Variations

Four different experimental configurations were tested to determine the role of hydrodynamic parameters on the tribological response of cartilage.

10.2.5.1 The Role of Sliding Speed

The first was to determine the role of sliding velocity on the dynamic equilibrium friction and compression response. Samples were loaded to 5 N and run in a monotonically decreasing speed sweep from 80 mm/s to 0.5 mm/s on the in-situ materials tester. Steady state conditions were defined by changes of < 0.01 μ/min and < 0.01 mm/min for friction and compression, respectively. This was repeated for a total of 5 samples.

10.2.5.2 The Role of Load

The second study investigated the role of load on the dynamic equilibrium friction and compression response. Samples were loaded to 1 or 5 N and run in a monotonically decreasing speed sweep from 80 mm/s to 0.5 mm/s on the in-situ materials tester. Steady state conditions were defined by changes of < 0.01 μ/min and

146

< 0.01 mm/min for friction and compression, respectively. This was repeated for N=3 at 1 N and N=5 at 5 N.

10.2.5.3 The Role of Sample Size and the Entrainment Zone

The third study investigated the role of sample size on the dynamic equilibrium friction and compression response. Samples were milled from 19 to 12.7 and 6.35 mm diameter. Following milling, samples were loaded to 2.5 N on the pin on disc materials tester. Samples were run in either a monotonically decreasing or increasing speed sweep from 1 mm/s to 500 mm/s. Steady state conditions were defined by changes of < 0.005 μ/min and < 0.001 mm/min for friction and compression, respectively. Since sample size could only be reduced not all samples were run at 19 or 12.7 mm diameter; this was done to limit the potential for propagating damage between subsequent tests. A total of 7 samples were used; of those 4 were run at 19 mm, 4 at 12.7 mm, and 6 at 6.35 mm diameter.

10.2.5.4 The Role of Hyaluronic Acid

The final study compared the tribological response of hyaluronic acid (53747, Sigma Aldrich), a long unbranched protein core that is common to many health care products due to its high affinity for water and shear thinning nature [33,227,265], to PBS. Hyaluronic acid (HA) is a major component of synovial fluid having a physiological concentration of ~3 mg/mL [34,227] and a molecular weight of ~2 MDa [33,265]. Based on the current literature, the shear thinning nature of synovial fluid is primarily attributed to HA [32–34,265]. The specific HA used in this study had a reported molecular weight of 1.5 to 1.8 MDa and was prepared as 3 mg/mL in PBS. To fully dissolve the HA in PBS required twice daily mixing for 48 hours.

Samples were loaded on the pin on disc materials tester at 5 N left to equilibrate in PBS + protease inhibitor. Following equilibration, the PBS bath was either replaced with fresh PBS or 10 ml of 3 mg/mL HA in PBS. A second equilibration period (1 hr) was conducted following the bath exchange. If the compression response remained in equilibrium, a monotonically increasing speed sweep was run (1-500 mm/s). If the compression response did not remain in equilibrium the sample was allowed to remain in static compression until achieving steady state. Steady state conditions were defined by changes of < 0.005 μ/min and < 0.001 mm/min for friction and compression, respectively. N=5 samples were run under HA lubrication and N=10 under PBS lubrication.

10.2.6 Statistical Methods

The steady state friction and compression were calculated as the average value of the last 10 cycles. Significant differences were identified using one-way ANOVAs in the statistical software pack JMP® Pro 13.0.0 with significance set at $p < 0.05$. Statistical comparisons were made between different groups at a given speed. Post-hoc multiple comparison tests were not conducted here.

10.3 Results

10.3.1 The Role of Sliding Speed

The first experiment was designed to probe the role of sliding speed on the steady state friction and compression response. A representative speed sweep is shown in Figure 10.3. As previously demonstrated in Figure 9.5, high-speed sliding produces a physiologically consistent friction coefficient of ~0.01. However, as speed was reduced the friction coefficient transitioned to much higher values. The data

demonstrate that the friction coefficient of AC is strongly speed dependent, a finding that agrees with the findings of previous authors [58,102] and is highly suggestive of the presence of hydrodynamic forces [57,58,102,220].
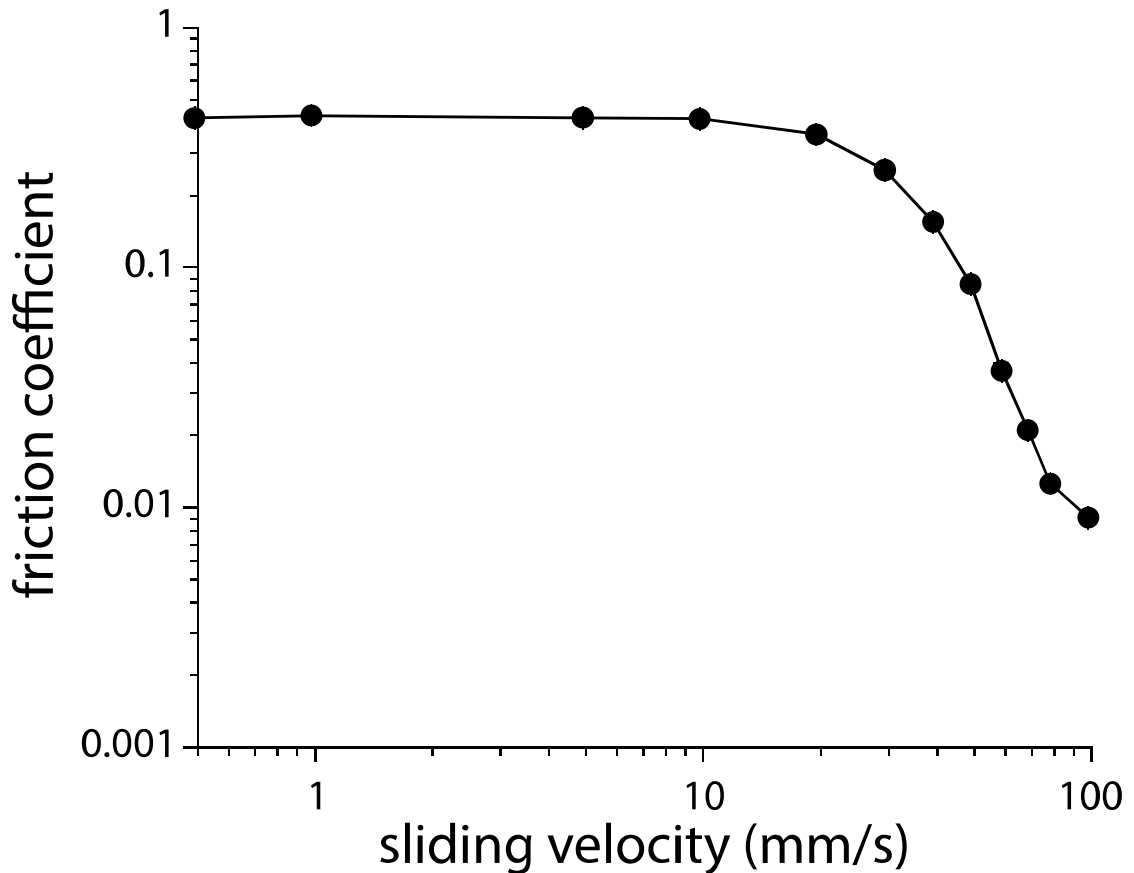
Figure 10.3 Friction coefficient versus sliding speed for a representative sample. Data were collected on the in-situ materials tester section *8.2.4 In-Situ Materials Tester*. Figure is adapted with permission [266].

The mean steady state friction coefficient and compression responses of N=5 independent cartilage samples in the cSCA are plotted as a function of speed in Figure

10.4. At speeds below 10 mm/s, the steady state friction coefficients of all five samples were in the range from 0.1 to 0.5 and were largely independent of speed below 10 mm/s. Beyond a critical speed between 10 and 30 mm/s, the friction coefficient of each sample transitioned toward low friction. At 80 mm/s, four of five samples had friction coefficients below 0.03; the sample that did not reach this threshold also had the highest transition speed. These differences in transition speeds may be driven by differences in cartilage curvature and material properties, both of which vary significantly throughout a joint [6,25,240,267], see Chapter 7 and *Appendix B.1 Material Properties and Profilometry*. Regardless of these differences, it appears likely that all five samples would have reached physiological friction coefficients (~0.02) [80,268] at physiological sliding speeds (100-150 mm/s) [36], a physical incapability of the in-situ materials tester (*4.6.1 In-Situ Materials Tester*). The steady state compression response in Figure 10.4B reveals significant variations in initial compression; this variation is due to large inter-sample variation in compression modulus and thickness [6]. Regardless of equilibrium compression, increased sliding speeds led to decreased steady state compression. On average, the samples thickened (decreased compression) by 160 ± 70 μm from low speed to high speed sliding (60-80 mm/s). Under high speed sliding all samples reached a mean steady state strain of 5 ± 3 %.
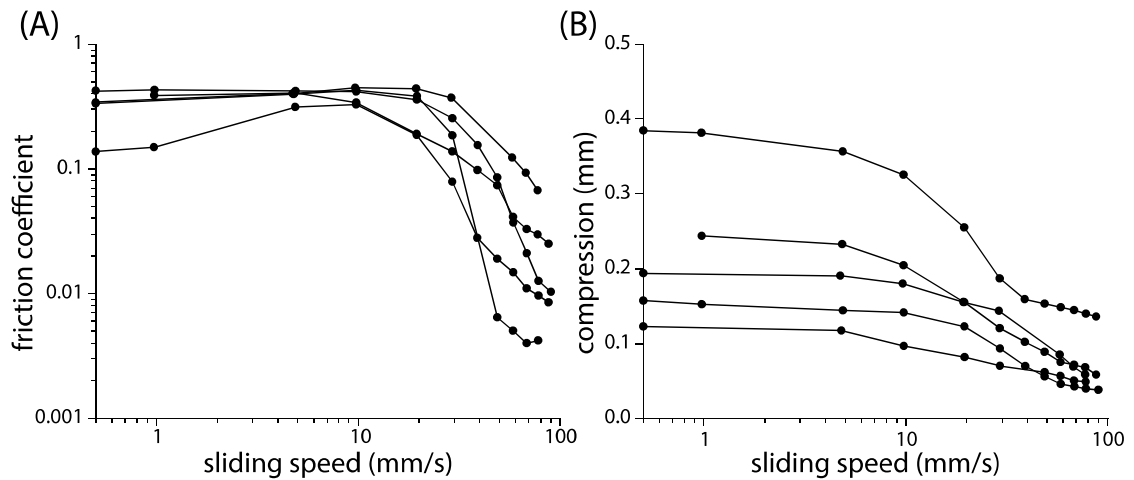
Figure 10.4 (A) Steady state friction and (B) compression as a function of sliding velocity under a normal load of 5 N. Data points are connected to indicate measures from the same sample. Data were collected on the in-situ materials tester section *8.2.4 In-Situ Materials Tester*. Figure is adapted with permission [245].

10.3.2 The Role of Load and Contact Stress

The second experiment was designed to probe the role of load and contact stress on the steady state friction and compression response. Based on Figure 9.2, loads of 5 and 1 N correspond to initial contact stresses of ~0.25 and ~0.1 MPa, respectively. The sliding speed was incrementally reduced following steady state at each speed condition.
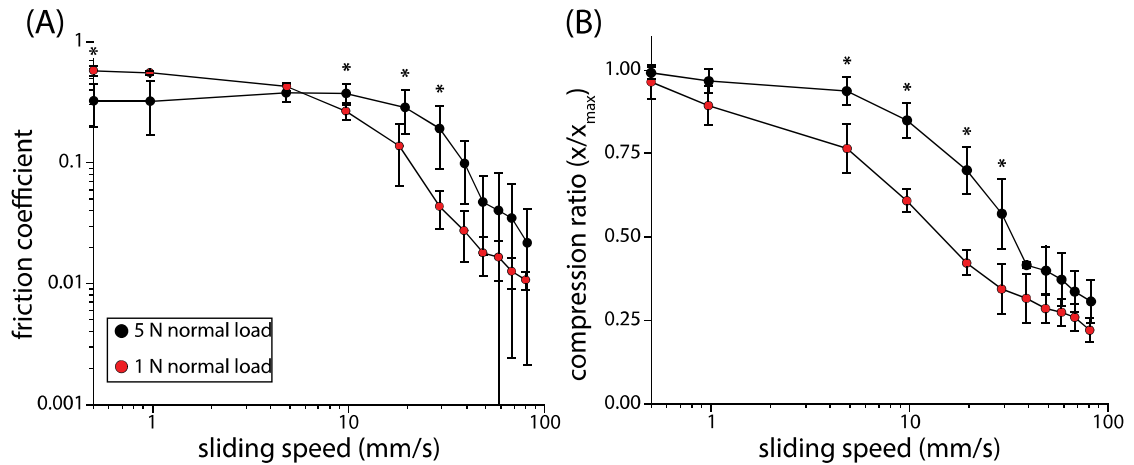
Figure 10.5 (A) Steady state friction and (B) compression ratio, x/x_{max}, as a function of sliding speed and load. Data points and error bars represent the mean ± standard deviation for N=3 and N=5 independent samples at 1 N and 5 N, respectively. Asterisks represent a statistically significant difference between the two load conditions. Note that due to the differences in the applied load (1 vs 5 N), absolute values of tissue compression varied greatly. The mean static equilibrium compression (x_{max}) for 1 and 5 N loads was 0.09 and 0.22 mm, respectively. Data were collected on the in-situ materials tester section *8.2.4 In-Situ Materials Tester*. Figure is adapted with permission [245].

The effects of load on the lubrication and fluid recovery responses of cartilage in the cSCA are illustrated in Figure 10.5. Both loading conditions can be seen to produce the same general response, i.e. decreased friction and compression with increased sliding speed. The compression ratio (compression / maximum compression) is shown in Figure 10.5B rather than absolute compression. This was done to account for the differences in equilibrium compression (0.09 at 1 N and 0.22 at 5 N). While not shown, the compression at 5 N was significantly greater than 1 N for all speeds.

At low (< 5 mm/s) and high (> 30 mm/s) sliding speeds the friction and compression ratios for 1 and 5 N loads are not significantly different (friction at 0.5 mm/s is significantly different). This finding demonstrates that load does not influence the asymptotic behavior of tribological rehydration, it does however influence the transition regime. Friction and compression recovered (transitioned) at lower speeds when loaded to 1 N compared to 5 N. Significant reductions in friction and compression began at speeds as low as 10 and 5 mm/s, respectively, and persisted until 30 mm/s.

The earlier onset of friction and compression reduction are consistent with the hypothesized competition between load-induced interstitial pressure (outflow) and speed-induced hydrodynamic pressure (inflow). It is interesting that while the compression ratio showed a shift in the onset of tribological rehydration, the 1 N load condition did not produce a significantly different high-speed compression ratio. In other words, while the hydrodynamic conditions were more favorable for the 1 N case, the absolute recovery of cartilage was less than the 5 N case (0.067 mm for 1 N and 0.151 mm for 5 N). While this finding may seem inconsistent, it demonstrates that as hydration increases so does the load-induced exudation rate (Figure 8.6).

10.3.3 The Role of Contact Geometry

The third experiment was designed to probe the role of contact geometry on the steady state friction and compression response. Fully hydrated samples were taken through a high to low (ramp-down) or low to high (ramp-up) speed sweep (0.1 to 500 mm/s) under a 2.5 N load. The use of a ramp-down versus a ramp-up speed sweep does not significantly alter the tribological response and further demonstrates the robust nature of the mechanism, see section *Appendix B.2 Ramp-Up & Ramp-Down*.

Furthermore, a 2.5 N load was used to help ensure an equivalent contact stress was applied between samples. Based on Figure 9.2, the estimated contact area under a 2.5 N load (F) is 12.5 mm^2, the smallest sample size (6.35 mm) has a projected contact area of 31.7 mm^2. The contact stress ($\sigma = F/A$) is roughly equivalent for all sample sizes because the contact area (A) is less than the sample area. In addition, it can be assumed that a convergence zone existed for all sample sizes.
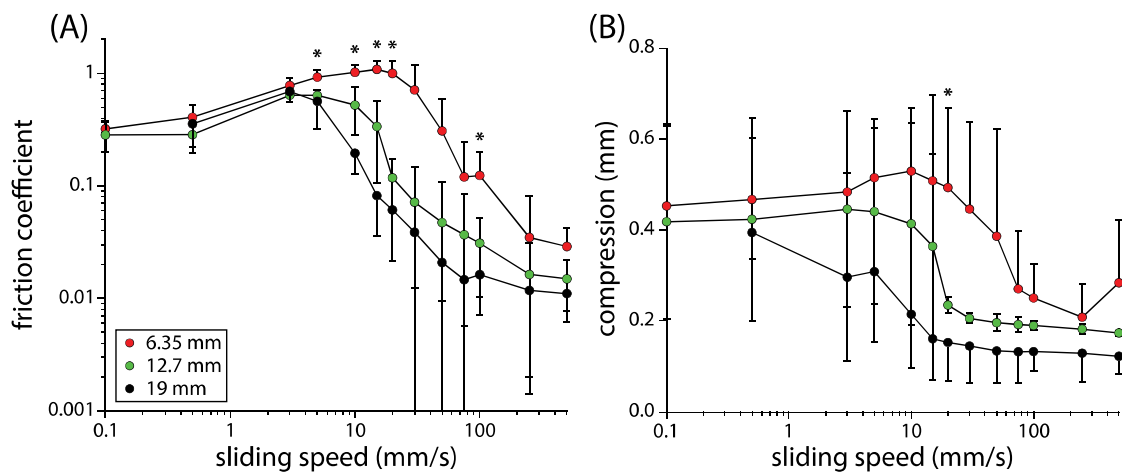
Figure 10.6 (A) Steady state friction and (B) compression for 7 osteochondral samples under a 2.5 N load. Samples underwent either a ramp-up or ramp-down speed sweep. Samples were milled from 19 mm (black markers) to 12.7 mm (green markers) to 6.35 mm diameter (red markers). Data points are plotted as the mean ± 95% confidence interval. Upper and lower error bars for 19 mm and 6.35 mm, respectively, have been removed for clarity. Asterisks indicate a statistically significant difference between the three geometric conditions. Experiments were performed on the pin on disc materials tester, section *10.2.3 Pin on Disc Materials Tester*.

A reduction in sample size generally led to an increase in friction and compression relative to larger sample sizes (Figure 10.6). At the slowest speeds, the

friction coefficient and compression between the 3 different conditions were nearly indistinguishable with average values of 0.33 and 0.43 mm, respectively. At speeds higher than 3 mm/s, the friction trends began to diverge. At 3 mm/s, the 19 mm diameter sample hit its peak friction coefficient of ~0.7; thereafter friction decreased with increased sliding speed down to a lower limit of ~0.01. The 12.7 mm diameter samples did not transition (decreased friction with increased speed) until between 3 and 5 mm/s, and reached a similar lower limit of ~0.01. The smallest sample size, 6.35 mm, required sliding speeds as high as 10 to 15 mm/s before transitioning and only achieved friction coefficients of ~0.03 at the highest sliding speeds. The steady state friction coefficient was significantly affected by sample size for speeds ranging from 5 to 20 mm/s and 100 mm/s. (Figure 10.6A).

While the transition points differ slightly in the compression response, the same relationships are observed (decreased compression with speed). In addition to shifts in the transition regime, it can also be observed that the lower limit for compression or maximum recovery is also size dependent, a feature that likely relates to the differences in minimum friction coefficient and the attenuation of tribological rehydration. Due to the previously observed higher variability in compression (Figure 10.4), only one statistically significant difference was observed for compression, occurring at a speed of 20 mm/s. While a larger sample population would likely demonstrate other significant differences, this limited population demonstrates that sample geometry does have a significant effect.

Since samples were run to steady state rather than for a predetermined period of time, the measured friction coefficient and compression are not artifacts of contact area [269]. The variations in friction and compression observed in Figure 10.6 are

believed to be caused by differences in tribological rehydration, and not alterations in contact stress, degradation, damage, or wear caused by subsequent testing (low speed friction and compression responses were unaffected by contact geometry). Since a reduction in sample size leads to a smaller entrainment zone for hydrodynamic fluid pressurization, the results appear to support the hypothesis that tribological rehydration is caused by speed-induced hydrodynamic pressure driven inflow.

10.3.4 The Role of Viscosity

The fourth experiment conducted was designed to probe the role of hyaluronic acid on the steady state friction and compression response (Figures 10.7 and 10.8). The use of a physiologically consistent HA solution — (3 mg/ml) [34,227] and (~1.5 MDa) [33,258,265] — significantly attenuated friction, by a factor of 2 to 4, between 1 and 100 mm/s. Furthermore, it appears that a slower transition speed is required when using the HA solution. These findings suggest a dual effect of HA, i.e. boundary lubrication and visco-supplementation. The slow speed friction reductions of Figure 10.7 suggest that HA acts as a boundary lubricant [144]. However, extensive research in the area of cartilage lubrication appears to refute the role of HA as an isolated boundary lubricant [77]. A potential explanation for this discrepancy comes from more recent work in the field that suggests a lubrication synergy between lubricin and HA [77,207,270,271], where lubricin is the principle boundary lubricant and acts to trap HA causing an elasto-viscous transition [77,91]. While the use of lubricin was purposely avoided in these studies, it cannot be ruled out that trace amounts remained adhered to the cartilage surface following tissue extraction; even trace levels of lubricin have been demonstrated to provide an enhanced lubrication effect [270,272].

The second effect of HA appears to be a visco-supplementation effect, which presents as a lateral shift in the friction response (Figure 10.7). As Figure 10.8 demonstrates this also leads to an earlier onset of tribological rehydration. It is important to note that only the transition regime is significantly affected by the use of HA. To better highlight these differences the sample-by-sample compression fraction (x^*) was calculated as: $x^* = x \cdot (x_{max} - x_{min})^{-1}$, where x is the compression at a given speed and x_{max} and x_{min} are the maximum and minimum compression, respectively, for the sample of interest. Figure 10.8B very clearly highlights the shift in the compression response. Since cartilage compression is assumed to be unaffected by boundary lubrication (there may be a small effect on confinement and shear strain) the lateral shift in the curve is believed to be caused by the higher viscosity HA solution. From hydrodynamic theory, a higher viscosity solution will increase the hydrodynamic fluid pressure; therefore, this result further supports the hypothesis that hydrodynamic forces are an underlying mechanism of tribological rehydration.
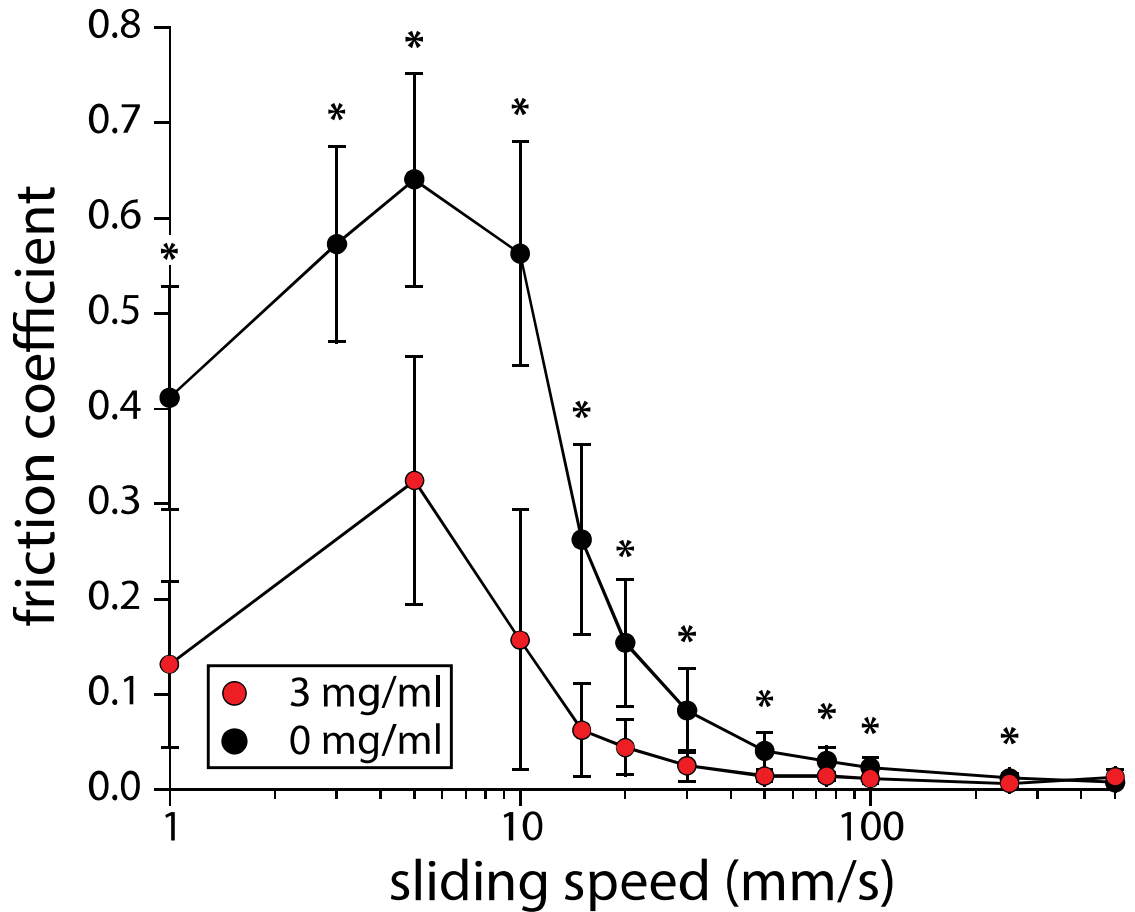
Figure 10.7 Friction coefficient versus speed for two different lubricating fluids (3 mg/ml of HA in PBS and 0 mg/ml of HA in PBS). The study was performed with 15 cartilage samples (N=5 for 3 mg/ml and N=10 for 0 mg/ml). Data points are plotted as the mean ± 95% confidence interval. Asterisks indicate statistically significant differences between the two solutions tested. Tests were not paired due to excessive test durations which may lead to degradation, damage, or wear and may confound follow up studies. Experiments were conducted on the pin on disc materials tester, see section *10.2.3 Pin on Disc Materials Tester*.
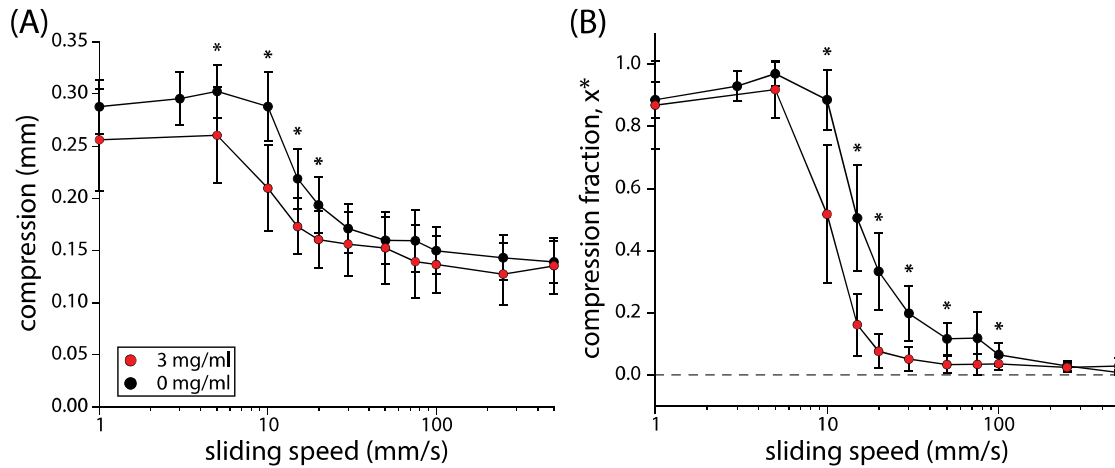
Figure 10.8 (A) Compression and (B) compression fraction versus speed for two different lubricating fluids (3 mg/ml of HA in PBS and 0 mg/ml of HA in PBS). The study was performed with 15 cartilage samples (N=5 for 3 mg/ml and N=10 for 0 mg/ml). Data points are plotted as the mean ± 95% confidence interval. Asterisks indicate statistically significant differences between the two solutions tested. Tests were not paired due to excessive test durations which may lead to degradation, damage, or wear and may confound follow up studies. Experiments were conducted on the pin on disc materials tester, see section *10.2.3 Pin on Disc Materials Tester*.

It should be noted that during high-speed sliding with the HA solution, there was insufficient time for the fluid to re-enter the wear track, in other words it was too viscous. Attempts were made to intervene (custom PTFE wiper blade) and force fluid into the wear track; however, the efficacy of this action is unknown. All speeds and lubricating conditions were subjected to this same intervention technique to prevent any bias.

10.4 Discussion

The final aim of this dissertation was designed to evaluate the role of the mechanical environment on tribological rehydration. In this study, 30 osteochondral

samples were extracted from mature bovine stifle joints and run under various sliding conditions until reaching steady state conditions. The specific conditions investigated were the roles of sliding speed (0.5 to 500 mm/s), load (1 and 5 N), sample size (19, 12.7, and 6.35 mm diameter), and viscosity (0 and 3 mg/ml HA in PBS).

As demonstrated by all the figures in this study, an increase in sliding speed beyond a critical threshold leads to reduced friction and a simultaneous recovery in compression. For the 'standard' experiment (19 mm diameter sample loaded to 5 N) this speed threshold was ~10 mm/s. The previous chapters demonstrate that this compression recovery is caused by an influx of fluid (tribological rehydration). This rehydration effect simultaneously reduces friction and compression by restoring WL and IFP, respectively. On average, from 0.5 to 80 mm/s, tribological rehydration led to a 15X and 160 μm reduction in friction coefficient and compression, respectively. The role of sliding speed in the SCA and cSCA configuration has been previously identified. Dowson and co-workers first noticed that increased sliding speeds in a cSCA contact led to a reduction in friction and proposed the development of hydrodynamic fluid films [58], a finding and conclusion further supported by Striolo and co-workers [273]. Bonassar and co-workers followed up on this work, using a fixed versus tilt-pad bearing design on SCA contacts [251]. Their results demonstrate that under the fixed pad design, which produced a convergence zone, friction was strongly dependent on sliding speed. However, based on the relatively high friction coefficients at all speeds (up to 50 mm/s) they believed it was unlikely that a fluid film had developed [102]. They proposed that the permeable interface of AC partially depleted the developing film, and thus led to mixed-mode lubrication [102] or possibly elasto-viscous lubrication [77,91]. The lubrication regimes proposed by the previous

authors are all rooted in hydrodynamic lubrication theory and rely solely on the observation of reduced friction as a function of increased speed. This work adds to the work of the previous authors by demonstrating that friction recovery is accompanied by compression recovery, a result that suggests the friction reduction effect may be caused by the recovery of WL.

The role of load is investigated in section *10.3.2 The Role of Load and Contact Stress*. In Figure 10.5A it can be observed that a reduction in load from 5 N (~0.25 MPa contact stress) to 1 N (~0.1 MPa contact stress) causes an earlier (slower speed) friction transition. The friction transition at 1 N occurred at ~5 mm/s, while at 5 N it was found at ~10 mm/s. Figure 10.5A also seems to suggest that reduced loading leads to reduced friction coefficients overall, albeit not significantly. The earlier transition speed is further supported by the compression ratio (Figure 10.5B). The data again demonstrate the phenomenon of tribological rehydration and the role of hydrodynamic forces. In classical hydrodynamic lubrication one of the most commonly varied parameters, other than sliding speed, is load [102,216]. Higher loads require higher hydrodynamic forces to separate contacts [58,216,220,253,274]. In a typical Stribeck curve, this would manifest as an increased friction coefficient and decreased film thickness with load [274]. The role of load, contact stress, or equilibrium strain was previously investigated by Gleghorn and Bonassar who found that as strain was increased (increased load) friction increased [251]. In their study, which used SCA contacts, the strain effect was much more pronounced on the fixed-pad system which forced a convergent wedge versus the tilt pad system that allowed for mated or near mated contact. This is again in direct agreement with the results presented here and the role of hydrodynamic forces in tribological rehydration.

Under the observations of Dowson and co-workers [58] and Bonassar and co-workers [102], the decision was made to also vary the contact geometry or sample size. As previously mentioned, samples were extracted as 19 mm diameter osteochondral cores. The sample diameter was reduced to 12.7 and 6.35 mm using an in-house CNC mill, see section *9.2.2 Sample Geometry*. Figure 10.6A demonstrates that at slow sliding speeds friction was nearly indistinguishable, while at higher sliding speeds larger samples produced lower friction coefficients. A similar response was again found in the compression response. The most important finding was that the transition regime was a function of sample diameter, where smaller samples required higher sliding speeds to achieve meaningful tribological rehydration. From Figure 10.6A, the peak friction for 19, 12.7, and 6.35 mm diameter samples under a 2.5 N load occurred at 3, 5, and 15 mm/s, respectively. Following this critical speed, friction decreased with increased sliding speed. It is interesting that for the 6.35 mm diameter case, there is a very obvious increase in compression between 3 and 20 mm/s. Over this speed range, the compression increased by ~0.05 mm compared to the slowest speed condition. Under these same speeds the friction coefficient increased by ~2.4X compared to the slowest speed condition.

Dowson and co-workers previously demonstrated that the friction reducing effect of sliding speed was intimately dependent upon the presence of a convergent wedge [58] while Gleghorn and Bonassar demonstrated that a fixed-pad cartilage bearing (cSCA contact) produced lower friction with increased sliding speed. The results of section *10.3.3 The Role of Contact Geometry* further support these findings, and offers the additional observation of compression recovery. The compression

results again suggest that friction recovers as hydration (compression) is restored, a finding that suggests WL is the cause of friction reduction.

The role of synovial fluid has been possibly one of the most heavily studied topics in joint function. The questions related to synovial fluid are to identify its molecular composition [34], determine the specific roles of each constituent [13,77,207,208,271,272,275–277], and to understand what changes occur during joint degeneration and how they influence the tribological response [115,258,265]. In a very generic sense, synovial fluid is described as a distillate of blood plasma with the addition of HA and phospholipids [24,74–79]. Of specific note, PRG 4 (proteoglycan 4) or more commonly known as lubricin or superficial zone protein has been associated with the boundary lubrication of AC. The literature has almost undisputedly revealed that PRG 4 endows cartilage with the ability to reduce friction by ~2X [13,76,77,116,207,277–280]. HA on the other hand has had a fairly less defined role in the boundary lubrication of AC, a feature that may be related to a lubricating synergy between PRG 4 and HA [77,271]. Regardless of HA's efficacy as a boundary lubricant, it has been almost unanimously identified as the main contributor to synovial fluid's viscosity [32–34,77,265,272,276]. The decision to study isolated HA was made based on the well-known effect of viscosity on hydrodynamics [34,50,51,56,225,231,281].

As demonstrated by Figure 10.7, the addition of HA at a physiologically consistent concentration led to an overall reduction in friction and lateral shift in the curve. Due to the apparent dual effect (boundary and visco-supplementation) of HA on the friction response it is easier to identify the role of HA on tribological rehydration using Figure 10.7. The compression response in Figure 10.8A, better highlighted in

Figure 10.8B, demonstrates that under HA lubrication significantly slower speeds are required for tribological rehydration. The results again support the role of hydrodynamics in tribological rehydration. From hydrodynamics theory, an increase in the fluid viscosity will lead to an increase in the hydrodynamic pressure under otherwise constant conditions [56,221,225,231,282–284]. In traditional fluid film theory, this would be interpreted as the ability to generate a thicker film and thus produce lower friction coefficients. As previously stated, it is unlikely that fluid films are being developed here. However, it is likely that hydrodynamic pressures do play a role in tribological rehydration and thus friction and compression should transition at lower speeds as demonstrated by Figures 10.7 and 10.8. The lack of significant differences at higher speeds is likely a result of shear thinning in which the coiled and looped HA chains, which occupy a large solvent domain, become straightened out and resemble the viscosity of water and PBS [4,33,50].

From a clinical perspective, it would appear that joint activity, reduced joint loading, and HA support cartilage longevity through reduced shear stress and tissue strain. Epidemiological studies have repeatedly shown that normal and routine joint activity places a person at lower risk for joint disease [45–49,192,285], although the mechanisms responsible for this have remained elusive. Tribological rehydration identified as a major risk factor for developing joint disease [38,138,285–287]. Research has found that for every pound of body weight, joint loads are increased by 3X. As demonstrated by this study, an increase in load leads to a delayed onset of tribological rehydration and may thus explain the chondroprotective nature of weight loss.

In this chapter, it was demonstrated that the mechanical environment of articular joints plays a major role in cartilage lubrication and tribological rehydration. Furthermore, each of the parameters studied (velocity, load, contact geometry, and fluid viscosity) support the hypothesis that hydrodynamic forces are at least a partial contributor to sliding induced fluid recovery (tribological rehydration).

<center>**Chapter 11**</center>

<center>**DISCUSSION**</center>

11.1 Hertzian Contact Mechanics of Articular Cartilage

The first half of this dissertation focused on developing a biphasic model for Hertzian contact of articular cartilage. The use of a Hertzian (rigid sphere) contact was choose as it produces a physiologically consistent response, allows for rapid equilibration, localized contact, zero stress concentrators, and supports tribological experiments. In Chapter 4 a sliding tribo-mechanics model was developed to describe how the migrating contact area is able to maintain tribological functionality. The results demonstrated that the speed of contact migration is critical to maintaining maximum hydration and thus peak IFP, while the tensile-to-compressive modulus ratio, E^*, defines the maximum achievable IFP.

The original model formulation which was defined over a range of sliding speed was redefined for a range of indentation rates in Chapter 5. Furthermore, this new model included substrate effects (contact stiffening) and comparisons to gold standards. The gold standards required the use of plane-ended indentation and were fit to a linear biphasic or tension-compression biphasic model. Despite the use of different indentation techniques and contact stresses the models showed good quantitative agreement, giving support to the Hertzian model.

In Chapter 6 the Hertzian biphasic theory was extended to accommodate simpler and more common creep and creep-relaxation (combination of creep and stress relaxation) indentation methods. Creep involves the use of a fixed load and

<center>166</center>

tracking of compression over time, while stress relaxation applied a fixed displacement and tracks load over time, both of which are standard on most indentation/load/test frames. The model not only included substrate effects but also strain dependent permeability. This final form of the model was validated against a custom finite element model for a rigid sphere indenting a fibrous biphasic layer. The two models displayed excellent quantitative agreement and again supported the use of the Hertzian biphasic theory.

The primary advantage of the biphasic model developed here is the rapid solution times (~20 s) and a high degree of accuracy (comparisons to gold standards). With this model, a spatial study of the bovine stifle joint was performed (Chapter 7). In this study, 200 osteochondral cores underwent tribological contact and Hertzian rate based indentation. The results provided a tribological and material property map of the bovine stifle joint and support the hypothesis that changes in cartilage contact patterns (soft tissue damage) will lead to altered tribological stresses that may initiate joint degeneration.

11.2 Tribological Rehydration

The second half of this dissertation investigated the coupling of interstitial and hydrodynamic pressure fields. In Chapter 8 an experimental study of hydrodynamics in impermeable cartilage contacts was performed. The results demonstrated that when the cartilage interface was made impermeable, substantial fluid films were formed at the sliding interface. However, restoring the native permeable interface demonstrated a fundamentally different phenomenon. This shift in tribological behavior was explored in Chapter 9 and questioned whether or not interfacial sliding could restore tissue hydration and lubrication. It was demonstrated that a loaded sliding cartilage

contact could, in-fact, maintain and recover hydration and lubrication without migration, unloading, or bath exposure. This finding precluded all other hypothesized mechanisms of cartilage recovery and was termed tribological rehydration. The last chapter (Chapter 10) investigated the role of the mechanical environment on tribological rehydration. It was demonstrated that the same parameters that govern hydrodynamic fluid films also govern the tribological response of cartilage and suggests tribological rehydration may have a hydrodynamic origin. Tribological rehydration offers a potential explanation to the somewhat non-intuitive result that joint activity is chondroprotective.

11.3 The Mechanism of Tribological Rehydration

Figure 11.1 outlines the hypothesized mechanism underlying tribological rehydration. During contact, the cartilage is compressed and fluid is exuded from the tissue. Relative motion of the contacting bodies drags fluid into the convergent wedge created by the natural geometry of the tissue. When the hydrodynamic pressure exceeds the interstitial pressure, fluid will flow into the cartilage leading to a recovery of hydration and lubrication. As Figure 11.2A demonstrates, the point of entry is likely near the edge of contact. Recent work by Graham et al. demonstrates that sliding in a cSCA contact causes a small (0.6 nm Stoke's radius) fluorescent molecule, Alexa Fluor 633, to penetrate the cartilage contact with a gradient from the contact periphery (convergent wedge) towards the center [264], see section *Appendix B.3 Solute Accumulation*. From this, it seems likely that fluid would flow along this same gradient.

As sliding continues and tissue hydration increases (decreased compression) so does the exudation rate, see Figure 11.3B. Eventually, the rehydration rate is balanced

by the exudation rate. As sliding speed slows, the hydrodynamic pressure becomes less competitive and the rehydration rate is no longer competitive with the exudation rate; this leads to a new dynamic equilibrium. The effect of sliding speed is further supported by the work of Graham et al. (see section *Appendix B.3 Solute Accumulation*) [264]. This hypothesis represents a unique coupling of the interstitial and hydrodynamic lubrication hypotheses of joint lubrication.
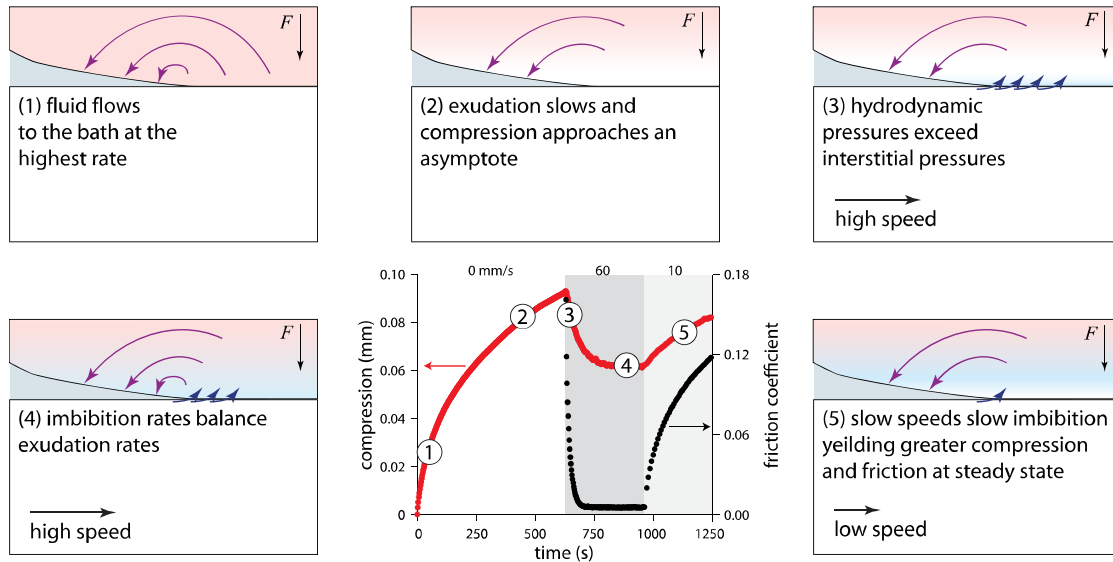
Figure 11.1 The proposed mechanism of tribological rehydration. (1) Initial contact and deformation cause maximal pressurization of interstitial fluid, which typically supports 90-99% of the applied load. Interstitial pressure drives flow toward the low-pressure bath along paths of least resistance; flow may occur through the tissue, through percolated 'channels' formed by contact with the rough cartilage surface, or a combination thereof. (2) Compression increases as interstitial fluid flows, resulting in increased load carrying by the solid, decreased interstitial pressure, and decreased compression (exudation or strain) rate. (3) Interfacial sliding draws fluid into the convergent wedge where it is subsequently pressurized via hydrodynamics and forced into the contacting cartilage surface. As compression decreases, interstitial pressure, especially at the frictional interface, increases resulting in decreased friction and increased exudation rates; the system achieves dynamic equilibrium (4) once the exudation rate matches the rehydration rate. The transition to slower sliding speeds produces decreased hydrodynamic pressure, and a decreased rehydration rate; this results in increased compression and friction (5). Image is adapted with permission [215].

A conceptual model of cartilage lubrication and hydration is shown in Figure 11.2B. The model is based on the hypothesized mechanism of tribological rehydration and its effect on the functional performance of AC. In this model, cartilage is

170

represented as a sink, and tribological rehydration as the hose filling the sink. Recalling that cartilage function is directly tied to hydration, the goal is to keep the sink full at all times. To keep the sink full, tribological rehydration (the hose) must, at minimum, match the drainage rate. Similar to a hose, the duration of filling and flow rate can be altered to achieve maximum rehydration. As demonstrated in Chapter 10 and Figure 11.3, the sliding duration, speed, load, and geometry directly influence the volume and rate of fluid recovery. In general, longer sliding durations, higher sliding speeds, lower loads, and larger samples provide for greater recovery.

(A)   (B)
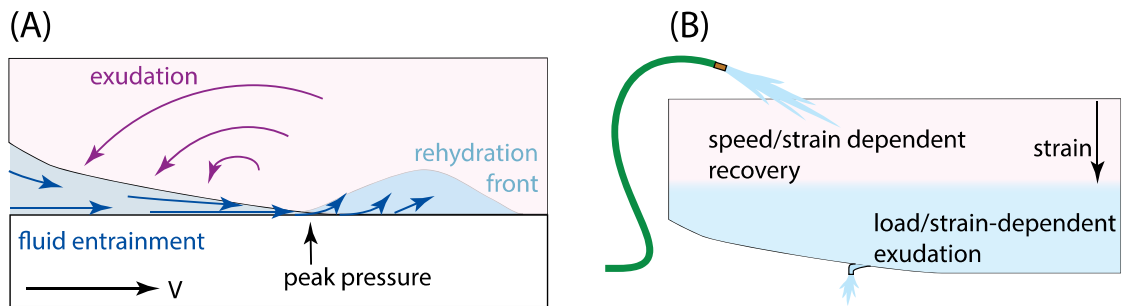
Figure 11.2 (A) Hypothesized mechanism of tribological rehydration. (B) Role of tribological rehydration in maintaining and restoring WL. Figure is adapted with permission [245,266].

11.4 Tribological Rehydration Rates

A small study was conducted to investigate the exudation and rehydration rates for 10 different cartilage samples. The results are displayed in Figure 11.3. In the first case (Figure 11.3A), N=3 cartilage samples were loaded to 5 N and held static for 90 minutes prior to sliding between 1 and 100 mm/s. This condition was repeated for 9 different speeds. The exudation rate (red line) was calculated as the compression rate 2 min prior to sliding. The rehydration rate was defined as the filling rate and is

represented as the hose in Figure 11.2B. While we cannot directly probe the filling

rate, we can measure the recovery in tissue compression, which corresponds to a

change in the fluid level (Figure 11.2B). Conserving mass it can be stated that the

rehydration rate is the sum of the recovery rate (change in fluid level) and the

exudation rate (fluid leaving). As demonstrated by the figure, the exudation rate was

consistently $\sim 2 \cdot 10^{-5}$ mm/s following 90 min of static compression and was

independent of loading history. The rehydration rate (blue filled markers), on the other

hand, was a strong function of speed reaching rates that were 30X greater than those

of exudation.

In the second case, N=7 samples were loaded statically to 5 N for different

periods of time (0.5 to 180 min). Following static contact, the samples were slid at 100

mm/s. The exudation (red filled markers) rehydration rate (blue filled markers) were

calculated as described previously; however, for 0.5 and 1 min static loading times the

exudation rate was taken over the entire static contact time. The results demonstrate

that exudation rate is a strong function of dwell time, where longer dwell times lead to

reduced exudation rates that span almost 3 orders of magnitude. The rehydration rate

is similarly dependent on dwell time where longer periods of static contact lead to

greater rehydration rates at a given speed (100 mm/s). Interestingly, the rehydration

rate only spans about 1 order of magnitude and reaches an apparent maximum rate of

$\sim 2 \cdot 10^3$ nm/s. The results further demonstrate that this peak rehydration rate occurs

after ~ 20 min of static contact.

The results of Figure 11.3 demonstrate some very interesting features of

tribological rehydration. First, not only is the magnitude of rehydration (compression

recovery) speed dependent, but so is the rate of rehydration (fluid is pumped in faster

at higher speed). Second, the rehydration rate under a 5 N load at 100 mm/s has an upper limit of ~ $2 \cdot 10^{-3}$ mm/s. This upper limit occurs only once cartilage has achieved significant dehydration and it may serve to limit the fluid shear encountered during rehydration. Limiting fluid shear maybe crucial in the tribological rehydration process to prevent negative biomechanical cues [7]. The specific mechanism leading to the regulation (limit) of rehydration is currently unknown. The third feature worth noting is that tribological rehydration is not competitive with load-driven exudation at all contact times. Figure 11.3B demonstrates that dwell times < 1 min will lead to further exudation, dwell times ~ 1 min will maintain compression, and dwell times > 1 min will undergo compression recovery.

The evidence provided in this section demonstrates that tribological rehydration is competitive with load driven fluid exudation. The results also suggest some interesting flow limiting dynamics that will require further investigation.
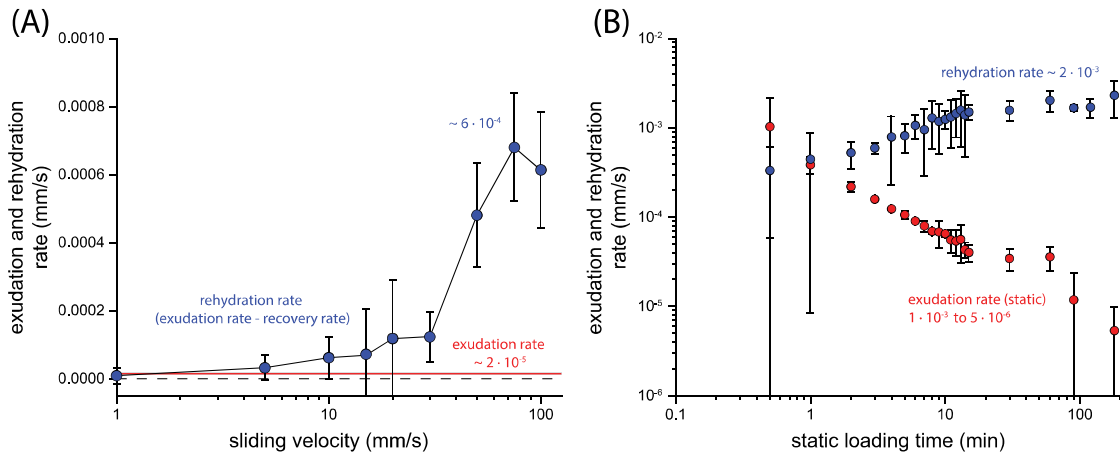
Figure 11.3 (A) Rehydration rate as a function of sliding speed following 90 min of 5 N static equilibration, N=3. (B) Exudation and rehydration rates for different static dwell times, N=7. Note that load was maintained at 5 N and sliding speed was 100 mm/s. In all cases the rehydration rate was calculated over the first 5 cycles. Experiments were conducted on the pin on disc materials tester, see section *10.2.3 Pin on Disc Materials Tester*.

11.5 The Role of Tribological Rehydration

To date, the recovery of interstitial fluid in joints has been attributed to osmotic swelling during intermittent bath exposures within a migrating contact [37,84,116] or the mechanical pumping effect of unloading [116,288]. Although numeric solutions and finite element studies have demonstrated that migration alone can maintain interstitial fluid [110,117], the literature contains no theoretical analysis for the passive swelling hypothesis of joint recovery. There are, however, established theoretical reasons to question the feasibility of the hypothesis. First, the migrating component (e.g. femoral condyle) must not only soak enough fluid during intermittent exposure to promote its own recovery, it must more than compensate for exudation by the stationary component (e.g. tibial plateau), which is being driven by substantial fluid pressures on the order of the contact stress (1-5 MPa in most physiological conditions

[138]). To date, cartilage recovery has only been hypothesized to occur through Donnan osmotic swelling and mechanical pumping (contact loading and unloading) [254,289–294]. The osmotic pressure is approximately the product of equilibrium compressive modulus and strain; this assumes the collagen network provides negligible contribution to the equilibrium modulus [293,294]. The osmotic pressure of cartilage is established by the proteoglycans (charged solvated biopolymers) which include electrostatic (Donnan) and non-electrostatic (configurational entropy) interactions [293,295].

Using representative values (~0.5 MPa, ~10% strain [185]), the osmotic swelling pressure is expected to be in the range of 1-10% those driving exudation. Given the anatomy of a typical joint and the relative amounts of time any one region spends in contact versus free-swelling, it isn't obvious that osmotic recovery is capable of balancing exudation under typical conditions.

Linn's whole joint experiments, demonstrate that joint articulation maintains and restores tissue hydration [80]. According to Linn, this is due to intermittent bath exposure of the contact (free-swelling). However, Linn was un-aware of tribological rehydration and mechanical pumping as they had not yet been discovered, both of which participate in joint articulation. As a test of the relative rates of joint and cSCA recovery, Linn's whole joint recovery measurements [80] were replicated in Figure 11.4 using the cSCA configuration. The cSCA configuration was used as a point of comparison as it eliminated the possible contributions from free-swelling and mechanical pumping. Under dynamic conditions, the intact ankle joint of Linn's study stabilized and recovered to ~0.1 mm of compression (two cartilage surfaces). The same basic mechanics were observed in the cSCA (Figure 11.4B); the tissue

175

compressed to ~0.06 mm during sliding, thinned during static loading, and recovered during sliding at about the same rate as that observed by Linn. The results indicate that tribological rehydration alone is capable of producing the same recovery dynamics exhibited by joints.
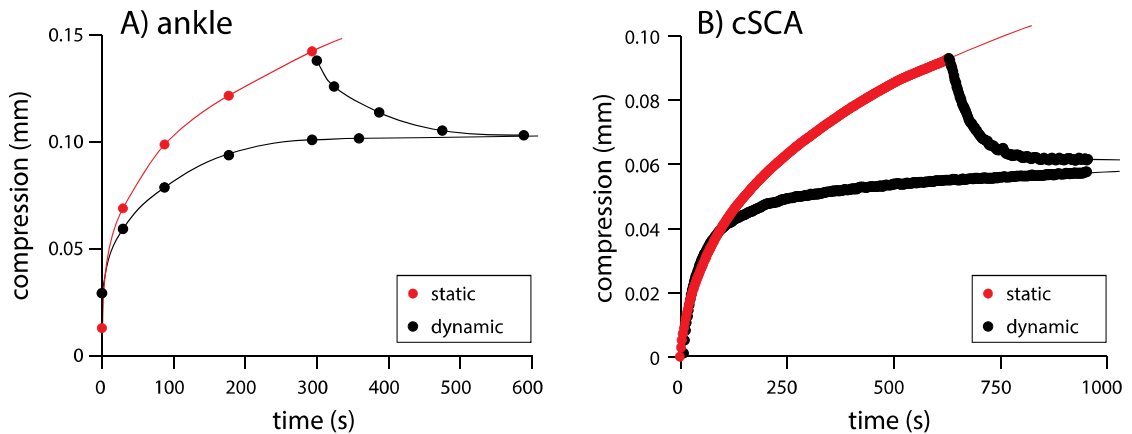
Figure 11.4 Comparison between Linn's results [80] and those from comparable experiments with the cSCA. The figures demonstrate striking resemblance despite grossly different loads, contact areas, reciprocation lengths, material properties, and testing configuration (whole joint versus cSCA). (A) The testing configuration of Linn used a canine ankle which includes the possibilities of recovery via free swelling during intermittent bath exposure and tribological rehydration. (B) The cSCA configuration eliminated free swelling as a potential recovery mechanism, effectively isolating tribological rehydration. Image was adapted with permission [215]. Data were collected on the in-situ materials tester section *8.2.4 In-Situ Materials Tester.*

The literature leaves little doubt that excessive joint space narrowing is synonymous with joint disease [247,285,296,297]. The relationship between thickness and health likely reflects the beneficial effects of: 1) interstitial hydration and pressure on lubrication, 2) fluid content on biochemistry, 3) pressure/flow on cellular

176

stimulation, and 4) fluid flow on nutrient and waste transport. Given the low modulus of cartilage and the large contact pressures sustained in-vivo, substantial IFP must exist at all times to maintain healthy joint space. Since joints thin during inactivity (load-driven fluid exudation), recovery during activity is the primary means by which joint space thinning is prevented in the long-term [298–300]. Activity is the engine that drives and sustains important mechanical, tribological, and biological functions in the joint, which helps explain why running reduces risk of osteoarthritis [45] and why immobilization increases risk of osteoarthritis [297]. To date, osmotic swelling and mechanical pumping from loading and unloading are the only hypotheses capable of explaining this recovery phenomenon in joints. The work present in this dissertation provides: (1) the first evidence of an alternate hypothesis, (2) a feasible conceptual framework for the relevant mechanics, (3) experimental evidence that supports tribological rehydration as a significant contributor to the recovery response of natural joints, and (4) helps resolve why the literature appears to simultaneously support and refute the WL and fluid film theories of joint lubrication (tribological rehydration appears to recover WL through a hydrodynamic mechanism). If tribological rehydration is an important contributor to the recovery response of joints, as the results suggest it is, then tribological rehydration must also be an important contributor to the preservation of joint health.

Chapter 12

LIMITATIONS

The physiological structure and function of mammalian joints is without a doubt much more complex than the tribo-mechanics models, experimental configurations, and well-controlled conditions described in this dissertation. The decision to remove certain aspects of the physiological condition was necessary to provide basic science and mechanistic insights.

In Chapter 4 a tribo-mechanics model of a rigid sphere sliding on a non-linearly elastic biphasic half-space was developed. In natural joints cartilage is typically interfaced with another cartilage surface; however, using mated cartilage introduces two unknowns and decoupling how much each body contributes to the overall response is quite challenging. The rigid sphere was chosen over other counter bodies as it has been shown to produce a physiologically consistent response (IFP and lubrication) that is indistinguishable from the native contact [28,84].

In Chapters 5 and 6 the tribo-mechanics model of Chapter 4 was expanded upon to include substrate effects and strain dependent permeability, features that were aimed at improving the model. To verify that the added model complexity was appropriate the results were compared to gold standards in the literature. Chapter 7 applied these tribo-mechanics models to a population of bovine stifle joints to study the spatial distribution of tribological and material properties. Here the use of the spherical contact enabled surface sensitive measurements of the articular cartilage with high spatial resolution and in-situ tribometry.

In Chapter 8 the cartilage interface was made to be impermeable by the use of a thin polymeric membrane. The goal of this study was to demonstrate consistency with hydrodynamics without the confounding effects of WL. The polymer membrane successfully achieved this goal but did alter the interfacial chemistry and possibly the surface roughness during tribological contact. The extent to which these factors may have influenced the results are currently unknown.

In Chapter 9 cartilage samples were interfaced with a flat glass microscope slide. This configuration was a necessary condition that led to the discovery of tribological rehydration (sliding induced fluid recovery). Natural and mated cartilage contacts undergoing linear reciprocated sliding or rolling are by definition migrating contacts [28,83,84,99] and represent a coupled problem. Migrating contacts maintain hydration and function due to the combination of a high Péclet number [28,84], free swelling [117], and potentially tribological rehydration. To eliminate these confounding factors of contact migration and free swelling, a stationary contact area (i.e. a rigid flat) was required. Both glass microscope slides and polished steel flats are considered standards for the SCA configuration. Microscope slides were chosen out of convenience, consistency, and contact transparency for imaging the contact area.

In Chapter 10 a solution of 3 mg/ml hyaluronic acid in saline was used to model the physiological viscosity characteristics of joints and determine its role in tribological rehydration. It is important to note that even isolated hyaluronic acid has a complex rheology (hyaluronic acid viscosity depends on molecular weight, concentration, and shear rate) [33,226,227,301,302]. The key result from section *10.3.4 The Role of Viscosity* is that hyaluronic acid initiated an earlier onset of tribological rehydration. This was likely due to the enhanced solution viscosity; thus,

synovial will likely cause a similar effect. Another fluid that might have been suitable to more directly investigate the viscosity effect is polyethylene glycol (mostly Newtonian fluid); however, this would have been done at the expense of physiological relevance.

Another limitation was the use of a sub-physiological load (5 N) and contact stress (~0.25 MPa). The use of a low contact stress probably benefited tribological rehydration as the interstitial pressures were lower, and thus the hypothesized hydrodynamic fluid pressures could more easily rehydrate the tissue. Future work should be aimed at demonstrating tribological rehydration at more physiologically relevant conditions.

Finally, the cartilage used in these studies comes from mature bovine stifle joints. While differences do exist between human and bovine joints [202,303], there has been no evidence to suggest the fundamental mechanics and lubrication phenomenon differ [84,115]. Furthermore, preliminary studies on equine joints have produced comparable responses. Future work should be aimed at demonstration that tribological rehydration is preserved across all mammalian articulating joints.

Chapter 13

FUTURE WORK

The discovery of tribological rehydration has generated a lot of interest in the biotribology and biomechanics communities from both an engineered bearing point of view and for maintaining and restoring joint health. Some potential ongoing and future studies related to the application of tribological rehydration are described below.

Tribological rehydration is defined as sliding induced fluid recovery in articular cartilage; while this is an accurate description of the phenomenon, it doesn't describe the mechanism responsible for it. As previously mentioned, there seems to be an interaction between the interstitial and hydrodynamic pressure fields. Should tribological rehydration function as a simple coupling of these two theories, it becomes readily apparent that an overwhelming number of variables needs to be considered and modeled, see Figure 13.1. This work has already demonstrated initial evidence that speed, load, geometry, viscosity and permeability play a role in tribological rehydration [215]. Other authors also support the roles of speed, load, geometry, and potentially viscosity in cartilage lubrication [58,77,82,251,272,276]. While material properties were only measured for selected studies, the natural variations in tensile modulus (5.4X), compressive modulus (4.5X), and permeability (4X) [6] did not appear to play a role in the mechanism. However, it is likely that more dramatic changes in the material properties (tissue damage) may lead to an altered response. Furthermore, while sample size did play a role, the gross curvature ($R = 16.4$ to 33.8 mm) of the sample did not (all samples were convex). In preliminary studies

concave samples, taken from the tibial plateau, demonstrated little to no rehydration capacity in the SCA configuration. Future work should focus on establishing the relative contribution of each of these parameters to tribological rehydration.

One of the biggest questions that remains is to define the role of tissue degradation on the efficacy of tribological rehydration. It is well established that proteoglycan depletion and collagen matrix disruption occur during joint degeneration [115,147,148,159,178,304–307]. These structural alterations lead to higher tissue permeability (less fluid drag), lower compressive moduli, and lower tensile moduli [85,308–310]. This in turn alters the peak and duration of interstitial pressure [85,308,309], which directly alters the filling and loss dynamics of the lubrication sink. Referring back to Figure 11.2B, these structural alterations would be similar to putting a bigger drain in a smaller sink. While the sink maybe easier to fill up initially (tribological rehydration), it will drain faster due to both the larger drain and the smaller size of the reservoir. Under this framework it may be possible to establish protective and therapeutic doses of joint activity for persons with compromised joints.
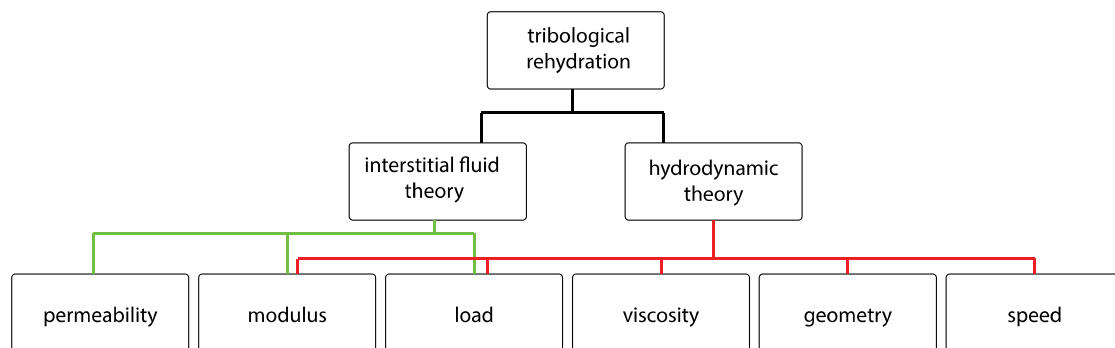
Figure 13.1   Flow chart describing the minimum number of variables to be considered in the theory of tribological rehydration.

Excessive tissue strain has been shown to upregulate catabolic responses and downregulate matrix synthesis [7,8], responses which have a direct negative impact on cartilage homeostasis. Understanding the role of tribological rehydration in mitigating daily strain in-vivo is possibly the most impactful next step. In Figure 13.2, it can be observed that static loading (standing, siting, etc.) in-vivo leads to increased strain with time [248]. However, joint activity rapidly arrests the strain response at ~5% [185]. The maintenance of strain demonstrates the retention of tissue hydration and function and thus it appears that joint activity plays a critical role in maintaining joint health. It is also worth noting that joint activity is capable of not only maintaining but also restoring hydration [80,298,300,311], demonstrating that joint activity doesn't simply arrest fluid exudation but rather drives fluid back into cartilage to replace what was previously lost, see Figure 11.4.

The extent to which tribological rehydration participates in active joint recovery remains an outstanding question. Recovery during joint activity is supported by at least one other recovery mechanism — osmotic swelling. Osmotic swelling in cartilage is induced by the electro-chemical gradient between the bath and the tissue. Following loading and fluid exudation, osmotic stress pulls fluid back into cartilage. However, osmotic forces can only overcome exudation forces once the cartilage has been unloaded; the novel aspect of tribological rehydration is that it doesn't require unloading. Furthermore, tribological rehydration (in theory) shouldn't depend on osmotic pressure.
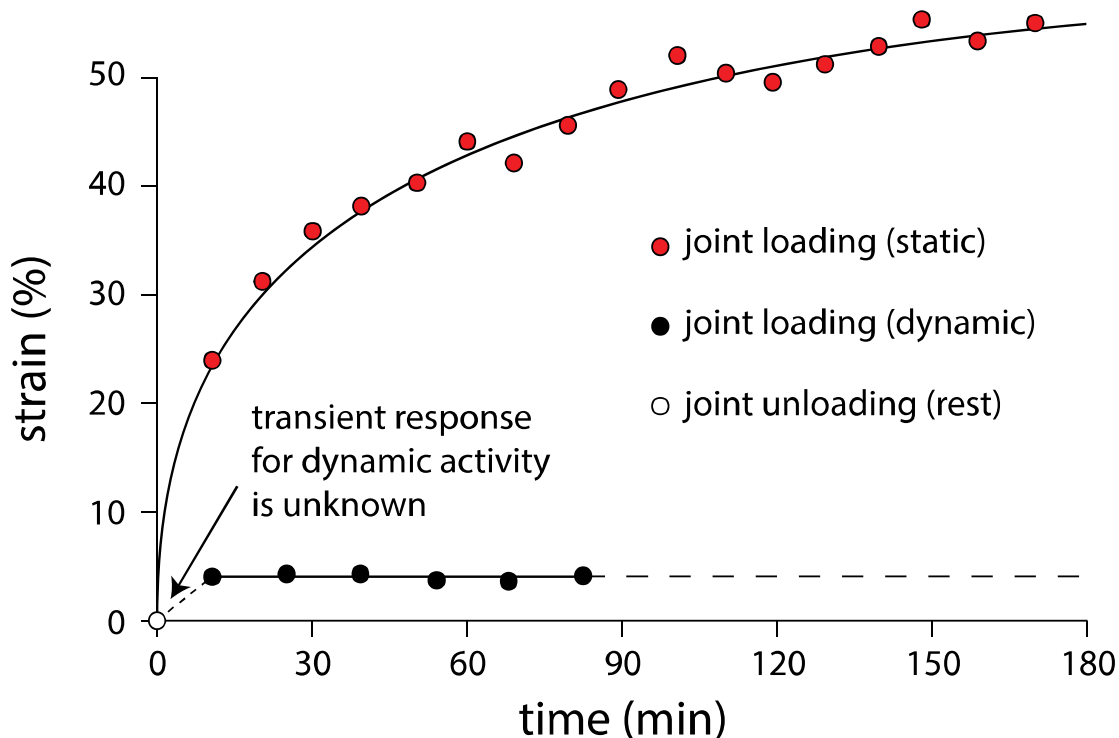
Figure 13.2 In-vivo cartilage strain versus time during static loading [248] and dynamic activity (knee bends) [185]. Data were digitized and replotted [185,248].

13.1 Major Contributions to Science

This dissertation makes several major contributions to science with a specific emphasis on cartilage hydration, mechanics, and lubrication.

1. An analytical Hertzian biphasic model was developed to quickly, easily, and reliably extract the material and functional properties of cartilage contacts. With this model users can predict contact stresses during sliding and design experiments to achieve target contact stresses.

2. The Hertzian biphasic model was applied to a large population of bovine stifle cartilage to demonstrate model utility and the spatial variation in material and tribological properties.

3. It was experimentally demonstrated that hydrodynamic forces do exist in cartilage contacts. This was demonstrated by eliminating the permeable interface of articular cartilage with a polymer film. While this experiment supports the role of hydrodynamics in cartilage contacts, it does not support the development of hydrodynamic fluid films.

4. While the roles of speed and sample geometry on friction have been known for some time, the mechanism responsible for this relationship has been typically associated with the development of a fluid film. Here it was demonstrated that friction reductions correspond to reductions in compression and thus a rehydration of the tissue. This phenomenon was termed tribological rehydration.

5. A detailed investigation into the role of the mechanical environment (speed, load, contact geometry, and viscosity) demonstrated consistency with the hypothesis that hydrodynamic forces are at least partially responsible for tribological rehydration.

6. The results of this dissertation provide a fundamental framework to begin modeling the phenomenon of tribological rehydration.

7. Due to the transient nature of the friction and compression recovery, the lack of film formation and collapse dynamics, and the magnitude of thickness recovery, it is unlikely that a full fluid film was formed. While the development of fluid films solves the friction and wear problem of many man-made bearing systems, cartilage requires both tribological functionality and fluid transport. The movement of fluid within cartilage supports nutrient and waste transport, growth, remodeling, biochemical equilibrium, stress shielding, and lubrication.

Chapter 14

CLOSING REMARKS

In summary, the first half of this dissertation details the development, validation, and application of an analytical contact mechanics model for studying biphasic materials undergoing Hertzian contact. In the second half of this dissertation, a novel fluid recovery phenomenon termed tribological rehydration was discovered. Tribological rehydration is defined as sliding induced fluid recovery and appears to have hydrodynamic origins. The exact nature of how hydrodynamic and interstitial pressure fields interact has yet to be fully elucidated. Furthermore, much has yet to be understood about the physiological significance of tribological rehydration compared to that of free swelling and/or mechanical pumping. At the very least, the discovery of tribological rehydration offers a new and exciting path forward in the field of cartilage mechanics, fluid transport for tissue engineering, and joint disease.

REFERENCES

[1]   C.W. McCutchen, The frictional properties of animal joints, Wear. 5 (1962) 1–17.

[2]   M.J. Elders, The increasing impact of arthritis on public health, J. Rheumatol. 27 (2000) 6–8.

[3]   J.W.J. Bijlsma, F. Berenbaum, F.P.J.G. Lafeber, Osteoarthritis: An update with relevance for clinical practice, Lancet. 377 (2011) 2115–2126. doi:10.1016/S0140-6736(11)60243-2.

[4]   V.C. Mow, W.M. Lai, Recent Developments in Synovial Joint Biomechanics, Siam Rev. 22 (1980) 275–317. doi:Doi 10.1137/1022056.

[5]   R. Altman, S. Lim, R.G. Steen, V. Dasa, Hyaluronic acid injections are associated with delay of total knee replacement surgery in patients with knee osteoarthritis: Evidence from a large U.S. health claims database, PLoS One. 10 (2015) 1–13. doi:10.1371/journal.pone.0145776.

[6]   A.C. Moore, D.L. Burris, Tribological and material properties for cartilage of and throughout the bovine stifle: support for the altered joint kinematics hypothesis of osteoarthritis, Osteoarthr. Cartil. 23 (2015) 161–169. doi:DOI 10.1016/j.joca.2014.09.021.

[7]   D.R. Carter, G.S. Beaupre, M. Wong, R.L. Smith, T.P. Andriacchi, D.J. Schurman, The mechanobiology of articular cartilage development and degeneration, Clin. Orthop. Relat. Res. (2004) S69–S77. doi:DOI 10.1097/01.blo.0000144970.05107.7e.

[8]   T.P. Andriacchi, A. Mundermann, R.L. Smith, E.J. Alexander, C.O. Dyrby, S. Koo, A framework for the in vivo pathomechanics of osteoarthritis at the knee, Ann. Biomed. Eng. 32 (2004) 447–457.

[9]   M.A. David, M.K. Smith, R.N. Pilachowski, A.T. White, R.C. Lock, C. Price, Early, Focal Changes in Cartilage Cellularity and Structure Following Surgically-Induced Meniscal Destabilization in the Mouse, J. Med. Virol. (2016). doi:10.1002/jmv.23443.

[10]   J. Sanchez-Adams, H.A. Leddy, A.L. Mcnulty, C.J. O 'conor, F. Guilak, The Mechanobiology of Articular Cartilage: Bearing the Burden of Osteoarthritis, (n.d.). doi:10.1007/s11926-014-0451-6.

[11]   T. Hayami, M. Pickarski, G.A. Wesolowski, J. McLane, A. Bone, J. Destefano, G.A. Rodan, L.T. Duong, The Role of Subchondral Bone Remodeling in Osteoarthritis: Reduction of Cartilage Degeneration and Prevention of Osteophyte Formation by Alendronate in the Rat Anterior Cruciate Ligament Transection Model, Arthritis Rheum. 50 (2004) 1193–1206. doi:10.1002/art.20124.

[12]   N. Bellamy, J. Campbell, V. Robinson, T. Gee, R. Bourne, G. Wells, Viscosupplementation for the treatment of osteoarthritis of the knee, Cochrane Database Syst. Rev. (2006). doi:Artn Cd005321Doi 10.1002/14651858.Cd005321.Pub2.

[13]   G.D. Jay, B.C. Fleming, B.A. Watkins, K.A. McHugh, S.C. Anderson, L.X. Zhang, E. Teeple, K.A. Waller, K.A. Elsaid, Prevention of Cartilage Degeneration and Restoration of Chondroprotection by Lubricin Tribosupplementation in the Rat Following Anterior Cruciate Ligament Transection, Arthritis Rheum. 62 (2010) 2382–2391. doi:Doi 10.1002/Art.27550.

[14]   J.R. Steadman, W.G. Rodkey, K.K. Briggs, Microfracture technique for full-thickness chondral defects: Technique and clinical results, Op Tech Orthop. 7 (1997) 300–304. doi:10.1016/S1048-6666(97)80033-X.

[15]   E. Basad, B. Ishaque, G. Bachmann, H. Stürz, J. Steinmeyer, Matrix-induced autologous chondrocyte implantation versus microfracture in the treatment of cartilage defects of the knee: A 2-year randomised study, Knee Surgery, Sport. Traumatol. Arthrosc. 18 (2010) 519–527. doi:10.1007/s00167-009-1028-1.

[16]   G. Morgese, E. Cavalli, M. Müller, M. Zenobi-Wong, E.M. Benetti, Nanoassemblies of Tissue-Reactive, Polyoxazoline Graft-Copolymers Restore the Lubrication Properties of Degraded Cartilage, ACS Nano. (2017) acsnano.6b07847. doi:10.1021/acsnano.6b07847.

[17]   R.A.C. Siemieniuk, I.A. Harris, T. Agoritsas, R.W. Poolman, R. Brignardello-Petersen, S. Van de Velde, R. Buchbinder, M. Englund, L. Lytvyn, C. Quinlan, L. Helsingen, G. Knutsen, N.R. Olsen, H. Macdonald, L. Hailey, H.M. Wilson, A. Lydiatt, A. Kristiansen, Arthroscopic surgery for degenerative knee arthritis and meniscal tears: a clinical practice guideline, Bmj. (2017) j1982. doi:10.1136/bmj.j1982.

[18]   B. Johnstone, M. Alini, M. Cucchiarini, G.R. Dodge, D. Eglin, F. Guilak, H. Madry, A. Mata, R.L. Mauck, C.E. Semino, M.J. Stoddart, Tissue engineering for articular cartilage repair--the state of the art., Eur. Cell. Mater. 25 (2013) 248–67. http://www.ncbi.nlm.nih.gov/pubmed/23636950 (accessed November 20, 2016).

[19]   F.T. Moutos, L.E. Freed, F. Guilak, A biomimetic three-dimensional woven composite scaffold for functional tissue engineering of cartilage, Nat. Mater. 6 (2007) 162–167. doi:10.1038/nmat1822.

[20]   D. Butler, S. Goldstein, F. Guilak, Functional tissue engineering: the role of biomechanics, Ann Arbor. (n.d.). http://tribology.asmedigitalcollection.asme.org/pdfaccess.ashx?url=/data/journals/jbendy/26109/570_1.pdf (accessed February 24, 2017).

[21]   D. Dowson, Z.-M. Jin, Micro-elastohydrodynamic lubrication of synovial joints, Eng. Med. 15 (1986) 63–65.

[22]   G.A. Ateshian, The role of interstitial fluid pressurization in articular cartilage lubrication, J. Biomech. 42 (2009) 1163–1176. doi:10.1016/j.jbiomech.2009.04.040.

[23]   J. Charnley, The Lubrication of Animal Joints in Relation to Surgical Reconstruction by Arthroplasty, Ann. Rheum. Dis. 19 (1960) 10–19. doi:Doi 10.1136/Ard.19.1.10.

[24]   H. Forster, J. Fisher, The influence of loading time and lubricant on the friction of articular cartilage, Proc. Inst. Mech. Eng. Part H-Journal Eng. Med. 210 (1996) 109–119.

[25]   J. Hohe, G. Ateshian, M. Reiser, K.-H. Englmeier, F. Eckstein, Surface size, curvature analysis, and assessment of knee joint incongruity with MRI in vivo, Magn. Reson. Med. 47 (2002) 554–561. doi:10.1002/mrm.10097.

[26]   A.C. Moore, B.K. Zimmerman, X. Chen, X.L. Lu, D.L. Burris, Experimental characterization of biphasic materials using rate-controlled Hertzian indentation, Tribol. Int. 89 (2015) 2–8. doi:http://dx.doi.org/10.1016/j.triboint.2015.02.001.

[27]   A.C. Moore, J.F. DeLucca, D.L. Burris, D.M. Elliott, Quantifying cartilage contact modulus, tensile modulus, and permeability with Hertzian biphasic creep, J. Tribol. (2015).

[28]   A.C. Moore, D.L. Burris, An analytical model to predict interstitial lubrication

of cartilage in migrating contact areas, J. Biomech. 47 (2014) 148–153. doi:DOI 10.1016/j.jbiomech.2013.09.020.

[29]   V.C. Mow, G.A. Ateshian, R.L. Spilker, Biomechanics of Diarthroidal Joints - a Review of 20 Years of Progress, J. Biomech. Eng. Asme. 115 (1993) 460–467.

[30]   G.W. Greene, B. Zappone, O. Söderman, D. Topgaard, G. Rata, H. Zeng, J.N. Israelachvili, Anisotropic dynamic changes in the pore network structure, fluid diffusion and fluid flow in articular cartilage under compression, Biomaterials. 31 (n.d.) 3117–3128.

[31]   C.G. Armstrong, W.M. Lai, V.C. Mow, An Analysis of the Unconfined Compression of Articular-Cartilage, J. Biomech. Eng. Asme. 106 (1984) 165–173.

[32]   L. Dintenfass, Lubrication in Synovial Joints, Nature. 197 (1963) 496-. doi:Doi 10.1038/197496b0.

[33]   E. Shimada, G. Matsumura, Viscosity and Molecular Weight of Hyaluronic Acids, 78 (1975) 513–517.

[34]   D. V Davies, Properties of synovial fluid, Arch. Proc. Inst. Mech. Eng. Conf. Proc. 1964-1970 (Vols 178-184), Var. Titles Label. Vol. A to S. 181 (1966) 25–29. doi:10.1243/PIME_CONF_1966_181_203_02.

[35]   R.G. Budynas, J.K. Nisbett, Mechanical Engineering Design, 2011.

[36]   J.P. Paul, Approaches to Design - Force Actions Transmitted by Joints in Human Body, Proc. R. Soc. Ser. B-Biological Sci. 192 (1976) 163–172. doi:DOI 10.1098/rspb.1976.0004.

[37]   S.S. Pawaskar, Z.M. Jin, J. Fisher, Modelling of fluid support inside articular cartilage during sliding, Proc. Inst. Mech. Eng. Part J-Journal Eng. Tribol. 221 (2007) 165–174. doi:Doi 10.1243/13506501jet241.

[38]   J.C. Ihn, S.J. Kim, I.H. Park, In vitro study of contact area and pressure distribution in the human knee after partial and total meniscectomy., Int. Orthop. 17 (1993) 214–8. doi:10.1007/BF00194181.

[39]   B. Balakrishnan, R. Banerjee, Biopolymer-based hydrogels for cartilage tissue engineering, Chem. Rev. 111 (2011) 4453–4474. doi:10.1021/cr100123h.

[40]   V.C. Mow, C.C. Wang, C.T. Hung, The extracellular matrix, interstitial fluid

and ions as a mechanical signal transducer in articular cartilage, Osteoarthr. Cartil. 7 (1999) 41–58. doi:10.1053/joca.1998.0161.

[41] M.B. Albro, N.O. Chahine, R. Li, K. Yeager, C.T. Hung, G.A. Ateshian, Dynamic loading of deformable porous media can induce active solute transport, J. Biomech. 41 (2008) 3152–3157. doi:10.1016/j.jbiomech.2008.08.023.

[42] N.O. Chahine, M.B. Albro, E.G. Lima, V.I. Wei, C.R. Dubois, C.T. Hung, G.A. Ateshian, Effect of Dynamic Loading on the Transport of Solutes into Agarose Hydrogels, Biophys. J. 97 (2009) 968–975. doi:10.1016/j.bpj.2009.05.047.

[43] A. Maroudas, P. Bullough, S.A. V Swanson, M.A.R. Freeman, The permeability of articular cartilage, J. Bone Jt. Surg. 50 (1968).

[44] R.C. Evans, T.M. Quinn, Dynamic compression augments interstitial transport of a glucose-like solute in articular cartilage., Biophys. J. 91 (2006) 1541–1547. doi:10.1529/biophysj.105.080366.

[45] P.T. Williams, Effects of Running and Walking on Osteoarthritis and Hip Replacement Risk, Med. Sci. Sports Exerc. 45 (2013) 1292–1297. doi:Doi 10.1249/Mss.0b013e3182885f26.

[46] D.J. Hunter, F. Eckstein, Exercise and osteoarthritis, J. Anat. 214 (2009) 197–207. doi:DOI 10.1111/j.1469-7580.2008.01013.x.

[47] N.E. Lane, D.A. Bloch, P.D. Wood, J.F. Fries, Aging, long-distance running, and the development of musculoskeletal disability, Am. J. Med. 82 (1987) 772–780. doi:10.1016/0002-9343(87)90014-3.

[48] N.E. Lane, B. Michel, A. Bjorkengren, J. Oehlert, H. Shi, D.A. Bloch, J.F. Fries, The risk of osteoarthritis with running and aging: a 5-year longitudinal study., J. Rheumatol. 20 (1993) 461–8. http://www.ncbi.nlm.nih.gov/pubmed/8478853 (accessed June 6, 2017).

[49] P.M. Newton, V.C. Mow, T.R. Gardner, J. a Buckwalter, J.P. Albright, The Effect of Lifelong Exercise on Canine Articular Cartilage, Am. J. Sports Med. 25 (1997) 282–287. doi:10.1177/036354659702500302.

[50] E. Jones, Joint lubrication, Lancet. (n.d.). http://www.thelancet.com/journals/lancet/article/PIIS0140-6736(00)56557-X/abstract (accessed November 8, 2016).

[51] M.A. Macconaill, The function of intra-articular fibrocartilages, with special

reference to the knee and inferior radio-ulnar joints, J. Anat. 66 (1932) 210–227.

[52]   D. Dowson, Modes of Lubration in Human Joints, Proc. IMechE. 181 (1967) 45–54.

[53]   V. Wright, D. Dowson, Lubrication and Cartilage, J. Anat. 121 (1976) 107–118.

[54]   D. Dowson, V. Wright, M.D. Longfield, Human joint lubrication, Biomed. Eng. (NY). 4 (1969) 160–165.

[55]   C.W. McCutchen, Sponge-hydrostatic and weeping bearings. , Nature. 184 (1959) 1284–1285.

[56]   B.J. Hamrock, Fundamentals of Fluid Film Lubrication, 1994.

[57]   B.J. Hamrock, D. Dowson, Elastohydrodynamic Lubrication of Elliptical Contacts for Materials of Low Elastic-Modulus I - Fully Flooded Conjunction, Trans. ASME, J. Lubr. Technol. 100 (1978) 236–245. doi:429.

[58]   P.S. Walker, D. Dowson, M.D. Longfield, V. Wright, "Boosted lubrication" in synovial joints by fluid entrapment and enrichment, Ann. Rheum. Dis. 27 (1968) 512–520.

[59]   D. Dowson, A. Unsworth, V. Wright, Analysis of Boosted-Lubrication in Human Joints, J. Mech. Eng. Sci. 12 (1970) 364-.

[60]   J.S. Hou, V.C. Mow, W.M. Lai, M.H. Holmes, An analysis of the squeeze-film lubrication mechanism for articular cartilage, J. Biomech. 25 (1992) 247–259.

[61]   S.C. Sharma, S.C. Jain, D.K. Bharuka, Influence of recess shape on the performance of a capillary compensated circular thrust pad hydrostatic bearing, Tribol. Int. 35 (2002) 347–356. doi:10.1016/S0301-679X(02)00013-0.

[62]   M. Scaraggi, G. Carbone, D. Dini, Experimental evidence of micro-EHL lubrication in rough soft contacts, Tribol. Lett. 43 (2011) 169–174. doi:10.1007/s11249-011-9794-6.

[63]   N.M. Bujurke, R.B. Kudenatti, Surface roughness effects on squeeze film poroelastic bearings, Appl. Math. Comput. 174 (2006) 1181–1195. doi:10.1016/j.amc.2005.06.007.

[64]   A. Erdemir, Review of engineered tribological interfaces for improved boundary lubrication, Tribol. Int. 38 (2005) 249–256. doi:10.1016/j.triboint.2004.08.008.

[65]   S.M. Hsu, R.S. Gates, Boundary lubricating films: formation and lubrication mechanism, Tribol. Int. 38 (2005) 305–312. doi:10.1016/j.triboint.2004.08.021.

[66]   E. Rabinowicz, Friction and wear of materials, 2nd ed., 1995.

[67]   F.C. Linn, E.L. Radin, Lubrication of animal joints. III. The effect of certain chemical alterations of the cartilage and lubricant, Arthritis Rheum. 11 (1968) 674–682.

[68]   H.S. Khare, a. C. Moore, D.R. Haidar, L. Gong, J. Ye, J.F. Rabolt, D.L. Burris, Interrelated Effects of Temperature and Environment on Wear and Tribochemistry of an Ultralow Wear PTFE Composite, J. Phys. Chem. C. 119 (2015) 16518–16527. doi:10.1021/acs.jpcc.5b00947.

[69]   J. Ye, A.C. Moore, D.L. Burris, Transfer Film Tenacity: A Case Study Using Ultra-Low-Wear Alumina-PTFE, Tribol. Lett. 59 (2015) 1–11. doi:10.1007/s11249-015-0576-4.

[70]   R.I. Tanner, An Alternative Mechanism for Lubrication of Synovial Joints, Phys. Med. Biol. 11 (1966) 119-. doi:Doi 10.1088/0031-9155/11/1/312.

[71]   M. Hlavacek, J. Novak, The Role of Synovial-Fluid Filtration by Cartilage in Lubrication of Synovial Joints .3. Squeeze-Film Lubrication - Axial Symmetry under Low Loading Conditions, J. Biomech. 28 (1995) 1193–1198. doi:Doi 10.1016/0021-9290(94)00180-C.

[72]   M. Hlavacek, D. Vokoun, The influence of articular surface incongruity on lubrication and contact pressure distribution of loaded synovial joints, Proc. Inst. Mech. Eng. Part H-Journal Eng. Med. 212 (1998) 11–22. doi:Doi 10.1243/0954411981533782.

[73]   M. Hlavacek, A note on an asymptotic solution for the contact of two biphasic cartilage layers in a loaded synovial joint at rest, J. Biomech. 32 (1999) 987–991. doi:Doi 10.1016/S0021-9290(99)00082-2.

[74]   J.S. Hou, M.H. Holmes, W.M. Lai, V.C. Mow, Boundary conditions at the cartilage-synovial fluid interface for joint lubrication and theoretical verifications., J. Biomech. Eng. 111 (1989) 78–87. doi:10.1115/1.3168343.

[75]   S.M.T. Chan, C.P. Neu, G. DuRaine, K. Komvopoulos, A.H. Reddi, Atomic force microscope investigation of the boundary-lubricant layer in articular cartilage, Osteoarthr. Cartil. 18 (2010) 956–963. doi:10.1016/j.joca.2010.03.012.

[76]   E.D. Bonnevie, J.L. Puetzer, L.J. Bonassar, Enhanced boundary lubrication properties of engineered menisci by lubricin localization with insulin-like growth factor I treatment, J. Biomech. 47 (2014) 2183–2188. doi:10.1016/j.jbiomech.2013.10.028.

[77]   E.D. Bonnevie, D. Galesso, C. Secchieri, I. Cohen, L.J. Bonassar, Elastoviscous Transitions of Articular Cartilage Reveal a Mechanism of Synergy between Lubricin and Hyaluronic Acid., PLoS One. 10 (2015) e0143415. doi:10.1371/journal.pone.0143415.

[78]   E.D. Bonnevie, V.J. Baro, L.Y. Wang, D.L. Burris, In Situ Studies of Cartilage Microtribology: Roles of Speed and Contact Area, Tribol. Lett. 41 (2011) 83–95.

[79]   E.D. Bonnevie, M.L. Delco, N. Jasty, L. Bartell, L.A. Fortier, I. Cohen, L.J. Bonassar, Chondrocyte death and mitochondrial dysfunction are mediated by cartilage friction and shear strain, Osteoarthr. Cartil. 24 (2016) S46. doi:10.1016/j.joca.2016.01.107.

[80]   F.C. Linn, Lubrication of animal joints, J. Bone Jt. Surg. 49 (1967) 1079–1098.

[81]   H. Forster, J. Fisher, The influence of continuous sliding and subsequent surface wear on the friction of articular cartilage, Proc. Inst. Mech. Eng. Part H-Journal Eng. Med. 213 (1999) 329–345. doi:Doi 10.1243/0954411991535167.

[82]   S. Kienle, K. Boettcher, L. Wiegleb, J. Urban, R. Burgkart, O. Lieleg, T. Hugel, Comparison of friction and wear of articular cartilage on different length scales, J. Biomech. 48 (2015) 3052–3058. doi:10.1016/j.jbiomech.2015.07.027.

[83]   M.A. Accardi, D. Dini, P.M. Cann, Experimental and numerical investigation of the behaviour of articular cartilage under shear loading-Interstitial fluid pressurisation and lubrication mechanisms, Tribol. Int. 44 (2011) 565–578. doi:DOI 10.1016/j.triboint.2010.09.009.

[84]   M. Caligaris, G.A.A. Ateshian, Effects of sustained interstitial fluid pressurization under migrating contact area, and boundary lubrication by synovial fluid, on cartilage friction, Osteoarthr. Cartil. 16 (2008) 1220–1227. doi:10.1016/j.joca.2008.02.020.

[85]   S.H. Park, R. Krishnan, S.B. Nicoll, G.A. Ateshian, Cartilage interstitial fluid load support in unconfined compression, J. Biomech. 36 (2003) 1785–1796.

[86]   M.A. Soltz, G.A. Ateshian, A conewise linear elasticity mixture model for the analysis of tension-compression nonlinearity in articular cartilage, J. Biomech.

Eng. Asme. 122 (2000) 576–586. doi:Doi 10.1115/1.1324669.

[87]   M.A. Soltz, G.A. Ateshian, Experimental verification and theoretical prediction of cartilage interstitial fluid pressurization at an impermeable contact interface in confined compression, J. Biomech. 31 (2006) 594. doi:Doi 10.1016/S0021-9290(98)00105-5.

[88]   M.D. Longfield, D. Dowson, P.S. Walker, V. Wright, "Boosted lubrication" of human joints by fluid enrichment and entrapment, Biomed. Eng. (NY). 4 (1969) 517–522.

[89]   V.C. Mow, W.Y. Gu, F.H. Chen, Structure and Function of Articular Cartilage, in: V.C. Mow, R. Huskies (Eds.), Basic Orthop. Biomech. Mechanobiol., 2005.

[90]   J. Klein, Hydration lubrication, Friction. 1 (2013) 1–23. doi:10.1007/s40544-013-0001-7.

[91]   A.C. Dunn, W.G. Sawyer, T.E. Angelini, Gemini Interfaces in Aqueous Lubrication with Hydrogels, Tribol. Lett. 54 (2014) 59–66. doi:DOI 10.1007/s11249-014-0308-1.

[92]   A.C. Dunn, A.A. Pitenis, J.M. Uruena, K.D. Schulze, T.E. Angelini, W.G. Sawyer, Kinetics of aqueous lubrication in the hydrophilic hydrogel Gemini interface, Proc. Inst. Mech. Eng. Part H J. Eng. Med. 229 (2015) 889–894. doi:10.1177/0954411915612819.

[93]   A. Oloyede, N. d. Broom, The Generalized Consolidation of Articular Cartilage: An Investigation of Its Near-Physiological Response to Static Load, Connect. Tissue Res. 31 (1994) 75–86. doi:10.3109/03008209409005637.

[94]   M.A. Biot, Theory of Elasticity and Consolidation for a Porous Anisotropic Solid, J. Appl. Phys. 26 (1955) 182–185. doi:Doi 10.1063/1.1721956.

[95]   R. Krishnan, M. Kopacz, G.A. Ateshian, Experimental verification of the role of interstial fluid prezzurization in cartilage lubrication, J. Orthop. Res. 22 (2004) 565–570.

[96]   N.M. Bachrach, V.C. Mow, F. Guilak, Incompressibility of the solid matrix of articular cartilage under high hydrostatic pressures, J. Biomech. 31 (1998) 445–451. doi:Doi 10.1016/S0021-9290(98)00035-9.

[97]   C.C.-B. Wang, J.-M. Deng, G. a Ateshian, C.T. Hung, An automated approach for direct measurement of two-dimensional strain distributions within articular cartilage under unconfined compression., J. Biomech. Eng. 124 (2002) 557–

567. doi:10.1115/1.1503795.

[98]   C.Y. Huang, M.A. Soltz, M. Kopacz, V.C. Mow, G.A. Ateshian, Experimental verification of the roles of intrinsic matrix viscoelasticity and tension-compression nonlinearity in the biphasic response of cartilage, J. Biomech. Eng. Asme. 125 (2003) 84–93. doi:Doi 10.1115/1.1531656.

[99]   G.A. Ateshian, H.Q. Wang, A Theoretical Solution for the Frictionless Rolling-Contact of Cylindrical Biphasic Articular-Cartilage Layers, J. Biomech. 28 (1995) 1341–1355.

[100]   K. Boettcher, S. Kienle, J. Nachtsheim, R. Burgkart, T. Hugel, O. Lieleg, The structure and mechanical properties of articular cartilage are highly resilient towards transient dehydration, Acta Biomater. 29 (2016) 180–187. doi:10.1016/j.actbio.2015.09.034.

[101]   C. Tudor-Locke, C.L. Craig, Y. Aoyagi, R.C. Bell, K.A. Croteau, I. De Bourdeaudhuij, B. Ewald, A.W. Gardner, Y. Hatano, M.A. Tully, S.N. Blair, How many steps/day are enough? For older adults and special populations, Int. J. Behav. Nutr. Phys. Act. 8 (2011) 80. doi:10.1186/1479-5868-8-80.

[102]   J.P. Gleghorn, L.J. Bonassar, Lubrication mode analysis of articular cartilage using Stribeck surfaces, J. Biomech. 41 (2008) 1910–1918. doi:DOI 10.1016/j.jbiomech.2008.03.043.

[103]   M. Hlavacek, The Role of Synovial-Fluid Filtration by Cartilage in Lubrication of Synovial Joints .1. Mixture Model of Synovial-Fluid, J. Biomech. 26 (1993) 1145–1150. doi:Doi 10.1016/0021-9290(93)90062-J.

[104]   M. Hlavacek, The Role of Synovial-Fluid Filtration by Cartilage in Lubrication of Synovial Joints .2. Squeeze-Film Lubrication - Homogeneous Filtration, J. Biomech. 26 (1993) 1151–1160. doi:Doi 10.1016/0021-9290(93)90063-K.

[105]   M. Hlavacek, Squeeze-film lubrication of the human ankle joint with synovial fluid filtrated by articular cartilage with the superficial zone worn out, J. Biomech. 33 (2000) 1415–1422. doi:Doi 10.1016/S0021-9290(00)00109-3.

[106]   R.L. Spilker, P.S. Donzelli, V.C. Mow, A Transversely Isotropic Biphasic Finite-Element Model of the Meniscus, J. Biomech. 25 (1992) 1027–1045.

[107]   R.L. Spilker, J.K. Suh, V.C. Mow, A Finite-Element Analysis of the Indentation Stress-Relaxation Response of Linear Biphasic Articular-Cartilage, J. Biomech. Eng. Asme. 114 (1992) 191–201.

[108] B. Cohen, W.M. Lai, V.C. Mow, A transversely isotropic biphasic model for unconfined compression of growth plate and chondroepiphysis, J. Biomech. Eng. Asme. 120 (1998) 491–496.

[109] G.A. Ateshian, H. Wang, Rolling resistance of articular cartilage due to interstitial fluid flow, Proc. Inst. Mech. Eng. Part H-Journal Eng. Med. 211 (1997) 419–424.

[110] G.A. Ateshian, H. Wang, A theoretical solution for the frictionless rolling contact of cylindrical biphasic articular cartilage layers, J. Biomech. 28 (1995) 1341–1355. doi:10.1016/0021-9290(95)00008-6.

[111] S. Park, R. Krishnan, S.B. Nicoll, G.A. Ateshian, Cartilage interstitial fluid load support in unconfined compression, J. Biomech. 36 (2003) 1785–1796. doi:10.1016/S0021-9290(03)00231-8.

[112] M.A. Soltz, G.A. Ateshian, Experimental verification and theoretical prediction of cartilage interstitial fluid pressurization at an impermeable contact interface in confined compression, J. Biomech. 31 (1998) 927–934. doi:Doi 10.1016/S0021-9290(98)00105-5.

[113] M.A. Soltz, G.A. Ateshian, Experimental verification and theoretical prediction of cartilage interstitial fluid pressurization at an impermeable contact interface in confined compression, J. Biomech. 31 (1998) 927–934. doi:10.1016/S0021-9290(98)00105-5.

[114] R. Krishnan, M. Kopacz, G. a Ateshian, Experimental verification of the role of interstitial fluid pressurization in cartilage lubrication., J. Orthop. Res. 22 (2004) 565–570. doi:10.1016/j.orthres.2003.07.002.

[115] M. Caligaris, C.E.E. Canal, C.S.S. Ahmad, T.R.R. Gardner, G.A.A. Ateshian, Investigation of the frictional response of osteoarthritic human tibiofemoral joints and the potential beneficial tribological effect of healthy synovial fluid, Osteoarthr. Cartil. 17 (2009) 1327–1332. doi:DOI 10.1016/j.joca.2009.03.020.

[116] C.W. McCutchen, The frictional properties of animal joints, Wear. 5 (1962) 1–17. doi:10.1016/0043-1648(62)90176-X.

[117] S.S. Pawaskar, Z.M. Jin, J. Fisher, Modelling of fluid support inside articular cartilage during sliding, Proc. Inst. Mech. Eng. Part J J. Eng. Tribol. 221 (2007) 165–174. doi:10.1243/13506501JET241.

[118] W.C. Hayes, L.M. Keer, G. Herrmann, L.F. Mockros, A mathematical analysis for indentation tests of articular cartilage, J. Biomech. 5 (1972) 541–551.

doi:10.1016/0021-9290(72)90010-3.

[119] G.A. Ateshian, W.M. Lai, W.B. Zhu, V.C. Mow, An Asymptotic Solution for the Contact of 2 Biphasic Cartilage Layers, J. Biomech. 27 (1994) 1347–1360.

[120] V.C. Mow, M.C. Gibbs, W.M. Lai, W.B. Zhu, K.A. Athanasiou, Biphasic Indentation of Articular-Cartilage .2. A Numerical Algorithm and an Experimental-Study, J. Biomech. 22 (1989) 853–861.

[121] C.W. MacMinn, E.R. Dufresne, J.S. Wettlaufer, Large Deformations of a Soft Porous Material, Phys. Rev. Appl. 5 (2016) 44020. doi:10.1103/PhysRevApplied.5.044020.

[122] W.C. Bae, B.L. Schumacher, R.L. Sah, Indentation probing of human articular cartilage: Effect on chondrocyte viability, Osteoarthr. Cartil. 15 (2007) 9–18. doi:DOI 10.1016/j.joca.2006.06.007.

[123] A.C. Moore, J.F. DeLucca, D.M. Elliott, D.L. Burris, Quantifying Cartilage Contact Modulus, Tension Modulus, and Permeability With Hertzian Biphasic Creep., J. Tribol. 138 (2016) 414051–414057. doi:10.1115/1.4032917.

[124] V. Mow, X.E. Guo, Mechano-electrochemical properties of articular cartilage: Their inhomogeneities and anisotropies, Annu. Rev. Biomed. Eng. 4 (2002) 175–209. doi:DOI 10.1146/annurev.bioeng.4.110701.120309.

[125] a Maroudas, Transport of solutes through cartilage: permeability to large molecules., J. Anat. 122 (1976) 335–347.

[126] M. Wong, M. Siegrist, K. Goodwin, Cyclic tensile strain and cyclic hydrostatic pressure differentially regulate expression of hypertrophic markers in primary chondrocytes, Bone. 33 (2003) 685–693. doi:Doi 10.1016/S8756-3282(03)00242-4.

[127] M.A. Soltz, G.A. Ateshian, Interstitial fluid pressurization during confined compression cyclical loading of articular cartilage, Ann. Biomed. Eng. 28 (2000) 150–159. doi:Doi 10.1114/1.239.

[128] R. Krishnan, M. Kopacz, G.A. Ateshian, Experimental verification of the role of interstitial fluid pressurization in cartilage lubrication, J. Orthop. Res. 22 (2004) 565–570. doi:10.1016/j.orthres.2003.07.002.

[129] R. Krishnan, E.N. Mariner, G.A. Ateshian, Effect of dynamic loading on the frictional response of bovine articular cartilage, J. Biomech. 38 (2005) 1665–1673. doi:DOI 10.1016/j.jbiomech.2004.07.025.

[130] V.C. Mow, S.C. Kuei, W.M. Lai, C.G. Armstrong, Biphasic Creep and Stress-Relaxation of Articular-Cartilage in Compression - Theory and Experiments, J. Biomech. Eng. Asme. 102 (1980) 73–84.

[131] S.S. Pawaskar, J. Fisher, Z.M. Jin, Robust and General Method for Determining Surface Fluid Flow Boundary Conditions in Articular Cartilage Contact Mechanics Modeling, J. Biomech. Eng. Asme. 132 (2010).

[132] L.K. Agbezuge, H. Deresiewicz, Indentation of a Consolidating Half-Space, Isr. J. Technol. 12 (1974) 322–338.

[133] X.M. Chen, A.C. Dunn, W.G. Sawyer, M. Sarntinoranont, A biphasic model for micro-indentation of a hydrogel-based contact lens, J. Biomech. Eng. Asme. 129 (2007) 156–163. doi:Doi 10.1115/1.2472373.

[134] I.O. for Standardization, Evaluation of measurement data — Guide to the expression of uncertainty in measurement, 2008. doi:10.1373/clinchem.2003.030528.

[135] S. Ebara, R. Kelkar, L. Bigliani, Bovine glenoid cartilage is less stiff than humeral head cartilage in tension, Trans Orthop Res Soc. 19 (1994) 146.

[136] K.L. Johnson, Contact Mechanics, Cambridge University Press, UK, 1985.

[137] G.A. Ateshian, A theoretical formulation for boundary friction in articular cartilage, J. Biomech. Eng. Asme. 119 (1997) 81–86.

[138] R.A. Brand, Joint Contact Stress: A Reasonable Surrogate for Biological Processes?, Iowa Orthop. J. 25 (2005) 82–94.

[139] S. Park, K.D. Costa, G.A. Ateshian, Microscale frictional response of bovine articular cartilage from atomic force microscopy, J. Biomech. 37 (2004) 1679–1687. doi:10.1016/j.jbiomech.2004.02.017.

[140] A. Thambyah, G.R. Zhang, W. Kim, N.D. Broom, Impact induced failure of cartilage-on-bone following creep loading: A microstructural and fracture mechanics study, J. Mech. Behav. Biomed. Mater. 14 (2012) 239–247. doi:DOI 10.1016/j.jmbbm.2012.06.007.

[141] J.M. Mansour, Biomechanics of cartilage, Kinesiol. Mech. Pathomechanics Hum. Mov. (2003) 66–79.

[142] G.J. Huang, L. LeResche, C.W. Critchlow, M.D. Martin, M.T. Drangsholt, Risk factors for diagnostic subgroups of painful temporomandibular disorders

(TMD)., J. Dent. Res. 81 (2002) 284–288. doi:10.1177/154405910208100412.

[143] J. Pickard, E. Ingham, J. Egan, J. Fisher, Investigation into the effect of proteoglycan molecules on the tribological properties of cartilage joint tissues, Proc. Inst. Mech. Eng. Part H-Journal Eng. Med. 212 (1998) 177–182.

[144] C.J. Bell, E. Ingham, J. Fisher, Influence of hyaluronic acid on the time-dependent friction response of articular cartilage under different conditions, Proc. Inst. Mech. Eng. Part H-Journal Eng. Med. 220 (2006) 23–31.

[145] E. Northwood, J. Fisher, A multi-directional in vitro investigation into friction, damage and wear of innovative chondroplasty materials against articular cartilage, Clin. Biomech. 22 (2007) 834–842. doi:DOI 10.1016/j.clinbiomech.2007.03.008.

[146] S. Akizuki, V.C. Mow, F. Muller, J.C. Pita, D.S. Howell, D.H. Manicourt, Tensile Properties of Human Knee-Joint Cartilage .1. Influence of Ionic Conditions, Weight Bearing, and Fibrillation on the Tensile Modulus, J. Orthop. Res. 4 (1986) 379–392. doi:DOI 10.1002/jor.1100040401.

[147] L.A. Setton, D.M. Elliott, V.C. Mow, Altered mechanics of cartilage with osteoarthritis: human osteoarthritis and an experimental model of joint degeneration, Osteoarthr. Cartil. 7 (1999) 2–14.

[148] D.M. Elliott, F. Guilak, T.P. Vail, J.Y. Wang, L.A. Setton, Tensile properties of articular cartilage are altered by meniscectomy in a canine model of osteoarthritis, J. Orthop. Res. 17 (1999) 503–508. doi:DOI 10.1002/jor.1100170407.

[149] A.D. Pearle, R.F. Warren, S.A. Rodeo, Basic science of articular cartilage and osteoarthritis, Clin. Sports Med. 24 (2005) 1–+. doi:DOI 10.1016/j.csm.2004.08.007.

[150] V.J. Baro, E.D. Bonnevie, X. Lai, C. Price, D.L. Burris, L. Wang, Functional characterization of normal and degraded bovine meniscus: Rate-dependent indentation and friction studies, Bone. 51 (2012) 232–240.

[151] R. Krishnan, M. Caligaris, R.L.L. Mauck, C.T.T. Hung, K.D.D. Costa, G.A.A. Ateshian, Removal of the superficial zone of bovine articular cartilage does not increase its frictional coefficient, Osteoarthr. Cartil. 12 (2004) 947–955. doi:DOI 10.1016/j.joca.2004.08.009.

[152] M.L. Oyen, Poroelastic nanoindentation responses of hydrated bone, J. Mater. Res. 23 (2008) 1307–1314. doi:Doi 10.1557/Jmr.2008.0156.

[153] A.F. Mak, W.M. Lai, V.C. Mow, Biphasic Indentation of Articular-Cartilage .1. Theoretical-Analysis, J. Biomech. 20 (1987) 703–714.

[154] V.C. Mow, S.C. Kuei, W.M. Lai, C.G. Armstrong, Biphasic Creep and Stress Relaxation of Articular Cartilage in Compression: Theory and Experiments, J. Biomech. Eng. 102 (1980) 73. doi:10.1115/1.3138202.

[155] M. Stevanovic, M.M. Yovanovich, J.R. Culham, Modeling Contact between Rigid Sphere and Elastic Layer Bonded to Rigid Substrate, IEEE Trans. COMPONENTS Packag. Technol. 24 (2001) 207–212.

[156] W.T. Chen, P.A. Engel, Impact and contact stress analysis in multilayer media, Int. J. Solids Struct. 8 (1972) 1257–1281. doi:http://dx.doi.org/10.1016/0020-7683(72)90079-0.

[157] X.L. Lu, D.D. Sun, X.E.E. Al Guo, Indentation Determined Mechanoelectrical Properties And Fixed Charged Density of Articular Cartilage, Ann Biomed Eng. 32 (2004) 370–379.

[158] S.A. Maas, B.J. Ellis, G.A. Ateshian, J.A. Weiss, FEBio: Finite Elements for Biomechanics, J. Biomech. Eng. Asme. 134 (2012). doi:Artn 011005Doi 10.1115/1.4005694.

[159] I.M.P. Basalo, R.L. Mauck, T.A.N. Kelly, S.B. Nicoll, F.H. Chen, C.T. Hung, G.A. Ateshian, Cartilage interstitial fluid load support in unconfined compression following enzymatic digestion, J. Biomech. Eng. Asme. 126 (2004) 779–786. doi:Doi 10.1115/1.1824123.

[160] M.A. Sweigart, C.F. Zhu, D.M. Burt, P.D. deHoll, C.M. Agrawal, T.O. Clanton, K.A. Athanasiou, Intraspecies and interspecies comparison of the compressive properties of the medial meniscus, Ann. Biomed. Eng. 32 (2004) 1569–1579.

[161] A.K. Williamson, A.C. Chen, R.L. Sah, Compressive properties and function-composition relationships of developing bovine articular cartilage, J. Orthop. Res. 19 (2001) 1113–1121.

[162] S.S. Chen, Y.H. Falcovitz, R. Schneiderman, A. Maroudas, R.L. Sah, Depth-dependent compressive properties of normal aged human femoral head articular cartilage: Relationship to fixed charge density, Osteoarthr. Cartil. 9 (2001) 561–569. doi:10.1053/joca.2001.0424.

[163] G.E. Kempson, S.A. V Swanson, C.J. Spivey, M.A.R. Freeman, Patterns of Cartilage Stiffness on Normal and Degenerate Human Femoral Heads, J.

Biomech. 4 (1971) 597-. doi:Doi 10.1016/0021-9290(71)90049-2.

[164] G.E. Kempson, M.A.R. Freeman, S.A. V Swanson, Determination of a Creep Modulus for Articular Cartilage from Indentation Tests on Human Femoral Head, J. Biomech. 4 (1971) 239-. doi:Doi 10.1016/0021-9290(71)90030-3.

[165] J.R. Parsons, J. Black, Viscoelastic Shear Behavior of Normal Rabbit Articular-Cartilage, J. Biomech. 10 (1977) 21–29. doi:Doi 10.1016/0021-9290(77)90026-4.

[166] S.M. Elmore, P. Carmeci, G. Norris, L. Sokoloff, Nature of Imperfect Elasticity of Articular Cartilage, J. Appl. Physiol. 18 (1963) 393-.

[167] R.Y. Hori, L.F. Mockros, Indentation Tests of Human Articular-Cartilage, J. Biomech. 9 (1976) 259–268. doi:Doi 10.1016/0021-9290(76)90012-9.

[168] J.M. Coletti, S.L.Y. Woo, W.H. Akeson, Comparison of Physical Behavior of Normal Articular Cartilage and Arthroplasty Surface, J. Bone Jt. Surgery-American Vol. A 54 (1972) 147-.

[169] L. Sokoloff, Elasticity of Aging Cartilage, Fed. Proc. 25 (1966) 1089-.

[170] W.C. Hayes, G. Herrmann, L.F. Mockros, L.M. Keer, Mathematical-Analysis for Indentation Tests of Articular-Cartilage, J. Biomech. 5 (1972) 541-. doi:Doi 10.1016/0021-9290(72)90010-3.

[171] C.G. Armstrong, W.M. Lai, V.C. Mow, An Analysis of the Unconfined Compression of Articular Cartilage, J. Biomech. Eng. 106 (1984) 165. doi:10.1115/1.3138475.

[172] E.P. Chan, Y.H. Hu, P.M. Johnson, Z.G. Suo, C.M. Stafford, Spherical indentation testing of poroelastic relaxations in thin hydrogel layers, Soft Matter. 8 (2012) 1492–1498. doi:Doi 10.1039/C1sm06514a.

[173] G.J. Miller, E.F. Morgan, Use of microindentation to characterize the mechanical properties of articular cartilage: comparison of biphasic material properties across length scales, Osteoarthr. Cartil. 18 (2010) 1051–1057. doi:DOI 10.1016/j.joca.2010.04.007.

[174] H. Hertz, On the contact of Elastic Solids, J. Für Die Reine Und Angew. Math. (1881).

[175] F.F. Ling, A New Model of Articular Cartilage in Human Joints, J. Lubr. Technol. 96 (1974) 449. doi:10.1115/1.3452000.

[176] M.A. Soltz, G.A. Ateshian, A Conewise Linear Elasticity Nonlinearity in Articular Cartilage, Bioengineering. 122 (2000).

[177] C.-Y. Huang, V.C. Mow, G.A. Ateshian, The Role of Flow-Independent Viscoelasticity in the Biphasic Tensile and Compressive Responses of Articular Cartilage, J. Biomech. Eng. 123 (2001) 410. doi:10.1115/1.1392316.

[178] L.A. Setton, V.C. Mow, F.J. Muller, J.C. Pita, D.S. Howell, Mechanical-Properties of Canine Articular-Cartilage Are Significantly Altered Following Transection of the Anterior Cruciate Ligament, J. Orthop. Res. 12 (1994) 451–463. doi:DOI 10.1002/jor.1100120402.

[179] W.M. Lai, V.C. Mow, Drag-Induced Compression of Articular-Cartilage during a Permeation Experiment, Biorheology. 17 (1980) 111–123.

[180] M.H. Holmes, V.C. Mow, The Nonlinear Characteristics of Soft Gels and Hydrated Connective Tissues in Ultrafiltration, J. Biomech. 23 (1990) 1145–1156. doi:Doi 10.1016/0021-9290(90)90007-P.

[181] ISO, Guide to the Expression of Uncertainty in Measurement (Corrected and Reprinted in 1995), 1993.

[182] S. Maas, D. Rawlins, J. Weiss, G. Ateshian, FEBio theory manual, Musculoskelet. Res. Lab. Univ. Utah, Salt Lake City, UT. (2011).

[183] G.A. Ateshian, V. Rajan, N.O. Chahine, C.E. Canal, C.T. Hung, Modeling the matrix of articular cartilage using a continuous fiber angular distribution predicts many observed phenomena, J. Biomech. Eng. 131 (2009) 61003.

[184] A.C. Chen, W.C. Bae, R.M. Schinagl, R.L. Sah, Depth- and strain-dependent mechanical and electromechanical properties of full-thickness bovine articular cartilage in confined compression, J. Biomech. 34 (2001) 1–12. doi:Doi 10.1016/S0021-9290(00)00170-6.

[185] F. Eckstein, M. Tieschky, S. Faber, K.-H.H. Englmeier, M. Reiser, Functional analysis of articular cartilage deformation, recovery, and fluid flow following dynamic exercise in vivo, Anat. Embryol. (Berl). 200 (1999) 419–424. doi:10.1007/s004290050291.

[186] C.-Y. Huang, M.A. Soltz, M. Kopacz, V.C. Mow, G.A. Ateshian, Experimental Verification of the Roles of Intrinsic Matrix Viscoelasticity and Tension-Compression Nonlinearity in the Biphasic Response of Cartilage, J. Biomech. Eng. 125 (2003) 84. doi:10.1115/1.1531656.

[187] J.S. Jurvelin, M.D. Buschmann, E.B. Hunziker, Optical and mechanical determination of poisson's ratio of adult bovine humeral articular cartilage, J. Biomech. 30 (1997) 235–241. doi:10.1016/S0021-9290(96)00133-9.

[188] C.C.-B. Wang, N.O. Chahine, C.T. Hung, G.A. Ateshian, Optical determination of anisotropic material properties of bovine articular cartilage in compression, J. Biomech. 36 (2003) 339–353. doi:10.1016/S0021-9290(02)00417-7.

[189] L.S. Lohmander, P.M. Englund, L.L. Dahl, E.M. Roos, The long-term consequence of anterior cruciate ligament and meniscus injuries - Osteoarthritis, Am. J. Sports Med. 35 (2007) 1756–1769. doi:Doi 10.1177/0363546507307396.

[190] A.M. Bendele, Animal models of osteoarthritis, J Musculoskel Neuron Interact. 4 (2001) 363–376.

[191] S. Koo, J.H. Rylander, T.P. Andriacchi, Knee joint kinematics during walking influences the spatial cartilage thickness distribution in the knee, J. Biomech. 44 (2011) 1405–1409. doi:DOI 10.1016/j.jbiomech.2010.11.020.

[192] J.L. Coleman, M.R. Widmyer, H.A. Leddy, G.M. Utturkar, C.E. Spritzer, C.T. Moorman, F. Guilak, L.E. DeFrate, Diurnal variations in articular cartilage thickness and strain in the human knee, J. Biomech. 46 (2013) 541–547. doi:DOI 10.1016/j.jbiomech.2012.09.013.

[193] G. Li, S.E. Park, L.E. DeFrate, M.E. Schutzer, L.N. Ji, T.J. Gill, H.E. Rubash, The cartilage thickness distribution in the tibiofemoral joint and its correlation with cartilage-to-cartilage contact, Clin. Biomech. 20 (2005) 736–744. doi:DOI 10.1016/j.clinbiomech.2005.04.001.

[194] H. Sittek, F. Eckstein, A. Gavazzeni, S. Milz, B. Kiefer, E. Schulte, M. Reiser, Assessment of normal patellar cartilage volume and thickness using MRI: an analysis of currently available pulse sequences, Skeletal Radiol. 25 (1996) 55–62. doi:10.1007/s002560050032.

[195] L. Shi, D.B. Brunski, V.I. Sikavitsas, M.B. Johnson, A. Striolo, Friction coefficients for mechanically damaged bovine articular cartilage, Biotechnol. Bioeng. 109 (2012) 1769–1778. doi:Doi 10.1002/Bit.24435.

[196] J. Li, T.D. Stewart, Z. Jin, R.K. Wilcox, J. Fisher, The influence of size, clearance, cartilage properties, thickness and hemiarthroplasty on the contact mechanics of the hip joint with biphasic layers, J. Biomech. 46 (2013) 1641–1647. doi:10.1016/j.jbiomech.2013.04.009.

[197] S. Park, R. Krishnan, S.B. Nicoll, G.A. Ateshian, Cartilage interstitial fluid load support in unconfined compression Following Enzymatic Digestion, J. Biomech. 36 (2003) 1785–1796. doi:10.1016/S0021-9290(03)00231-8.

[198] E.D. Bonnevie, V.J. Baro, L. Wang, D.L. Burris, Fluid load support during localized indentation of cartilage with a spherical probe, J. Biomech. 45 (2012) 1036–1041. doi:DOI 10.1016/j.jbiomech.2011.12.019.

[199] D.L. Burris, W.G. Sawyer, Addressing Practical Challenges of Low Friction Coefficient Measurements, Tribol. Lett. 35 (2009) 17–23. doi:DOI 10.1007/s11249-009-9438-2.

[200] J. Ranstam, Repeated measurements, bilateral observations and pseudoreplicates, why does it matter?, Osteoarthr. Cartil. 20 (2012) 473–475. doi:DOI 10.1016/j.joca.2012.02.011.

[201] D.H. Cortes, J.T. Nathan, J.F. DeLucca, E.M. Dawn, Elastic, permeability and swelling properties of human intervertebral disc tissues: A benchmark for tissue engineering, J. Biomech. 47 (n.d.) 2088–2094.

[202] K.A. Athanasiou, M.P. Rosenwasser, J.A. Buckwalter, T.I. Malinin, V.C. Mow, Interspecies Comparisons of Insitu Intrinsic Mechanical-Properties of Distal Femoral Cartilage, J. Orthop. Res. 9 (1991) 330–340.

[203] O.D. Schipplein, T.P. Andriacchi, Interaction between Active and Passive Knee Stabilizers during Levelwalking, J. Orthop. Res. 9 (1991) 113–119. doi:DOI 10.1002/jor.1100090114.

[204] G.E. Kempson, Relationship between the Tensile Properties of Articular-Cartilage from the Human Knee and Age, Ann. Rheum. Dis. 41 (1982) 508–511. doi:Doi 10.1136/Ard.41.5.508.

[205] M.M. Temple, W.C. Bae, M.Q. Chen, M. Lotz, D. Amiel, R.D. Coufts, R.L. Sah, Age- and site-associated biomechanical weakening of human articular cartilage of the femoral condyle, Osteoarthr. Cartil. 15 (2007) 1042–1052. doi:DOI 10.1016/j.joca.2007.03.005.

[206] V.C. Mow, R. Huiskes, Basic orthopaedic biomechanics & mechano-biology, Lippincott Williams & Wilkins, 2005. https://books.google.com/books/about/Basic_Orthopaedic_Biomechanics_Mechano_b.html?id=_NA-qHOeYLQC (accessed April 20, 2017).

[207] G.D. Jay, J.R. Torres, D.K. Rhee, H.J. Helminen, M.M. Hytinnen, C.J. Cha, K. Elsaid, K.S. Kim, Y.J. Cui, M.L. Warman, Association between friction and

wear in diarthrodial joints lacking lubricin, Arthritis Rheum. 56 (2007) 3662–3669. doi:Doi 10.1002/Art.22974.

[208] K.A. Waller, L.X. Zhang, K.A. Elsaid, B.C. Fleming, M.L. Warman, G.D. Jay, Role of lubricin and boundary lubrication in the prevention of chondrocyte apoptosis., Proc. Natl. Acad. Sci. U. S. A. 110 (2013) 5852–7. doi:10.1073/pnas.1219289110.

[209] T. Little, M. Freeman, S.A. V Swanson, Experience on friction in the human hip joint, Lubr. Wear Joints. (1969) 110–114.

[210] D. Dowson, Paper 12: Modes of Lubrication in Human Joints, Proc. Inst. Mech. Eng. 41 (1966) 217–24. doi:10.1243/PIME.

[211] Z.M. Jin, D. Dowson, J. Fisher, The effect of porosity of articular cartilage on the lubrication of a normal human hip joint, Proc. Inst. Mech. Eng. Part H J. Eng. Med. 206 (1992) 117–124.

[212] M. Hlavacek, The Role of Synovial-Fluid Filtration by Cartilage in Lubrication of Synovial Joints .4. Squeeze-Film Lubrication - the Central Film Thickness for Normal and Inflammatory Synovial-Fluids for Axial Symmetry under High Loading Conditions, J. Biomech. 28 (1995) 1199–1205. doi:Doi 10.1016/0021-9290(94)00178-7.

[213] M. Hlavacek, Lubrication of the human ankle joint in walking with the synovial fluid filtrated by the cartilage with the surface zone worn out: steady pure sliding motion, J. Biomech. 32 (1999) 1059–1069. doi:Doi 10.1016/S0021-9290(99)00095-0.

[214] P.A. Smyth, R.E. Rifkin, R.L. Jackson, R.R. Hanson, A Surface Roughness Comparison of Cartilage in Different Types of Synovial Joints, J. Biomech. Eng. Asme. 134 (2012). doi:Artn 021006Doi 10.1115/1.4005934.

[215] A.C. Moore, D.L. Burris, Tribological rehydration of cartilage and its potential role in preserving joint health, Osteoarthr. Cartil. 25 (2016) 99–107. doi:10.1016/j.joca.2016.09.018.

[216] C. Myant, M. Fowell, H.A. Spikes, J.R. Stokes, L. Chang, An Investigation of Lubricant Film Thickness in Sliding Compliant Contacts, Tribol. Trans. 53 (2010) 684–694. doi:10.1080/10402001003693109.

[217] C. Myant, T. Reddyhoff, H.A. Spikes, Laser-induced fluorescence for film thickness mapping in pure sliding lubricated, compliant, contacts, Tribol. Int. 43 (2010) 1960–1969. doi:10.1016/j.triboint.2010.03.013.

[218] R. Dwyer, B. Drinkwater, C. Donohoe, The measurement of lubricant-film thickness using ultrasound, (2003). doi:10.1098/.

[219] E. Crinon, J.. Evans, The effect of surface roughness, oxide film thickness and interfacial sliding on the electrical contact resistance of aluminium, Mater. Sci. Eng. A. 242 (1998) 121–128. doi:10.1016/S0921-5093(97)00508-X.

[220] O. Reynolds, On the Theory of Lubrication and Its Application to Mr. Beauchamp Tower's Experiments, Including an Experimental Determination of the Viscosity of Olive Oil, Philos. Trans. R. Soc. London. 177 (1886) 157–234. doi:10.2307/109480.

[221] B.J. Hamrock, D. Dowson, Isothermal Elastohydrodynamic Lubrication of Point Contacts .1. Theoretical Formulation, J. Lubr. Technol. Asme. 98 (1976) 223–229.

[222] G. Neale, W. Nader, Practical significance of brinkman's extension of darcy's law: Coupled parallel flows within a channel and a bounding porous medium, Can. J. Chem. Eng. 52 (1974) 475–478. doi:10.1002/cjce.5450520407.

[223] G.I. Taylor, A model for the boundary condition of a porous material. Part 1, 49 (1971) 319–326. doi:10.1017/S0022112071002088.

[224] N.S. Beavers, E.L.D. Joseph, Boundary conditions at a naturally permeable wall, J . Fluid Mech. 30 (1967) 197–207. doi:10.1017/S0022112067001375.

[225] B.J. Hamrock, S.R. Schmid, B.O. Jacobson, Fundamentals of Fluid Film Lubrication, 2004.

[226] E.A. Balazs, The Physical Properties of Synovial Fluid and the Special Role of Hyaluronic Acid, Disord. Knee. (1974) 63–75.

[227] E. a Balazs, D. Watson, I.F. Duff, S. Roseman, Hyaluronic acid in synovial fluid. I. Molecular parameters of hyaluronic acid in normal and arthritis human fluids., Arthritis Rheum. 10 (1967) 357–376. doi:DOI 10.1002/art.1780100407.

[228] J.B. Segur, H.E. Oberstar, Viscosity of Glycerol and Its Aqueous Solutions, Ind. Eng. Chem. 43 (1951) 2117–2120. doi:10.1021/ie50501a040.

[229] M. Hlavacek, The thixotropic effect of the synovial fluid in squeeze-film lubrication of the human hip joint, Biorheology. 38 (2001) 319–334.

[230] G.R. Higginson, R. Norman, A model investigation of squeeze-film lubrication in animal joints., Phys. Med. Biol. 19 (1974) 785–792. doi:10.1088/0031-

9155/19/6/001.

[231] B.J. Hamrock, D. Dowson, Elastohydrodynamic Lubrication of Elliptical Contacts for Materials of Low Elastic Modulus I—Fully Flooded Conjunction, J. Lubr. Technol. 100 (1978) 236. doi:10.1115/1.3453152.

[232] J. de Vicente, J.R. Stokes, H.A. Spikes, The frictional properties of Newtonian fluids in rolling - Sliding soft-EHL contact, Tribol. Lett. 20 (2005) 273–286. doi:10.1007/s11249-005-9067-3.

[233] C.J. Hooke, The elastohydrodynamic lubrication of elliptical point contacts operating in the isoviscous region, Arch. Proc. Inst. Mech. Eng. Part J J. Eng. Tribol. 1994-1996 (Vols 208-210). 209 (1995) 225–234. doi:10.1243/PIME_PROC_1995_209_433_02.

[234] S. Lee, N.D. Spencer, Aqueous lubrication of polymers: Influence of surface modification, Tribol. Int. 38 (2005) 922–930. doi:10.1016/j.triboint.2005.07.017.

[235] J.M. Urueña, A.A. Pitenis, R.M. Nixon, K.D. Schulze, T.E. Angelini, W. Gregory Sawyer, Mesh Size Control of Polymer Fluctuation Lubrication in Gemini Hydrogels, Biotribology. 1 (2015) 24–29. doi:10.1016/j.biotri.2015.03.001.

[236] P.A. Smyth, I. Green, Analysis of Coupled Poroviscoelasticity and Hydrodynamic Lubrication, Tribol. Lett. 65 (2017) 1–10. doi:10.1007/s11249-016-0787-3.

[237] B.L. Wong, W.C. Bae, J. Chun, K.R. Gratz, M. Lotz, R.L. Sah, Biomechanics of cartilage articulation: Effects of lubrication and degeneration on shear deformation, Arthritis Rheum. 58 (2008) 2065–2074. doi:10.1002/art.23548.

[238] A. Gkousioudi, D.S. Tzeranis, G.P. Kanakaris, M. Saloufas, L.G. Alexopoulos, Quantifying Cartilage Biomechanical Properties Using a Linearized Frequency-Domain Method, Ann. Biomed. Eng. (2017). doi:10.1007/s10439-017-1861-1.

[239] A.E. Peters, E.J. Comerford, S. Macaulay, K.T. Bates, R. Akhtar, Micromechanical properties of canine femoral articular cartilage following multiple freeze-thaw cycles, J. Mech. Behav. Biomed. Mater. 71 (2017) 114–121. doi:10.1016/j.jmbbm.2017.03.006.

[240] J. Kosel, I. Giouroudi, C. Scheffer, E. Dillon, P. Erasmus, Anatomical Study of the Radius and Center of Curvature of the Distal Femoral Condyle, J. Biomech. Eng. Asme. 132 (2010). doi:Artn 091002Doi 10.1115/1.4002061.

[241] Z.A. Cohen, D.M. McCarthy, S.D. Kwak, P. Legrand, F. Fogarasi, E.J. Ciaccio, G.A. Ateshian, Knee cartilage topography, thickness, and contact areas from MRI: In- vitro calibration and in-vivo measurements, Osteoarthr. Cartil. 7 (1999) 95–109. doi:10.1053/joca.1998.0165.

[242] K.D. Schulze, A.I. Bennett, S.L. Marshall, K.G. Rowe, A.C. Dunn, Real area of contact in a soft transparent interface by particle exclusion microscopy, ASME J. Tribol. in press (2016) 1–6. doi:10.1115/1.4032822.

[243] A. Hagiwara, T. Takahashi, K. Sawai, A. Iwamoto, M. Shimotsuma, C. Yoneyama, K. Seiki, M. Itoh, T. Sasabe, M. Lee, Lymph nodal vital staining with newer carbon particle suspensions compared with india ink: experimental and clinical observations, 25 (1992) 84–89.

[244] F. Eckstein, M. Reiser, K.H. Englmeier, R. Putz, In vivo morphometry and functional analysis of human articular cartilage with quantitative magnetic resonance imaging - from image to data, from data to theory, Anat. Embryol. (Berl). 203 (2001) 147–173. doi:DOI 10.1007/s004290000154.

[245] D.L. Burris, A.C. Moore, Elucidating the role of hydrodynamics in cartilage and joint lubrication, Biotribology. (n.d.).

[246] F. Eckstein, B. Lemberger, T. Stammberger, K.. H. Englmeier, M. Reiser, Patellar cartilage deformation in vivo after static versus dynamic loading, J. Biomech. 33 (2000) 819–825. doi:10.1016/S0021-9290(00)00034-8.

[247] D.J. Hunter, F. Eckstein, Exercise and osteoarthritis, J. Anat. 214 (2009) 197–207. doi:10.1111/j.1469-7580.2008.01013.x.

[248] C. Herberhold, S. Faber, T. Stammberger, M. Steinlechner, R. Putz, K.H.H. Englmeier, M. Reiser, F. Eckstein, In situ measurement of articular cartilage deformation in intact femoropatellar joints under static loading, J. Biomech. 32 (1999) 1287–1295. doi:10.1016/S0021-9290(99)00130-X.

[249] F. Eckstein, M. Hudelmaier, R. Putz, The effects of exercise on human articular cartilage, J. Anat. 208 (2006) 491–512. doi:10.1111/j.1469-7580.2006.00546.x.

[250] N. Sakai, Y. Hagihara, T. Furusawa, N. Hosoda, Y. Sawae, T. Murakami, Analysis of biphasic lubrication of articular cartilage loaded by cylindrical indenter, Tribol. Int. 46 (2012) 225–236. doi:10.1016/j.triboint.2011.03.016.

[251] J.P. Gleghorn, L.J. Bonassar, Lubrication mode analysis of articular cartilage using Stribeck surfaces, J. Biomech. 41 (2008) 1910–1918. doi:10.1016/j.jbiomech.2008.03.043.

[252] F.C. Linn, Lubrication of animal joints: II the mechanism, J. Biomech. 1 (1968) 193–205. doi:10.1115/1.3554927.

[253] T. Beauchamp, First Report on Friction Experiments, (1883). http://www.publications.parliament.uk/pa/cm199899/cmselect/cmhealth/074/07 407.htm.

[254] A.J. Grodzinsky, V. Roth, E. Myers, W.D. Grossman, V.C. Mow, The significance of electromechanical and osmotic forces in the nonequilibrium swelling behavior of articular cartilage in tension, J. Biomech. Eng. 103 (1981) 221–231. doi:10.1115/1.3138284.

[255] G.A. Ateshian, M.A. Soltz, R.L. Mauck, I.M. Basalo, C.T. Hung, W.M. Lai, The Role of Osmotic Pressure and Tension-Compression Nonlinearity in the Frictional Response of Articular Cartilage, Transp. Porous Media. 50 (2003) 5–33.

[256] M.A. Sidebottom, B.A. Krick, Transducer misalignment and contact pressure distributions as error sources in friction measurement on small-diameter pin-on-disk experiments, Tribol. Lett. 58 (2015) 1–6. doi:10.1007/s11249-015-0500-y.

[257] A.H. Lee, S.E. Szczesny, M.H. Santare, D.M. Elliott, Investigating Mechanisms of Tendon Damage by Measuring Multi-scale Recovery Following Tensile Loading, Acta Biomater. (2017). doi:10.1016/j.actbio.2017.04.011.

[258] J.M. Antonacci, T.A. Schmidt, L.A. Serventi, M.Z. Cai, Y.L. Shu, B.L. Schumacher, C.W. McIlwraith, R.L. Sah, Effects of equine joint injury on boundary lubrication of articular cartilage by synovial fluid: Role of hyaluronan, Arthritis Rheum. 64 (2012) 2917–2926. doi:10.1002/art.34520.

[259] K.L. Harris, A.A. Pitenis, W.G. Sawyer, B.A. Krick, G.S. Blackman, D.J. Kasprzak, C.P. Junk, PTFE Tribology and the Role of Mechanochemistry in the Development of Protective Surface Films, Macromolecules. 48 (2015) 3739–3745. doi:10.1021/acs.macromol.5b00452.

[260] A.A. Pitenis, K.L. Harris, C.P. Junk, G.S. Blackman, W.G. Sawyer, B.A. Krick, Ultralow Wear PTFE and Alumina Composites: It is All About Tribochemistry, Tribol. Lett. 57 (2015) 4. doi:10.1007/s11249-014-0445-6.

[261] J. Ye, H.S. Khare, D.L. Burris, Transfer film evolution and its role in promoting ultra-low wear of a PTFE nanocomposite, Wear. 297 (2013) 1095–1102.

[262] B. Gould, A. Greco, Investigating the Process of White Etching Crack Initiation in Bearing Steel, Tribol. Lett. 62 (2016) 26. doi:10.1007/s11249-016-0673-z.

[263] B. Gould, A. Greco, The Influence of Sliding and Contact Severity on the Generation of White Etching Cracks, Tribol. Lett. 60 (2015) 29. doi:10.1007/s11249-015-0602-6.

[264] B.T. Graham, A.C. Moore, D.L. Burris, C. Price, Sliding enhances fluid and solute transport into buried articular cartilage contacts, Osteoarthr. Cartil. (n.d.).

[265] V.C. Mow, W.M. Lai, Recent Developments in Synovial Joint Biomechanics, SIAM Rev. 22 (1980) 275–317. doi:10.1137/1022056.

[266] A.C. Moore, D.L. Burris, Methods of isolating the effects of hydration on cartilage lubrication, Tribol. - Mater. Surfaces Interfaces. (n.d.).

[267] J. Kosel, I. Giouroudi, C. Scheffer, E. Dillon, P. Erasmus, Anatomical study of the radius and center of curvature of the distal femoral condyle., J. Biomech. Eng. 132 (2010) 91002. doi:10.1115/1.4002061.

[268] J. Charnley, The Lubrication of Animal Joints, Symp. Biomech. (1959).

[269] M.J. Carter, I.M. Basalo, G.A. Ateshian, The temporal response of the friction coefficient of articular cartilage depends on the contact area, J. Biomech. 40 (2007) 3257–3260.

[270] T.E. Ludwig, M.M. Hunter, T.A. Schmidt, Cartilage boundary lubrication synergism is mediated by hyaluronan concentration and PRG4 concentration and structure, BMC Musculoskelet. Disord. 16 (2015) 386. doi:10.1186/s12891-015-0842-5.

[271] G.W. Greene, X. Banquy, D.W. Lee, D.D. Lowrey, J. Yu, J.N. Israelachvili, Adaptive mechanically controlled lubrication mechanism found in articular joints, Proc. Natl. Acad. Sci. 108 (2011) 5255–5259. doi:10.1073/pnas.1101002108.

[272] T.A. Schmidt, N.S. Gastelum, Q.T. Nguyen, B.L. Schumacher, R.L. Sah, Boundary lubrication of articular cartilage - Role of synovial fluid constituents, Arthritis Rheum. 56 (2007) 882–891.

[273] L. Shi, V.I. Sikavitsas, A. Striolo, Experimental friction coefficients for bovine cartilage measured with a pin-on-disk tribometer: Testing configuration and lubricant effects, Ann. Biomed. Eng. 39 (2011) 132–146. doi:10.1007/s10439-010-0167-3.

[274] R. Stribeck, Characteristics of plain and roller bearings, Zeit. VDI. 46 (1902).

[275] C. Myant, P. Cann, In contact observation of model synovial fluid lubricating mechanisms, Tribol. Int. 63 (2013) 97–104. doi:10.1016/j.triboint.2012.04.029.

[276] T.A. Schmidt, R.L. Sah, Effect of synovial fluid on boundary lubrication of articular cartilage, Osteoarthr. Cartil. 15 (2007) 35–47. doi:10.1016/j.joca.2006.06.005.

[277] K.A. Elsaid, G.D. Jay, M.L. Warman, D.K. Rhee, C.O. Chichester, Association of articular cartilage degradation and loss of boundary-lubricating ability of synovial fluid following injury and inflammatory arthritis, Arthritis Rheum. 52 (2005) 1746–1755. doi:Doi 10.1002/Art.21038.

[278] E.I. Drewniak, G.D. Jay, B.C. Fleming, J.J. Crisco, Comparison of two methods for calculating the frictional properties of articular cartilage using a simple pendulum and intact mouse knee joints, J. Biomech. 42 (2009) 1996–1999. doi:10.1016/j.jbiomech.2009.05.024.

[279] K.A. Waller, L.X. Zhang, K.A. Elsaid, B.C. Fleming, M.L. Warman, G.D. Jay, Role of lubricin and boundary lubrication in the prevention of chondrocyte apoptosis., Proc. Natl. Acad. Sci. U. S. A. 110 (2013) 5852–7. doi:10.1073/pnas.1219289110.

[280] T.A. Schmidt, R.L. Sah, Effect of synovial fluid on boundary lubrication of articular cartilage, Osteoarthr. Cartil. 15 (2007) 35–47. doi:DOI 10.1016/j.joca.2006.06.005.

[281] D. V Davies, The synovial joints of the skate (Raia)., J. Anat. 82 (1948) 9–20.3. http://www.ncbi.nlm.nih.gov/pubmed/17105050 (accessed November 8, 2016).

[282] B.J. Hamrock, D. Dowson, Isothermal Elastohydrodynamic Lubrication of Point Contacts .4. Starvation Results, Mech. Eng. 99 (1977) 142.

[283] B.J. Hamrock, D. Dowson, Isothermal Elastohydrodynamic Lubrication of Point Contacts .3. Fully Flooded Results, Mech. Eng. 99 (1977) 143.

[284] B.J. Hamrock, D. Dowson, Isothermal Elastohydrodynamic Lubrication of Point Contacts .2. Ellipticity Parameter Results, J. Lubr. Technol. Asme. 98 (1976) 375–383.

[285] C. Cooper, S. Snow, T.E. Mcalindon, S. Kellingray, B. Stuart, D. Coggon, P.A. Dieppe, Risk factors for the incidence and progression of radiographic knee osteoarthritis, Arthritis Rheum. 43 (2000) 995–1000. doi:10.1002/1529-0131.

[286] Z. Abusara, M. Von Kossel, W. Herzog, In Vivo Dynamic Deformation of

Articular Cartilage in Intact Joints Loaded by Controlled Muscular Contractions, PLoS One. 11 (2016) e0147547. doi:10.1371/journal.pone.0147547.

[287] M.R. Widmyer, G.M. Utturkar, H.A. Leddy, J.L. Coleman, C.E. Spritzer, C.T. Moorman, L.E. DeFrate, F. Guilak, High body mass index is associated with increased diurnal strains in the articular cartilage of the knee, Arthritis Rheum. 65 (2013) n/a-n/a. doi:10.1002/art.38062.

[288] V.V.C. Mow, M.M.H. Holmes, W. Lai, W. Michael Lai, Fluid transport and mechanical properties of articular cartilage: A review, J. Biomech. 17 (1984) 377–394. doi:10.1016/0021-9290(84)90031-9.

[289] A. Maroudas, Physicochemical Properties of Cartilage in Light of Ion Exchange Theory, Biophys. J. 8 (1968) 575-.

[290] A. Maroudas, P. Bullough, Permeability of Articular Cartilage, Nature. 219 (1968) 1260-.

[291] S.R. Eisenberg, A.J. Grodzinsky, Swelling of articular cartilage and other connective tissues: Electromechanochemical forces, J. Orthop. Res. 3 (1985) 148–159. doi:10.1002/jor.1100030204.

[292] M.D. Buschmann, A Molecular Model of Proteoglycan-Associated Electrostatic Forces in Cartilage Mechanics, J. Biomech. Eng. 117 (1995) 179. doi:10.1115/1.2796000.

[293] C. Canal Guterl, C.T. Hung, G.A. Ateshian, Electrostatic and non-electrostatic contributions of proteoglycans to the compressive equilibrium modulus of bovine articular cartilage, J. Biomech. 43 (2010) 1343–1350. doi:10.1016/j.jbiomech.2010.01.021.

[294] E. Han, S.S. Chen, S.M. Klisch, R.L. Sah, Contribution of proteoglycan osmotic swelling pressure to the compressive properties of articular cartilage, Biophys. J. 101 (2011) 916–924. doi:10.1016/j.bpj.2011.07.006.

[295] N.O. Chahine, F.H. Chen, C.T. Hung, G. a Ateshian, Direct measurement of osmotic pressure of glycosaminoglycan solutions by membrane osmometry at room temperature., Biophys. J. 89 (2005) 1543–1550. doi:10.1529/biophysj.104.057315.

[296] R.S. Fife, K.D. Brandt, E.M. Braunstein, B.P. Katz, K.D. Shelbourne, L.A. Kalasinski, S. Ryan, Relationship Between Arthroscopic Radiographic Evidence of Joint Space of the Knee, 34 (1991).

[297] B. Vanwanseele, E. Lucchinetti, E. Stüssi, The effects of immobilization on the characteristics of articular cartilage: current concepts and future directions, Osteoarthr. Cartil. 10 (2002) 408–419. doi:10.1053/joca.2002.0529.

[298] R. Ekholm, B.E. Ingelmark, Functional thickness variations of human articular cartilage, Acta Soc. Med. Ups. 57 (1951) 39–59.

[299] R. Ekholm, B. Norbäck, On the relationship between articular changes and function, Acta Orthop. 21 (1951) 81–98.

[300] B.E. Ingelmark, R. Ekholm, A study on variations in the thickness of articular cartilage in association with rest and periodical load; an experimental investigation on rabbits, Upsala Lakareforen. Forh. 53 (1947) 61–74.

[301] A. Maroudas, Hyaluronic Acid Films, Proc. IMechE. (1967) 122–124.

[302] A. Ogston, J. Stanier, Some effects of hyaluronidase on the hyaluronic acid of ox synovial fluid, and their bearing on the investigation of pathological fluids, J. Physiol. 119 (1953) 253. doi:10.1113/jphysiol.1953.sp004843.

[303] S.D. Taylor, E. Tsiridis, E. Ingham, Z.M. Jin, J. Fisher, S. Williams, Comparison of human and animal femoral head chondral properties and geometries, Proc. Inst. Mech. Eng. Part H-Journal Eng. Med. 226 (2012) 55–62. doi:Doi 10.1177/0954411911428717.

[304] M.A. LeRoux, J. Arokoski, T.P. Vail, F. Guilak, M.M. Hyttinen, I. Kiviranta, L.A. Setton, Simultaneous changes in the mechanical properties, quantitative collagen organization, and proteoglycan concentration of articular cartilage following canine meniscectomy, J. Orthop. Res. 18 (2000) 383–392. doi:DOI 10.1002/jor.1100180309.

[305] M.H. Naka, K. Hattori, T. Ohashi, K. Ikeuchi, Evaluation of the effect of collagen network degradation on the frictional characteristics of articular cartilage using a simultaneous analysis of the contact condition, Clin. Biomech. 20 (2005) 1111–1118. doi:DOI 10.1016/j.clinbiomech.2005.06.009.

[306] J. Toyras, J. Rieppo, M.T. Nieminen, H.J. Helminen, J.S. Jurvelin, Characterization of enzymatically induced degradation of articular cartilage using high frequency ultrasound, Phys. Med. Biol. 44 (1999) 2723–2733.

[307] I.M. Basalo, D. Raj, R. Krishnan, F.H. Chen, C.T. Hung, G.A. Ateshian, Effects of enzymatic degradation on the frictional response of articular cartilage in stress relaxation, J. Biomech. 38 (2005) 1343–1349. doi:10.1016/j.jbiomech.2004.05.045.

[308] I.M. Basalo, F.H. Chen, C.T. Hung, G.A. Ateshian, Frictional response of bovine articular cartilage under creep loading following proteoglycan digestion with chondroitinase ABC, J. Biomech. Eng. Asme. 128 (2006) 131–134. doi:Doi 10.1115/1.2133764.

[309] I.M. Basalo, D. Raj, R. Krishnan, F.H. Chen, C.T. Hung, G.A. Ateshian, Effects of enzymatic degradation on the frictional response of articular cartilage in stress relaxation, J. Biomech. 38 (2005) 1343–1349. doi:DOI 10.1016/j.jbiomech.2004.05.045.

[310] R.K. June, D.P. Fyhrie, Enzymatic digestion of articular cartilage results in viscoelasticity changes that are consistent with polymer dynamics mechanisms, Biomed. Eng. Online. 8 (2009) 32. doi:10.1186/1475-925X-8-32.

[311] R. Ekholm, B. Norbxck, On the relationship between articular changes and function, Acta Orthop. Scand. (1951). http://www.tandfonline.com/doi/pdf/10.3109/17453675109024145 (accessed April 25, 2017).

[312] D.R. Haidar, J. Ye, A.C. Moore, D.L. Burris, Assessing quantitative metrics of transfer film quality as indictors of polymer wear performance, Wear. 380–381 (2017) 78–85. doi:10.1016/j.wear.2017.03.012.

Appendix A

Supplemental Methods

A.1 Effects of Dehydration
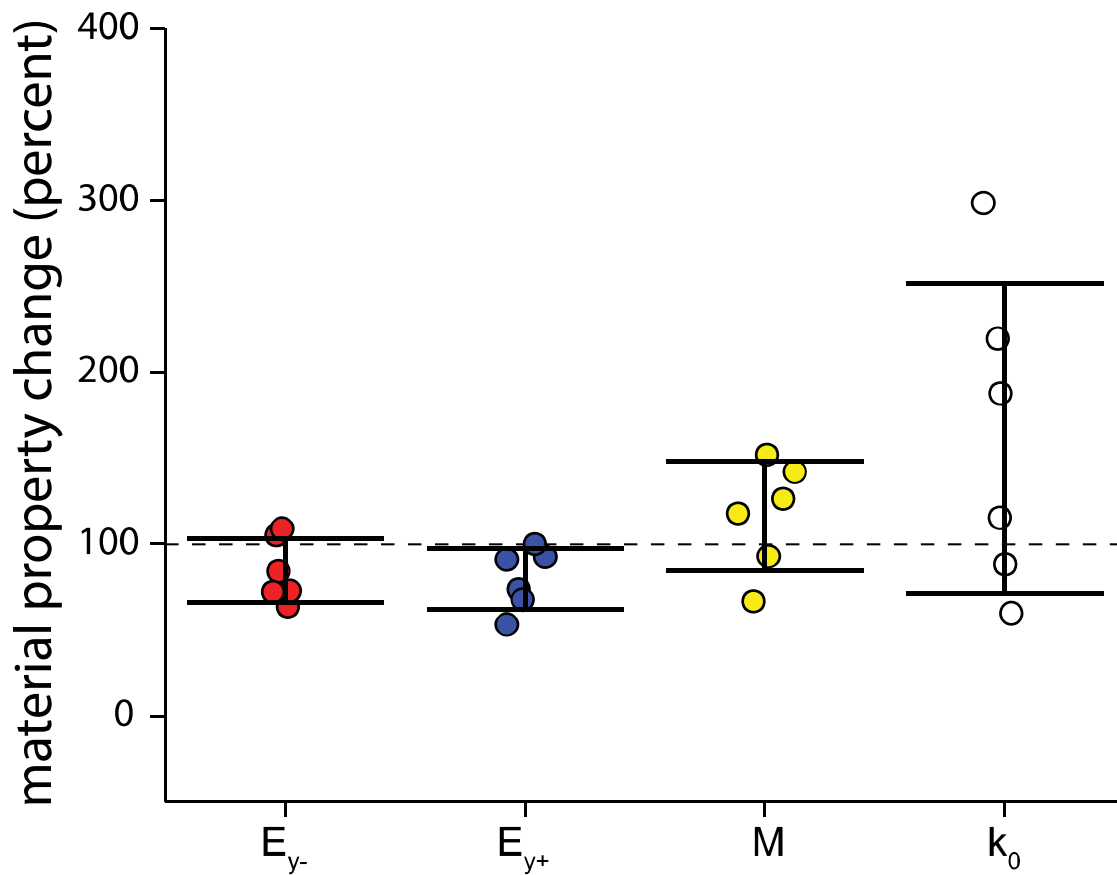
Figure A1. Six samples were evaluated for their material properties before and after dehydration and rehydration. Data are plotted as the percent change due to dehydration. Error bars represent the 95% confidence interval. Only the tensile modulus (E_{y+}) is significantly ($p < 0.05$, paired t-test) altered during tissue rehydration.

Dehydration has been shown to be an effective method of preserving cartilage samples. In Figure A1 six samples were dehydrated followed by rehydration and compared to their initial condition. The results suggest a slight decrease in the tensile (E_{y+}) and compressive modulus (E_{y-}); and a slight increase in the flow limiting constant (M) and unstrained permeability (k_0). While tissue dehydration may an effect on material properties the changes are well within the normal spatial variability of articular joints [6,89].

A.2   G-Code

An example G-code program is listed below for milling osteochondral cores from 19 mm to 12.7 mm diameter (Figure A2). To alter the script and cut a 6.35 mm diameter tissue core the g02 command lines are replaced with *g02 x-.203125 y0 i0 j0*.

```
g00 x0 y0 z0 f8

g01 x-.318125

f2

g01 z-.1

g02 x-.318125 y0 i0 j0

g01 z-.2

g02 x-.318125 y0 i0 j0
```

Figure A2. G-code script to cut a 12.7 mm diameter cylinder with a 4 mm diameter milling bit. Depth of cut was 2 steps of 2.54 mm for a total cut depth of 5.08 mm.

A.3 Profilometry Scan
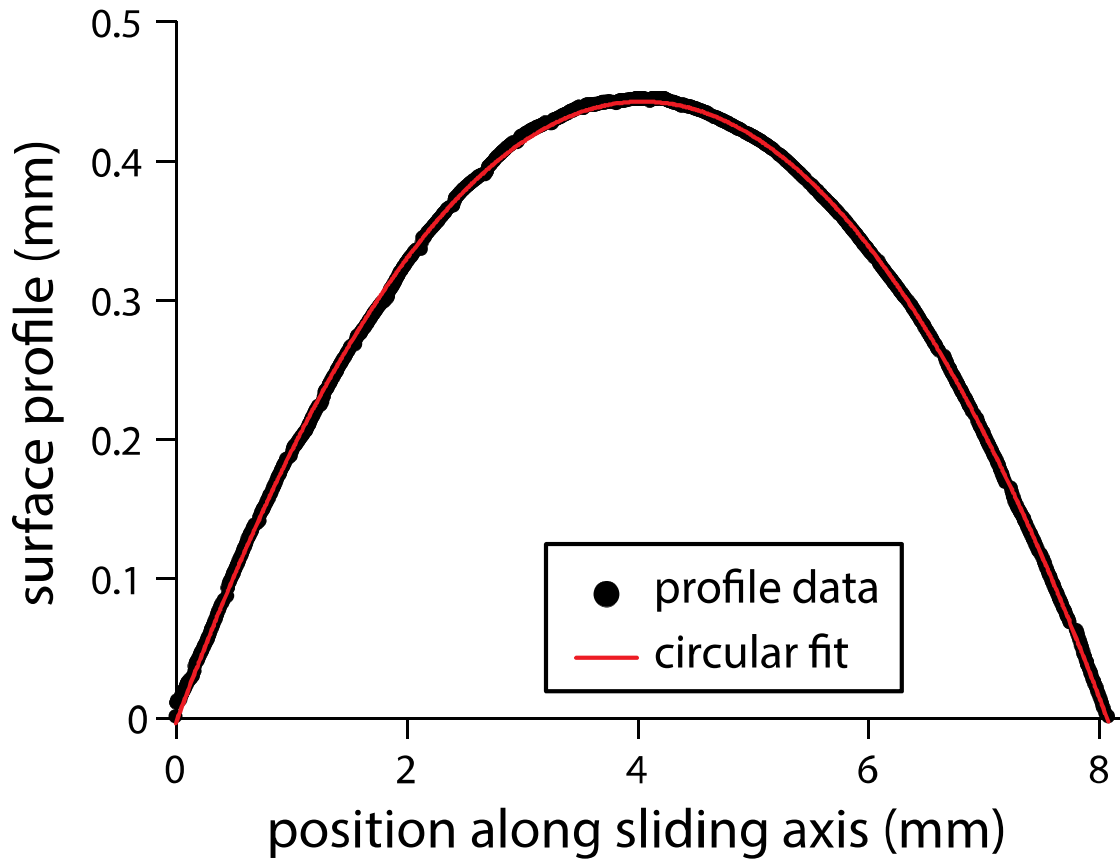
Figure A3. A representative profilometry scan of articular cartilage. The sample was scanned with the spherical micro-tribometer under ~5 mN load. The scanning head was a 6.35 mm dimeter borosilicate glass sphere.

A representative cartilage plug scan is shown in Figure A3. Due to the limited travel of the spherical micro-tribometer the maximum scan size was 8 mm. Furthermore, the vertical travel of the stage was limited to 800 μm. The scanning head was a 6.35 mm dimeter borosilicate glass sphere. The use of a large sphere produced a relatively large contact that made the measure less sensitive to the small scale topography and more sensitive to the gross curvature [312]. Furthermore, the scan speed which had to be maintained at a low value (0.12 mm/s) to not over run the

vertical re-positioning stage (load control) was likely insufficient to maintain peak IFP and thus the profile shown is a combination of both the elastic and flow-dependent deformation.

A.4   Long Term Equilibration
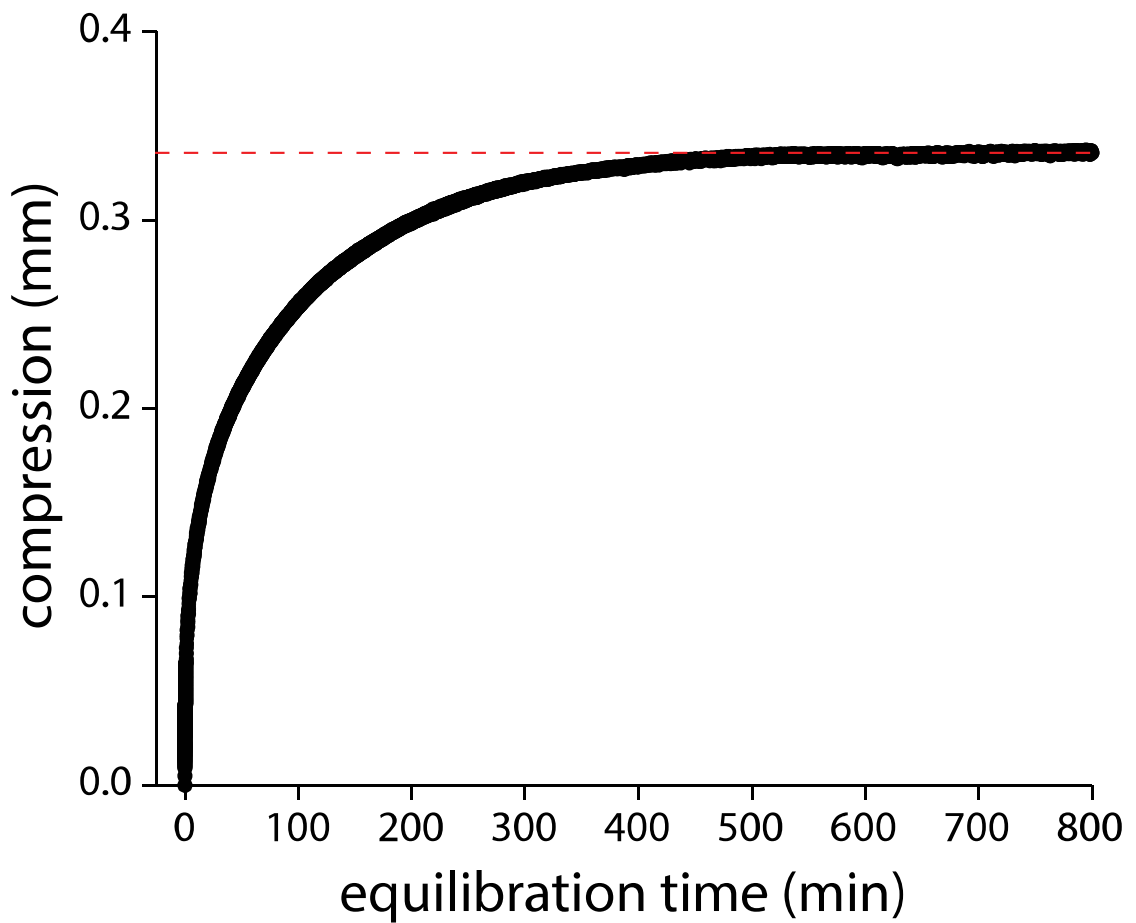
Figure A4.   A representative equilibration curve for a sample loaded on the pin on disc materials tester. The sample was equilibrated under a 2.5 N static load for more than 13 hours.

To demonstrate that long term equilibration and bath replenishment produced a stable and normal equilibration response a representative sample was plotted in Figure A4. As demonstrated by the figure it took nearly 8 hours for the sample to reach equilibrium; thereafter the sample maintained a constant level of compression. The equilibration time varied from sample to sample and was generally between 3 and 10 hours. These long periods of equilibration demonstrate why most studies in the literature have avoided using large osteochondral cores. The results further demonstrate that the deionized water feed system described in section *10.2.3 Pin on Disc Materials Tester* did not greatly alter the bath salinity, an effect that would manifest as a continuous increase or decrease in compression. This transient effect has been observed previously when the system feed rate was insufficient or excessive.

Appendix B

Supplemental Results

B.1   Material Properties and Profilometry

Table B1.   Material properties of each sample used in Chapter 9. Table is adapted with permission [215].

sample number	sample diameter (mm)	equilibrium modulus (MPa)	tensile modulus (MPa)	permeability (mm^4/Ns)	tissue thickness (mm)	radius of curvature (mm)
1	19	0.77	4.08	0.00101	0.991	N/A
2	6.35	0.77	4.08	0.00101	0.991	N/A
3	19	0.42	2.64	0.00161	1.81	N/A
4	19	1.89	14.2	0.00040	1.35	16.4
5	12.7	1.29	13.7	0.00057	0.85	20.5
6	12.7	0.66	7.3	0.00114	0.77	33.8

The material properties, tissue thickness, and radius of curvature for each sample used in Chapter 9 are listed in Table B1. The samples are listed in no particular order with reference to the text. The properties demonstrate that a representative and diverse sample population was used to demonstrate the findings and conclusions of this work.

B.2   Ramp-Up & Ramp-Down
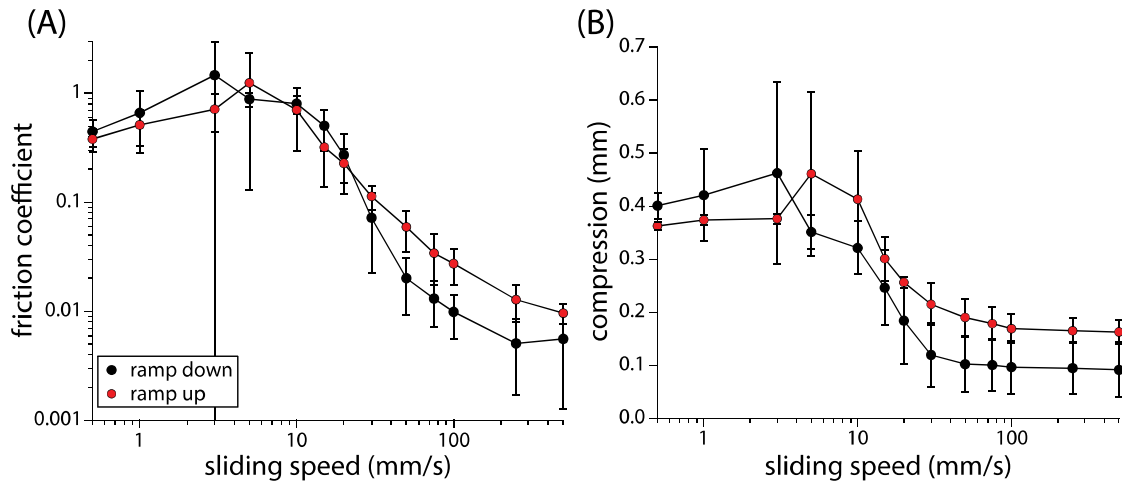
Figure B1. (A) Friction coefficient and (B) compression versus sliding speed in a ramp down ramp up experiment. Data is plotted as the mean ± 95% confidence interval for N=3 samples. Experiments were performed on the pin on disc materials tester, section *10.2.3 Pin on Disc Materials Tester*.

A ramp-down (500 to 0.5 mm/s) followed by a ramp-up (0.5 to 500 mm/s) experiment was conducted on N=3 samples. The results are shown in Figure B1. The data demonstrate that in general the tribological response is preserved regardless of the speed sweep direction. It is worth noting that in general the ramp-down (500 to 0.5 mm/s) produced the lowest friction coefficients and compression. Furthermore, the ramp-down protocol appears to achieve peak friction and deformation at a lower speed. While this effect is not significantly different, which could be due to an insufficient sample size, it provides an interesting area of exploration. Potential contributors to this asymmetry in the tribological response are degradation based effects due to the long (36+ hours) testing durations and/or damage (wear) related effects caused by the transition from lubricious high-speed sliding to low speed (high friction) conditions.

B.3 Solute Accumulation
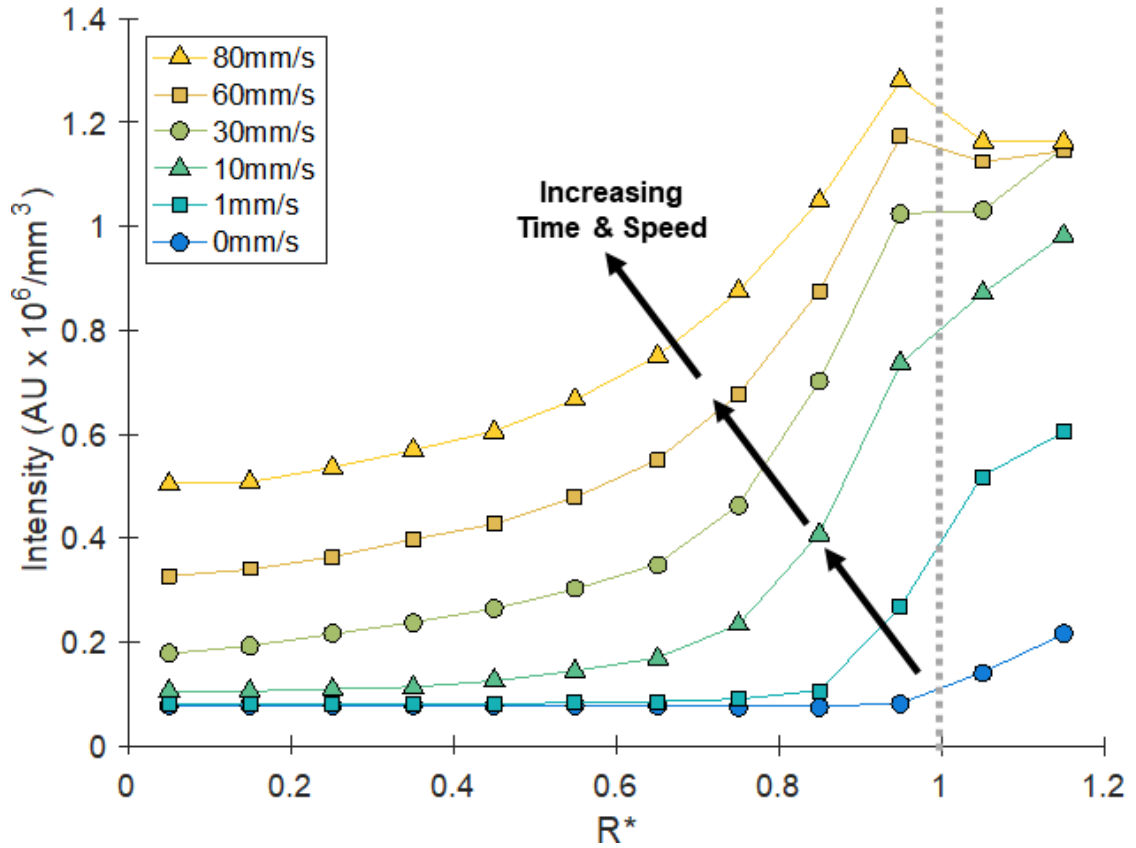
Figure B.2   Accumulated solute intensity as a function of dimensionless contact radius $R^* = r/a$, where r is the radial position and a is the contact radius. The sample was slid for 2 min intervals at increasing sliding speed. Image is adapted with permission [264].

A recent study by Graham et al. investigated the propagation of solute into cartilage during sliding in the cSCA contact [264]. Figure B.2 demonstrates that at slow sliding speeds solute accumulation is low and isolated to the edge of contact. As the speed increases toward physiological values the solute intensity increases and

makes its way toward the center of contact. The fact that the gradient is always from the edge of contact toward the center of contact suggests solute (fluid) flows from the contact periphery towards the center.

Appendix C

Figure and Text Reuse Permissions

C.1 Figure and Text Reuse Permissions

M Gmail

Axel Moore <axelcmoore@gmail.com>

Requesting Permission for Figure Use in Thesis [ref:_00DU0lfis,_5000BbrU3n:ref]

plosone <plosone@plos.org>
To: "axelcmoore@gmail.com" <axelcmoore@gmail.com>

Fri, Jun 2, 2017 at 7:15 AM

Dear Dr. Moore,

Thank you for your message. PLOS ONE publishes all of the content in the articles under an open access license called "CC-BY." This license allows you to download, reuse, reprint, modify, distribute, and/or copy articles or images in PLOS journals, so long as the original creators are credited (e.g., including the article's citation and/or the image credit). Additional permissions are not required. You can read about our open access license here: http://journals.plos.org/plosone/s/licenses-and-copyright

There are many ways to access our content, including HTML, XML, and PDF versions of each article. Higher resolution versions of figures can be downloaded directly from the article.

Thank you for your interest in PLOS ONE and for your continued support of the Open Access model. Please do not hesitate to be in touch with any additional questions.

Kind regards,

Emma Darkin
Staff EO
PLOS ONE

Case Number: 05237477

──────── Original Message ────────
From: Axel Moore [axelcmoore@gmail.com]
Sent: 01/06/2017
To: plosone@plos.org
Subject: Requesting Permission for Figure Use in Thesis

Hello PLOS One,

I am sorry I couldn't figure this out on your website but I am trying to request permission to use a figure in my thesis.

The publication is titled: Elastoviscous Transitions of Articular Cartilage Reveal a Mechanism of Synergy between Lubricin and Hyaluronic Acid. Published in 2015 with the DOI: 10.1371/journal.pone.0143415 <https://doi.org/10.1371/journal.pone.0143415>. I am not the author of this article, I am requesting to use Figure 2B. The figure will not be modified in anyway.

The figure will appear in my thesis titled: Tribological Rehydration: Sliding Induced Fluid Recovery of Articular Cartilage. My thesis will be submitted in July 2017 through the University of Delaware.

Thank you for your time and consideration,

Best,
Axel

Figure C1.   Figure permission for ref [77].

C.2   Figure and Text Reuse Permissions

227

Figure C2.   Figure and text permission for ref [28].

C.3   Figure and Text Reuse Permissions

Copyright Clearance Center

RightsLink®

Account Info   Help

Title:	Journal of tribology	Logged in as:
Article ID:	0742-4787	Axel Moore
Publication:	Publication1	Account #:
Publisher:	CCC Republication	3001149655
Date:	Jan 1, 1984	LOGOUT
Copyright © 1984, CCC Republication		

Order Completed

Thank you for your order.

This Agreement between Axel C Moore ("You") and American Society of Mechanical Engineers ASME ("American Society of Mechanical Engineers ASME") consists of your order details and the terms and conditions provided by American Society of Mechanical Engineers ASME and Copyright Clearance Center.

License number	Reference confirmation email for license number
License date	Jun, 02 2017
Licensed content publisher	American Society of Mechanical Engineers ASME
Licensed content title	Journal of tribology
Licensed content date	Jan 1, 1984
Type of use	Thesis/Dissertation
Requestor type	Academic institution
Format	Print, Electronic
Portion	chapter/article
Title or numeric reference of the portion(s)	Entire article: Quantifying Cartilage Contact Modulus, Tension Modulus, and Permeability With Hertzian Biphasic Creep
Title of the article or chapter the portion is from	Entire article: Quantifying Cartilage Contact Modulus, Tension Modulus, and Permeability With Hertzian Biphasic Creep
Editor of portion(s)	N/A
Author of portion(s)	N/A
Volume of serial or monograph	N/A
Page range of portion	
Publication date of portion	July 2017
Rights for	Main product
Duration of use	Life of current edition
Creation of copies for the disabled	no
With minor editing privileges	yes
For distribution to	Worldwide
In the following language(s)	Original language of publication
With incidental promotional use	no
Lifetime unit quantity of new product	Up to 499
Made available in the following markets	Education
Specified additional information	I am requesting to use, edit, re-write the published work in my dissertation to be submitted through the University of Delaware in July 2017.
The requesting person/organization	Moore, Axel
Order reference number	
Author/Editor	Moore, Axel

Figure C3.   Figure and text permission for ref [27].

C.4   Figure and Text Reuse Permissions

ELSEVIER LICENSE
TERMS AND CONDITIONS

Jun 01, 2017

This Agreement between Axel C Moore ("You") and Elsevier ("Elsevier") consists of your license details and the terms and conditions provided by Elsevier and Copyright Clearance Center.

License Number	4120310788954
License date	Jun 01, 2017
Licensed Content Publisher	Elsevier
Licensed Content Publication	Journal of Biomechanics
Licensed Content Title	Lubrication mode analysis of articular cartilage using Stribeck surfaces
Licensed Content Author	Jason P. Gleghorn, Lawrence J. Bonassar
Licensed Content Date	Jan 1, 2008
Licensed Content Volume	41
Licensed Content Issue	9
Licensed Content Pages	9
Start Page	1910
End Page	1918
Type of Use	reuse in a thesis/dissertation
Intended publisher of new work	other
Portion	figures/tables/illustrations
Number of figures/tables/illustrations	1
Format	both print and electronic
Are you the author of this Elsevier article?	No
Will you be translating?	No
Order reference number	
Original figure numbers	Fig 3B
Title of your thesis/dissertation	Tribological Rehydration: Sliding Induced Fluid Recovery of Articular Cartilage
Expected completion date	Jul 2017
Estimated size (number of pages)	90
Elsevier VAT number	GB 494 6272 12
Requestor Location	Axel C Moore 130 Academy Street 126 Spencer Lab NEWARK, DE 19716 United States Attn: Axel C Moore

Figure C4.   Figure permission for ref [251].

C.5   Figure and Text Reuse Permissions

**ELSEVIER LICENSE
TERMS AND CONDITIONS**

Jun 01, 2017

This Agreement between Axel C Moore ("You") and Elsevier ("Elsevier") consists of your license details and the terms and conditions provided by Elsevier and Copyright Clearance Center.

License Number	4120300575959
License date	Jun 01, 2017
Licensed Content Publisher	Elsevier
Licensed Content Publication	Tribology International
Licensed Content Title	Experimental characterization of biphasic materials using rate–controlled Hertzian indentation
Licensed Content Author	A.C. Moore,B.K. Zimmerman,X. Chen,X.L. Lu,D.L. Burris
Licensed Content Date	Sep 1, 2015
Licensed Content Volume	89
Licensed Content Issue	n/a
Licensed Content Pages	7
Start Page	2
End Page	8
Type of Use	reuse in a thesis/dissertation
Intended publisher of new work	other
Portion	full article
Format	both print and electronic
Are you the author of this Elsevier article?	Yes
Will you be translating?	No
Order reference number	
Title of your thesis/dissertation	Tribological Rehydration: Sliding Induced Fluid Recovery of Articular Cartilage
Expected completion date	Jul 2017
Estimated size (number of pages)	90
Elsevier VAT number	GB 494 6272 12
Requestor Location	Axel C Moore 130 Academy Street 126 Spencer Lab NEWARK, DE 19716 United States Attn: Axel C Moore
Publisher Tax ID	98-0397604
Total	0.00 USD

Figure C5. Figure and text permission for ref [26].

C.6 Figure and Text Reuse Permissions

ELSEVIER ORDER DETAILS

Jun 01, 2017

Order Number	501275438
Order date	Jun 01, 2017
Licensed Content Publisher	Elsevier
Licensed Content Publication	Osteoarthritis and Cartilage
Licensed Content Title	Tribological rehydration of cartilage and its potential role in preserving joint health
Licensed Content Author	A.C. Moore, D.L. Burris
Licensed Content Date	January 2017
Licensed Content Volume	25
Licensed Content Issue	1
Licensed Content Pages	9
Start Page	99
End Page	107
Type of Use	reuse in a thesis/dissertation
Intended publisher of new work	other
Portion	full article
Format	both print and electronic
Are you the author of this Elsevier article?	Yes
Will you be translating?	No
Order reference number	
Title of your thesis/dissertation	Tribological Rehydration: Sliding Induced Fluid Recovery of Articular Cartilage
Expected completion date	Jul 2017
Estimated size (number of pages)	90
Elsevier VAT number	GB 494 6272 12
Requestor Location	Axel C Moore 130 Academy Street 126 Spencer Lab NEWARK, DE 19716 United States Attn: Axel C Moore
Publisher Tax ID	98-0397604
Total	Not Available

Figure C6.   Figure and text permission for ref [215].

C.7 Figure and Text Reuse Permissions

ELSEVIER ORDER DETAILS

Jun 01, 2017

Order Number	501275426
Order date	Jun 01, 2017
Licensed Content Publisher	Elsevier
Licensed Content Publication	Osteoarthritis and Cartilage
Licensed Content Title	Tribological and material properties for cartilage of and throughout the bovine stifle: support for the altered joint kinematics hypothesis of osteoarthritis
Licensed Content Author	A.C. Moore, D.L. Burris
Licensed Content Date	January 2015
Licensed Content Volume	23
Licensed Content Issue	1
Licensed Content Pages	9
Start Page	161
End Page	169
Type of Use	reuse in a thesis/dissertation
Intended publisher of new work	other
Portion	full article
Format	both print and electronic
Are you the author of this Elsevier article?	Yes
Will you be translating?	No
Order reference number	
Title of your thesis/dissertation	Tribological Rehydration: Sliding Induced Fluid Recovery of Articular Cartilage
Expected completion date	Jul 2017
Estimated size (number of pages)	90
Elsevier VAT number	GB 494 6272 12
Requestor Location	Axel C Moore 130 Academy Street 126 Spencer Lab NEWARK, DE 19716 United States Attn: Axel C Moore
Publisher Tax ID	98-0397604
Total	Not Available

Figure C7.   Figure and text permission for ref [6].